

DE GRUYTER

Ponnadurai Ramasami (Ed.)

DENSITY FUNCTIONAL THEORY

ADVANCES IN APPLICATIONS

Copyright
except for the
material
reproduced
herein
under
the
terms
of the
Creative
Commons
Attribution
3.0 licence
http://creativecommons.org/licenses/by/3.0/

DE GRUYTER Publishing : eBook collection (EBSCO) : 10.1515/9783110433514_001 : Ponnadurai Ramasami : Density Functional Theory : Advances in Applications : 9783110433514

Ponnadurai Ramasami (Ed.)
Density Functional Theory

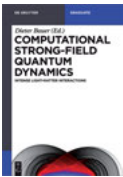
Also of interest



Computational Sciences

Ramasami (Ed.), 2017

ISBN 978-3-11-046536-5, e-ISBN 978-3-11-046721-5



Computational Strong-Field Quantum Dynamics Intense Light-Matter Interactions

Bauer (Ed.), 2017

ISBN 978-3-11-041725-8, e-ISBN 978-3-11-041726-5

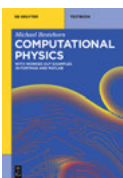


Optimal Structural Design

Contact Problems and High-Speed Penetration

Banichuk, Ivanova, 2017

ISBN 978-3-11-053080-3, e-ISBN 978-3-11-053118-3



Computational Physics

With Worked Out Examples in FORTRAN and MATLAB

Besthorn, 2018

ISBN 978-3-11-051513-8, e-ISBN (PDF) 978-3-11-051514-5



Physical Sciences Reviews.

e-ISSN 2365-659X

Density Functional Theory



Advances in Applications

Edited by
Ponnadurai Ramasami

DE GRUYTER

Editor

Prof. Dr. Ponnadurai Ramasami

University of Mauritius

Department of Chemistry

Réduit 80837

Mauritius

p.ramasami@uom.ac.mu

Department of Chemistry

College of Science, Engineering and Technology

University of South Africa

South Africa

ISBN 978-3-11-056675-8

e-ISBN (PDF) 978-3-11-056819-6

e-ISBN (EPUB) 978-3-11-056695-6

Library of Congress Control Number: 2018961307

Bibliographic information published by the Deutsche Nationalbibliothek

The Deutsche Nationalbibliothek lists this publication in the Deutsche Nationalbibliografie; detailed bibliographic data are available on the Internet at <http://dnb.dnb.de>.

© 2019 Walter de Gruyter GmbH, Berlin/Boston

Typesetting: Integra Software Services Pvt. Ltd.

Printing and binding: CPI books GmbH, Leck

Cover image: noLimit46/iStock/Getty Images Plus

www.degruyter.com

Preface

A virtual conference on computational science (VCCS-2017) was organized online from 1st to 31st August 2017. This was the fifth virtual conference which was started in 2013. The month of August was chosen to commemorate the birth anniversary of Erwin Schrödinger, the father of quantum mechanics, on 12th August.

There were 25 presentations for the virtual conference with 110 participants from 15 countries. A secured platform was used for virtual interactions of the participants. After the virtual conference, there was a call for full papers to be considered for publication in the conference proceedings. Manuscripts were received and they were processed and reviewed as per the policy of De Gruyter.

This book is a collection of the eleven accepted manuscripts based on density functional theory method. These manuscripts cover a range of topics from fundamental to applied science using computational methods. Chowdhury and Jana studied the optical properties of monolayer BeC under an external electric field. Rhyman *et al.* performed computations on the derivatives of Favipiravir as potential drugs for Ebola virus. Gümüş and Gümüş investigated the structural and electronic properties of a series of dicyano dibenzo[f,h]quinoxaline using different functionals and the 6-311+G(d,p) basis set. Mulwa and Dejeune synthesized and investigated γ -Al₂O₃:Ce³⁺Cu²⁺ as a phosphor material. Dhar and Jana analyzed the optical properties of defected germanene mono-layer. Gulati and Kakkar studied on the storage and adsorption capacities of gases on metal-organic frameworks. Ouma and Meyer probed the metastability of the boron-vacancy complex in silicon. Kavitha *et al.* explored the molecular structure and vibrational spectra of 2-(4-bromophenyl)-3-(4-hydroxyphenyl)1,3-thiazolidin-4-one and its selenium analogue. Kuznetsov studied the complex formation between the core-modified ZnP(X)₄ (X=P and S) without any substituents or linkers and semiconductors Zn₆S₆ nanoparticles. Palafox analyzed the scaling procedures to improve wave numbers of vibrational spectra. Sekar *et al.* reported on the substituent effects on linear and nonlinear optical properties of fluorescent (E)-2-(4-halophenyl)-7-arylstyrylimidazo[1,2-a]pyridine.

I hope that these chapters will add to literature and they will be useful references.

To conclude, VCCS-2017 was a successful event and I would like to thank all those who have contributed. I would also like to thank the Organising and International Advisory committee members, the participants and the reviewers.

Prof. Ponnadurai Ramasami

Contents

Preface — V

List of Contributing authors — XIII

Suman Chowdhury and Debnarayan Jana

**1 Optical properties of monolayer BeC under an external electric field:
A DFT approach — 1**

- 1.1 Introduction — 1
- 1.2 Computational details — 2
- 1.3 Results and discussion — 4
 - 1.3.1 Electronic properties — 4
 - 1.3.2 Optical properties — 5
- 1.4 Conclusions — 14
- References — 15

Lydia Rhyman, Mahir Tursun, Hassan H. Abdallah, Yee Siew Choong, Cemal Parlak, Prashant Kharkar and Ponnadurai Ramasami

**2 Theoretical investigation of the derivatives of favipiravir (T-705) as
potential drugs for Ebola virus — 19**

- 2.1 Introduction — 20
- 2.2 Methodology — 20
 - 2.2.1 Ab initio — 20
- 2.3 Docking — 21
 - 2.3.1 Protein structure — 21
 - 2.3.2 Ligand structure — 21
 - 2.3.3 Molecular docking simulation — 21
- 2.4 Results and discussion — 21
- 2.5 Vibrational studies — 25
- 2.6 Electronic spectrum — 26
- 2.7 Molecular docking — 29
- 2.8 Conclusions — 30
- References — 31

Ayşegül Gümüş and Selçuk Gümüş

**3 Potential thermally activated delayed fluorescence properties of a series
of 2,3-dicyanopyrazine based compounds — 33**

- 3.1 Introduction — 33
- 3.2 Method of calculation — 35
- 3.3 Results and discussion — 36

- 3.3.1 Semiconductor properties — 38
- 3.3.2 TADF properties — 42
- 3.4 Conclusion — 45
- References — 45

Winfred Mueni Mulwa and Francis Birhanu Dejene

4 γ -Al₂O₃:Ce³⁺Cu²⁺ as a phosphor material; DFT+U and experimental approach — 49

- 4.1 Introduction — 49
- 4.2 Methodology — 50
 - 4.2.1 Experimental details — 50
 - 4.2.2 Computational details — 51
- 4.3 Results and discussion — 52
 - 4.3.1 X-ray diffraction (XRD) and XCrySDen analysis — 53
 - 4.3.2 SEM analysis — 55
 - 4.3.3 HR-TEM analysis — 56
 - 4.3.4 Energy dispersive X-ray spectroscopy (EDS) analysis — 56
 - 4.3.5 Electronic analysis — 57
 - 4.3.6 Optical analysis — 59
 - 4.3.7 Charge density — 60
 - 4.3.8 Conclusion — 61
 - References — 62

Namrata Dhar and Debnarayan Jana

5 A DFT perspective analysis of optical properties of defected germanene mono-layer — 65

- 5.1 Introduction — 65
- 5.2 Computational methodology — 68
- 5.3 Results and discussions — 69
 - 5.3.1 Geometric optimization — 69
 - 5.3.2 Optical properties of arsenic and gallium doped germanene — 72
 - 5.3.3 Optical properties of beryllium doped and vacancy induced germanene — 74
- 5.4 Comparison between As, Ga and Be doped germanene systems — 78
- 5.5 Conclusions and future directions — 78
- References — 79

Archa Gulati and Rita Kakkar

6 DFT studies on storage and adsorption capacities of gases on MOFs — 83

- 6.1 Introduction — **83**
- 6.2 Water stability of MOFs — **85**
- 6.2.1 DFT studies — **86**
- 6.3 Adsorption and storage of fuel gases in MOFs — **87**
- 6.3.1 Hydrogen (H₂) gas — **88**
- 6.3.2 Methane (CH₄) — **94**
- 6.3.3 Acetylene (C₂H₂) — **99**
- 6.4 Capture and separation of the carbon dioxide (CO₂) gas in MOFs — **99**
- 6.4.1 Computational modeling for CO₂ capture — **101**
- 6.4.2 CO₂ separation in MOFs — **103**
- 6.5 Conclusions — **105**
- References — **106**

Cecil NM Ouma and Walter E Meyer

7 Metastability of the boron-vacancy complex in silicon: Insights from hybrid functional calculations — 113

- 7.1 Introduction — **113**
- 7.2 Computation details — **114**
- 7.3 Results and discussion — **115**
- 7.4 Conclusion — **120**
- References — **120**

Helen P. Kavitha, Lydia Rhyman and Ponnadurai Ramasami

8 Molecular structure and vibrational spectra of 2-(4-bromophenyl)-3-(4-hydroxyphenyl) 1,3-thiazolidin-4-one and its selenium analogue: Insights using HF and DFT methods — 123

- 8.1 Introduction — **123**
- 8.2 Computational method — **124**
- 8.3 Results and discussion — **124**
- 8.3.1 Structural parameters — **124**
- 8.3.2 Vibrational frequencies — **128**
- 8.3.3 Atomic charges — **128**
- 8.3.4 Molecular orbitals surfaces — **129**
- 8.3.5 Natural bond orbital analysis (NBO) — **130**
- 8.4 Conclusions — **131**
- References — **131**

Aleksey E. Kuznetsov

9 Complexes between core-modified porphyrins $ZnP(X)_4$ ($X = P$ and S) and small semiconductor nanoparticle Zn_6S_6 : are they possible? — 135

- 9.1 Introduction — 136
- 9.2 Results and discussion — 138
 - 9.2.1 Structural features of the Zn_6S_6 - $ZnP(X)_4$ complexes — 138
 - 9.2.2 Binding energies in the Zn_6S_6 - $MP(X)_4$ complexes — 140
 - 9.2.3 NBO charges in the Zn_6S_6 - $MP(X)_4$ complexes — 140
- 9.3 Conclusions and perspectives — 141
- References — 143

M. Alcolea Palafox

10 DFT computations on vibrational spectra: Scaling procedures to improve the wavenumbers — 147

- 10.1 Introduction — 147
- 10.2 DFT methods — 149
- 10.3 Wavenumber calculation — 152
 - 10.3.1 Error in the calculated wavenumbers — 153
- 10.4 Scaling procedures for the wavenumbers — 156
 - 10.4.1 Procedures based on scaling the force constants — 160
 - 10.4.2 Procedures based on scaling the wavenumbers directly — 162
 - 10.4.3 Anharmonic calculation of the wavenumbers — 180
 - 10.4.4 Wavenumber corrections for the experimental solid state sample — 181
- 10.5 Summary and conclusions — 183
- References — 185

Siddheshwar D. Jadhav, Ponnadurai Ramasami and Nagaiyan Sekar

11 Substituent effects on linear and nonlinear optical properties of fluorescent (E)-2-(4-halophenyl)-7-arylstyrylimidazo[1,2-A] pyridine: spectroscopic and computational methods — 193

- 11.1 Introduction — 194
- 11.2 Materials and methods — 195
 - 11.2.1 Material and theoretical methods — 195
- 11.3 Results and discussion — 196
 - 11.3.1 Absorption, vertical excitation and computed emission — 196
 - 11.3.2 Estimation of difference in dipole moments ($\mu_e - \mu_g$) — 200
 - 11.3.3 Frontier molecular orbitals (FMOs) of the push-pull chromophores — 203
 - 11.3.4 Mulliken charges analysis — 204
 - 11.3.5 Natural bond orbital — 205

11.4	NLO properties — 208
11.4.1	NLO properties by Solvatochromic method — 208
11.4.2	NLO properties by DFT method — 210
11.4.3	Solvent polarity effect — 210
11.4.4	Effect of alkylamino substitution group — 212
11.4.5	Effect of replacement of bromo with chloro group — 215
11.4.6	Fundamental limits and intrinsic NLO properties — 215
11.4.7	Two-photon absorption cross section — 218
11.5	Vibrational and electronic nonlinear optical properties — 219
11.6	Linear and nonlinear properties trends and correlation with bond length alternation (BLA) and bond order alternation (BOA) — 219
11.7	Conclusion — 222
	References — 223

Index	— 229
--------------	--------------

List of Contributing authors

Debnarayan Jana

Department of Physics
University of Calcutta
92 A.P.C Road
Kolkata -700009, India,
cujanad@yahoo.com
Chapter 1, 5

Suman Chowdhury

Department of Physics,
Bangabasi College,
19, Rajkumar Chakraborty Sarani,
Kolkata 700009, W.B., India,
sumanchowdhury88@gmail.com
Chapter 1

Lydia Rhyman

University of Mauritius,
Computational Chemistry Group,
Department of Chemistry,
Faculty of Science,
80837 Réduit, Mauritius,
lyd.rhyman@gmail.com
Chapter 2, 8

Mahir Tursun

Department of Physics,
Science Faculty,
Anadolu University,
Eskişehir, 26470, Turkey
Chapter 2

Hassan H. Abdallah

Chemistry Department,
College of Education,
Salahaddin University,
Erbil, Iraq
Chapter 2

Yee Siew Choong

Institute for Research in Molecular Medicine
(INFORMM),
Universiti Sains Malaysia,
Malaysia
Chapter 2

Cemal Parlak

Department of Physics, Science Faculty,
Ege University,
İzmir, Bornova, 35100,
Turkey
Chapter 2

Prashant Kharkar

SPP School of Pharmacy and Technology
Management,
SVKM's NMIMS,
V. L. Mehta Road, Vile Parle (West),
Mumbai-400056, India
Chapter 2

Ponnadurai Ramasami

University of Mauritius,
Computational Chemistry Group,
Department of Chemistry,
Faculty of Science,
80837 Réduit, Mauritius
p.ramasami@uom.ac.mu
Chapter 2, 8, 11

Selçuk Gümüş

Faculty of Science,
Department of Chemistry,
Van Yuzuncu Yil University,
65080, Van, Turkey,
gumuss@gmail.com
Chapter 3

Ayşegül Gümüş

Faculty of Science,
Department of Chemistry,
Van Yuzuncu Yil University,
65080, Van, Turkey,
Chapter 3

Winfred Mueni Mulwa

Department of Physics,
University of the Free State-Qwaqwa Campus,
Private Bag x13,
Phuthaditjhaba 9866, South Africa,
mulwawinfred@gmail.com
Chapter 4

<https://doi.org/10.1515/9783110568196-202>

XIV — List of Contributing authors

Francis Birhanu Dejene

Department of Physics,
University of the Free State-Qwaqwa Campus,
Private Bag x13,
Phuthaditjhaba 9866, South Africa,
Chapter 4

Namrata Dhar

Department of Physics
University of Calcutta
92 A.P.C Road
Kolkata -700009, India,
Chapter 5

Rita Kakkar

Computational Chemistry Laboratory,
Department of Chemistry,
University of Delhi,
Delhi 110007, India,
rkakkar@chemistry.du.ac.in,
Chapter 6

Archa Gulati

Computational Chemistry Laboratory,
Department of Chemistry,
University of Delhi,
Delhi 110007, India,
Chapter 6

Cecil NM Ouma

Faculty of Engineering,
HySA Infrastructure CoC,
North-West University,
Private Bag X6001,
Potchefstroom, 2531, South Africa,
moronaphtaly84@gmail.com
Chapter 7

Walter E Meyer

Department of Physics,
University of Pretoria,
Private Bag X20,
Pretoria 0028, South Africa
Chapter 7

Helen Kavitha

Department of Chemistry,
SRM University,
Ramapuram,
Chennai 600089,
Tamil Nadu, India,
helenkavithap@yahoo.co.in
Chapter 8

Aleksey E. Kuznetsov

Instituto de Química,
Universidade de São Paulo – SP,
Av. Prof. Lineu Prestes,
748 – Butantã,
CEP: 05508-000, São Paulo, SP, Brazil,
aleksey73kuznets@gmail.com
Chapter 9

M. Alcolea Palafox

Departamento de Química-Física I,
Facultad de Ciencias Químicas, Universidad
Complutense,
Madrid, Spain,
alcolea@ucm.es
Chapter 10

Siddheshwar D. Jadhav

Department of Dyestuff Technology,
Institute of Chemical Technology,
N. P. Marg, Matunga,
Mumbai (MH)40001, India
Chapter 11

Nagaiyan Sekar

Department of Dyestuff Technology,
Institute of Chemical Technology,
N. P. Marg, Matunga,
Mumbai (MH)40001, India
nethi.sekar@gmail.com
Chapter 11

Suman Chowdhury and Debnarayan Jana

1 Optical properties of monolayer BeC under an external electric field: A DFT approach

Abstract: BeC, a two-dimensional hypercoordinated nanostructure carbon compound, has been the focus of the nanoworld because of its high value of dynamical stability, in-plane stiffness, carrier mobility and the existence of band gap. In this work, we have explored the electronic and the optical properties of this material under the influence of static external perpendicular electric field within the framework of density functional theory. Under the influence of a uniform electric field, the band gap changes within the meV range. The electron energy loss function study reveals that this material has optical band gaps which remain constant irrespective of the applied electric field strength. The optical property also exhibits interesting features when the applied field strength is within 0.4–0.5 V/Å. We have also tried to explain the optical data from the respective band structures and thus paving the way to understand qualitatively the signature of the optical anisotropy from the birefringence study.

Keywords: electronic properties, optical properties, density functional theory

1.1 Introduction

The era of two-dimensional (2D) materials has started through the experimental discovery of graphene in 2004 [1–5]. It has attracted the scientific community because of its unusual and exotic properties. For an example, the charge carriers in graphene move at a very high speed due to its linear dispersion relation at the K point on the Brillouin zone (BZ). So, it is natural to think of using pure graphene in the electronic industry. But because of its zero band gap at the Fermi energy, its use in electronic industry as a switch is restricted. So, opening of band gap with suitable order of magnitude in graphene has been an important key issue in the study of 2D materials. Various possible ways have been predicted to open band gap in graphene: by B-N doping [6–9], by chemical functionalization [10–12] and by applying strain [13]. Topological defects like Stone–Wales defects and local defects like voids can also alter the electronic structure of graphene significantly [14–16].

It is now clear that pristine graphene can no longer be used as a switch. One has to break the sublattice symmetry in a controllable manner. In all the previously men-

This article has previously been published in the journal *Physical Sciences Reviews*. Please cite as: Chowdhury, S., Jana, D. Optical properties of monolayer BeC under an external electric field: A DFT approach *Physical Sciences Reviews* [Online] **2018**, 3. DOI: 10.1515/psr-2017-0162

<https://doi.org/10.1515/9783110568196-001>

tioned ways, opening up of band gaps occur but rather in an uncontrollable way. Applying a tunable external electric field can be an effective viable way to control this band gap opening problem in graphene. Here again the problem with graphene is that, its sublattice symmetry is not broken due to the application of an external electric field. It is due to its intrinsic planarity in the structure. After few years of the discovery of graphene, a new 2D material has been predicted which is the graphene analog of 2D silicon, named as silicene [17–21]. Later, it has been experimentally realized [22] on silver (Ag) surface. Silicene possesses similar properties of that of graphene apart from the fact that it has an intrinsic buckling in the structure. Kamal et al. [23] have studied the electronic and optical properties of a transverse external static electric field on silicene. Their studies have also been corroborated by other groups [24–26].

Carbon being the backbone of organic and biochemistry, in most cases, the carbon atoms are found to be hypercoordinated. So, the search for materials having hypercoordinated carbon atoms is very crucial for the development of these two fields [27–29]. After the suggestion put forward by Hoffmann et al. [30] that electronically planar tetracoordinated carbon could be stabilized, several hypercoordinated carbon compounds have been identified both theoretically and experimentally [31–33]. In order to stabilize the hypercoordinated carbon, beryllium has been found to be an ideal ligand [34]. Many planar hypercoordinated carbons have been found to be beryllium stabilized [35–37]. Recently, some 2D nanomaterials have been proposed such as Be_2C and Be_5C_2 with quasi-planar hexa- as well as pentacoordinated carbons [38, 39].

Very recently, a new 2D material (BeC) has been predicted by Liu et al. [40] which is composed of beryllium (Be) and carbon (C) that are found to be semiconducting in its pristine form. They have used global particle-swarm optimization method to find its dynamical stability (up to 2000 K), in-plane stiffness (145.54 N/m), carrier mobility ($\sim 10^4 \text{ cm}^2 \text{ V}^{-1} \text{ s}^{-1}$) and indirect band gap of 1.01 eV. These data make BeC a suitable candidate in electronics and photoelectronics industry. Motivated by the huge potential of BeC, here we have studied the electronic and optical properties of BeC under the influence of a uniform transverse static external electric field through first principles density functional theory (DFT).

1.2 Computational details

All the calculations have been performed within the framework of DFT [41–43], using generalized gradient approximation (GGA) according to Perdew–Burke–Ernzerhof (PBE) [44] parametrization which is implemented in the SIESTA [45–47] code. Well-tested Troullier–Martins [48] norm conserving pseudopotentials have been adopted in a fully separable form of Kleinman and Bylander for all the elements. Double ζ polarized basis set is employed throughout the calculation. The sampling of the BZ has been done using a $10 \times 10 \times 1$ Monkhorst–Pack (MP) [49] of k points. But the PDOS calculation has been performed by using $60 \times 60 \times 1$ MP of k points. A 300 Ry mesh cutoff has been used for the expansion of the reciprocal space of the total charge

density. During the iteration process, the diagonalization method is used. All the doped structures are optimized by minimizing the forces on each atom below 0.02 eV\AA^{-1} using the standard conjugate-gradient (CG) technique. The criteria of convergence for the energy of the self-consistent field is set to be 10^{-5} eV . All the systems are simulated with a 15 \AA of vacuum perpendicular to the 2D surface to avoid the artificial interaction between the images. The static external electric field has been applied perpendicular to the plane of the sample. In Figure 1.1, we have depicted the top and side views of the monolayer BeC structure under the influence of an externally applied static perpendicular electric field. Besides, the optical properties have also been studied and an attempt has been made to interpret the result from the respective band structures. The imaginary part of the dielectric function $\epsilon_2(\omega)$ in the long wavelength limit ($q \rightarrow 0$), which denotes the real transition between the occupied and unoccupied electronic states, is calculated from first-order time-dependent perturbation theory [7, 19, 20, 50, 51]:

$$\epsilon_2(\omega) = \frac{2e^2\pi}{\Omega\epsilon_0} \sum_{k,v,c} |\langle \psi_k^c | \mathbf{u} \cdot \mathbf{r} | \psi_k^v \rangle|^2 \delta(E_k^c - E_k^v - \omega)$$

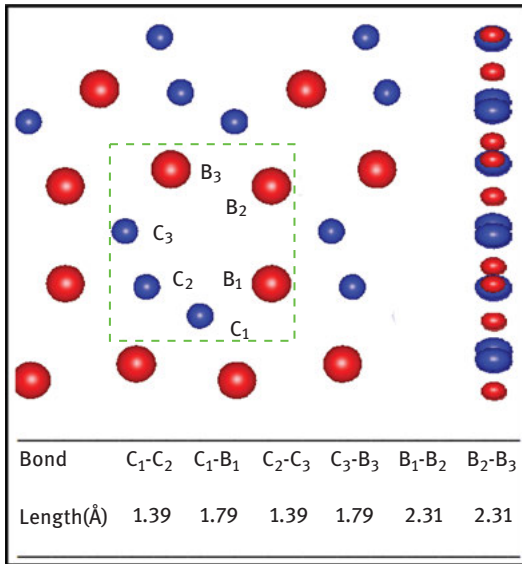


Figure 1.1: (Left panel) Top view and side view of the monolayer BeC structure. The red and blue balls, respectively, denote the carbon and the beryllium atoms. The unit cell is denoted by the green-colored box. The bonds and the corresponding bond lengths are also shown.

where Ω is the unit cell volume, ϵ_0 is the free space permittivity, ω is the photon frequency and ψ_k^c , ψ_k^v are the wave function of the conduction band (CB) and the valence band (VB) respectively. \mathbf{u} and \mathbf{r} represent, respectively, the polarization and

the position vector of the electromagnetic (EM) field. The real part of the dielectric function ($\epsilon_1(\omega)$) can be obtained from $\epsilon_2(\omega)$ by using Kramers–Kronig relation [52, 53]. The complex refractive index (N) is related to the complex dielectric function by the relation $N = \sqrt{\epsilon(\omega)}$. From this relation, the real ($n(\omega)$) and the imaginary ($k(\omega)$) parts of the complex refractive index can be extracted to be:

$$n(\omega) = \left(\frac{\sqrt{\epsilon_1^2 + \epsilon_2^2} + \epsilon_1}{2} \right)^{\frac{1}{2}}; \quad k(\omega) = \left(\frac{\sqrt{\epsilon_1^2 + \epsilon_2^2} - \epsilon_1}{2} \right)^{\frac{1}{2}}$$

The electron energy loss function (EELF) ($L(\omega)$), which is a measure of collective excitation of plasma, is calculated by the relation

$$L(\omega) = \text{Im} \left(-\frac{1}{\epsilon(\omega)} \right) = \frac{\epsilon_2}{\epsilon_1^2 + \epsilon_2^2}$$

1.3 Results and discussion

1.3.1 Electronic properties

The pristine system has been reported to be an intrinsic semiconductor with an indirect band gap of 1.01 eV [40]. In Figure 1.2, we have illustrated the band structure that we have obtained and also that is depicted in Ref. [40] and partial density of states (PDOS) of pristine BeC that we have simulated. It is quite much clear from the figure that the valence band maxima (VBM) and the conduction band minima (CBM) lie along the same k point (here Γ) in our calculation. This eventually renders the band gap of this intrinsically semiconducting material direct. We believe that the direct nature of the band gap originates from the significantly large difference of the lattice constants with our structure and that of Ref. [40]. From the PDOS, it can be observed that the $C - 2p_z$ orbitals contribute maximum. $C - 2s$ and $Be - 2s$

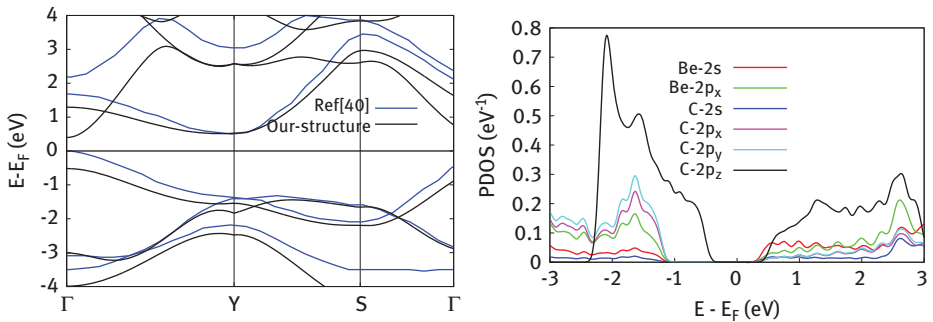


Figure 1.2: (Left panel) Comparison of GGA–PBE band structure of our simulated pristine BeC to that shown in Ref. [40]. (Right panel) PDOS of pristine BeC that we have obtained.

orbitals contribute least because they are the core states. It can also be inferred that the three orbitals $Be - 2p_x$, $C - 2p_x$ and $C - 2p_y$ hybridize. Now, in order to use this material in the electronic industry, we need to tune the band gap by some external influences. In this work, we have tried to investigate the change in band gap under the application of a static uniform external electric field. In Figure 1.3, we have presented the variation of the intrinsic band gap with external electric field. Here, we have considered the magnitude of the electric field from 0.1 to 0.9 V/Å. From the figure, it can be observed that the band gap initially increases up to 0.5 V/Å, but then it starts decreasing. The band gap is seen to vary within 60 meV. So, the band gap can be tuned within the meV range by applying static external perpendicular electric field. In Figure 1.4 and Figure 1.5, we have depicted, respectively, the band structure and the PDOS for four different field strengths. From Figure 1.4, it is clear that the nature of the band gap does not change upon applying external electric field. This is due to the fact that as BeC has planar structure (see Figure 1.1), so its inversion symmetry remains preserved upon application of an external electric field [24]. All the band gaps are seen to be direct and also the nature of the PDOS does not change. After applying electric field, here also the $C - 2p_z$ orbitals contribute maximum and the three orbitals $Be - 2p_x$, $C - 2p_x$ and $C - 2p_y$ are seen to be hybridized.

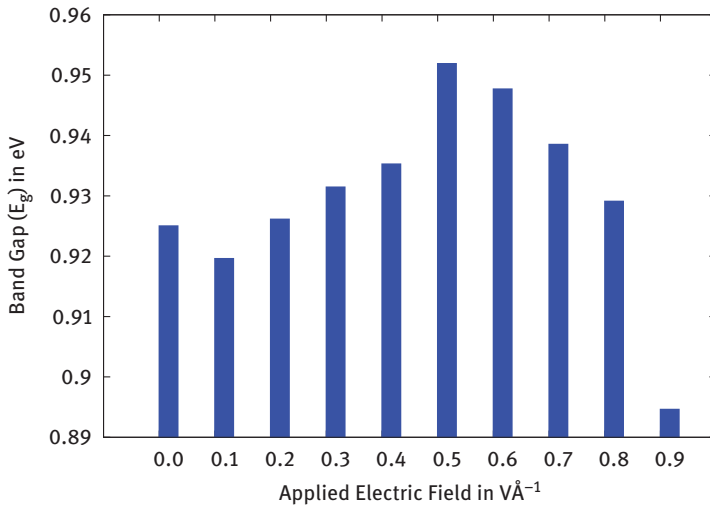


Figure 1.3: Variation of band gap with varying strengths of external electric field.

1.3.2 Optical properties

1.3.2.1 Dielectric properties

The dielectric functions are related to the electronic band structure of the material. ϵ_1 is related to the amount of stored energy within the medium and ϵ_2 is related to the dissipation of the energy within the medium. $\epsilon_1(0)$ is known as the static dielectric

6 — 1 Optical properties of monolayer BeC

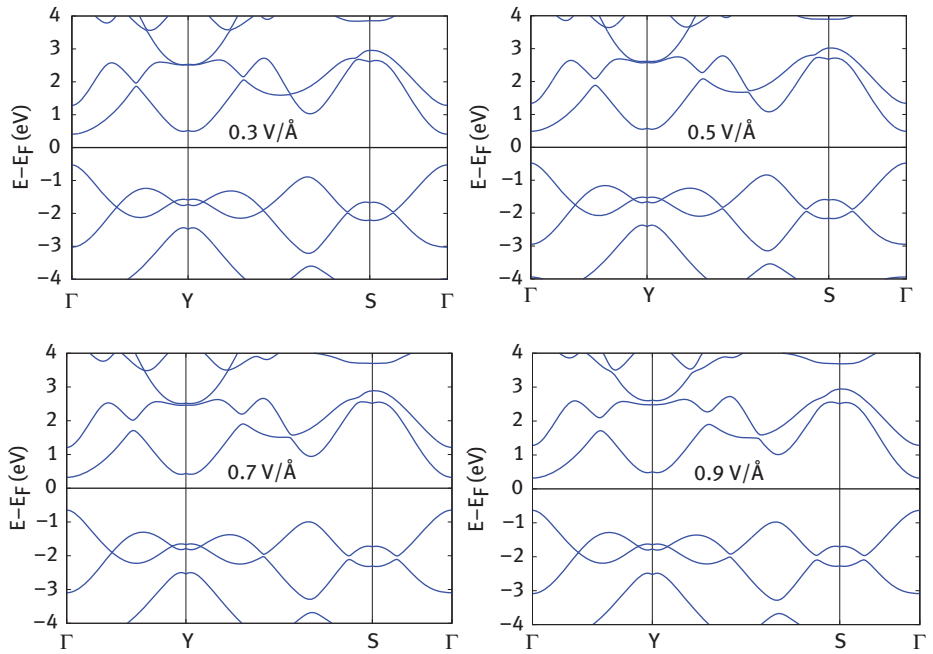


Figure 1.4: Band structure for four different electric field strengths.

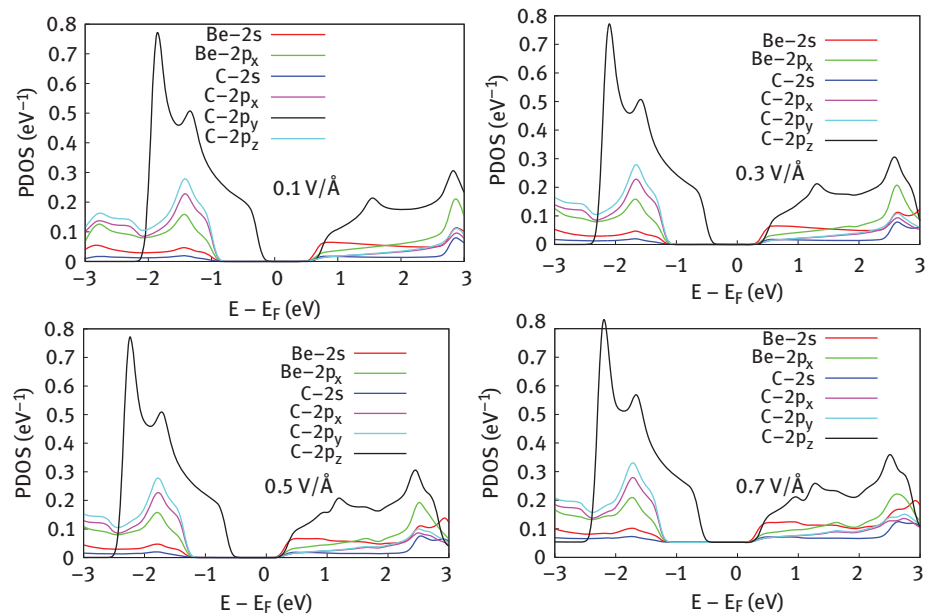


Figure 1.5: Partial DOS for four different electric field strengths.

constant (SDC) which is related to the material's behavior at low or constant frequency. The characteristic frequency at which the real part of the dielectric function vanishes ($\epsilon_1(\omega_p) = 0$) is known as plasma frequency (PF). At these frequencies, $\epsilon_1(\omega)$ changes from negative to positive. This behavior corresponds to the collective excitations of the electrons.

In Figures 1.6 and 1.7, we have depicted the frequency-dependent imaginary ($\epsilon_2(\omega)$) and real ($\epsilon_1(\omega)$) parts of the dielectric function for different applied electric field strengths. In Table 1.1 and Table 1.2, we have shown, respectively, the SDC and PF for parallel and perpendicular polarizations. From both the figures and the tables, the most interesting feature can be observed between the applied electric fields of 0.4 and 0.5 V/Å. For both the polarizations, there is a sudden jump in the optical activity that can be noted. For parallel polarization, the value of the SDC changes from 7.50 to 11.55. Then, it increases continuously up to the range we have considered, i.e., 0.9 V/Å. This same trend is observed for perpendicular polarization. Here, the SDC changes from 1.85 to 2.41. As we know, the low- and the high-energy regime is dominated, respectively, for parallel and perpendicular polarizations. So the changes

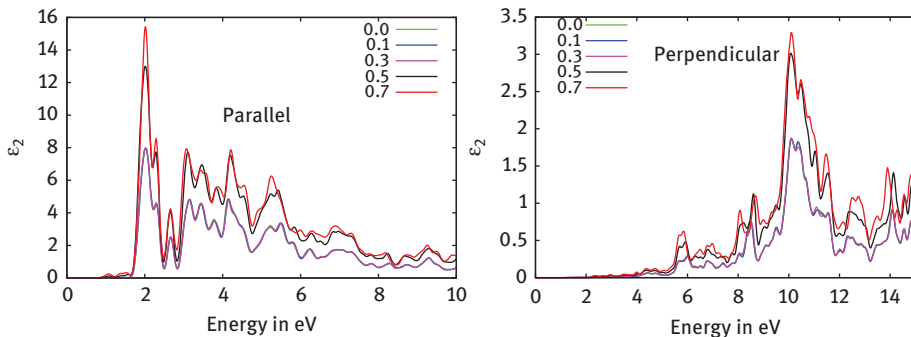


Figure 1.6: Frequency-dependent imaginary part of the dielectric function for different applied electric field strengths for (left panel) parallel and (right panel) perpendicular polarization.

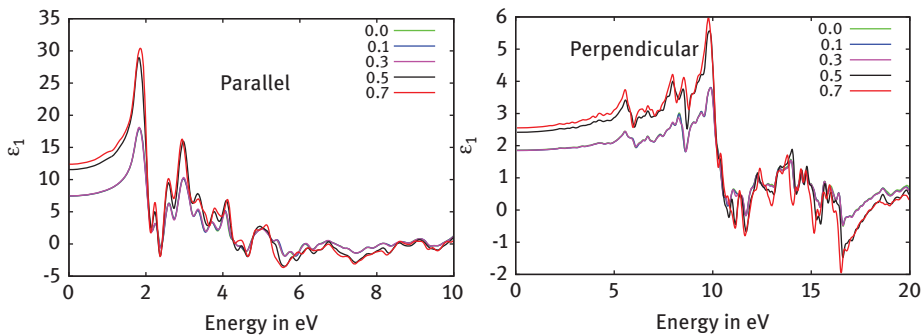


Figure 1.7: Frequency-dependent real part of the dielectric function for different applied electric field strengths for (left panel) parallel and (right panel) perpendicular polarization.

Table 1.1: Static dielectric constant (SDC) and plasma frequencies (PF) for different applied electric field strengths for parallel polarization.

Applied field in V/Å	SDC (parallel)	PF (parallel) in eV
0.0	7.45	2.36,2.42,4.32,4.69,5.46, 6.52,6.94,8.11,8.27, 8.48,9.30,9.67
0.1	7.45	2.34,2.42,4.34,4.73,5.49, 6.11,6.17,6.50,6.94,8.09, 8.24,8.47,9.30,9.68
0.2	7.46	2.36,2.42,4.34,4.72,5.47, 6.11,6.17,6.49,6.93,8.09, 8.24,8.47,9.31,9.69
0.3	7.47	2.34,2.42,4.32,4.72,5.46, 6.12,6.20,6.49,6.92,8.08, 8.24,8.45,9.33,9.67
0.4	7.50	2.33,2.41,4.31,4.73,5.43, 6.12,6.22,6.57,6.91,8.10, 8.22,8.42,9.31,9.68
0.5	11.55	2.31,2.42,4.28,4.74,5.35, 6.68,6.80,8.51,8.66,8.95, 9.27
0.6	11.82	2.31,2.41,4.28,4.44,4.50, 4.74,5.27,6.68,6.80,8.51, 8.67,8.92,9.27
0.7	12.39	2.33,2.42,4.53,4.74,5.26, 8.52,8.75,8.88,9.23
0.8	11.21	2.33,2.43,4.30,4.74,5.46, 6.65,6.80,8.94,9.28
0.9	12.95	2.35,2.41,4.57,4.73,5.22, 8.51,9.17

in SDC for perpendicular polarization are not as large as that of parallel polarization. From Table 1.1 and Table 1.2, it can be noted that with increasing electric field strength, the number of PF increases at the low-energy regime and decreases in the high-energy regime for parallel polarization. However, an opposite trend is found for perpendicular polarization, where the number of PF decreases at the low-energy regime and increases in the high-energy regime with increasing electric field strength. This indicates that in the low-energy sector, the electronic excitation is more for parallel polarization. This is the actual physical reason why the parallel polarization dominates the low-energy regime. The opposite trend is observed for perpendicular polarization which proves its dominant nature in the high-energy regime. In Tables 1.3 and 1.4, we have tried to interpret the optical data from the band structure, respectively, for parallel and perpendicular polarizations. We have

Table 1.2: Static dielectric constant (SDC) and plasma frequencies (PFs) for different applied electric field strength for perpendicular polarization.

Applied field in V/Å	SDC (perpendicular)	PF (perpendicular) in eV
0.0	1.86	11.59,11.75,16.49, 17.26
0.1	1.85	11.60,11.75,16.51, 17.36
0.2	1.85	11.60,11.75,16.51, 17.37
0.3	1.85	11.60,11.75,16.51, 17.37
0.4	1.85	11.60,11.75,16.51, 17.38
0.5	2.41	10.73,10.89,11.04, 11.24,11.54,11.85, 15.19,15.55,16.44,18.02
0.6	2.46	10.74,10.88,10.97, 11.25,11.56,11.88, 15.55,16.39,17.95
0.7	2.55	10.91,11.25,11.48,11.88 15.02,15.29,15.33,15.47, 16.11,17.94
0.8	2.35	10.66,10.91,11.52,11.84, 15.27,15.56,16.21,16.31 16.47,18.05
0.9	2.64	11.08,11.85,12.81,12.92, 13.60,13.80,13.86,13.98,14.80,15.39, 15.64,15.88,18.07

also listed the energy at the VB (E_{VB}) and at the CB (E_{CB}) for each transition. For each electric field strength, we have considered the highest peak in the $\epsilon_2(\omega)$ data and tried to identify the corresponding transition from the band structure only at the high symmetry points at the BZ. Because transitions at the high symmetry points are more probable than the other points at the BZ for 2D materials. From Table 1.3, it can be seen that all the transitions occur at the Y point of the BZ. So, for parallel polarization, the highest peak corresponds to a single transition at the high symmetric Y point of the BZ. Looking carefully into the energy range, it is obvious that all the transitions occur mainly from the top of the VB to the bottom of the CB. Mostly, the π bands are situated in this energy regime. So, all these transitions correspond to π to π^* type of transitions. The situation becomes more interesting if we look into Table 1.4. Here, for perpendicular polarization, the highest peak corresponds to multiple transitions. Here all the high symmetric points contribute in the transition process. Moreover, if we look into the energy range, we can observe that some transitions occur from the

Table 1.3: Identification of the highest transition of ϵ_2 for parallel polarization from band structure. E_{VB} and E_{CB} are, respectively, the energy at the VB and the CB between which the transition occurs.

Applied field (V/Å)	Highest peak position of ϵ_2 (parallel) in eV	BZ point	E_{VB} (eV)	E_{CB} (eV)
0.0	2.02	Y	-1.32	0.74
0.1	2.02	Y	-1.32	0.74
0.2	2.02	Y	-1.31	0.74
0.3	2.02	Y	-1.56	0.49
0.4	2.02	Y	-1.56	0.49
0.5	2.01	Y	-1.51	0.53
0.6	2.00	Y	-1.69	0.33
0.7	2.01	Y	-1.65	0.38
0.8	2.01	Y	-1.32	0.73
0.9	2.03	Y	-1.62	0.41

deep of the VB to the bottom of the CB. As the σ bonds are stronger than the π bonds, so these type of transitions correspond to σ to π^* type of transitions. There exist other transitions occurring from top of the VB to the deep of the CB. These type of transitions correspond to π to σ^* type of transitions. As the high-energy region is affected in perpendicular polarization, σ band is associated in these kinds of transitions. In Figure 1.8, we have shown two band structures for each polarization. In the left panel of Figure 1.8, we have depicted the π bands which are associated with the C_{2p_z} electrons and shown the transition correspond to the 2.02 eV peak in the corresponding ϵ_2 data for parallel polarization under the applied electric field of 0.1 V/Å. We know that different orbitals can contribute to one particular band. Now, in the left panel of Figure 1.8, we have taken into consideration the contribution of C_{2p_z} orbitals denoted by the blue thick lines. Whereas, in the right panel of Figure 1.8, we have depicted both the π and the σ bands (here contributions of different orbitals are not taken into consideration) and shown the respective transition corresponding to the 10.09 eV peak in the corresponding ϵ_2 data for perpendicular polarization under the applied electric field of 0.1 V/Å.

1.3.2.2 Electron energy loss function (EELF)

The EELF describes the energy loss of fast-moving electrons in a material. In Figure 1.9, we have shown the EELF for both parallel and perpendicular polarizations. The peaks in $L(\omega)$ reveal collective excitations of the electrons corresponding to PF, i.e., dip in the dielectric function. Actually, these peaks indicate the point of transitions of electrons from semiconducting to dielectric. From Figure 1.9, we can estimate the optical band gap of BeC, i.e., up to that point in the energy axis where no excitations of electrons can be observed. Here it can be

Table 1.4: Identification of the highest transition of ϵ_2 for perpendicular polarization from band structure.

Applied field (V/Å)	Highest peak position of ϵ_2 (perpendicular) in eV	BZ point	E_{VB} (eV)	E_{CB} (eV)
0.0	10.09	Γ	-8.48	1.52
		Y	-7.28	2.76
		S	-7.24	2.85
			-6.06	4.10
0.1	10.09	Γ	-8.48	1.52
		Y	-8.48	1.52
			-7.29	2.74
		S	-1.32	8.82
0.2	10.10	S	-7.24	2.88
			-6.06	4.10
		Γ	-8.48	1.52
			-8.48	1.53
0.3	10.10		-6.27	3.88
		Y	-7.29	2.74
			-1.31	8.83
		S	-7.24	2.89
0.4	10.10		-6.05	4.09
		Γ	-8.48	1.53
			-6.27	3.88
			-8.73	1.28
0.5	10.10		-6.51	3.63
		Y	-7.53	2.48
			-1.56	8.59
		S	-7.49	2.64
0.6	10.10		-6.30	3.82
		Γ	-8.73	1.28
			-6.51	3.63
			-8.72	1.28
0.7	10.10	Y	-7.53	2.48
			-2.42	7.77
			-1.56	8.61
		S	-7.48	2.64
0.8	10.10		-6.29	3.80
		Γ	-8.72	1.28
			-8.72	1.28
			-8.67	1.34
0.9	10.07	Y	-7.47	2.52
		S	-7.43	2.69
			-6.24	3.79
		Γ	-8.67	1.34

(continued)

Table 1.4 (continued)

Applied field (V/Å)	Highest peak position of ϵ_2 (perpendicular) in eV	BZ point	E_{VB} (eV)	E_{CB} (eV)
0.6	10.07	Γ	-8.85	1.15
			-6.36	3.61
		Y	-7.66	2.32
			-7.66	2.47
		S	-7.61	2.49
			-6.42	3.54
0.7	10.10	Γ	-8.81	1.22
			-7.63	2.39
		Y	-2.49	7.65
			-1.65	8.51
		S	-7.57	2.52
			-8.81	1.22
0.8	10.11	Γ	-8.49	1.52
			-7.30	2.75
		Y	-7.30	2.76
			-1.32	8.83
		S	-7.25	2.89
			-6.06	4.11
0.9	10.09	Γ	-8.49	1.52
			-8.80	1.28
		Y	-7.62	2.41
			-2.48	7.66
		S	-1.62	8.46
			-7.56	2.48
Γ	-8.80	1.28		

advocated that irrespective of the applied electric field, the optical band gap remains the same for both the polarizations. For parallel polarization, the optical band gap is seen to extend up to ~ 2 eV, whereas for perpendicular polarization, it is extended upto ~ 5 eV.

1.3.2.3 Refractive index: Birefringence characteristics

A material is said to possess birefringence characteristics if the velocity is different in different polarization directions. It can be determined from the real part of the refractive index ($n(\omega)$) from the following expression:

$$\Delta n(\omega) = n_e(\omega) - n_o(\omega)$$

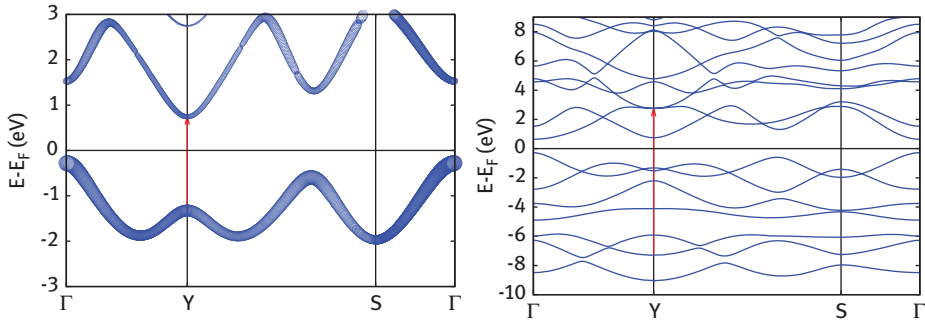


Figure 1.8: (Left panel) π band in case of parallel polarization when 0.1 V/\AA is applied. The transition corresponding to 2.02 eV peak in the ϵ_2 data is shown in red-colored arrow. (Right panel) The transition corresponding to 10.10 eV peak in the ϵ_2 data is shown in red-colored arrow for perpendicular polarization under the applied electric field of 0.1 V/\AA .

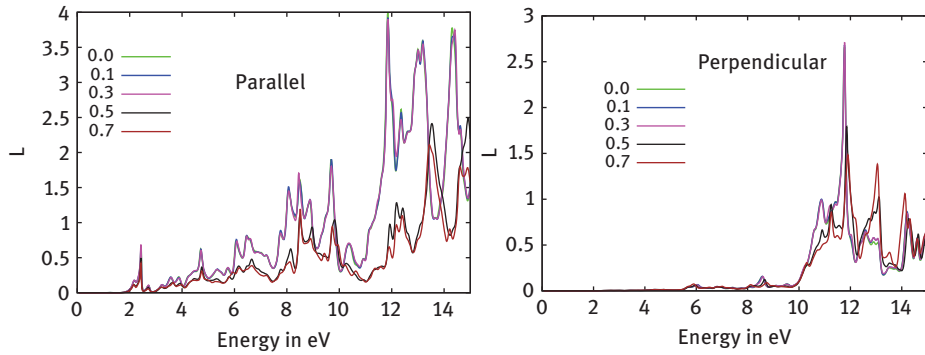


Figure 1.9: (Left panel) EELF for parallel and (right panel) perpendicular polarizations.

where $n_e(\omega)$ and $n_o(\omega)$ are the refractive indices when the electric field of the EM wave is directed parallel and perpendicular to the c -axis, respectively.

In Figure 1.10, we have illustrated the real part of the refractive index for both parallel and perpendicular polarizations. From the figure, the signature of optical anisotropy can be observed. In order to further understand the optical anisotropy of BeC, in Figure 1.11, we have shown the birefringence properties of BeC as a function of the energy of the incident EM wave for each externally applied electric field. It should be brought to notice that $\Delta n(0) < 0$, i.e., BeC possesses negative static birefringence. In Figure 1.11, we can see that up to 5 eV , the value of Δn is indeed negative except at an extremely narrow window of energy ($2.36\text{--}2.46 \text{ eV}$). This means that the value of the refractive index for the ordinary ray is more than that of the extraordinary ray. But after $\sim 5 \text{ eV}$, it goes above the positive x -axis. This suggests that after $\sim 5 \text{ eV}$, the extraordinary ray dominates over the ordinary ray. The refractive index is highest in that

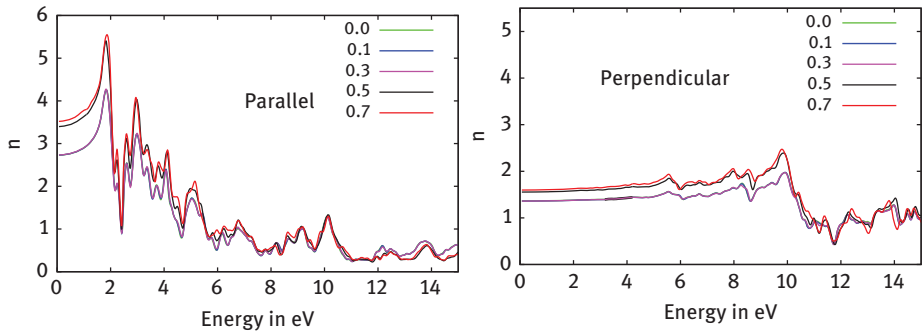


Figure 1.10: (Left panel) Real part of the refractive index for parallel and (right panel) perpendicular polarizations.

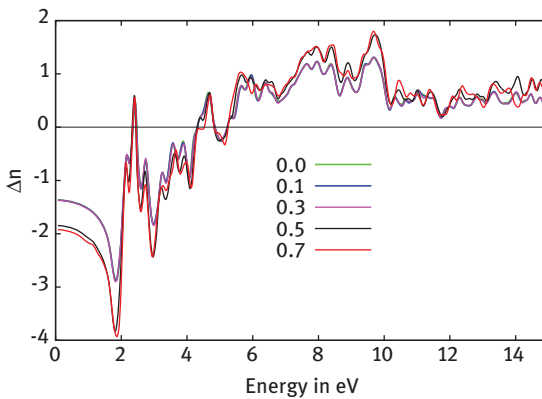


Figure 1.11: Birefringence as a function of incident energy for each externally applied electric field.

direction where the density of ions is the highest. From Figure 1.10, it can be inferred that in BeC, the velocity of light is greatest when it polarizes along the direction of the electrons in the lattice because of its interaction with the loosely bound π electrons. However, the velocity decreases when the polarization is perpendicular because in perpendicular polarization, the EM wave interacts with the strongly bound σ electrons of the BeC lattice.

1.4 Conclusions

The electronic and optical properties of tetracoordinated carbon compound BeC has been studied within the realm of DFT. The nature of the band gap has been found to be direct in contrary to that has been reported in Ref. [40]. From our study, it has been revealed that there are modifications in the band gap up to 60 meV with varying external electric field. The optical property study shows interesting features

between the electric field range of 0.4 and 0.5 V/Å. Within this range, a sudden jump of optical activity has been found. The number of PF suddenly increases within this electric field range. We have also tried to interpret the optical data from the band structure. From the band structure, it has been observed that for parallel polarization, the transitions are mostly π to π^* transitions. And all the transitions occur at the Y point of the BZ. However, for perpendicular polarization, for each external electric field strength, the highest point in the ϵ_2 data corresponds to multiple transitions. It has been noticed that in this case all the BZ points contribute in the optical transition. From the EELF study, it has been noticed that the optical band gaps are same for both the polarizations irrespective of the applied electric field strength. The value of the optical band gap is ~ 2 eV and ~ 5 eV for parallel and perpendicular polarizations, respectively. The calculation involving the birefringence property of this material indicates that the static value of the birefringence is negative for each electric field strength. The velocity of the EM wave has been noticed to be higher when the polarization is parallel, whereas it decreases for perpendicular polarization.

Acknowledgment: The authors would like to acknowledge Mr. Arnab Majumdar, Prof. C-S Liu and Prof. X-J Ye for fruitful discussions.

References

- [1] Geim AK. Nobel lecture: Random walk to graphene. *Rev Mod Phys.* 2011;83:851–862.
- [2] Geim AK. Graphene: status and prospects. *Science.* 2009;324:1530–4.
- [3] Novoselov KS. Nobel lecture: Graphene: Materials in the flatland. *Rev Mod Phys.* 2011;83:837–49.
- [4] Neto A, Guinea F, Peres N, Novoselov K, Geim A. The electronic properties of graphene. *Rev Mod Phys.* 2008;81:109 (54pp).
- [5] Novoselov K, Geim A, Morozov S, Jiang D, Zhang Y, Dubonos S, Grigorieva I, Firsov A. Electric field effect in atomically thin carbon films. *Science.* 2004;306:666–669.
- [6] Nath P, Sanyal D, Jana D. Semi-metallic to semiconducting transition in graphene nanosheet with site specific co-doping of boron and nitrogen. *Physica E.* 2014;56:64–68.
- [7] Nath P, Chowdhury S, Sanyal D, Jana D. Ab-initio calculation of electronic and optical properties of nitrogen and boron doped graphene nanosheet. *Carbon.* 2014;73:275–282.
- [8] Shinde PP, Kumar V. Direct band gap opening in graphene by BN doping: Ab initio calculations. *Phys Rev B.* 2011;84:125 401–06.
- [9] Rani P, Kumar VK. Designing band gap of graphene by B and N dopant atoms. *RSC Adv.* 2013;3:802–812.
- [10] Kuila T, Bose S, Mishra AK, Khanra P, Kim NH, Lee JH. Chemical functionalization of graphene and its applications. *Prog Mater Sci.* 2012;57:1061–1105.
- [11] Woinska M, Milowska KZ, Majewski JA. Electronic structure of graphene functionalized with boron and nitrogen. *Phys Status Solidi C.* 2013;10:1167–71.
- [12] Thakur J, Saini SH, Singh M, et al. The electronic and magnetic properties of B-doping Stone-Wales defected graphene decorated with transition-metal atoms. *Physica E.* 2016;78:35–40.

- [13] Ni ZH, Yu T, Lu YH, Wang YY, Feng YP, Shen ZX. Uniaxial strain on graphene: Raman spectroscopy study and band-gap opening. *ACS Nano*. 2008;2:2301–2305.
- [14] Chowdhury S, Baidya S, Nafday D, et al. A real-space study of random extended defects in solids: Application to disordered stone-wales defects in graphene. *Physica E*. 2014;61:191–197.
- [15] Chowdhury S, Jana D, Mookerjee A. Conductance of disordered graphene sheets: A real space approach. *Physica E*. 2015;74:347–354.
- [16] Chowdhury S, Jana D, Sadhukhan B, et al. Configuration and self-averaging in disordered systems. *Ind J Phys*. 2016;90:649–657.
- [17] Cahangirov S, Topsakal M, Akturk E, Sahin H, Ciraci S. Two- and one-dimensional honeycomb structures of silicon and germanium. *Phys Rev Lett*. 2009;102:236,804.
- [18] Majumdar A, Chowdhury S, Nath P, Jana D. Defect induced magnetism in planar silicene: a first principles study. *RSC Adv*. 2014;4:32,221–32,227.
- [19] Das R, Chowdhury S, Majumdar A, Jana D. Optical properties of p and al doped silicene: a first principles study. *RSC Adv*. 2014;5:41–50.
- [20] Chowdhury S, Nath P, Jana D. Shape dependent magnetic and optical properties in silicene nanodisks: A first principles study. *J Phys Chem Solid*. 2015;83:32–39.
- [21] Chowdhury S, Jana D. A theoretical review on electronic, magnetic and optical properties of silicene. *Rep Prog Phys*. 2016;79:126,501 (57pp).
- [22] Vogt P, Padova PD, Quaresima C, et al. Silicene: Compelling experimental evidence for graphenelike two-dimensional silicon. *Phys Rev Lett*. 2012;108:155,501.
- [23] Kamal C, Banerjee A, Chakrabarti A. Properties of two-dimensional silicon versus carbon systems. USA: CRC Press, 2016.
- [24] Ni Z, Liu Q, Tang K, Zheng J, Zhou J, Qin R, Gao Z, Yu D, Lu J. Tunable bandgap in silicene and germanene. *Nano Lett*. 2012;12:113.
- [25] Drummond ND, Zolyomi V, Falko VI. Electrically tunable band gap in silicene. *Phys Rev B*. 2012;85:075,423 (7pp).
- [26] Ezawa M. A topological insulator and helical zero mode in silicene under an inhomogeneous electric field. *New J Phys*. 2012;14:033,003 (11pp).
- [27] Yang LM, Ganz E, Chen Z, Wang ZX, v R Schleyer P. Four decades of the chemistry of planar hypercoordinate compounds. *Angew Chem Int Ed*. 2015;54:9468–9501.
- [28] Keese R. Carbon flatland: Planar Tetracoordinate Carbon and Fenestranes. *Chem Rev*. 2006;106:4787–4808.
- [29] Merino G, Mendez-Rojas MA, Vela A, Heine T. Recent advances in planar tetracoordinate carbon chemistry. *J Comput Chem*. 2007;28:362–372.
- [30] Hoffmann R, Alder RW, Wilcox CF. Planar tetracoordinate carbon. *J Am Chem Soc*. 1970;92:4992–4993.
- [31] Li X, Wang LS, Boldyrev AI, Simons J. Tetracoordinated planar carbon in the Al_4C Anion. A Combined Photoelectron Spectroscopy and Ab Initio Study. *J Am Chem Soc*. 1999;121:6033–6038.
- [32] Pei Y, An W, Ito K, v R Schleyer P, Zeng XC. Planar pentacoordinate carbon in CaI_5^+ : A Global Minimum. *J Am Chem Soc*. 2008;130:10,394–10,400.
- [33] Averkiev BB, Zubarev DY, Wang LM, Huang W, Wang LS, Boldyrev AI. Carbon Avoids Hypercoordination in CB_6^- , CB_6^{2-} , and $C_2B_5^-$ Planar Carbon-Boron Clusters. *J Am Chem Soc*. 2008;130:9248–9250.
- [34] Wang ZX, Zhang CG, Chen ZF, v R Schleyer P. Planar Tetracoordinate Carbon Species Involving Beryllium Substituents. *Inorg Chem*. 2008;47:1332–1336.
- [35] Jimenez-Halla JOC, Wu YB, Wang ZX, Islas R, Heine T, Merino G. CaI_4Be and $CaI_3Be_2^-$: global minima with a planar pentacoordinate carbon atom. *Chem Commun*. 2010;46:8776–8778.

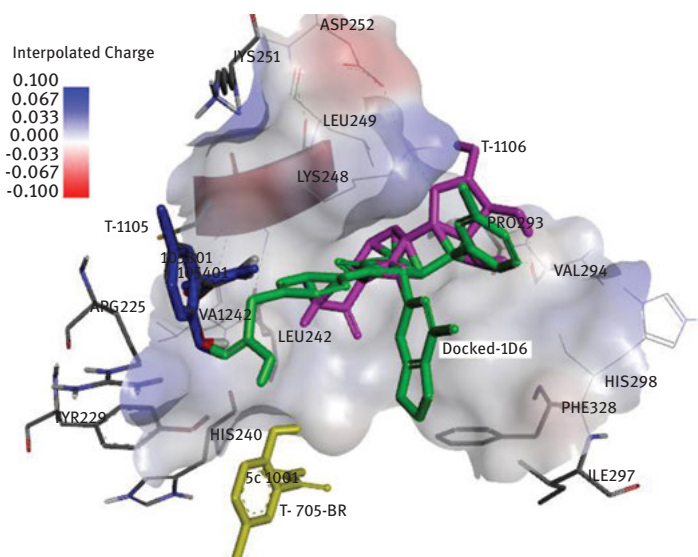
- [36] Grande-Aztatzi R, Cabellos JL, Islas R, Infante I, Mercero JM, Restrepo A, Merino G. Planar pentacoordinate carbons in CBe_5^{4-} derivatives. *Phys Chem Chem Phys*. 2015;17:4620–4624.
- [37] Guo JC, Ren GM, Miao CQ, Tian WJ, Wu YB, Wang XT. $CBe_5H_n^{n-4}$ ($n = 2-5$): Hydrogen-Stabilized Be_5 Pentagons Containing Planar or Quasi-Planar Pentacoordinate Carbons. *J Phys Chem A*. 2015;119:13,101–13,106.
- [38] Li Y, Liao Y, Chen Z. Be(2)C monolayer with quasi-planar hexacoordinate carbons: a global minimum structure. *Angew Chem Int Ed*. 2014;53:7248–7252.
- [39] Wang Y, Li F, Li Y, Chen Z. Semi-metallic Be_5C_2 monolayer global minimum with quasi-planar pentacoordinate carbons and negative Poissons ratio. *Nat Commun*. 2016;7:11,488 (7pp).
- [40] Liu CS, Zhu HH, Ye XJ, Yan XH. Prediction of a new BeC monolayer with perfectly planar tetracoordinate carbons. *Nanoscale*. 2017;9:5854–5858.
- [41] Hohenberg P, Kohn W. Inhomogeneous electron gas. *Phys Rev*. 1964;136:B864 – B871.
- [42] Kohn W, Sham LJ. Self-consistent equations including exchange and correlation effects. *Phys Rev*. 1965;140:A1133 – A1138.
- [43] Kohn W. Nobel lecture: Electronic structure of matterwave functions and density functionals. *Rev Mod Phys*. 1999;71:1253–1266.
- [44] Perdew JP, Burke K, Ernzerhof M. Generalized gradient approximation made simple. *Phys Rev Lett*. 1996;77:3865.
- [45] Ordejon P, Artacho E, Soler JM. Self-consistent order-N density-functional calculations for very large systems. *Phys Rev B* 1996 R10,441–R10,444 53.
- [46] Ordejon P, Artacho E, Soler JM. Density functional method for very large systems with LCAO basis sets. *Int J Quantum Chem*. 1997;65:453–461.
- [47] Soler JM, Artacho E, Gale JD, Garca A, Junquera J, Ordejon P, Sanchez-Portal D. The siesta method for ab initio order-n materials simulation. *J Phys Condens Matter*. 2002;14:2745–2779.
- [48] Troullier N, Martins JL. Efficient pseudopotentials for plane-wave calculations. ii. operators for fast iterative diagonalization. *Phys Rev B*. 1993;43:8861–8869.
- [49] Monkhorst HJ, Pack JD. Special points for Brillouin-zone integrations. *Phys Rev B*. 1976;13:5188–5192.
- [50] Jana D, Sun CL, Chen LC, Chen KH. Effect of chemical doping of boron and nitrogen on the electronic, optical, and electrochemical properties of carbon nanotubes. *Prog Mat Sci*. 2013 6;58:565–635.
- [51] Mahan GD. *Many Particle Physics*. New York: Plenum, 1990.
- [52] Chowdhury S, Das R, Nath P, Jana D, Sanyal D. Electronic and Optical Properties of Boron- and Nitrogen-Functionalized Graphene Nanosheet, Chemical functionalization of Carbon Nanomaterials. *Chemistry and Applications* ed V K Thakur and M K Thakur, Ch-42. New York: CRC Press. ISBN: 978-1-48-225394-8. 2015:949–957.
- [53] Dressel M, Gruner G. *Electrodynamics of Solids*. UK: Cambridge University Press, 2002.

Lydia Rhyman, Mahir Tursun, Hassan H. Abdallah, Yee Siew Choong, Cemal Parlak, Prashant Kharkar and Ponnadurai Ramasami

2 Theoretical investigation of the derivatives of favipiravir (T-705) as potential drugs for Ebola virus

Abstract: Density functional theory (DFT) method was used to compute the structural and vibrational parameters of favipiravir (T-705) in the gas phase. The functional used was B3LYP in conjunction with the 6-311++G(d,p) basis set. We also computed these parameters for unsubstituted T-705 and derivatives of T-705 by substituting fluorine by chlorine, bromine and the cyanide group. There is a good comparison between the computed and experimental parameters for T-705 and therefore, the predicted data should be reliable for the other compounds for which experimental data is not available. We extended our DFT study to include molecular docking involving the Ebola virus viral protein 35 (VP35). The docking results indicate that the T-705 and its chlorine and bromine analogues have comparable free energy of binding with VP35.

Graphical Abstract:



Keywords: DFT, docking, T-705, Ebola, structure, spectroscopy

This article has previously been published in the journal *Physical Sciences Reviews*. Please cite as: Rhyman, L., Tursun, M., Abdallah, H. H., Choong, Y. S., Parlak, C., Kharkar, P., Ramasami, P. Theoretical investigation of the derivatives of favipiravir (T-705) as potential drugs for Ebola virus. *Physical Sciences Reviews* [Online] 2018, 3. DOI: 10.1515/psr-2017-0198

<https://doi.org/10.1515/9783110568196-002>

2.1 Introduction

In 1975, Ebola was first identified in the Democratic Republic of Congo formerly known as Zaire [1]. Ebola viruses are known to be the most lethal pathogens against mankind [2]. The reappearance of the Ebola outbreak was officially notified on 22 March 2014 in Guinea [3]. Although this outbreak was declared over by World Health Organisation (WHO) in 14 January 2016 [4], on the same day, one case was reported by the Ministry of Health in Sierra Leone [1]. So far, over 28 500 people are infected and more than 11 300 persons died due to Ebola [1]. Ebola causes economic, society and emotional disturbances and affect international air travel [5, 6]. The early symptoms of Ebola infections are fever, diarrhea and vomiting, ultimately leading to haemorrhagic symptoms [7]. Transmission of Ebola occurs through contact with virus contaminated body fluids, materials contaminated with these fluids and infected bats or animals [8].

This brief overview of Ebola over almost 40 years is frightening but challenging. Therefore, Ebola has aroused the interest of scientists to find an effective drug for the treatment of this disease [9]. This is more important because viruses are known to undergo antigenic changes leading to the disease becoming acute [10]. There are several potential drugs that have been tested against Ebola [11]. However, to date the performance of Ebola drugs is still being questioned [12]. One of the drugs which has been cited to act against Ebola is T-705 favipiravir and its related compounds [13]. There is also a detailed review of T-705 and its related compounds as broad spectrum inhibitors of RNA-viral infections [14]. T-705 was first prepared by Furuta et al. [15] and Shi et al. [16] reported a modified procedure with four steps to improve the yield and reduce the cost of the production of T-705.

The elegant comment, in 2013, by De Clercq on antivirals: past, present and future, opens the avenue for antiviral therapy [17]. Comments by the same author on dancing with chemical formula on antivirals lead to several potential compounds which can be tested and used efficiently [18, 19]. It is also reported that halogen effect should be considered in drug design [20]. We have been tempted by these reports [17–20] and a recent contribution by some of us [21] to undertake a systematic theoretical study of unsubstituted T-705 and substituting fluorine of T-705 by other halogens namely chlorine and bromine and the cyanide group. We investigated these compounds in terms of their structural and spectroscopic parameters using density functional theory (DFT) method. We also complemented the study using molecular dynamics.

2.2 Methodology

2.2.1 Ab initio

All DFT computations were performed with the Gaussian 09 suite of programs [22] running on Gridchem [23–25]. The DFT method was used to optimize T-705 and its derivatives. The functional used was B3LYP and the basis set for all atoms was

6-311++G(d,p). Frequency computations based on the same geometry optimization method (tight criteria) were used to confirm the nature of the stationary points. The electronic energies, geometrical parameters, atomic charges, energy of the highest occupied molecular orbital (HOMO), energy of the lowest unoccupied molecular orbital (LUMO), uncorrected harmonic wavenumbers and infra-red intensities were computed.

2.3 Docking

2.3.1 Protein structure

The starting structure of Ebola virus viral protein 35 (VP35) was obtained from PDB (PDB id: 4IBG) [26]. All heteroatoms and water molecules were removed from the VP35. Polar hydrogen atoms, Kollman-Amber united atom partial charges and solvation parameters were added by utilizing AutoDockTools [27].

2.3.2 Ligand structure

The initial structure of 1D6 was obtained from the ligand of VP35 (PDB id: 4IBG) [26] while the coordinates for T-705, T705-Br, T705-Cl, T1105 and T1106 were generated using Hyperchem 7.0 [28]. All ligands were retained with polar hydrogen atoms. Gasteiger charges and torsional angles were added by utilizing AutoDockTools [27]. Figure 2.1 shows the chemical structure of all the above-mentioned ligands including T-705-CN.

2.3.3 Molecular docking simulation

Grid maps of $60 \times 60 \times 60$ points with 0.375 \AA spacing generated by AutoGrid3 were centered at the ligand binding site in the VP35 crystal structure. The docking was performed employing Lamarckian genetic algorithm with pseudo-Solis and Wets local search with population size of 50 and energy evaluation of 2,500,000; root mean square tolerance of 1.0 \AA and 100 docking runs by AutoDock 3.0 [27]. The ligand conformation with lowest free energy of binding in the most populated cluster was selected for comparison.

2.4 Results and discussion

The energetic and some molecular parameters of the compounds studied in the gas phase in the C_s symmetry are collected in Table 2.1. It is worth to note that the compounds have large dipole moment and this is an essential criteria for drug-receptor interaction [29].

The theoretical and experimental geometrical parameters of T-705 are summarized in Table 2.2. The structural parameters of the optimized structures of all

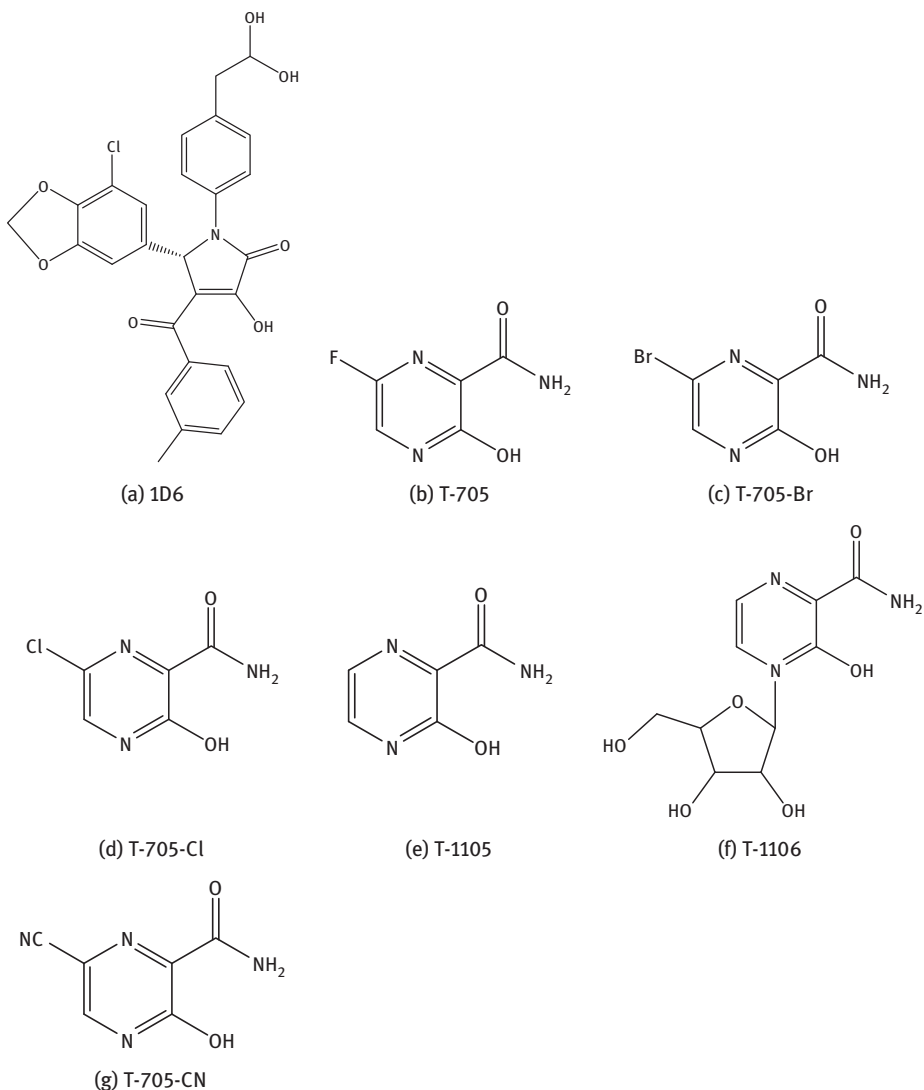


Figure 2.1: The chemical structure of (a) 1D6 (PDB id 4IBG), (b) T-705, (c) T-705-Br, (d) T-705-Cl, (e) T-1105, (f) T-1106 and (g) T-705-CN.

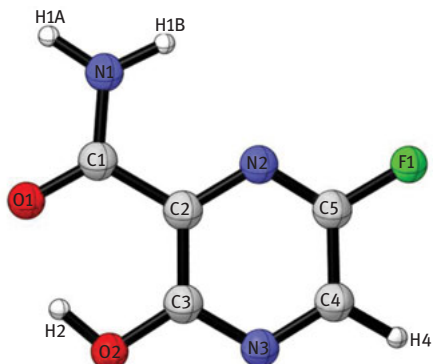
compounds studied are summarized Tables S1a-S1e (available from the corresponding author). In general, there is a good agreement between the predicted and experimental parameters for T-705 and therefore, the predicted data for the other compounds should be reliable. These structural parameters will be useful when these compounds are synthesized and characterized.

To clarify the vibrational frequencies, it is essential to examine the geometry of the compound. A very small change in the geometry can potentially cause substantial

Table 2.1: Energetic and relevant parameters of the compounds studied in C_s symmetry.

	T-1105	T-705	T-705-Cl	T-705-Br	T-705-CN
ΔG (Hartree)	-508.343851	-607.623509	-967.977882	-3081.89912	-600.608953
Dipole moment (Debye)	4.616	3.240	3.347	3.399	2.752
Thermal total energy (kcal/mol)	73.0	68.3	67.6	67.4	73.0
Heat capacity (kcal/mol.K)	30.5	33.4	34.5	34.9	36.6
Entropy (cal/mol.K)	87.7	92.0	95.0	98.0	97.2
Vibrational energy (kcal/mol)	71.2	66.6	65.8	65.6	71.2
Zero point vibrational energy (kcal/mol)	68.0	62.9	61.8	61.4	66.9
Rotational constant (GHz)					
A	2.398	1.830	1.690	1.631	1.680
B	1.291	0.959	0.688	0.442	0.719
C	0.839	0.629	0.489	0.348	0.504

variations in their frequencies. Regarding the computations, the largest difference between the experimental and calculated bond lengths (angle/torsion) is 0.17 Å for O2-H2 (2.6° for C3-O2-H2/1.4° for N3-C4-C5-F1). Generally, it is expected that the bond distances calculated by electron correlated methods are longer than the experimental distance. This situation is clearly observed in Table 2.2 especially where hydrogen is present. The observed difference in OH bond distances is not due to the theoretical shortcomings since experimental results are also subject to variations owing to insufficient data to calculate the equilibrium structure and which are sometimes averaged over zero point vibrational motion. In X-ray structure the error in the position of the hydrogen atoms is such that their bonding parameters greatly vary compared to the non-hydrogen atoms. Intra- or intermolecular hydrogen bonding is also an important factor in the crystalline state of compound which usually leads to shortening of the OH bond. This compound is planar and has an intramolecular O9-H10...O12 hydrogen bond as H10-O12: 1.880 Å, O9-O12: 2.591 Å and O9-H10-O12: 144° [30]. These experimental values have been supported by theoretical results and calculated as about 1.723 Å, 2.610 Å and 147°, respectively. In general, the computed parameters are in excellent agreement with the reported experimental data. The root mean square deviation (RMSD)/mean absolute deviation (MAD) values between the experimental and calculated bond lengths, bond angles and torsional are 0.081 Å/0.049 Å, 0.966°/0.795°, and 0.779°/0.706° respectively. The difference in values noticed in the present study may be due to the fact that the experimental results were obtained at solid phase and the molecular rotations were restricted, while the theoretical results were obtained in the gas phase.

Table 2.2: Structural parameters, root mean square deviation and mean absolute deviation of T-705 computed using the B3LYP/6-311++G(d,p) method in the gas phase.


Bond lengths (Å)	Experimental [30]	Computed	Bond angles (°)	Experimental	Computed
C1-O1	1.244	1.237	N2-C5-F1	116.8	117.6
C1-N1	1.318	1.346	N2-C5-C4	123.3	123.0
C1-C2	1.481	1.491	F1-C5-C4	119.9	119.4
C2-N2	1.335	1.341	C1-N1-H1A	120.0	119.1
C2-C3	1.397	1.416	C1-N1-H1B	120.0	120.0
C3-O2	1.328	1.327	H1A-N1-H1B	120.0	120.9
C3-N3	1.340	1.338	C5-N2-C2	116.3	117.1
C4-N3	1.306	1.323	C4-N3-C3	117.0	117.9
C4-C5	1.390	1.399	C3-O2-H2	109.5	106.9
C4-H4	0.930	1.085	Dihedral angles (°)	Experimental	Computed
C5-N2	1.295	1.302	O1-C1-C2-N2	179.2	180.0
C5-F1	1.339	1.344	N1-C1-C2-N2	-0.4	0.0
N1-H1A	0.860	1.007	O1-C1-C2-C3	-0.7	0.0
N1-H1B	0.860	1.009	N1-C1-C2-C3	179.7	180.0
O2-H2	0.820	0.990	N2-C2-C3-O2	179.1	180.0
Bond angles (°)	Experimental	Computed	C1-C2-C3-O2	-1.0	0.0
O1-C1-N1	123.1	123.5	N2-C2-C3-N3	-1.0	0.0
O1-C1-C2	119.7	120.5	C1-C2-C3-N3	178.9	180.0
N1-C1-C2	117.3	116.0	N3-C4-C5-N2	-0.9	0.0
N2-C2-C3	121.4	120.9	N3-C4-C5-F1	178.6	180.0
N2-C2-C1	118.0	118.6	F1-C5-N2-C2	-179.3	-180.0
C3-C2-C1	120.7	120.6	C4-C5-N2-C2	0.2	0.0
O2-C3-N3	115.6	116.8	C3-C2-N2-C5	0.7	0.0
O2-C3-C2	123.5	122.7	C1-C2-N2-C5	-179.2	-180.0
N3-C3-C2	120.8	120.5	C5-C4-N3-C3	0.6	0.0
N3-C4-C5	121.2	120.7	O2-C3-N3-C4	-179.8	-180.0
N3-C4-H4	119.4	118.4	C2-C3-N3-C4	0.3	0.0
C5-C4-H4	119.4	120.9			
RMSD of bond length	0.081 Å		MAD of bond length	0.049 Å,	
RMSD of bond angle	0.966°		MAD of bond angle	0.795°,	
RMSD of torsional angle	0.779°		MAD of torsional angle	0.706°	

2.5 Vibrational studies

All the theoretical wavenumbers for T-705, along with corresponding vibrational assignments and intensities are given in Table 2.3. The simulated vibrational spectra are depicted in Figure 2.2. All the computed wavenumbers presented in this paper are obtained within the harmonic approximation. The theoretical wavenumbers of all the compounds studied are also collected in Tables S1a-S1e. This allows describing the vibrational motion in terms of independent vibrational modes, each of which is governed by a simple one-dimensional harmonic potential. The compound consists of 15 atoms, having 39 normal vibrational modes, and it belongs to the point group C_s . The 39 modes of vibrations account for the irreducible representations $\Gamma_v = 27A' + 12A''$ of the C_s point group. The assignments of vibrational modes for the investigated symmetry have been provided by VEDA 4. The following are some of the important vibrational motions that were predicted: NH_2 , OH, CH, C = O, C-O, CF, CC, CN and ring vibrations.

Table 2.3: Computed wavenumbers (cm^{-1}) of T-705 in the gas phase.

Mode		Assignments ^a	B3LYP/6-311++G(d,p)		
		PED ($\geq 10\%$) ^b	ν^c	I_R^d	I_R^d
ν_1	A'	$\nu_a(NH_2)$ (99)	3717	98.04	7.51
ν_2	A'	$\nu_s(NH_2)$ (99)	3582	70.74	18.99
ν_3	A'	$\nu(OH)$ (99)	3326	412.71	12.87
ν_4	A'	$\nu(CH)$ (100)	3177	7.61	30.09
ν_5	A'	$\nu(C=O)$ (75) + $\delta(NH_2)$ (10) + $\delta(OH)$ (10)	1718	407.70	12.65
ν_6	A'	ν_{ring} (66) + $\delta(NH_2)$ (20) + $\delta(OH)$ (10)	1618	79.82	17.61
ν_7	A'	ν_{ring} (67) + $\delta(OH)$ (20) + $\delta(NH_2)$ (10)	1611	9.21	9.03
ν_8	A'	$\delta(NH_2)$ (85) + ν_{ring} (10)	1594	164.73	13.49
ν_9	A'	ν_{ring} (59) + $\nu(CO)$ (21) + $\nu(CN)$ (14)	1487	125.34	0.34
ν_{10}	A'	$\delta(OH)$ (59) + ν_{ring} (30)	1465	546.75	0.14
ν_{11}	A'	$\nu(CC)$ (56) + $\delta(OH)$ (20) + $\delta(NH)$ (15)	1429	89.60	80.82
ν_{12}	A'	$\nu(CO)$ (52) + $\delta(CH)$ (41)	1369	0.54	15.77
ν_{13}	A'	$\delta(CH)$ (71) + ν_{ring} (15)	1341	17.87	1.35
ν_{14}	A'	$\nu(CF)$ (52) + $\delta(CH)$ (33) + $\delta(OH)$ (10)	1277	110.66	6.83
ν_{15}	A'	ν_{ring} (93)	1233	149.06	2.23
ν_{16}	A'	$\delta(NH_2)$ (35) + ν_{ring} (32) + $\delta(CH)$ (27)	1131	21.45	1.88
ν_{17}	A'	$\nu(CN)$ (63) + ν_{ring} (20)	1092	6.60	12.79
ν_{18}	A'	δ_{ring} (75) + $\delta(NH_2)$ (20)	987	28.43	24.06
ν_{19}	A''	$\gamma(CH)$ (94)	936	9.19	0.10
ν_{20}	A'	δ_{ring} (80) + $\delta(NH_2)$ (13)	828	38.85	7.13
ν_{21}	A''	$\gamma(OH)$ (96)	823	104.27	0.37
ν_{22}	A''	$\gamma(CC)$ (70) + γ_{ring} (16)	796	12.23	1.63
ν_{23}	A''	$\gamma(CN)$ (48) + γ_{ring} (45)	749	0.00	1.44
ν_{24}	A'	δ_{ring} (91)	706	15.10	20.21

(continued)

Table 2.3 (continued)

Mode		Assignments ^a	B3LYP/6-311++G(d,p)		
			PED ($\geq 10\%$) ^b	ν^c	I_{IR}^d
v ₂₅	A'	δ_{ring} (92)	667	44.52	1.42
v ₂₆	A''	$\gamma(NH_2)$ (92)	628	0.23	1.62
v ₂₇	A''	γ_{ring} (60) + $\gamma(NH_2)$ (32)	579	3.56	0.06
v ₂₈	A'	$\delta(CC)$ (52) + δ_{ring} (40)	573	0.53	2.18
v ₂₉	A'	δ_{ring} (95)	498	1.95	20.35
v ₃₀	A''	γ_{ring} (80) + $\gamma(CH)$ (12)	472	49.31	0.05
v ₃₁	A'	$\delta(C=O)$ (58) + $\delta(CO)$ (33)	442	1.73	11.17
v ₃₂	A'	$\delta(CF)$ (48) + $\delta(CN)$ (37)	404	5.55	6.57
v ₃₃	A''	γ_{ring} (75) + $\gamma(NH_2)$ (18)	395	0.55	7.90
v ₃₄	A''	$\gamma(NH_2)$ (95)	364	178.53	0.46
v ₃₅	A'	$\delta(CO)$ (57) + $\delta(CC)$ (35)	352	7.22	1.45
v ₃₆	A'	$\delta(CN)$ (78) + $\delta(CF)$ (10)	215	13.17	15.47
v ₃₇	A''	$\gamma(CF)$ (80) + γ_{ring} (11)	171	0.02	4.24
v ₃₈	A''	$\gamma(CO)$ (72) + γ_{ring} (10) + $\gamma(C=O)$ (10)	130	0.01	22.37
v ₃₉	A''	$\gamma(C=O)$ (81) + $\gamma(CO)$ (11)	88	3.01	28.79

ν , δ and γ denote stretching, in plane bending and out of plane bending, respectively.

^aT-705 in the C_s symmetry. ^b PED data are taken from VEDA4. ^c Raw frequency. ^d I_{IR} and I_R : Calculated infrared (km/mol) and Raman ($\text{\AA}/\text{amu}$) intensities.

For the present compound, the high wavenumber region contains characteristic wavenumbers of the amine NH_2 , OH and CH stretchings. The carbonyl stretch of the compound is computed at 1718 cm^{-1} as both Raman and IR active band. These computations indicate that all the raw values for stretching vibrations will be within the expected range, together with scaling factor. Also, these raw values are consistent with previously reported data [31–33]. Similarly, C = O, C-O, CF, CC, CN and ring vibrations are found in the expected range and are in good agreement with the literature values [31–33]. The ring, C-O, CC, CN, CF stretching and NH_2 , CH, OH and ring in plane bending modes dominate the regions of $1600\text{--}700\text{ cm}^{-1}$, while the CH, OH, CC and CN out of plane bending modes are seen in the $900\text{--}700\text{ cm}^{-1}$. The CN, CF, C = O, C-O and C-C in plane and NH_2 , CF, C = O, C-O and ring out of plane bending vibrations are seen in the low frequency region. Vibrational modes in the low wavenumber region of the spectrum contain contributions of several internal coordinates and their assignment is a reduction approximation to one of two of the internal coordinates. All other vibrations are collected in Table 2.3.

2.6 Electronic spectrum

The UV–Vis spectra, electronic transitions, vertical excitation energies, absorbances and oscillator strengths of the compounds were calculated with the time-dependent

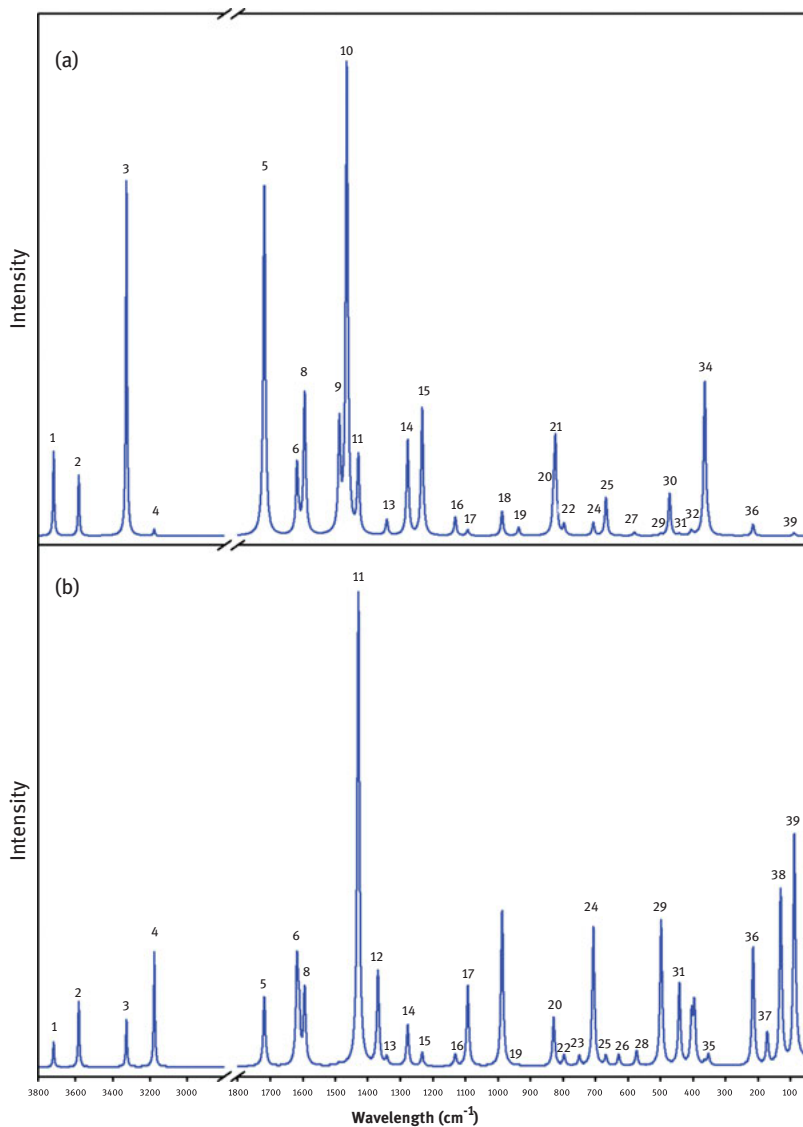


Figure 2.2: Theoretical (a) IR and (b) Raman spectra of T-705.

density functional theory (TD-DFT) [34] using the gas-phase optimized geometries. The simulated UV spectra of the compounds were shown in Figure 2.3. The major molecular characteristics of the electronic spectrum are collected in Table 2.4.

From UV spectra, the absorption bands were centered at 301.38, 293.52, 286.17, 284.40 and 275.43 nm in the gas phase for Br-, Cl-, F-, CN- and H-compound, respectively. For with CN-compound, HOMO-LUMO transition is close to T-705. According to periodic table from H to Br, it is suitable due to ordering atoms via

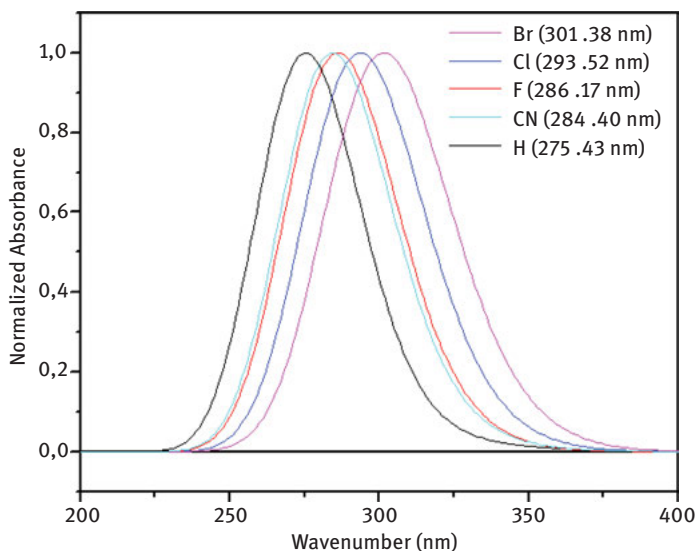


Figure 2.3: Simulated UV spectra of the compounds.

Table 2.4: Calculated wavelength, excitation energy and oscillator strength of the compounds.

Compound	λ (nm)	E (eV)	f	Major contribution
T-705-Br	322.9	3.84	0.0031	H-1 \rightarrow L (99%)
	301.4	4.11	0.1663	H \rightarrow L (92%)
	267.5	4.64	0.0010	H-2 \rightarrow L (36%)
T-705-Cl	321.2	3.86	0.0031	H-1 \rightarrow L (99%)
	293.5	4.22	0.1965	H \rightarrow L (92%)
	266.1	4.66	0.0010	H-3 \rightarrow L (96%)
T-705	318.7	3.89	0.0027	H-1 \rightarrow L (98%)
	286.2	4.33	0.2267	H \rightarrow L (90%)
	265.9	4.66	0.0011	H-3 \rightarrow L (96%)
T-705-CN	325.3	3.81	0.0032	H-1 \rightarrow L (99%)
	284.4	4.36	0.2113	H \rightarrow L (90%)
	271.6	4.56	0.0002	H-1 \rightarrow L-1 (95%)
T-1105	328.0	3.78	0.0035	H-1 \rightarrow L (99%)
	275.4	4.50	0.2191	H \rightarrow L (90%)
	264.5	4.69	0.0008	H-3 \rightarrow L (96%)

electro-negativity. As can be observed from Table 2.4, for T-705, the contribution to charge transition in 286.2 nm results from the HOMO to the LUMO with 90%. The largest contribution for 318.7 nm is assigned to H-1 \rightarrow L transition with 98%. H-3 \rightarrow L transition with 96% is computed at 265.9 nm.

The energy gaps between HOMO and LUMO are largely responsible for the chemical and spectroscopic properties of the molecules [35]. The energy values of HOMO and LUMO levels are presented in Table 2.5.

Table 2.5: HOMO and LUMO energy values (eV) of the compounds studied.

Parameters	T-1105	T-705	T-705-Cl	T-705-Br	T-705-CN
LUMO	-2.51	-2.85	-2.82	-2.82	-3.14
HOMO	-7.23	-7.37	-7.30	-7.24	-7.81
Gap	4.7	4.5	4.5	4.4	4.7

The density plot of the HOMO and LUMO of T-705 shown in Figure 2.4. These diagrams were plotted with a contour value of 0.02. It can be observed from Figure 2.4 that HOMO is delocalized on all atoms while LUMO is delocalized on all the atoms except on fluorine atom and OH group. The HOMO-LUMO gap is 4.5 eV which is sufficiently large to meet the viability criterion suggested by Hoffmann et al. [36].

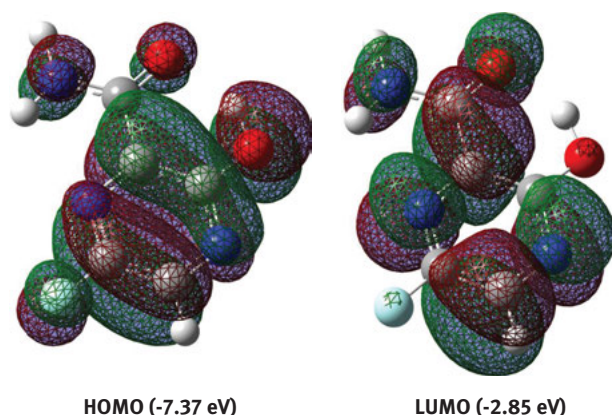


Figure 2.4: HOMO and LUMO of T-705.

2.7 Molecular docking

In addition to the DFT study, we supplemented this research work with molecular docking studies (Figure 2.5) relevant to drug-target interactions. The docking results indicate that 1D6 has the most favourable free energy of binding compared to other compounds (Table 2.6). It is also noted that the substitution of fluorine atom in T-705 by bromine atom in T-705-Br, chlorine atom in T-705-Cl and hydrogen atom in T-1105 does not improve the binding energy with VP35. Docked conformation shows that smaller compounds with pyrazine ring (T-705, T-705-Br, T-705-Cl and T-1105) were docked at deeper but relatively smaller pocket of VP35. The larger compounds are

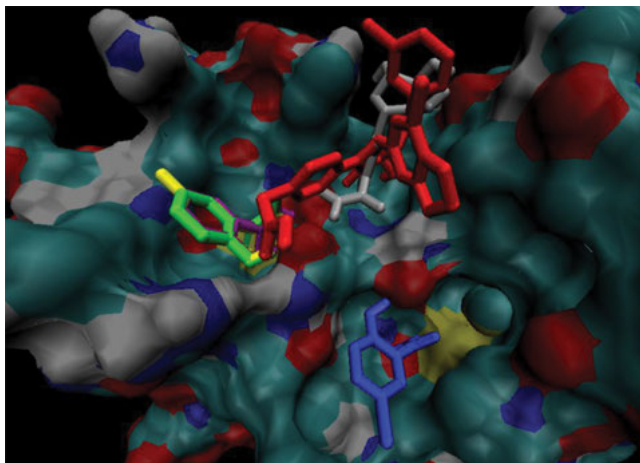


Figure 2.5: The docked conformation of (a) 1D6 (PDB id 4IBG; red stick), (b) T-705 (yellow stick), (c) T-705-Br (green stick), (d) T-705-Cl (blue stick), (e) T-1105 (purple stick), and (f) T-1106 (grey stick) in the binding pocket of Ebola virus VP35 (surface representation).

Table 2.6: Estimated free energy of binding for ligands docked into Ebola virus viral protein 35 (VP35).

Ligand	Free energy of binding (FEB; kcal/mol)
1D6	-6.50
T-705	-4.71
T-705-Br	-4.78
T-705-Cl	-4.89
T-1105	-4.59
T-1106	-5.46

bound at the same ligand binding site of VP35 (IFN inhibitory domain; IID). This docking simulation shows that in order to occupy the binding site of VP35 IID with a better binding affinity, the compound should consist of the essential benzene rings and pyrrolidinone scaffold as suggested by the recent study [14, 26, 27, 39].

2.8 Conclusions

This combined ab initio and docking study targeted unsubstituted T-705, T-705 and substituted T-705. Ab initio method based on DFT was used to predict the structural and spectroscopic parameters. The computed data compare favourably with literature for T-705 while the literature for the other compounds is limited. Therefore, the reported information for should be reliable for future investigations. The molecular

docking indicates that the compounds studied have comparable free energy of binding with VP35 although this is less when compared with 1D6 and T-1106.

Acknowledgements: The authors acknowledge the facilities from their respective universities.

References

- [1] Centers for disease controls and prevention. 2014. Outbreaks chronology: Ebola haemorrhagic fever. Available at: <http://www.cdc.gov/vhf/ebola/>. Accessed: Jan 2016.
- [2] Hayden E. The Ebola questions: scientists know a lot about the virus that causes Ebola — but there are many puzzles that they have yet to solve. *Nature*. 2014;514:554–7.
- [3] Baize S, Pannetier D, Oestereich L, et al. Emergence of Zaire Ebola virus disease in Guinea. *N Engl J Med*. 2014;371:1418–25.
- [4] <http://www.who.int/mediacentre/news/releases/2016/ebola-zero-liberia/en/>. Accessed: Dec 2016.
- [5] Ippolito G, Puro V, Piselli P. Ebola in West Africa: who pays for what in the outbreak? *New Microbiol*. 2015;38:1–3.
- [6] The Economist. Ebola's legacy after the passing, The virus will have a long-lasting impact on already poor countries. 2015. Available at: <http://www.economist.com/news/middle-east-and-africa/21637391-virus-will-have-long-lasting-impact-already-poor-countries-after>. Accessed: Dec. 2016.
- [7] Zhang Y, Li H, Cheng A. Ebola haemorrhagic fever. In: Li H, editor. *Radiology of infectious diseases: volume 1, Chapter 13*. Dordrecht, Heidelberg, New York, London: Springer Science+Business Media Dordrecht and People's Medical Publishing House, 2015.
- [8] Judson S, Prescott J, Munster V. Understanding Ebola virus transmission. *Viruses*. 2015;7:511–21.
- [9] Mendoza EJ, Qiu X, Kobinger GP. Progression of Ebola therapeutics during the 2014–2015 outbreak. *Trends Mol Med*. 2016;22:164–73.
- [10] Kaushik A, Tiwari S, Jayant RD, et al. Towards detection and diagnosis of Ebola virus disease at point-of-care. *Biosens Bioelectron*. 2016;75:254–72.
- [11] http://www.who.int/medicines/emp Ebola_q_as/en/. Accessed: Dec 2016.
- [12] Buttler D. Ebola drug trials set to begin amid crisis. *Nature*. 2014;513:156.
- [13] Furuta Y, Takahashi K, Shiraki K, et al. T-705 (Favipiravir) and related compounds: novel broad-spectrum inhibitors of RNA viral infections. *Antiviral Res*. 2009;82:95–102.
- [14] Furuta Y, Gowen BB, Takahashi K, et al. Favipiravir (T-705) a novel viral RNA polymerase inhibitor. *Antiviral Res*. 2013;100:446–54.
- [15] Furuta Y, Takahashi K. Inventors; Toyama Chemical Co., Ltd., assignee. Nitrogenous heterocyclic carboxamide derivatives or salts thereof and antiviral agents containing both. CA2339272A1. 2 Mar 2000.
- [16] Shi F, Zongtao L, Kong, L, et al. Synthesis and crystal structure of 6-fluoro-3-hydroxypyrazine-2-carboxamide. *Drug Discov Ther*. 2014;8:117–20.
- [17] De Clercq E. Antivirals: past, present and future. *Biochem Pharmacol*. 2013;85:727–44.
- [18] De Clercq E. Dancing with chemical formulae of antivirals: A personal account. *Biochem Pharmacol*. 2013;86:711–25.
- [19] De Clercq E. Dancing with chemical formulae of antivirals: A panoramic view (part 2). *Biochem Pharmacol*. 2013;86:1397–410.
- [20] Hernandez MZ, Cavalcanti SM, Moreira DR, et al. Halogen atoms in the modern medicinal chemistry: hints for the drug design. *Curr Drug Targets*. 2010;11:303–14.

- [21] Kharkar PS, Ramasami P, Choong YS, et al. Discovery of anti-Ebola drugs: a computational drug repositioning case study. *RSC Adv.* 2016;6:26329–40.
- [22] Frisch MJ, Trucks GW, Schlegel HB, et al. Gaussian 09, revision D.01. Wallingford CT: Gaussian, Inc, 2009.
- [23] Dooley R, Milfeld K, Guiang C, Pamidighantam S, Allen G. From proposal to production: lesson learned developing the computational chemistry grid cyberinfrastructure. *J Grid Comput.* 2006;4:195–208.
- [24] Milfeld K, Guiang C, Pamidighantam S, Giuliani J. Proceedings of the 2005 Linux Clusters: The HPC Revolution, NCSA University of Illinois, CHPC University of New Mexico and IBM, 2005.
- [25] Dooley R, Allen G, Pamidighantam S. Proceedings of the 13th Annual Mardi Gras Conference, CCT. Baton Rouge, LA: Louisiana State University, 2005:83.
- [26] Brown CS, Lee MS, Leung DW, et al. *In silico* derived small molecules bind the filovirus VP35 protein and inhibit its polymerase cofactor activity. *J Mol Biol.* 2014;426:2045–58.
- [27] Morris GM, Goodsell DS, Halliday RS, et al. Automated docking using a Lamarckian genetic algorithm and an empirical binding free energy function. *J Comput Chem.* 1998;19:1639–62.
- [28] HyperChem(TM) Professional 7.51, Hypercube, Inc., 1115 NW 4th Street, Gainesville, Florida 32601, USA.
- [29] Lien EJ, Guo Z-R, Li R-L, et al. Use of dipole moment as a parameter in drug-receptor interaction and quantitative structure-activity relationship studies. *J Pharm Sci.* 1982;71:641–55.
- [30] Shi F, Li Z, Kong L, et al. Synthesis and crystal structure of 6-fluoro-3-hydroxypyrazine-2-carboxamide. *Drug Discov Ther.* 2014;8:117–20.
- [31] Joseph T, Varghese HT, Panicker CY, et al. Vibrational spectroscopic investigations and computational study of 5-tert-Butyl-N-(4-trifluoromethylphenyl) pyrazine-2-carboxamide. *Spectrochim Acta A.* 2013;113:203–14.
- [32] Sakthivel S, Alagesan T, Al-Saadi AA, et al. Vibrational spectra of 3,5-diamino-6-chloro-N-(diaminomethylene) pyrazine-2-carboxamide: combined experimental and theoretical studies. *Spectrochim Acta A.* 2014;127:157–67.
- [33] Lukose J, Panicker CY, Nayak PS, et al. Synthesis, structural and vibrational investigation on 2-phenyl-N-(pyrazin-2-yl)acetamide combining XRD diffraction, FT-IR and NMR spectroscopies with DFT calculations. *Spectrochim Acta A.* 2015;135:608–16.
- [34] Runge E, Gross EKH. Density-functional theory for time-dependent systems. *Phys Rev Lett.* 1984;52:997–1000.
- [35] Atkins PW, De Paula J. *Atkins' physical chemistry.* Oxford: Oxford University Press; 2001.
- [36] Hoffmann R, Schleyer P, Schaefer HF. Predicting molecules—more realism, please!. *Angew Chem Int Ed.* 2008;47:7164–7.
- [37] Smither SJ, Eastaugh LS, Steward JA, et al. Post-exposure efficacy of oral T-705 (Favipiravir) against inhalational Ebola virus infection in a mouse model. *Antiviral Res.* 2014;104:153–5.

Supplemental Material: The online version of this article offers supplementary material (<https://doi.org/10.1515/psr-2017-0198>).

Ayşegül Gümüş and Selçuk Gümüş

3 Potential thermally activated delayed fluorescence properties of a series of 2,3-dicyanopyrazine based compounds

Abstract: 2,3-Dicyanopyrazine based acceptor was combined with a series of well studied donors to obtain donor-acceptor type potential thermally activated delayed fluorescence emitters. Their structural and electronic properties were computed theoretically at the level of density functional theory and time dependent density functional theory with the application of two different hybrid functionals and various basis sets. Almost all of the designed structures were computed to have the potential of being TADF compounds since they possess very narrow singlet-triplet gaps. Indeed, acridine-pyrazine (**9**) derivative was calculated to be the best candidate for the purpose among them.

Keywords: TADF, Dicyanopyrazine, donor-acceptor, DFT, TDDFT

3.1 Introduction

Light is a physical quantity that is emitted by a luminous body. An incident on the eye causes the sensation of sight through nerves. However, only a tiny proportion of the whole electromagnetic spectrum is visible to the human eyes. Although human capabilities for perception of light are highly elevated, only a very narrow range of the electromagnetic spectrum, which extends from the deepest violet (400 nm) to the deepest red (750 nm), can be seen by human. According to the wavelength and frequency, the color of light changes. The emission of wavelengths corresponding to the visible region requires a minimum excitation energy ranging between 1.8 and 3.1 eV [1].

There are two possible practical phenomenon to create light, namely incandescence and luminescence. Heated to a high enough temperature, a material starts glowing. The process of incandescence is emission of light from heat energy. When atoms or molecules are heated, they release some of their thermal vibrations as electromagnetic radiation in the form of incandescent light. This is the most common type of light obtained from the sun. The sun provides almost all of the heat, light, and

This article has previously been published in the journal *Physical Sciences Reviews*. Please cite as: Gümüş, A., Gümüş, S. Potential thermally activated delayed fluorescence properties of a series of 2,3-dicyanopyrazine based compounds. *Physical Sciences Reviews* [Online] **2018**, 3. DOI: 10.1515/psr-2017-0197

<https://doi.org/10.1515/9783110568196-003>

other forms of energy that are necessary for life on our planet by the process of incandescence. Luminescence, on the other hand, is cool emission caused by the movement of electrons within a substance from more energetic states to less energetic states and hence it is a process of giving off light without generating heat. This can be caused by absorption of photons, chemical or biochemical reactions, activity of subatomic particles, radiation, or stress on a crystal. The wavelength of light emitted is a characteristic of luminescent substance and not of the incident radiation [2, 3].

Fluorescence was experimentally demonstrated in 1852 that certain substances absorb the light of a narrow spectral region (e. g., blue light) and instantaneously emit light in another spectral region not present in the incident light (e. g., yellow light). Thus, fluorescence is the property of some atoms and molecules to absorb light at a particular wavelength and to subsequently emit light of longer wavelength after a brief interval, which is called the fluorescence lifetime [4]. Following excitation via ultraviolet or visible radiation, excited electrons release their excess energy in the form of photons, thereby making a back transition to the ground state (singlet state), emitting excitation energy as fluorescence. During these transitions the multiplicity of the system is conserved. On the other hand, phosphorescence is delayed luminescence which involves forbidden energy state transitions [1]. A triplet-singlet transition is much less probable than a single-singlet transition, thus, phosphorescence takes place in a longer time scale [5]. A simplified Jablonski diagram illustrating fluorescence and phosphorescence is shown in Figure 3.1. Reinhoudt's empirical rule states that the intersystem crossing (ISC) process will be effective when $\Delta\epsilon(S_1-T_1)$ is lower than 0.6 eV for all type of ligands [6].

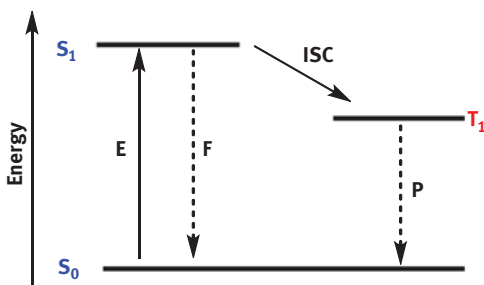


Figure 3.1: Illustration of fluorescence and phosphorescence. (**E**, **F** and **P** stand for Excitation, Fluorescence and Phosphorescence, respectively).

Light-emitting devices (LEDs) have been pronounced for almost 50 years, but until a decade ago, they were used as indicator lamps in electronic equipment. After this initiation, LED technology flourished due to its high efficiency, high reliability, rugged construction, durability, and the fact that it is toxic metals free. The search for brighter LEDs resulted in widening of application area such as; lighting, traffic

lighting, indicators, electronic billboards, headlamps for motor vehicles, flashlights, searchlights, cameras, store signs, destination signs on vehicles, general illumination, visual display, decorative purposes, etc. As better performance LED investigations go on the newest applications includes the use of organic materials.

The name OLED comes from the initials of Organic Light Emitting Diode. OLED is internationally recognized as unique light source that possesses the potential to replace conventional lighting source. It is a display device that sandwiches carbon-based (as the name implies) films between two charged electrodes, a metallic cathode and a transparent anode, usually being glass [7]. The organic films consist of a hole-injection layer, a hole-transport layer, an emissive layer and an electron-transport layer [8]. These organic arrays produce brighter light and utilize less energy [9–11].

OLED technology was invented by Eastman Kodak in the early 1980s. It is beginning to replace LCD technology in handheld devices such as PDAs and cellular phones because the technology is brighter, thinner, faster and lighter than LCDs, use less power, offer higher contrast and are cheaper to manufacture [12].

In an OLED, with the application of an electric field, electrons are transported through the lowest unoccupied molecular orbital (LUMO), while holes are transported through the highest occupied molecular orbital (HOMO) toward the emissive layer and recombine on the emitter molecules so as to form triplet or singlet excitons. When voltage is applied to the OLED cell, the injected positive and negative charges recombine in the emissive layer and create electro luminescent light. Unlike LCDs, which require backlighting, OLED displays are emissive devices – they emit light rather than modulate transmitted or reflected light [1].

In this work, we have constructed a series of dicyano dibenzo[f,h]quinoxaline (Figure 3.2) compounds and investigated the structural and electronic properties theoretically at the level of density functional theory. These D-A type compounds may be potential candidates for organic solar cell applications or organic light emitting diodes or fluorescent organic materials.

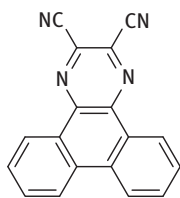


Figure 3.2: Structure of the parent compound (dibenzo[f,h]quinoxaline-2,3-dicarbonitrile).

3.2 Method of calculation

The three-dimensional ground state (S_0) geometries of all compounds were geometry optimized using DFT [13] with the Gaussian 09W [14] package program and

the hybrid functional B3LYP and M06-2X. B3LYP is composed of Becke's three parameter exchange functional (B3) [15] and the nonlocal correlation functional by Lee, Yang, and Parr (LYP) [16]. On the other hand, M06-2X is a set of four meta-hybrid GGA DFT functionals. They are constructed with empirical fitting of their parameters, but constraining to the uniform electron gas [17]. The suite has a very good response under dispersion forces, improving one of the biggest deficiencies in DFT methods. The s6 scaling factor on Grimme's long range dispersion correction is 0.20, 0.25 and 0.06 for M06-L, M06 and M06-2X respectively. Compare it with the values of 1.05 for B3LYP or 0.70 for PBE0 [18–20]. The basis set used for all atoms was 6–311 + G(d,p) for geometry optimizations.

For each compound, vibrational analyses were carried out using the same basis set employed in the corresponding geometry optimizations. The frequency analysis of none of the compounds yielded any imaginary frequencies, indicating that the structure of each molecule corresponds to at least a local minimum on the potential energy surface. The normal mode analysis was performed for 3N-6 vibrational degrees of freedom, with N being the number of atoms in the molecule.

The low-lying triplet (T) and singlet excited states (S) of the compounds were relaxed to obtain their minimum energy geometries using the TD-DFT. The vertical excitation energies and oscillator strengths were obtained for the lowest triplet and singlet transitions at the optimized ground state equilibrium geometries by using TD-DFT with a series of hybrid functionals and basis sets [21]. Optimized ground state structures were utilized to obtain the electronic absorption spectra, including maximum absorption wavelengths, oscillator strengths, and main configuration assignment by using TD-DFT. Although there exists some exceptions, information in the literature suggest that the analysis of the excitation energies with PBE0, wb97XD and CAM-B3LYP functionals predict the best agreement with the experimental data [22]. Therefore, for TD-DFT computations B3LYP/6-31G(d,p), B3LYP/6–311 + G(d,p), B3LYP/cc-PVTZ and CAM-B3LYP/6–311 + G(d,p) methods have been applied and the results have been compared.

3.3 Results and discussion

The demand for economically viable for large-scale power generation based on environmentally green materials with limitless availability and variety has forced people to search for novel ideas and applications. Organic semiconductor materials are cheaper alternatives to inorganic counterparts like Si. Organic photovoltaics can have extremely high optical absorption coefficients which provide potential for the production of very thin solar cells; therefore, they can be fabricated as thin flexible devices.

For fluorescent molecules, the radiative exciton fraction is typically assumed to be 0.25 [23, 24]. But, this value could be increased upto 1.0 by the introduction of phosphorescent emitters [25–27]. However, due to the need for rare metals like

iridium or platinum, which facilitate efficient spin-orbit coupling, it is very likely that the cost for the production of an OLED device will increase [28–30]. The classical limit of external quantum efficiency of OLEDs using fluorescent and phosphorescent emitters is 5% and 20%, respectively. Recently, the conversion of non-radiative triplets to radiative singlets has been a promising concept to enhance device efficiency over these limits [31].

Recently, TADF emitters have drawn much attention and many novel compounds with this behaviour have been synthesized [32–36]. By design modification, it is possible to spatially separate the HOMO and LUMO, causing a decrease of the energy gap ΔE_{ST} between the lowest excited singlet (S_1) and triplet (T_1) state. According to Boltzmann statistics, this results in efficient conversion of triplet to singlet excitons by reverse intersystem crossing (RISC), which is a thermally activated mechanism. Because the emission originates due to decay from the S_1 state, this mechanism is sometimes called singlet harvesting [34]. It is thus possible to enhance the fluorescence efficiency of OLEDs by an increase of the radiative exciton fraction. Therewith, OLEDs with external quantum efficiency data far beyond the classical limit and comparable to devices using phosphorescent emitters have been reported [36].

In other words, a small ΔE_{ST} value means that there is a small overlap integral between the wave functions of the ground and excited states of a luminescent molecule, thus minimizing electron–electron repulsion between the electron orbitals in the triplet state [32]. In this context, the ground state of the molecule is equivalent to HOMO level, and the excited state is in turn equivalent to LUMO. One useful strategy to minimize the overlap between the wave functions is to localize the electron densities of the HOMO and LUMO states on donor and acceptor moieties, respectively [33]. Additional steric separation that is achieved by introducing a spiro junction or bulky substituents between the acceptor and donor units also helps this effect [33].

With all these information from the literature in hand, we have designed a series of Donor-Acceptor (D-A) type dicyano dibenzo[f,h]quinoxaline derivatives in order to suggest potential TADF emitters (Figure 3.2). The parent compound (dicyano dibenzo [f,h]quinoxaline) was synthesized from benzil [37] and used as a precursor to obtain novel pyrazinoporphyrazines. The importance of dicyanopyrazine derivatives has been mentioned mainly in the chemical industry, food, agricultural and medicinal chemistry [38]. In this work, the pyrazine fused phenanthrene moiety with two cyano groups attached (dicyano dibenzo[f,h]quinoxaline) (**1**) was the acceptor, benzene (**2**), thiophene (**3**), thiophene oligomers (**3a–3c**), anthracene (**4**), pyrene (**5**), triphenylamine (**6**), carbazole (**7**), phenoxazine (**8**), and dihydroacridine (**9**) were donor compartments (Figure 3.3).

The parent compound (**1**) is the phenanthrene derivative of dicyanopyrazine and its crystals were prepared [37, 39]. The compound exhibited high decomposition point at 248–365 °C and could be purified by sublimation. The absorption maxima was computed to be 328 nm, which is very close to the experimental data of 318 nm in dimethylformamide [40]. According to the literature; phenanthrene derivative (**1**) did not show

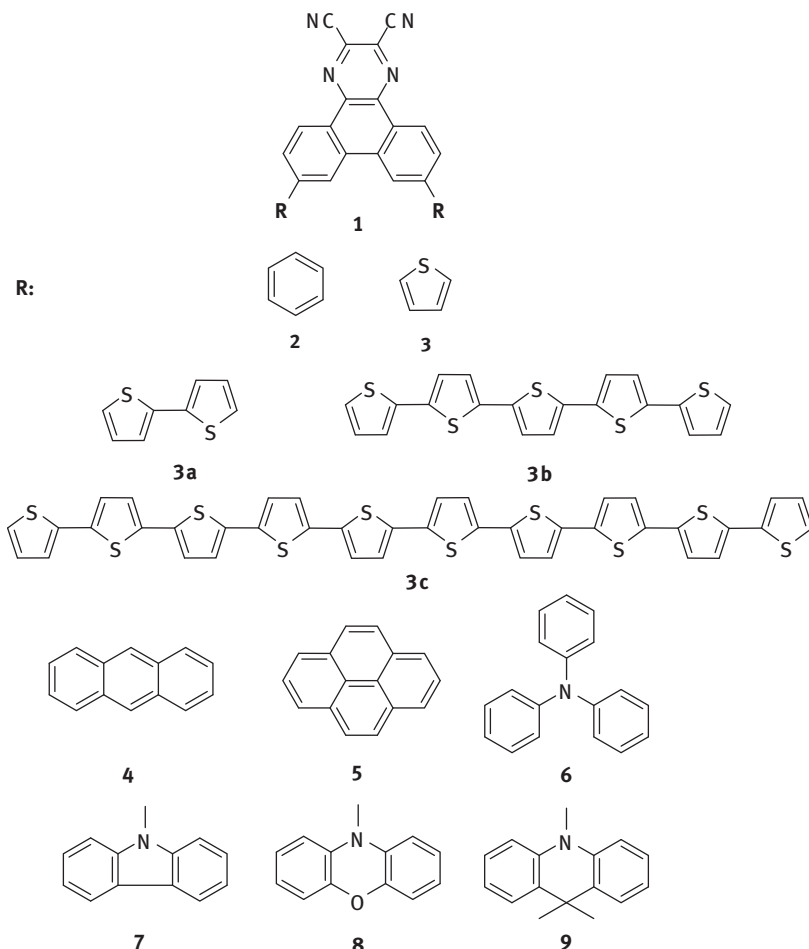


Figure 3.3: Structures of potential TADF compounds.

any field effect transistors (FET) characteristics indicated that some electron-accepting properties were necessary for producing the active conducting channel [39].

The idea of the present study emerged from the extensive spectroscopic investigations of the parent pyrazine compound performed in the literature [37, 39, 40]. Containing a well acceptor moiety in its structure, combination of **1** with donor units may produce potential TADF compounds.

3.3.1 Semiconductor properties

The electronic structure of all organic semiconductors is based on the conjugation of π -electrons. A conjugated organic system consists of alternating between single and

double carbon-carbon bonds. Single bonds are known as σ -bonds and are associated with localized electrons, while double bonds are composed of one σ -bond and one π -bond. The π -electrons are mobile and can jump between carbon atoms due to the mutual overlap of pi orbitals along the conjugation path, which causes the wave functions to delocalize over the conjugated skeleton. The empty π -bands are called the LUMO and π -bands filled with electrons are called the HOMO. The band gap (ΔE) of semiconductor materials ranges from 0.5 to 4.0 eV [41].

Frontier molecular orbital energies of the compounds were computed at the level of B3LYP/6-311 + G(d,p) and the results are given in Table 3.1. All computed band gap (ΔE) values have been found to be below 4 eV. As expected, the combination of donor units with acceptors is expected to reduce the inter-frontier molecular orbital energy gap of a compound due to extension of the conjugation path. The parent compound (**1**) had a band gap of 3.87 eV which was narrowed by the attachment of donor units. Therefore, all the compounds carry the potential of usage as semiconducting materials. The narrowest band gaps among all have been obtained for compounds **3c**, **8** and **9**.

Table 3.1: Results of computations (All data are in eV).

Compound	DFT			TD-DFT (ΔE_{ST})			
	B3LYP/6-311+(d,p)			B3LYP		CAM-B3LYP	
	HOMO	LUMO	ΔE	6-31(d,p)	6-311+(d,p)	cc-pvtz	6-311+(d,p)
1	-6.79	-2.92	3.87	0.25	0.22	0.21	0.53
2	-6.39	-2.86	3.53	0.18	0.17	0.18	0.41
3	-6.16	-2.91	3.25	0.12	0.05	0.06	0.47
3a	-5.66	-2.90	2.76	0.11	0.07	0.08	0.72
3b	-5.09	-2.92	2.17	0.11	0.06	0.07	0.76
3b_Me	-5.11	-2.91	2.20	0.07	0.06	0.06	0.30
3c	-4.81	-2.93	1.88	0.08	0.02	0.04	1.02
4	-5.48	-2.89	2.59	0.03	0.03	0.03	0.95
4_Me	-5.49	-2.79	2.70	0	0	0	0.03
5	-5.67	-2.84	2.83	0.06	0.04	0.04	0.21
6	-5.21	-2.71	2.50	0.16	0.14	0.15	0.41
7	-5.74	-3.01	2.73	0.18	0.16	0.16	0.38
8	-5.03	-3.14	1.89	0.04	0.04	0.04	0.21
9	-5.20	-3.13	2.07	0	0	0	0.01

The geometry optimized structure and 3D-frontier molecular orbital energy schemes of the compounds are given in Figures 3.4–3.8. The schemes for HOMO and LUMO give information about the reactivity of the compounds. HOMO provides basicity, while LUMO shows the Lewis acidity property of the corresponding system. Thus,

investigation into frontier molecular orbitals is very important. It is also important to know which atoms contribute to these orbitals because the reactivity centers are determined by these schemes. For the compounds to be potential candidates for TADF, it is critical to possess separate HOMO and LUMO to give small exchange energies. Steric hindrance which results in twisting between donor and acceptor units can successfully achieve this purpose [42–44]. The HOMOs of **D-A** structures are predominantly distributed on the donor moieties (Figures 3.4–3.8), whereas the LUMOs are localized over the acceptor core, and are composed of highly electron-withdrawing cyano units together with the pyrazine. This offers clear spatial separation of the HOMO and LUMO because of the large dihedral angles (ca. 25–90°) between the donor units and the cyano-containing phenanthrene pyrazine core. The HOMO and LUMO orbitals are distributed clearly on the donor and acceptor parts of the system, respectively.

The phenanthrene pyrazine compound (**1**) is rigid planar structure with full conjugated fused rings and the cyano groups. Thus, HOMO and LUMO are both distributed over the structure. In order to be able to achieve successful separation of the frontier molecular orbitals benzene (**2**) and thiophene (**3**) substitution were done on each side of the phenanthrene moiety of the parent compound (Figure 3.4).

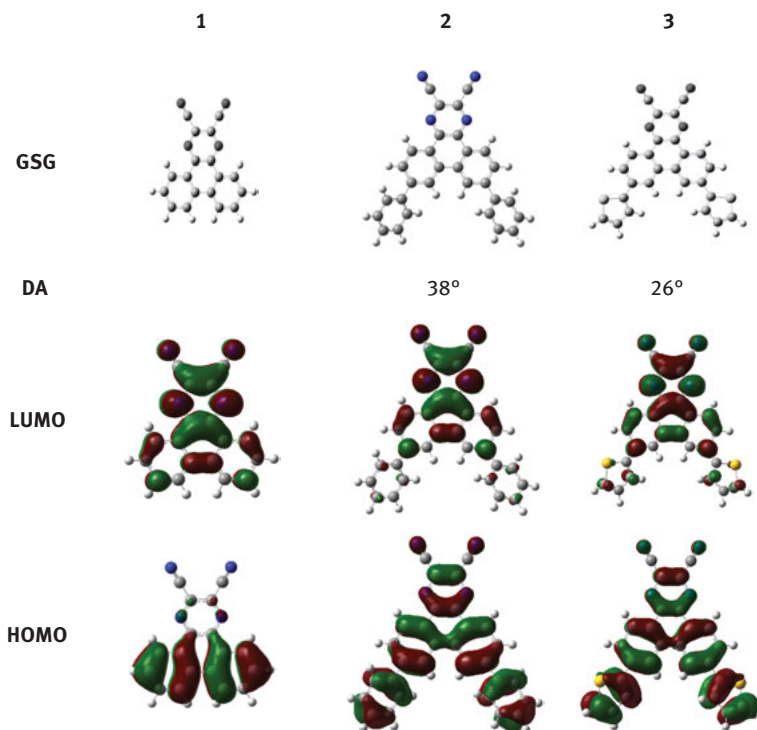


Figure 3.4: Ground State Geometry (GSG), Dihedral Angle (DA), HOMO and LUMO of 1–3.

Although geometry optimized structures of **2** and **3** resulted in a tilted structures from planarity with dihedrals 38° and 24° , respectively, still well separated HOMO and LUMO could not be observed. HOMO and LUMO energy levels have not changed enough for the duo, to possess better semiconducting ability, either.

The potential OLED applications of oligomeric thiophene systems have been investigated in the literature recently [45]. Therefore, we aimed to separate HOMO-LUMO distribution together with possible narrowing of the interfrontier molecular orbital energy gap due to extension of the conjugation by lengthening the thiophene linkage. 2 (**3a**), 5 (**3b**) and 10 (**3c**) thiophenes linked to the system in order to achieve better donor ability. Although, geometry optimized structures did not yield even more tilted structures, HOMO and LUMO could be separated. On the other hand, HOMO-LUMO energy gap was narrowed due to increase in the energy of the HOMO upon introduction of extended π system (Figure 3.5).

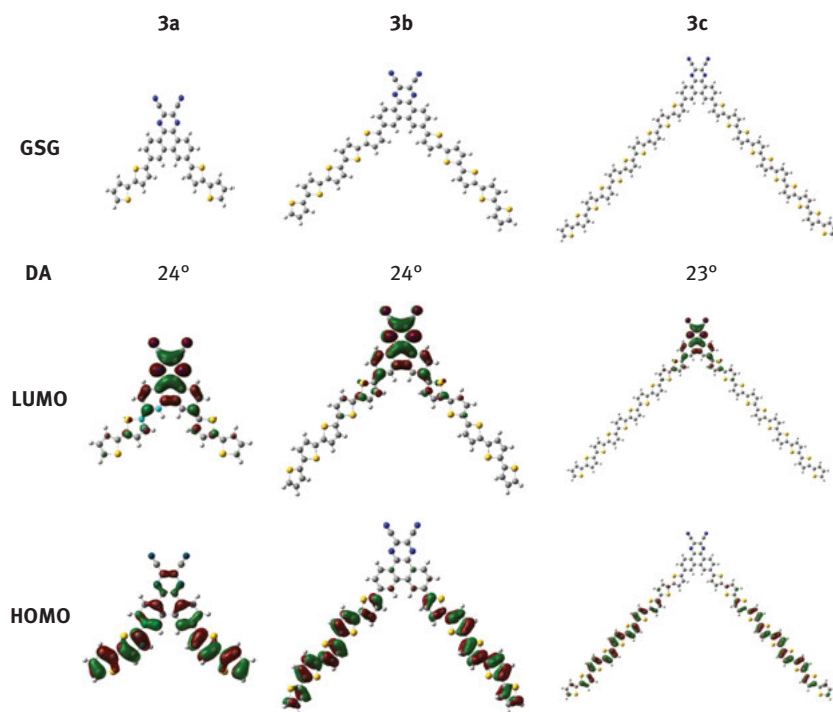


Figure 3.5: Ground State Geometry (GSG), Dihedral Angle (DA), HOMO and LUMO of **3a-3c**.

Anthracene [46], pyrene [47], triphenylamine [48], carbazole [49], phioxazine [50] and acridine [51] based OLED and TADF systems have been widely investigated in the literature. Therefore, combination of the present dicyano dibenzo[f,h]quinoxaline with each of the above may possibly produce potential candidates for OLED and

TADF compounds. The geometry optimized structures and the frontier orbitals of the compounds 4–9 are given in Figure 3.6 and Figure 3.7. The donor-acceptor dihedral angles for compounds 4–9 are promising (Anthracene 71°, pyrene 38°, triphenylamine 34°, carbazole 50°, pheoxazine 71° and acridine 90°) to achieve very well separation of the HOMO-LUMO distribution throughout the system. For compounds 4–9, HOMOs are located totally on the donor part and LUMOs are located on the acceptor part, leading to create good semiconductor materials with potential use in OLED devices.

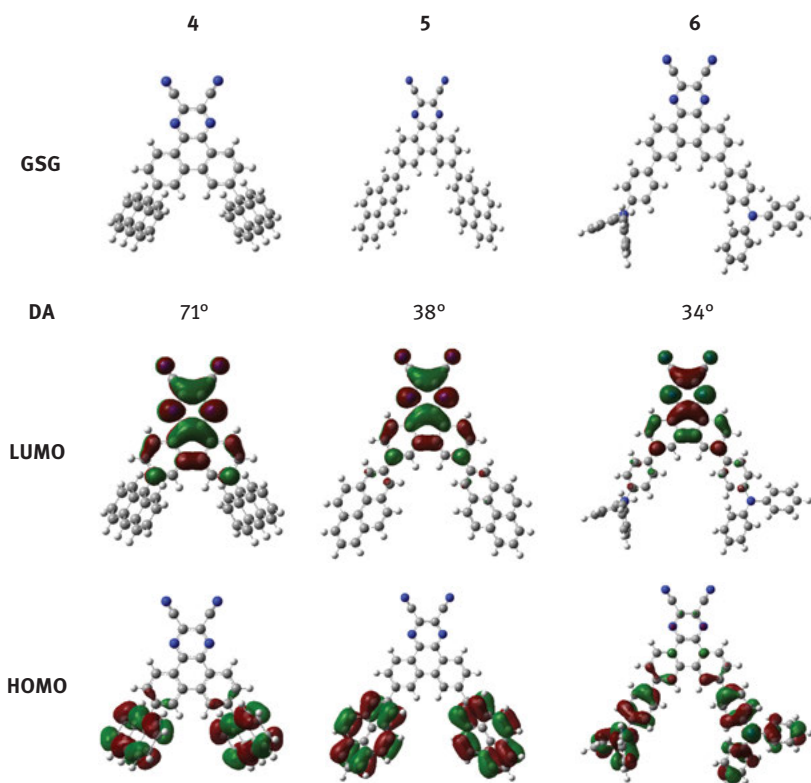


Figure 3.6: Ground State Geometry (GSG), Dihedral Angle (DA), HOMO and LUMO of 4–6.

3.3.2 TADF properties

One of the most important design considerations of TADF molecules is obtaining a small energy gap between the S_1 and T_1 states (ΔE_{ST}). A molecule meets this requirement only when its lowest-energy transition has low singlet–triplet exchange energy [52]. Current trends in the research into novel TADF emitters are mainly focused on

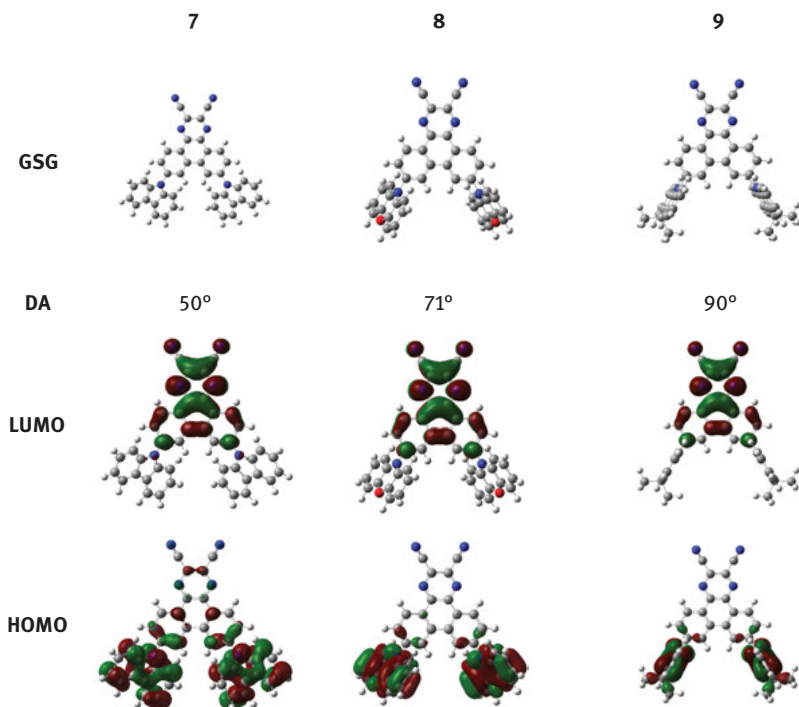


Figure 3.7: Ground State Geometry (GSG), Dihedral Angle (DA), HOMO and LUMO of 7–9.

intramolecular donor-acceptor (D-A)-type molecules, as in the present case [53]. Therefore, appropriate donor-acceptor units have to be selected carefully to obtain full-color TADF molecules, with their HOMO and LUMO being localized on different constituents. To obtain details about the geometric and electronic structures of **1–9** time-dependent density functional theory (TD-DFT) calculations were performed at the B3LYP/6-31G(d,p), B3LYP/6-311 + G(d,p), B3LYP/cc-PVTZ and CAM-B3LYP/6-311 + G(d,p) level. The HOMO, LUMO energies and the energy gap between singlet- and triplet-excited states for compounds **1–9** are given in Table 3.1.

The clear separation of the frontier molecular orbitals results in narrower ΔE_{ST} values. ΔE_{ST} data for **1** itself was computed to be 0.53 eV with CAM-B3LYP/6-311 + G(d,p) level. The ΔE_{ST} values for **2** and **3** slightly smaller from the parent but still needed to be improved. Thiophene oligomers did not work well due to uncut conjugation path (Table 3.1). Since ΔE_{ST} values ≤ 0.50 are considered to be productive for TADF potential, compounds **5–9** have been found to be best candidates for TADF emitters. Compound **9**, has been computed to possess very well separated HOMO-LUMO distribution and completely twisted geometry together with even degenerate T_1 and S_1 levels. Therefore it can be considered the most potential candidate for TADF emitter. Thus, the ΔE_{ST} values predicted by the TD-DFT calculations are small enough

for thermal repopulation of the S_1 state via $T_1 \rightarrow S_1$ RISC for almost all of the compounds, but especially for **5–9**. Among all, nine might suggest the highest potential as TADF emitters as they possess the narrowest S_1 - T_1 energy difference and best separated HOMO and LUMO schemes. All computed lowest-energy excited states may be described by the HOMO-LUMO transition, which corresponds to an intramolecular charge transfer (ICT) with small exchange energy.

Although anthracene derivative (**4**) have separate HOMO-LUMO distribution and 71° dihedral angle, it is calculated to possess 0.95 eV ΔE_{ST} data which is quite high to be considered to be a contestant. Therefore, we have decided to force a more tilted structure from planarity by introducing two methyl groups on each side of the molecule to form **4_Me**. The same procedure has been carried out for **3b**, too (Figure 3.8) to obtain **3b_Me**. The dihedral angles were improved to 85° and 40° for anthracene (**4_Me**) and five oligothiophene (**3b_Me**), respectively. 15° better tilt from the initial structure led to an improvement of -0.92 eV

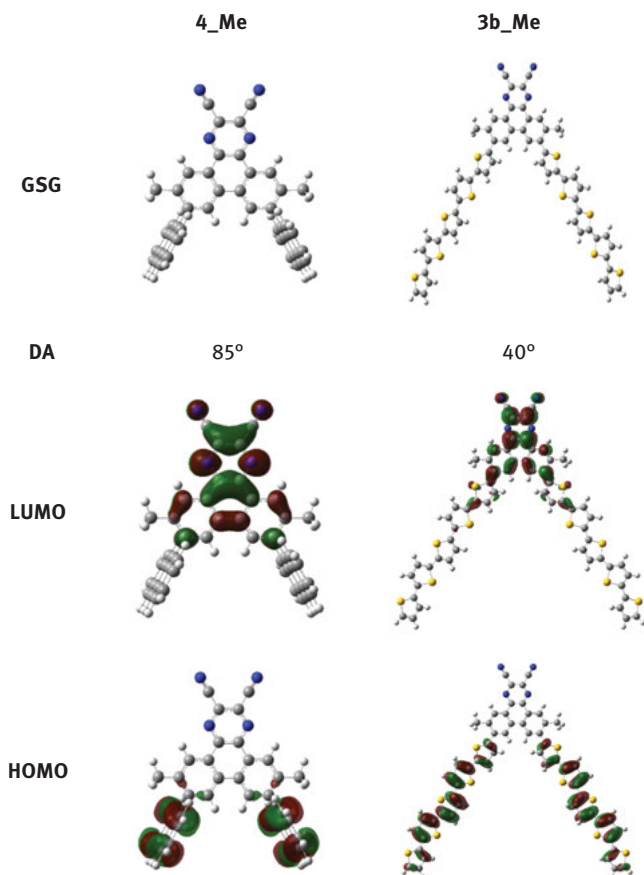


Figure 3.8: Ground State Geometry (GSG), Dihedral Angle (DA), HOMO and LUMO of **7–9**.

for **4_Me** to result a ΔE_{ST} value of 0.03 eV. For **3b_Me**, ΔE_{ST} data has been narrowed down to 0.30 eV.

3.4 Conclusion

A well known acceptor, namely, dicyano dibenzo[f,h]quinoxaline has been combined with mostly preferred donors to design potential TADF emitters. Their structural and electronic properties were computed with the application of density functional theory at different levels of theory.

Among the designed compounds **9**, **4_Me** and **3b_Me** were elected as the best candidates for TADF emitters due to their well separated HOMO-LUMO orbitals and ΔE_{ST} data. On the other hand, **3c** and **8** may be used as semiconductors since they possess interfrontier molecular orbital energy gap lower than 2 eV.

References

- [1] Kalyani NT, Swart H, Dhoble SJ. Principles and applications of organic light emitting diodes (OLEDs). Duxford, United Kingdom: Woodhead Printing, 2017.
- [2] Fourassier C. Luminescence encyclopedia of inorganic chemistry. New York: Academic Press, 1984.
- [3] Mc Keever SW. Thermoluminescence in solids. Cambridge: Cambridge University Press, 1985.
- [4] Sparks JS, Schelly RC, Smith WL, Davis MP, Tchernov D, Pierivone VA, et al. The covert world of fish biofluorescence: a phylogenetically widespread and phenotypically variable phenomenon. *PLoS One*. 2014;9:83259.
- [5] Schlyer BD, Schauerte JA, Steel DG, Gafni A. Time-resolved room temperature protein phosphorescence: nonexponential decay from single emitting tryptophans. *Biophys J*. 1994;67:1192–202.
- [6] deSa GF, Malta OL, deMello DC, Simas AM, Longo RL, Santa-Cruz PA, et al. Spectroscopic properties and design of highly luminescent lanthanide coordination complexes. *Coord Chem Rev*. 2000;196:165–95.
- [7] Binggeli C. Interior graphic standards. Student ed. New Jersey: Wiley, 2012.
- [8] Tsai YS, Hong LA, Juang FS, Chen CY. Blue and white phosphorescent organic light emitting diode performance improvement by confining electrons and holes inside double emitting layers. *J Lumin*. 2014;153:312–16.
- [9] Liu YF, Feng J, Zhang YF, Cui HF, Yin D, Bi YG, et al. Improved efficiency of indium-tin-oxide-free flexible organic light-emitting devices. *Org Electron*. 2014;15:478–83.
- [10] Zhang QY, Pita K, Buddhudu S, Kam CH. *J Phys D*. 2002;35:3085–90.
- [11] Xiaoxiao W, Fushan L, Wei W, Tailiang G. Flexible white phosphorescent organic light emitting diodes based on multilayered graphene/PEDOT: PSS transparent conducting film. *Appl Surf Sci*. 2014;295:214–18.
- [12] Patel BN, Prajapati MM. OLED: a modern display technology. *Interof Sci Res Pub*. 2014;4: 1–5.
- [13] Kohn W, Sham LJ. Self-consistent equations including exchange and correlation effects. *Phys Rev*. 1965;140:1133–38.
- [14] Frisch MJ, Trucks GW, Schlegel HB, Scuseria GE, Robb MA, Cheeseman JR, et al. Gaussian 09, Revision D.01. Wallingford CT: Gaussian, Inc., 2013.

- [15] Becke AD. Density-functional exchange-energy approximation with correct asymptotic behavior. *Phys Rev A*. 1988;38:3098–100.
- [16] Lee C, Yang W, Parr RG. Development of the Colle–Salvetti correlation energy formula into a functional of the electron density. *Phys Rev B*. 1988;37:785–89.
- [17] Zhao Y, Truhlar DG. The M06 suite of density functionals for main group thermochemistry, thermochemical kinetics, noncovalent interactions, excited states, and transition elements: two new functionals and systematic testing of four M06-class functionals and 12 other functionals. *Theor Chem Acc*. 2008;120:215–41.
- [18] Zhao Y, Truhlar DG. Density functional for spectroscopy: no long-range self-interaction error, good performance for rydberg and charge-transfer states, and better performance on average than B3LYP for ground states. *J Phys Chem A*. 2006;110:13126–30.
- [19] Zhao Y, Truhlar DG. A new local density functional for main-group thermochemistry, transition metal bonding, thermochemical kinetics, and noncovalent interactions. *J Chem Phys*. 2006;125:194101–18.
- [20] Karton A, Tarnopolsky A, Lamre JF, Schatz GC, Martin JML. Highly accurate first-principles benchmark data sets for the parametrization and validation of density functional and other approximate methods. derivation of a robust, generally applicable, double-hybrid functional for thermochemistry and thermochemical kinetics. *J Phys Chem*. 2008;112:12868–86.
- [21] Casida ME, Jamorski C, Casida KC, Salahub DR. Molecular excitation energies to high-lying bound states from time-dependent density-functional response theory: characterization and correction of the time-dependent local density approximation ionization threshold. *J Chem Phys*. 1998;108:4439–49.
- [22] Yanez SM, Moya SA, Zuniga C, Jiron GC. Theoretical assessment of TD-DFT applied to a ferrocene-based complex. *Comput Theor Chem*. 2017;1118:65–74.
- [23] Baldo MA, O'Brien DA, Thompson ME, Forrest SR. Excitonic singlet-triplet ratio in a semiconducting organic thin film. *Phys Rev B*. 1999;60:14422–28.
- [24] Segal M, Baldo MA, Holmes RJ, Forrest SR, Soos ZG. Excitonic singlet-triplet ratios in molecular and polymeric organic materials. *Phys Rev B*. 2003;68:75211–26.
- [25] Baldo MA, O'Brien DF, You Y, Shoustikov A, Sibley S, Thompson ME, et al. Highly efficient phosphorescent emission from organic electroluminescent devices. *Nature*. 1998;395:151–54.
- [26] Wilson JS, Dhoot AS, Seeley AJ, Khan MS, Köhler A, Friend RH. Spin-dependent exciton formation in π -conjugated compounds. Spin-dependent exciton formation in π -conjugated compounds. *Nature*. 2001;413:828–31.
- [27] Sun Y, Giebink NC, Kanno H, Ma B, Thompson ME, Forrest SR. Excitonic singlet-triplet ratio in a semiconducting organic thin film. *Phys Rev B*. 1999;60:14422–28.
- [28] Adachi C, Baldo MA, Thompson ME, Forrest SR. Nearly 100 % internal phosphorescence efficiency in an organic light-emitting device. *J Appl Phys*. 2001;90:5048–51.
- [29] O'Brien DF, Baldo MA, Thompson ME, Forrest SR. Improved energy transfer in electrophosphorescent devices. *Appl Phys Lett*. 1999;74:442–44.
- [30] Baldo MA, Lamansky S, Burrows PE, Thompson ME, Forrest SR. Very high-efficiency green organic light-emitting devices based on electrophosphorescence. *Appl Phys Lett*. 1999;75:4–6.
- [31] Meerholz K, Müller DC. Outsmarting waveguide losses in thin-film light-emitting diodes. *Adv Funct Mater*. 2001;11:251–53.
- [32] Endo A, Ogasawara M, Takahashi A, Yokoyama D, Kato Y, Adachi C. Thermally activated delayed fluorescence from Sn^{4+} -porphyrin complexes and their application to organic light emitting diodes — A novel mechanism for electroluminescence. *Adv Mater*. 2009;21:4802–06.
- [33] Endo A, Sato K, Yoshimura K, Kai T, Kawada A, Miyazaki H, et al. Efficient up-conversion of triplet excitons into a singlet state and its application for organic light emitting diodes. *Appl Phys Lett*. 2011;98:83302.

- [34] Czerwieńiec R, Yu J, Yersin H. Blue-Light Emission of Cu(I) Complexes and Singlet Harvesting. *Inorg Chem*. 2011;50:8293–301.
- [35] Leitl M, Küchle FR, Mayer HA, Wesemann L, Yersin H. Brightly blue and green emitting Cu(I) Dimers for singlet harvesting in OLEDs. *J Phys Chem A*. 2013;117:11823–36.
- [36] Uoyama H, Goushi K, Shizu K, Nomura H, Adachi C. Highly efficient organic light-emitting diodes from delayed fluorescence. *Nature*. 2012;492:234–38.
- [37] Khodae Z, Yahyazadeh A, Mahmoodi NO, Zanjanchi MA, Azimi V. One-pot synthesis and characterization of new cuprous pyrazinoporphyrazines containing peripherally functionalized units. *J Mol Struct*. 2012;1029:92–97.
- [38] Lee BH, Jaung JY, Jang SC, Yi SC. Synthesis and optical properties of push–pull type tetrapyr-azinoporphyrazines. *Dyes Pigments*. 2005;65:159–67.
- [39] Nishida JI, Murai S, Fujiwara E, Tada H, Tomura M, Yamashita Y. Preparation, Characterization, and FET Properties of Novel Dicyanopyrazinoquinoxaline Derivatives. *Org Lett*. 2004;6:2007–10.
- [40] Ivanov MA, Puzyk MV, Balashev KP. Spectroscopic and electrochemical properties of dichloro-diimine complexes of Au(III) and Pt(II) with 1,4-Diazine derivatives of o-phenanthroline. *Russ J Gen Chem*. 2006;76:843–48.
- [41] Atkins P, Overton T, Rourke J, Weller M, Armstrong F. Shriver & Atkins inorganic chemistry. 4th ed. Oxford: Oxford University Press, 2006.
- [42] Nakagawa T, Ku SY, Wong KT, Adachi C. Electroluminescence based on thermally activated delayed fluorescence generated by a spirobifluorene donor–acceptor structure. *Chem Commun*. 2012;48:9580–82.
- [43] Mehes G, Nomura H, Zhang Q, Nakagawa T, Adachi C. Enhanced electroluminescence efficiency in a spiro-acridine derivative through thermally activated delayed fluorescence. *Angew Chem Int Ed*. 2012;51:11311–15.
- [44] Nasu K, Nakagawa T, Nomura H, Lin CJ, Cheng CH, Tseng MR, et al. A highly luminescent spiro-anthracenone-based organic light-emitting diode exhibiting thermally activated delayed fluorescence. *Chem Commun*. 2013;49:10385–87.
- [45] Sengoku T, Yamao T, Hotta S. Organic light-emitting diodes based on layered films of thiophene/phenylene co-oligomers. *J Non-Crystalline Solids*. 2012;358:2525–29.
- [46] Aydemir M, Haykır G, Battal A, Jankus V, Sugunan SK, Dias FB, et al. High efficiency OLEDs based on anthracene derivatives: the impact of electron donating and withdrawing group on the performance of OLED. *Organic Electronics*. 2016;30:149–57.
- [47] Shan T, Gao Z, Tang X, He X, Gao Y, Li J, et al. Highly efficient and stable pure blue nondoped organic light-emitting diodes at high luminance based on phenanthroimidazole-pyrene derivative enabled by triple-triplet annihilation. *Dyes and Pigments*. 2017;142:189–97.
- [48] Wang S, Yan X, Cheng Z, Zhang H, Liu Y, Wang Y. Highly efficient near-infrared delayed fluorescence organic light emitting diodes using a phenanthrene-based charge-transfer compound. *Angew Chem Int Ed*. 2015;54:13068–72.
- [49] Çiçek B, Çalışır Ü, Tavaslı M, Tülek R, Teke A. Synthesis and optical characterization of novel carbazole Schiff bases. *J Mol Struct*. 2018;1153:42–47.
- [50] Li P, Cui Y, Song C, Zhang H. A systematic study of phenoxazine-based organic sensitizers for solar cells. *Dyes and Pigments*. 2017;137:12–23.
- [51] Seo JA, Gong MS, Song W, Lee JY. Molecular orbital controlling donor moiety for high-efficiency thermally activated delayed fluorescent emitters. *Chem Asian J*. 2016;11:868–73.
- [52] Turro NJ. *Modern molecular photochemistry*. Sausalito, CA: University Science Books, 1991.
- [53] Li J, Zhang Q, Nomura H, Miyazaki H, Adachi C. Thermally activated delayed fluorescence from $\pi\pi^*$ to $\pi\pi^*$ up-Conversion and its application to organic light-emitting diodes. *Appl Phys Lett*. 2014;105:13301–04.

Winfred Mueni Mulwa and Francis Birhanu Dejene

4 $\gamma\text{-Al}_2\text{O}_3\text{:Ce}^{3+}\text{Cu}^{2+}$ as a phosphor material; DFT+U and experimental approach

$\gamma\text{-Al}_2\text{O}_3\text{:Ce}^{3+}\text{Cu}^{2+}$ industrial applications in optical components

Abstract: The $\gamma\text{-Al}_2\text{O}_3$ and $\text{Ce}^{3+}\text{Cu}^{2+}$ -doped $\gamma\text{-Al}_2\text{O}_3$ powders have been synthesized by sol-gel method. Phases of the synthesized powders were characterized with X-ray diffraction. Morphological analysis and elemental composition of the samples were determined by scanning electron microscopy, high-resolution transmission electron microscopy and energy dispersive X-ray spectroscopy. Luminescence characterizations have been used to study the synthesized samples. *Ab initio* calculations by the use of local density approximation with the Hubbard U correlation were used to compute the structural, electronic and optical properties of $\gamma\text{-Al}_2\text{O}_3$ and $\text{Al}_2\text{O}_3\text{:Ce}^{3+}\text{Cu}^{2+}$. The results indicate that the particle size and morphology of the samples depend on the concentration of the dopants. In comparison with undoped $\gamma\text{-Al}_2\text{O}_3$ sample, the intensities of emission peaks at 430 and 458 nm of $\text{Ce}^{3+}\text{Cu}^{2+}$ -doped $\gamma\text{-Al}_2\text{O}_3$ powders have been enhanced. This shows that, increasing Ce^{3+} and Cu^{2+} concentration causes an increase in the number of emitting ions which is expected in order to increase the number of applications of $\gamma\text{-Al}_2\text{O}_3\text{:Ce}^{3+}\text{Cu}^{2+}$ composite powders. The photoluminescence spectrum detected at $\lambda_{\text{exc}} = 253$ nm shows a new peak located at 549 nm due to Cu^{2+} ions. This was confirmed computationally when the Ce_{4f} and Ce_{5d} states are found in the conduction band while the Cu_{4p} state was found at conduction band minimum and Cu_{3d} state at valence band maximum. This location of states showed there is no possible luminescence from the Ce^{3+} ions. The only possible luminescence was due to transition from Cu_{4p} to Cu_{3d} states.

Keywords: doped alumina, luminescence, DFT+U

4.1 Introduction

Alumina comprises of several metastable phases (boehmite $\rightarrow \gamma \rightarrow \delta \rightarrow \theta\text{-Al}_2\text{O}_3$) in addition to the stable rhombohedral α -alumina [1]. Among these metastable phases, $\gamma\text{-Al}_2\text{O}_3$ has been widely used in industrial applications such as adsorbents, catalysts, optical components, phosphors and soft abrasives [2, 3]. By investigating the emission spectra of pure $\gamma\text{-Al}_2\text{O}_3$ powders, Yu et al. [4] reported a blue luminescence band

This article has previously been published in the journal *Physical Sciences Reviews*. Please cite as: Mulwa, W. M., Dejene, F. B. $\gamma\text{-Al}_2\text{O}_3\text{:Ce}^{3+}\text{Cu}^{2+}$ as a phosphor material; DFT+U and experimental approach. *Physical Sciences Reviews* [Online] **2018**, 3. DOI: 10.1515/psr-2017-0165

<https://doi.org/10.1515/9783110568196-004>

at 422 nm related to defect level in the γ -Al₂O₃ powder. The luminescent properties have an advantage for flat-panel display techniques, which requires a purer blue emission. The pure and doped alumina powders or single crystals have recently attracted a great deal of research interest due to their optical properties and low cost. Considerable research efforts have been made on (1) the powder synthesis techniques and (2) appropriate dopants [4]. The main objective of these efforts is to obtain high-quality powders, emitting in the three basic colours [4]. Recently, many efforts have been directed towards the fabrication of good-quality powders to enhance their performance in currently existing applications as phosphors. The sol-gel technique is a very promising way of producing high-quality nanopowders. The structure and composition of these high-quality nanopowders especially γ -Al₂O₃ transition alumina have been the subject of a number of controversial works [5–7]. This led to the current study which investigates the composition of γ -Al₂O₃ as well as its structural, electronic and luminescent properties.

Considerable efforts of many other researchers have been directed towards the improvement of the optical properties of alumina by introduction of various dopants such as Si and Ti [8], Mg and Y [9], Cr and Ni [10]. For instance, Menon [11] observed that the interaction between Ce and Cu is the main cause of the high reactivity of the bimetallic catalyst in the total oxidation of toluene. This was realized after the total oxidation of toluene as volatile organic compound was studied over the binary metal oxide CuO-CeO₂/ γ -Al₂O₃. Given that catalytic oxidation is an important technique for the destruction of volatile organic compounds, it was necessary to investigate the structural, electronic and luminescence properties of γ -Al₂O₃:Ce³⁺Cu²⁺ powders.

In this work, sol-gel technique is used to synthesize γ -Al₂O₃ and γ -Al₂O₃:Ce³⁺Cu²⁺. In the synthesis of γ -Al₂O₃ and γ -Al₂O₃:Ce³⁺Cu²⁺ nanopowders, citric acid was used as a complexant agent which can effectively chelate metal ions with varying ionic sizes [12]. Citric acid as a convenient ligand is inexpensive and is a more effective complexing agent than other complexants producing fine ferrite powder with smaller particle size [13].

4.2 Methodology

The *ab initio* and characterization techniques used to investigate the properties of the Al₂O₃:Ce³⁺Cu²⁺ in this study are presented.

4.2.1 Experimental details

The structure of the powders was analysed using the Xcrysden program and the X-ray diffraction (XRD). The crystal size was analysed by use of XRD and the high resolution transmission electron microscopy (HRTEM). Morphology was analysed using the scanning electron microscope (SEM) and HRTEM. The absorption properties of the

oxides were investigated using UV-VIS-NIR spectrophotometer. The photoluminescence (PL) properties were determined using F- 7000 Fluorescence and the Franck-Condon equation while energy dispersive X-ray spectroscopy (EDS) gave the composition of the powders.

4.2.1.1 Materials and synthesis

$\text{Al}_2\text{O}_3:\text{Ce}^{3+}\text{Cu}^{2+}$ powders were prepared using commercially available cerium nitrate $\text{Ce}(\text{NO}_3)_3 \cdot 6\text{H}_2\text{O}$, copper nitrate $\text{Cu}(\text{NO}_3)_2 \cdot 4\text{H}_2\text{O}$, aluminium nitrate $\text{Al}(\text{NO}_3)_3 \cdot 9\text{H}_2\text{O}$ and citric acid $\text{C}_6\text{H}_8\text{O}_7 \cdot \text{H}_2\text{O}$ using the sol-gel technique [14]. The initial solution was prepared by dissolving aluminium nitrate and citric acid into deionized water. The concentration of aluminium nitrate was 0.5 M. The molar ratio of citric acid to aluminium nitrate was 0.5. The solution was placed on a hot plate (50°C) and constantly stirred for 3 h using a magnetic stirrer until it changed to yellowish solution. The temperature was then increased to 80°C and stirring continued for 2 h, after which the solution changed to a transparent sticky gel. The gel was transferred to an oven maintained at 300°C. All the liquid evaporated and high amount of gases were produced during the 1 h when the gel was in the oven. After the 1 h, the gel swells into a fluffy citrate precursor. This precursor was grounded into fine powders with the help of a mortar and a pistle. The fine powder was calcined at 950°C for 3 h in a muffle furnace to improve their crystallinity and optical properties. The synthesis of Al_2O_3 nanostructures with Ce^{3+} and Cu^{2+} cations as dopants was performed by adding different amounts of $\text{Ce}(\text{NO}_3)_3 \cdot 6\text{H}_2\text{O}$ and $\text{Cu}(\text{NO}_3)_2 \cdot 4\text{H}_2\text{O}$ to the $\text{Al}(\text{NO}_3)_3 \cdot 9\text{H}_2\text{O}$ precursor to obtain concentrations of 0.31, 0.62, 0.93 and 1.24 mol% $\text{Ce}^{3+}\text{Cu}^{2+}$.

4.2.1.2 Characterization techniques

The crystal structures of the powders were investigated using the Bruker AXS Discover diffractometer with $\text{Cu K}\alpha(1.5418 \text{ \AA})$ radiation. High-resolution transmission electron microscopy (HR-TEM) was done using the Shimadzu Superscan SSX-550 system. Scanning electron microscopy (SEM) and selected area electron diffraction (SAED) micrographs were used to determine the morphology of synthesized nanoparticles. The optical properties were obtained via the use of the Agilent HP1100 diode-array UV-visible spectrophotometer while photoluminescence (PL) spectroscopy was done using the Hitachi F-7000 fluorescence spectrometer.

4.2.2 Computational details

Ab initio calculations were carried out using Density functional theory and the Hubbard U term (DFT+ U) as implemented in the Quantum ESPRESSO code [15]. Within DFT+ U , the electron–electron interaction was expressed as the sum of the Hartree and exchange-correlation (XC) terms which is usually approximated. The

XC approximation within the DFT formalism was carried out using the local density approximation (LDA) as parameterized by Perdew–Wang [16]. The nuclei core’s effect on the system was analysed using norm-conserving pseudopotentials [17]. Using the following converged calculation parameters, kinetic energy cut-off of 60 Ry, Gaussian smearing of 0.02 eV, $8 \times 8 \times 8$ Monkhorst–Pack [18] *k*-point mesh and electronic energy convergence criterion of 10^{-6} Ry, a lattice constant of 7.79 Å and a band gap of 3.5 eV were obtained compared to experimental value of 7.91 Å [19] for the lattice constant. Another theoretical study obtained the lattice constant to be 7.89 Å [20]. The underestimation of the lattice constant with LDA is a known trend [21]. Band gap underestimation within LDA is also known and has been documented in several studies [22, 23]. However, it is also worth noting that, despite hybrid functionals being successful in overcoming the band gap under estimation issue [24], they are also known to fail in some cases such as in the prediction of the defect properties [25–27]. Using the optimized unit cell, a supercell of 80 atoms was obtained by multiplying the unit cell using a $2 \times 2 \times 2$ *k*-point mesh. The undoped γ -Al₂O₃ supercell was then optimized by relaxing only the atomic positions keeping the volume fixed using a $2 \times 2 \times 2$ Monkhorst–Pack [18] *k*-point mesh. The kinetic energy cut-off and electronic energy convergence were similar to that of the unit cell. The supercell was then doped by substituting two Al atoms with a Ce³⁺ and a Cu²⁺ atom (0.31–1.24% doping percentage). Although anion substitution is also possible, cation substitution results in lower substitution energies compared to the anion substitution in the case of rare earth-doped semiconductors [28, 29]. Al atoms occupy both the tetrahedral and octahedral sites within the lattice thus Ce³⁺Cu²⁺ doping was done on each of these sites. Since Ce³⁺ and Cu²⁺ are strongly correlated elements, we added the Hubbard correction term *U* to the Ce³⁺ 4*f* electrons and to the Cu²⁺ 3*d* electrons within the DFT+*U* formalism so as to properly account for their properties which could not have been accounted for in the case of using DFT alone. DFT+*U* is robust in accounting for the properties of transition metals as well as rare earth and lanthanide elements [30, 31]. The choice of *U* is however highly dependent on the material property being converged with respect to experimental findings. Common material properties that have been used to obtain the value of *U* include charge localization, Lattice parameter and band gap energy [32–34]. In this study, we have adopted the reported methodology of [35] where the calculated band gap energy was converged with respect to experimental band gap. A value of *U* = 4 eV for Ce³⁺ was chosen while that of Cu²⁺ was chosen to be 3 eV which substituted Al³⁺ in Al site.

4.3 Results and discussion

In this study, *ab initio* density function theory and the Hubbard *U* term (DFT+*U*) has been used to investigate structural, electronic and optical properties of semiconductor

metal oxides ($\text{Al}_2\text{O}_3:\text{Ce}^{3+}\text{Cu}^{2+}$). The Hubbard U value is known to overcome the failure of standard DFT in predicting the electronic properties in metal oxides. Experimental approach is also used in the current study to produce stoichiometric semiconducting metal oxides. The results of the study are as shown below.

4.3.1 X-ray diffraction (XRD) and XCrystal analysis

Comparison between the structural changes from experimental and computational approach of $\gamma\text{-Al}_2\text{O}_3$ and $\gamma\text{-Al}_2\text{O}_3:\text{Ce}^{3+}\text{Cu}^{2+}$ at different concentrations is shown in Figure 4.1. The diffraction patterns of Figure 4.1 confirm that all the samples consisted of spinel structure with space group $\text{Fd-}3\text{m}$ as indexed by JCPDS file no. 79-1557. The intensity of the peaks relative to the background signal demonstrates high crystallinity of the samples. Although the XRD patterns of $\gamma\text{-Al}_2\text{O}_3$ resemble those of $\gamma\text{-Al}_2\text{O}_3:\text{Ce}^{3+}\text{Cu}^{2+}$, the peaks have broadened on doping and their intensities also reduced. The diffraction peak broadening is as a result of the crystallite sizes and lattice strain. This means that large crystallite sizes cause sharp reflections where as small sizes lead to broad reflections. Variation in lattice spacing due to lattice strains can also cause broadening [36]. The crystalline sizes of the $\gamma\text{-Al}_2\text{O}_3$ and $\gamma\text{-Al}_2\text{O}_3:\text{Ce}^{3+}\text{Cu}^{2+}$

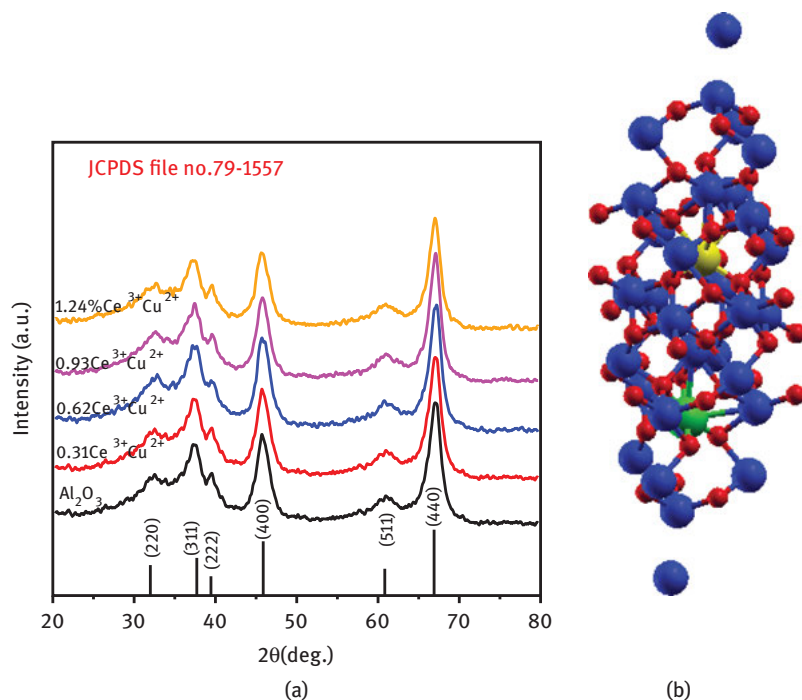


Figure 4.1: Structural analysis of $\gamma\text{-Al}_2\text{O}_3$ and $\gamma\text{-Al}_2\text{O}_3:\text{Ce}^{3+}\text{Cu}^{2+}$. The red, blue, green and yellow balls represent O, Al, Cu and Ce, respectively.

samples are in the same range confirming what was realized in Table 4.1 that doping did not cause major distortion of the crystal structure. In addition, this could be due to the fact that the procedure used to prepare all the samples in this study was the same. The peak broadening is attributed to lattice strain due to incorporation of the Ce³⁺ and Cu²⁺ activator ions. In all the doped samples, Ce³⁺ and Cu²⁺ are seated at the Al³⁺ site. The XRD results in Figure 4.1(a) are in good agreement with the computationally calculated bond lengths in Figure 4.1(b) and summarized in Table 4.1 which shows reduced bond lengths on doping. To the best of our knowledge, no DFT+*U* work has been done on Al₂O₃:Ce³⁺Cu²⁺ therefore no comparison with other DFT+*U* work was included in Table 4.1.

Table 4.1: DFT+*U* averaged Mulliken bond lengths of γ -Al₂O₃:Ce³⁺Cu²⁺ 0 < x ≤ 1.24 %.

	0%: Ce ³⁺ Cu ²⁺	1.24%: Ce ³⁺ Cu ²⁺
Al-O (Å)	1.85	1.79
O-O (Å)	2.64	2.62

These XRD results agree well with the Mulliken bond lengths as shown in Table 4.1. Table 4.1 confirms that if a bigger ionic radius is substituted into a smaller ionic radius site, the site enlarges while the bond lengths shrink. Figure 4.1(a) shows the peaks representing doped systems shift to lower angles (to the left) in comparison to the host peak. This shift was also witnessed by Qianping Sun et al. [37] where on doping ordered mesoporous gamma-alumina; the peaks shifted to the lower angles [38]. The peak (440) decrease in intensity is attributed to the distortion of the crystal structure of the host on incorporation of the dopant [39].

The width of the XRD peaks allows us to calculate the average crystallite size by using the Debye–Scherrer equation [24]. The analysis shows that the average crystallite size of γ -Al₂O₃:Ce³⁺Cu²⁺ at different doping concentration was approximated to be 5, 6, 8 and 9 nm for 0.31%, 0.62%, 0.93% and 1.24% doping, respectively. The crystallite size is estimated from the full width at half maximum (FWHM; β) and Debye–Scherrer formula according to the following equation:

$$d = \frac{0.89\lambda}{\beta \cos \theta} \quad (4.1)$$

where 0.89 is the shape factor, λ is the X-ray wavelength, β is the line broadening at half the maximum intensity (FWHM) in radians and θ is the Bragg angle. The formation of γ -Al₂O₃ is expected, because it is reported to be the most thermodynamically stable phase when the crystalline size (particle diameter) is less than approximately 13 nm.

4.3.2 SEM analysis

Figure 4.2 shows the SEM images of the sol-gel prepared $\gamma\text{-Al}_2\text{O}_3$. Figure 4.2(a) shows pristine $\gamma\text{-Al}_2\text{O}_3$ at 40,000 \times magnification, while Figure 4.2(b) shows pristine $\gamma\text{-Al}_2\text{O}_3$ at 70,000 \times magnification. Figure 4.2(c) shows $\gamma\text{-Al}_2\text{O}_3\text{:Ce}^{3+}\text{Cu}^{2+}$ at 40,000 \times magnification and Figure 4.2(d) shows $\gamma\text{-Al}_2\text{O}_3\text{:Ce}^{3+}\text{Cu}^{2+}$ at 70,000 \times magnification. Comparing Figure 4.2(a) and Figure 4.2(c), Figure 4.2(c) shows enlarged particles compared to Figure 4.2(a) although they are of the same magnification. This confirms an increase in number of particles after doping. It also confirms a higher agglomeration in the doped system than in the pristine system. The same happened to Figure 4.2(b) compared to Figure 4.2(d). Figure 4.2 reveals that both pristine and $\gamma\text{-Al}_2\text{O}_3\text{:Ce}^{3+}\text{Cu}^{2+}$ samples are nearly spherical in shape with a narrow diameter distribution. The SEM images of pure and doped $\gamma\text{-Al}_2\text{O}_3$ are in the nanometre range. The size distribution and particle appearance are irregular. The changes in size before and after doping could be as a result of nucleation mechanism in the growth process. A restrained nucleation rate and

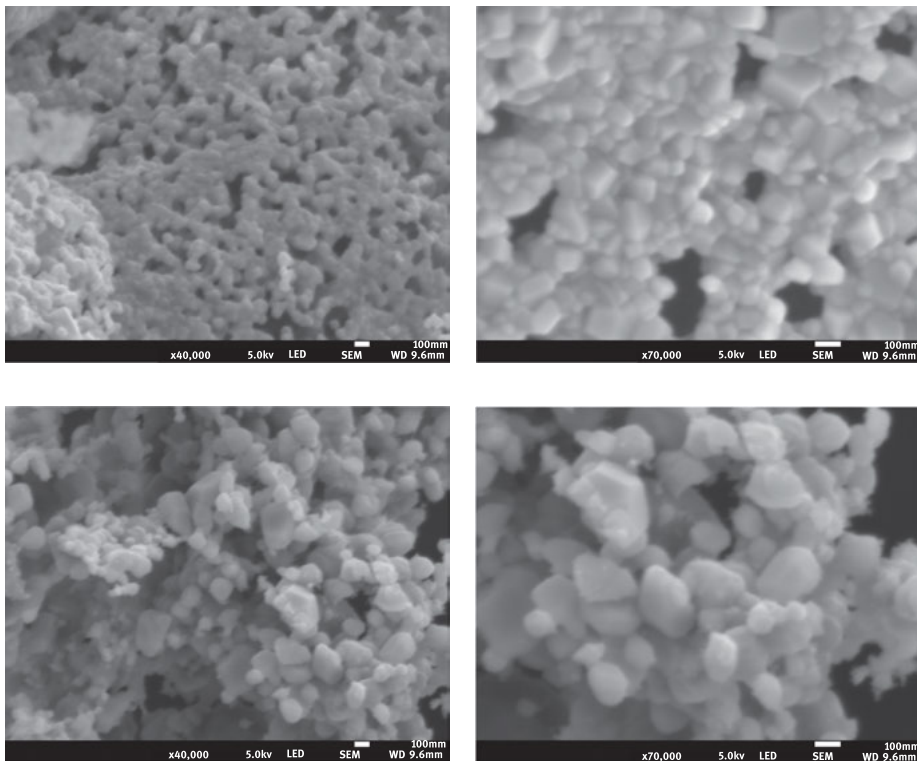


Figure 4.2: Comparison between $\gamma\text{-Al}_2\text{O}_3$ and $\gamma\text{-Al}_2\text{O}_3\text{:Ce}^{3+}\text{Cu}^{2+}$ SEM analysis at different magnifications.

a subsequent lower growth rate of samples may occur due to the difference in ionic radii of Cu^{2+} and Ce^{3+} from that of Al^{3+} . The difference in valence between Ce^{3+} , Cu^{2+} and Al^{3+} could also be another cause of change in size.

4.3.3 HR-TEM analysis

Figure 4.3 represents systems of 1.24% $\text{Ce}^{3+}\text{Cu}^{2+}$ doping in $\gamma\text{-Al}_2\text{O}_3$ with an average crystallite size of 10 ± 2 nm. This shows that the crystallite sizes from HR-TEM analysis are in agreement with those derived from XRD traces. The average grain size diameter of these doped systems is 20 nm which is confirmed by the SAED patterns. The SAED patterns show diffraction rings composed of discrete spots indicating decrease in grain size on doping. The diameter of the diffraction rings in SAED patterns was obtained by the use of imageJ program and it is consistent with $\sqrt{h^2 + k^2 + l^2}$ given that (hkl) represents the miller indices of planes corresponding to the ring. Using this relationship, the rings obtained from SAED corresponds to (440) , (400) , (311) planes. In XRD, these same planes show the highest intensity peaks, showing a good relation between XRD and SAED.

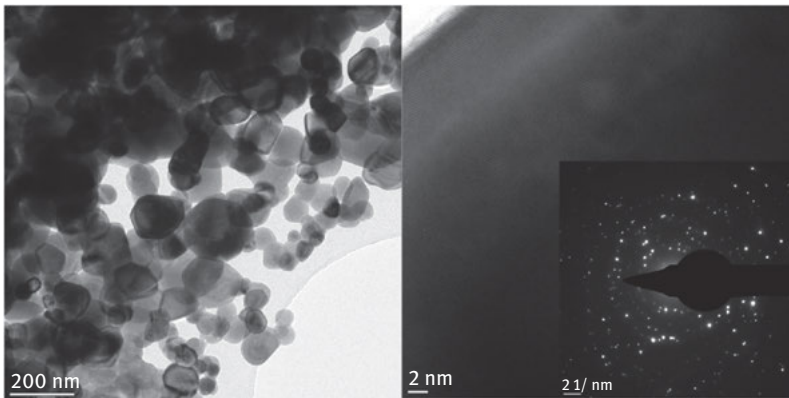


Figure 4.3: HR-TEM images of $\text{Al}_2\text{O}_3\text{:1.24 \% Ce}^{3+}\text{Cu}^{2+}$.

4.3.4 Energy dispersive X-ray spectroscopy (EDS) analysis

EDS allowed the determination of the chemical composition of the samples [40, 41]. These data were used to calculate the O/Al atomic ratios. Figure 4.4(a) shows peaks of Al^{3+} and O in pure $\gamma\text{-Al}_2\text{O}_3$. EDS spectrum from Figure 4.4(b) reports the presence Al^{3+} , O, Ce^{3+} and Cu^{2+} prove that the chemical composition of the powders was respected. $\gamma\text{-Al}_2\text{O}_3\text{:Ce}^{3+}\text{Cu}^{2+}$ co-doped system did not deviate from the initial stoichiometry and matched well with the initial degree of substitution. It is interesting to note

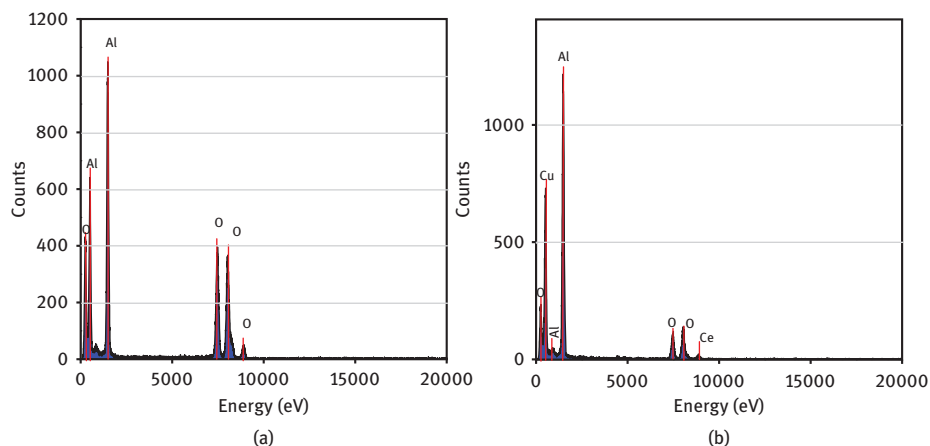


Figure 4.4: EDS spectrum of (a) $\gamma\text{-Al}_2\text{O}_3$ and (b) $\gamma\text{-Al}_2\text{O}_3:\text{Ce}^{3+}\text{Cu}^{2+}$.

that the synthesis and characterization conditions completely favoured the formation of $\gamma\text{-Al}_2\text{O}_3$ and $\gamma\text{-Al}_2\text{O}_3:\text{Ce}^{3+}\text{Cu}^{2+}$ systems and thus allowed us to study the effect of increasing Cu^{2+} and Ce^{3+} concentration in the $\gamma\text{-Al}_2\text{O}_3$.

4.3.5 Electronic analysis

Computationally, Figure 4.5(a) and Figure 4.5(b) reveal a direct band gap transition at Γ . The calculated band gap for $\gamma\text{-Al}_2\text{O}_3$ is 3.5 eV (Figure 4.5(a)), whereas our experimental band gap is 4.9 eV (Figure 4.5(d)). This discrepancy arises because of the inability of DFT to describe excited states [42]. Our band gap which is between the upper valence band and conduction band is 3.5 eV, which compares very well with 4.0 eV band gap realized by Gutiérrez et al. [43]. Ahuja et al. reported a band gap of 3.9 eV [44]. In order to determine the optical energy band gap of our powders, the UV-vis absorption spectrum was recorded. The reflectance spectrum shows a reflectance at 253 nm in the UV region (Figure 4.5(c)) which corresponds to an absorption (excitation) at 4.9 eV (Figure 4.5(d)). The UV-vis absorption spectrum of the samples may be attributed to photoexcitation of electron from valence band to conduction band. The optical energy band gap (E_g) was estimated (Figure 4.5(d)) by the method proposed by Tauc [45] according to the following equation:

$$(h\nu\alpha) \propto (h\nu - E_g)^n \quad (4.2)$$

where α is the absorbance, h is the Planck's constant, ν is the frequency, E_g is the optical energy band gap and n is a constant associated to the different types of electronic transitions ($n = 1/2, 2, 3/2$ and 3 for direct allowed, indirect allowed, direct

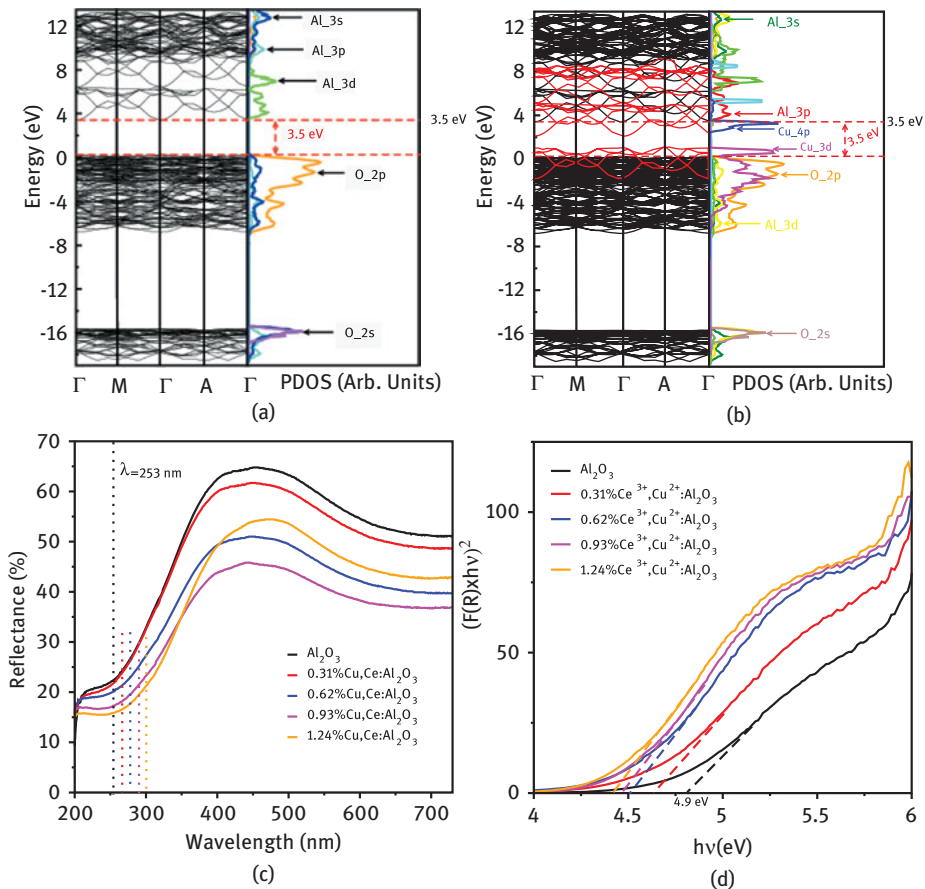


Figure 4.5: Relationship between reflectance spectrum, Kubelka–Munk plot and computational band structure.

forbidden and indirect forbidden transitions, respectively). E_g value for γ -Al₂O₃ nanoparticles is \sim 4.9 eV.

Computationally, Figure 4.5(b) shows a red shift on doping. The figure shows that there is no possible emission as a result of transition from Ce_5d (green colour) to Ce_4f (light blue) states. This is because these two states are found in the conduction band (Figure 4.5(b)). Cu_4p states are found at conduction band minimum, while Cu_3d states are found at valence band maximum (VBM). This gives a possible emission due to transition from Cu_4p to Cu_3d. The emission is through 2.5 eV (496 nm) which is in the bluish-green region of the visible spectrum. The reduction in band gap realized in Figure 4.5(b) computationally is confirmed experimentally in Figure 4.5(d) showing a good relation between calculated and experimental work. DFT is known to underestimate approximately 40% of the experimental band gap [46] that is why the

computational band gap for pristine $\gamma\text{-Al}_2\text{O}_3$ (Figure 4.5(a)) is 3.5 eV, while the experimental band gap is 4.9 eV (Figure 4.5(d)). This also shows DFT predicting the expected experimental band gap.

4.3.6 Optical analysis

The x -axis intercept obtained by extrapolating the linear portion of the curve is the transition energy for the doping concentration as shown in Figure 4.5(d). From our findings, it is clear that the electronic transition using DFT to calculate the optical absorption spectrum can be analysed in relation to Kubelka–Munk plots.

In order to know how possible it is to incorporate the dopants (Ce and Cu), *Ab initio* calculations were carried out to get the dopant substitutional energies at a given charge state q using the equation

$$E_{\text{dopant}}^q = E_{\text{undoped}} - E_{\text{doped}} + n\mu_{\text{Al}} - n\mu_{\text{Cu}} - n\mu_{\text{Ce}} + q(E_{\text{VBM}} + E_{\text{Fermi}}) + E_{\text{corr}} \quad (4.3)$$

where E_{undoped} is the total energy of pristine $\gamma\text{-Al}_2\text{O}_3$, E_{doped} is the total energy of doped $\gamma\text{-Al}_2\text{O}_3$, μ_{Al} , μ_{Ce} and μ_{Cu} are the chemical potentials of Al, Ce and Cu, respectively, n is the number of atoms substituted, E_{VBM} and E_{Fermi} are the energy of the VBM and fermi energy, respectively, while E_{corr} represents the supercell finite size corrections. A thermodynamic charge transition level $\varepsilon^{q/q'}$ was calculated using the equation

$$\varepsilon^{-2/-1} = \frac{(E_{\text{dopant}}^{-1} - E_{\text{dopant}}^{-2})}{((-2) - (-1))} \quad (4.4)$$

where E_{dopant}^{-1} and E_{dopant}^{-2} are the dopant substitutional energies for -1 and -2 charge states obtained using eq. (4.3). Each of thermodynamic transition levels usually has an associated optical transition. An optical transition can be obtained using the Franck–Condon principle as

$$E_{\text{PL}} = E_g - \varepsilon^{\text{therm}}(-2/-1) - E_{\text{rel}} \quad (4.5)$$

where, E_{PL} is the optical transition, E_g is the band gap energy, $\varepsilon^{\text{therm}}(-2/-1)$ is thermodynamic transition level which is obtained using eq. (4.4). Figure 4.6(a) shows the thermodynamic transition levels both in the Al_rich conditions as well as O_rich conditions. It was realized that the transition level in both cases was the same therefore the PL was calculated using 1.1 eV as the thermodynamic transition level. The schematic diagram of the calculated PL is represented in Figure 4.6(b). This calculated PL shows an emission in the bluish-green region (521 nm) which is in agreement with the emission in Figure 4.6(c). In Figure 4.6(c), the emission at 549 nm is in the bluish-green region which is attributed to emission from the Cu_{4p} states to

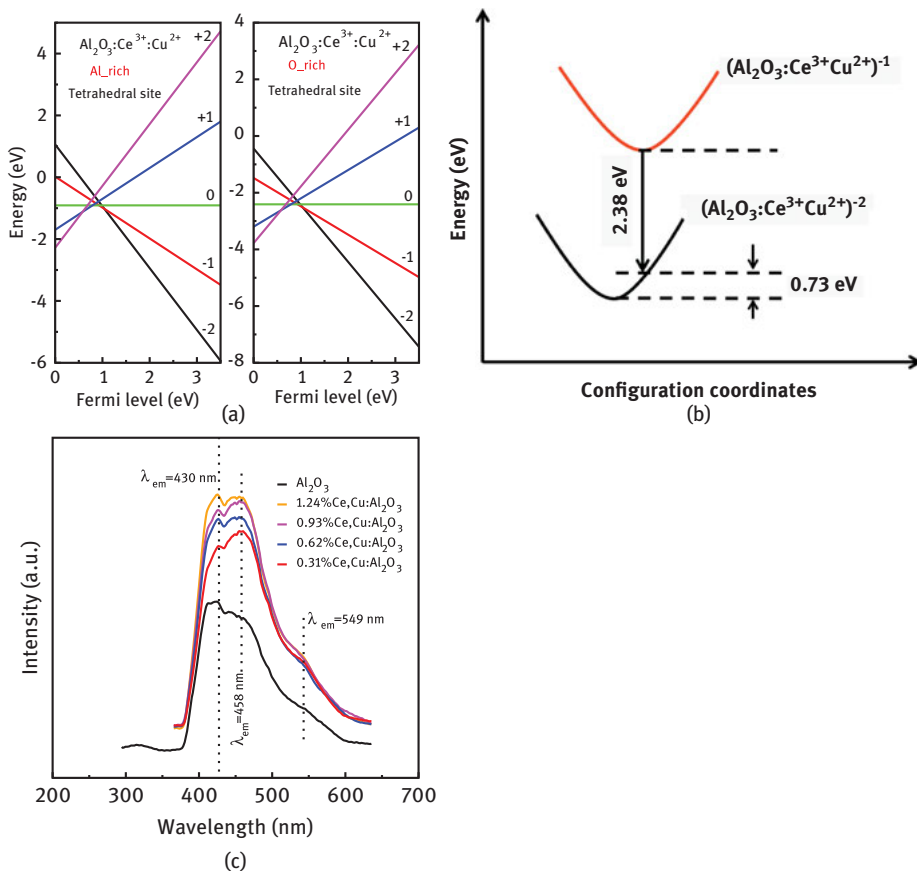


Figure 4.6: (a) DFT calculated thermodynamic transition levels, (b) calculated photoluminescence and (c) experimental photoluminescence.

Cu_{3d} states as confirmed computationally in Figure 4.5(b). The emission at 43 and 458 nm is both in pristine and doped $\gamma\text{-Al}_2\text{O}_3$ which can be attributed to the oxygen vacancies most probably created during annealing (synthesis). In PL analysis, the knowledge on charge density distribution around each atom is important. It is therefore discussed below.

4.3.7 Charge density

Figure 4.7 presents the electronic charge density plots for the defective spinel structure of $\gamma\text{-Al}_2\text{O}_3$ which is calculated using the LDA+ U exchange potential. The stoichiometric $\gamma\text{-Al}_2\text{O}_3$ structure is a perfect insulator, and formation of charge-free carriers is not anticipated from our calculation. From Figure 4.7, clearly, the electronic cloud is mostly distributed around the oxygen nuclei. A highly polar

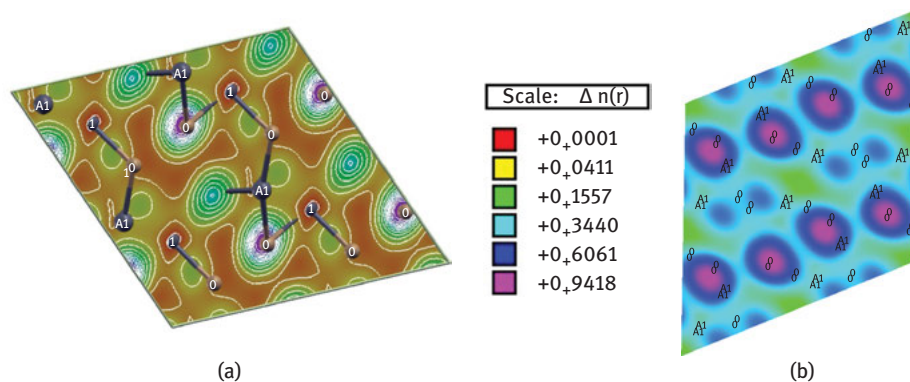


Figure 4.7: (a) $\gamma\text{-Al}_2\text{O}_3:\text{Ce}^{3+}\text{Cu}^{2+}$ charge density contour diagram (b) the cross-section plane perpendicular to plane a) and containing all the Al, Ce, Cu and O atoms.

bond is formed in the Al–O line as expected from a large electronegativity difference between Al and O atoms. However, there is no charge accumulation along the Al–O bonds, indicating essentially ionic bonding. Figure 4.7(a) shows the contours indicating the boundaries of charge distribution. In addition, it is observed in Figure 4.7(b) that distribution of the charge density is not uniform around different Al lattice sites. Al atoms are far from each other and thereby cannot be strongly bonded to each other. These observations are in agreement with the quantitative ionic charge analysis [47]. The thermometer shows that the magenta colour has the highest charge with the red colour with the least amount of charge. The dense and nearly spherical contours away from the Al nuclei are from the peaking in Al 3s3p orbitals.

4.3.8 Conclusion

Undoped $\gamma\text{-Al}_2\text{O}_3$ and $\gamma\text{-Al}_2\text{O}_3:\text{Ce}^{3+}\text{Cu}^{2+}$ powders with different morphologies were successfully synthesized using the sol-gel technique with the presence of citric acid as the complexant. Structural characterizations as well as theoretical calculations show a defective cubic spinel structure. From the XRD data and SAED diffraction patterns analysis, $\gamma\text{-Al}_2\text{O}_3$ and $\gamma\text{-Al}_2\text{O}_3:\text{Ce}^{3+}\text{Cu}^{2+}$ are highly crystalline. The SEM micrographs showed that the particles are spherical in shape, while the HR-TEM micrographs showed a grain size of approximately 10 nm. Properties computed using the DFT+*U* technique were found to be consistent with experimental observations, an indication that theoretical computations with the DFT formalism can be a useful tool that can aid and/or guide experimental investigations.

Funding: This work is based on the research supported in part by the National Research Foundation of South Africa. The Grant holder acknowledges that opinions,

findings and conclusions or recommendations expressed in any publication generated by the NRF-supported research are that of the author(s) and that the NRF accepts no liability whatsoever in this regard.

References

- [1] Tahmasebpour M, Babaluo A, Shafiei S, Pipelzadeh E. Studies on the synthesis of α -Al₂O₃ nanopowders by the polyacrylamide gel method. *Pow Technol.* 2009;191:91–7.
- [2] Khan SZ, Liu Z, Li L. Characteristics of γ -Al₂O₃ nanoparticles generated by a continuous-wave laser ablation in liquid. *Appl Phys.* 2010;101:781–7.
- [3] Toshima R, Miyamaru H, Asahara J, Murasawa T, Takahashi A. Ion-induced luminescence of alumina with time-resolved spectroscopy. *J Nucl Technol.* 2002;39:15–8.
- [4] Yu ZQ, Chang D, Li C. Blue photoluminescent properties of pure nanostructured γ -Al₂O₃. *J Mater Res.* 2001;16:1890–3.
- [5] Paglia G, Rohl AL, Buckley CE, Gale JD. Determination of the structure of γ -alumina from interatomic potential and first-principles calculations: The requirement of significant numbers of non-spinel positions to achieve an accurate structural model. *Phys Rev B.* 2005;71:224115.
- [6] Zhou RS, Snyder RL. Structures and transformation mechanisms of the η , γ and θ transition aluminas. *Acta Crystallogr.* 1991;B47:617.
- [7] Sohlberg K, Pennycook SJ, Pantelides ST. Explanation of the observed dearth of three-coordinated Al on γ -alumina surfaces. *J Am Chem Soc.* 1999;121:7493.
- [8] Mehta SK, Sengupta S. Gamma dosimetry with Al₂O₃ thermo-luminescent phosphor. *Phys Med Biol.* 1976;21:955–64.
- [9] Osvay M, Biro T. Aluminium oxide in TL dosimetry. *Nucl Instrum Methods.* 1980;175:60–1.
- [10] Lapraz D, Iacconi P, Daviller D, Guilhot B. Thermostimulated luminescence and fluorescence of α -Al₂O₃: Cr³⁺ samples (Ruby). Influence of the Cr³⁺ concentration. *Phys StatSolidi (A).* 1991;126:521–31.
- [11] Menon U. Toluene total oxidation over CuO-CeO₂/Al₂O₃: structural and kinetic characterization. Ghent, Belgium: Department of Chemical Engineering and Technical Chemistry, Ghent University, 2013.
- [12] Wu KH, Ting TH, Li MC. Sol-gel auto-combustion synthesis of SiO₂-doped NiZn ferrite by using various fuels. *J Magn Magn Mater.* 2006;298:25–32.
- [13] Patil JY, Khandekar MS, Mulla IS. Combustion synthesis of magnesium ferrite as liquid petroleum gas (LPG) sensor: effect of sintering temperature. *Curr Appl Phys.* 2012;12:319–24.
- [14] Wang SF, Zhuang CF, Yuan YG, Xiang X, Sun GZ, Ding QP, et al. Synthesis and photoluminescence of γ -Al₂O₃ and C-doped γ -Al₂O₃ Powders. *Trans Ind Ceram Soc.* 2014;73:37–42.
- [15] Giannozzi P, Baroni S, Bonini N, Calandra M, Car R, Cavazzoni C, et al. QUANTUM ESPRESSO: a modular and open-source software project for quantum simulations of materials. *J Phys Condens Matter.* 2015;21:395502.
- [16] Perdew JP, Wang Y. Accurate and simple analytic representation of the electron-gas correlation energy. *Phys Rev B.* 1992;45:13244.
- [17] Hamann DR, Schluter M, Chiang C. Norm-conserving pseudopotentials. *Phys Rev Lett.* 1979;43:1494–7.
- [18] Monkhorst HJ, Pack JD. Special points for Brillouin-zone integrations. *Phys Rev B.* 1976;13:5188–92.
- [19] Zhou RS, Snyder RL. Structures and transformation mechanisms of the η , γ and θ transition aluminas. *Struct Sci.* 1991;47:617–30.

- [20] Gutiérrez G, Taga A, Johansson B. Theoretical structure determination of γ -Al₂O₃. *Phys Rev B*. 2001;65:12101.
- [21] Ouma CN, Mapela MZ, Makau NW, Amolo GO, Maezono R. Quantum Monte Carlo study of pressure-induced phase transition in GaAs. *Phys Rev B*. 2012;86:104115.
- [22] Paier J, Marsman M, Hummer K, Kresse G, Gerber IC, Angyán JG. Screened hybrid density functionals applied to solids. *J Chem Phys*. 2006;124:154709.
- [23] Heyd J, Peralta JE, Scuseria GE, Martin RL. Energy band gaps and lattice parameters evaluated with the Heyd-Scuseria-Ernzerhof screened hybrid functional. *J Chem Phys*. 2005;123:174101.
- [24] Wagner CN. Direct methods for the determination of atomic-scale structure of amorphous solids (X-ray, electron, and neutron scattering). *J Non-Cryst Solids*. 1978;31:1–40.
- [25] Maeta T, Sueoka K. Density functional theory calculations of stability and diffusion mechanisms of impurity atoms in Ge crystals. *J Appl Phys*. 2014;116:73505.
- [26] Chroneos A, Uberuaga BP, Grimes RW. Carbon, dopant, and vacancy interactions in germanium. *J Appl Phys*. 2007;102:83707.
- [27] Chroneos A, Bracht H, Grimes RW, Uberuaga BP. Vacancy-mediated dopant diffusion activation enthalpies for germanium. *Appl Phys Lett*. 2008;92:172103.
- [28] Sanna S, Hourahine B, Frauenheim T, Gerstmann U. Theoretical study of rare earth point defects in GaN. *Phys Status Solidi*. 2008;5:2358–60.
- [29] Sanna S, Schmidt W, Frauenheim T, Gerstmann U. Rare-earth defect pairs in GaN: LDA+U calculations. *Phys Rev B*. 2009;80:104120.
- [30] Himmetoglu B, Floris A, De Gironcoli S, Cococcioni M. Hubbard-corrected DFT energy functionals: The LDA+U description of correlated systems. *J Quantum Chem*. 2014;114:14–49.
- [31] Cococcioni M, De Gironcoli S. Linear response approach to the calculation of the effective interaction parameters in the LDA+U method. *Phys Rev B*. 2005;71:35105.
- [32] Nolan M, Grigoleit S, Sayle DC, Parker SC, Watson GW. Density functional theory studies of the structure and electronic structure of pure and defective low index surfaces of ceria. *Surf Sci*. 2005;576:217–29.
- [33] Castleton CW, Kullgren J, Hermansson K. Tuning LDA+U for electron localization and structure at oxygen vacancies in ceria. *J Chem Phys*. 2007;127:244704.
- [34] Bennett LJ, Jones G. The influence of the Hubbard U parameter in simulating the catalytic behaviour of cerium oxide. *Phys Chem Chem Phys*. 2014;16:21032–8.
- [35] Mulwa WM, Ouma CN, Onani MO, Dejene FB. Energetic, electronic and optical properties of lanthanide doped TiO₂: An *ab initio* LDA+U study. *J Solid State Chem*. 2016;237:129–37.
- [36] Bindu P, Sabu T. Estimation of lattice strain in ZnO nanoparticles: X-ray peak profile analysis. *J Theor Appl Phys*. 2014;8:123–34.
- [37] Sun Q, Zheng Y, Li Z, Zheng Y, Xiao Y, Cai G, et al. Synthesis, characterization and insights into stable and well organized hexagonal mesoporous zinc-doped alumina as promising metathesis catalysts carrier. *Phys Chem Chem Phys*. 2013;15:5670–6.
- [38] Qianping S, Ying Z, Zhaohui L, Yong Z, Yihong X, Guohui C, Kemei W. Studies on the improved thermal stability for doped ordered mesoporous γ -alumina. *Phys. Chem. Chem. Phys*. 2013;15:5670–6.
- [39] Bhagavannarayana B, Parthiban S, Meenakshisundaram S. An interesting correlation between crystalline perfection and second harmonic generation efficiency on KCl- and oxalic acid-doped ADP crystals. *Cryst Growth Des*. 2008;8:446–51.
- [40] Piispanen MH, Arvilommi SA, van der Broeck B, Nuutinen LH, Tiainen MS, Perämäki PJ, et al. A comparative study of fly ash characterization by LA-ICP-MS and SEM-EDS. *Energy Fuels*. 2009;23:3451–6.

- [41] Carta D, Corrias A, Falqui A, Brescia R, Fantechi E, Pineider F, et al. EDS, HRTEM/STEM, and X-ray absorption spectroscopy studies of co-substituted maghemite nanoparticles. *J Phys Chem C*. 2013;117:9496–506.
- [42] Hybertsen MS, Louie SG. First-principles theory of quasiparticles: calculation of band gaps in semiconductors and insulators. *Phys Rev Lett*. 1985;55:1418.
- [43] Gutiérrez G, Taga A, Johansson B. Theoretical structure determination of γ -Al₂O₃. *Phys Rev B*. 2001;65:012101.
- [44] Ahuja R, Osorio-Guillen JM, Souza de Almeida J, Holm B, Yching W, Johansson B. Electronic and optical properties of γ -Al₂O₃ from ab initio theory. *J Phys Condens Matter*. 2004;16:2891–900.
- [45] Hauser E, Zirke RJ, Tauc J, Hauser JJ, Nagel SR. Optical properties of amorphous metallic alloys. *Phys Rev Lett*. 1973;30:1978.
- [46] Perdew JP. Density functional theory and the band gap problem. *Int J Quantum Chem*. 1985;18:497–523.
- [47] Menéndez-Proupin E, Gutiérrez G. Electronic properties of bulk γ -Al₂O₃. *Phys Rev B*. 2005;72:035116.

Namrata Dhar and Debnarayan Jana

5 A DFT perspective analysis of optical properties of defected germanene mono-layer

Abstract: Germanene, germanium version of graphene, is a novel member in the two-dimensional (2D) materials family. In this present study, a theoretical analysis involving optical properties of defected free standing (FS) germanene layer has been performed within density functional theory (DFT) framework. FS buckled germanene exhibits many fascinating and unconventional optical properties due to introductions of adatoms and voids. Arsenic (As), gallium (Ga) and beryllium (Be) are chosen as doping elements. Doping sites (same or different sub-lattice positions) play a crucial role to improve various optical properties. While Be doping, concentrations of Be are increased up to 18.75% and void concentrations are increased up to 15.62% (keeping fixed 3.12% Be concentration). Emergence of several plasma frequencies occur in case of both parallel and perpendicular polarizations for defected germanene layers. Energy positions of peaks corresponding to maximum of imaginary parts of dielectric constants are red shifted for some As and Ga incorporated systems compared to pristine germanene. Absorption spectra peaks are more prominent for Be doped systems rather than void added systems. In addition, conductivity in infrared (IR) region is very high for the Be doped configurations in case of parallel polarization. Along with these, changes in other optical properties like refractive index, reflectivity, electron energy loss spectroscopy etc. are also analyzed briefly in this present study. We hope, this theoretical investigation may be regarded as an important tool to design novel opto-electronic tuning devices involving germanene in near future.

Keywords: germanene, density functional theory, doping and vacancy, electronic properties, Optical properties

5.1 Introduction

Discovery of a new material germanene, hexagonal graphene counterpart of germanium (Ge) [1, 2], has enriched two-dimensional (2D) materials family in recent years and opened a vast unexplored door to the researchers after graphene and silicene [3–5]. This new member germanene exhibits different properties which are similar to graphene in many aspects in its free standing (FS) form. But, in contrast, germanene possesses a buckled configuration rather than a planar structure of

This article has previously been published in the journal *Physical Sciences Reviews*. Please cite as: Dhar, N., Jana, D. A DFT perspective analysis of optical properties of defected germanene mono-layer *Physical Sciences Reviews* [Online] **2018**, 3. DOI: 10.1515/psr-2017-0164

<https://doi.org/10.1515/9783110568196-005>

graphene [6]. Behera et al. have reported that, buckled germanene is more stable than planar configuration [7]. Mixed sp^2 - sp^3 hybridization and high value of spin-orbit coupling of germanene lead to this buckled structure of germanene [8, 9]. Hexagonal flat germanene has been synthesized by Davila et al. very recently using gold (111) surface at substrate [10]. At the same time, buckled germanene has been fabricated by another group Li et al. using platinum (111) substrate [11]. Madhushankar et al. have reported experimentally that, germanene based field effect transistors (FET) devices are very efficient with high current on/off ratio and electron carrier mobility [12]. Rather, intrinsic carrier mobility of germanene is also higher than graphene or silicene [13]. So, this new member demands major research concern for advancement of 2D nano-technology based on germanene and its heterostructure [14, 15]. Unconventional electronic and optical properties of these 2D materials makes them more fascinating in the field of material science [16, 17]. Like graphene, germanene also exhibits linear dispersion relation and valence band (VB) and conduction band (CB) touches each other at Dirac K point. But inclusion of spin orbit coupling opens a gap ~ 24.3 meV at Dirac K point [18]. In order to apply germanene in nano-devices, basic requirement is to open a finite amount of bandgap at Dirac K point. Pang et al. via a density functional theory (DFT) study have investigated about structural, electronic and magnetic properties of 3d transition metal (TM) adsorbed germanene layer [19]. They have elucidated that TM adsorbed germanene systems exhibit non-magnetic metal, non-magnetic semiconductor, ferromagnetic metal, ferromagnetic semiconductor and ferromagnetic half-metal like characteristics features. In another DFT based study, Dhar et al. have reported that, it is possible to transform semi-metallic property of germanene to semiconducting and metallic nature by introducing suitable foreign elements like arsenic (As), gallium (Ga) or their co-doping in bare germanene [20]. This investigation clearly indicates the fact that, doping sites (whether it is same or different sub-lattice sites) play a very crucial role in order to improve electronic and optical properties of germanene. Several previous calculations have also indicated the fact that, non-magnetic germanene can behave as a magnetic structure by introduction of suitable doping of foreign element like beryllium (Be) or creating void in pristine layer [21]. It can be elucidated from this analysis that, variation of doping as well as void concentrations in pristine germanene modify electronic, optical and magnetic properties of germanene significantly. Li et al. have concluded that, chromium adsorbed germanene is metallic in nature and exhibits a significant magnetic moment $\sim 4.40 \mu_B$ [22]. Dhar et al. through a very recent first principle based analysis have explored that carbon decorated FS germanene possesses magnetic moment $\sim 4.04 \mu_B$ [23]. Liang et al. have estimated about the effect of surface functionalization and strain engineering on the structural, electronic and magnetic properties of hydrogenated, fluorinated and chlorinated FS Ge-nanosheet [24]. Electronic properties of germanene superlattices have been explored by Li et al. via first principles theory [25]. They have revealed that, sizable bandgap

(maximum ~ 250 meV) can be opened in germanene superlattices by sub-lattice equivalence breaking. Rupp et al. [26] have investigated about stability and electronic properties of boron (B) and nitrogen (N) hydrogenated germanene called germanane. They have calculated that, N and B doping allow germanene to act like n and p types semiconductor respectively. Moreover, Pang et al. have also pointed that, in case of alkali metal adsorbed germanene, Dirac cone moves below Fermi level and system behaves like n type doped structure [27]. Ni et al. have indicated the effects of vertical electric field on electronic properties of FS germanene [28]. Their study has opened the possibility to fabricate FET devices out of pristine silicene and germanene mono-layers experimentally.

Along with electronic and magnetic properties study, several theoretical investigations have already been carried out on optical properties of pristine and defected Ge-nanosheet. Matthes et al. [29] have reported that, despite of having very small thickness, optical absorbance of these 2D materials is not vanishing. Rather they achieve finite large values at optical resonance frequencies. Ozelik et al. have estimated real and imaginary parts of dielectric constant of silicene and germanene [30] within DFT framework. They have confirmed that, there are three main peaks in imaginary part of dielectric constant of germanene.

Motivated from previous investigations and fascinating unconventional properties of germanene, we have performed a DFT perspective analysis about defected FS buckled germanene systems. Doping of foreign elements or introducing void in bare system both can be treated as defect formation. As and Ga are natural choice of doping in germanene framework because of close radius matching of Ge with As and Ga. As a result, lattice deformation is expected to be comparatively small for these types of substitutional doping elements. These adatoms are incorporated in same (equivalent) and different (non-equivalent) sub-lattice positions of germanene individually. Our study has revealed that doping sites play crucial role in modifications of several optical properties of germanene. In addition, Be has also been introduced in bare germanene. Be is a very light weighted and extremely stiff hard metal which has huge applications in electronics, aerospace, defense industries, X-ray and other radiation machineries etc. [31]. Moreover, atomic radius of Be also matches almost 90 % with that of Ge. Along with this, researchers have already chosen this material for substitutional doping purpose in graphene, silicene etc. [32–35]. Concentrations of Be have been increased up to 18.75 % to observe modifications of optical properties. It has been also estimated from our work that, voids affect essentially the optical properties of germanene. We have increased void concentrations up to 15.62% keeping fixed Be concentration 3.12%. There are several prominent changes in optical properties like dielectric functions, absorption spectra, electron energy loss spectroscopy (EELS), reflectivity, conductivity etc. in these defected germanene systems as discussed in following sections. Thus, we have explored that, it is possible to tailor optical properties of germanene by choosing various ways.

5.2 Computational methodology

All necessary estimations were calculated using DFT, with the spin polarized generalized gradient approximation of Perdew, Burke and Ernzerhof functional [36] using double- ξ plus polarization basis set as implemented in SIESTA software package [37–39]. A $4 \times 4 \times 1$ supercell of germanene containing 32 Ge atoms in X - Y plane has been used. The mesh cutoff is set to 300 Ry. The vacuum space in Z direction is about 20 Å to neglect spurious interactions between the neighboring slabs. Brillouin zone is sampled in k space with the equivalent of a $24 \times 24 \times 1$ Monkhorst-Pack (MP) [40] of k point grid. Convergence precision for total energy of the self-consistent field cycle is taken as 10^{-5} eV. The atoms were allowed to relax until the residual forces were smaller than 0.05 eV/Å for As and Ga doped systems and 0.1 eV/Å for Be doped and void added structures. Number of empty bands is set to 400, which is sufficiently large enough to estimate optical properties, and gives accurate results due to inclusion of high frequency effects in interband transitions. Excitonic effects, however, are not taken into account.

Complex dielectric function $\varepsilon(\omega)$ is interpreted as, $\varepsilon(\omega) = \varepsilon_1(\omega) + i\varepsilon_2(\omega)$, $\varepsilon_1(\omega)$ and $\varepsilon_2(\omega)$ are real and imaginary parts of $\varepsilon(\omega)$ respectively and ω is frequency of electromagnetic (EM) wave in energy unit. Applying first order time dependent perturbation theory in the dipole approximation $\varepsilon_2(\omega)$ is calculated as [41–43],

$$\varepsilon_2(q \rightarrow 0_{\vec{u}}, \hbar\omega) = \frac{2e^2\pi}{\Omega\varepsilon_0} \sum_{k, v, c} |\langle \psi_k^c | \vec{u} \cdot \vec{r} | \psi_k^v \rangle|^2 \delta(E_k^c - E_k^v - E) \quad (5.1)$$

Here, Ω is volume of unit cell, ε_0 is permittivity in vacuum. \vec{u} and \vec{r} represent polarization and position vectors of electric field of EM wave respectively. ω is the photon frequency, ψ_k^c , ψ_k^v are the wave function of the CB and the VB respectively $\varepsilon_1(\omega)$ depends on $\varepsilon_2(\omega)$ and they are connected via Kramers-Kronig relation. Both types of polarizations (parallel or perpendicular) of EM field are taken into account for optical calculations. For parallel polarization electric field is applied along X axis and for perpendicular polarization the same is applied along Z axis. The value of optical broadening used in the computations for all optical calculations is set at 0.2 eV. The complex refractive index ($N(\omega)$) of a material is related to $\varepsilon(\omega)$ by the expression

$$N(\omega) = \sqrt{\varepsilon(\omega)} \quad (5.2)$$

where, $N(\omega) = n(\omega) + ik(\omega)$. n and k are the real and imaginary part of refractive index. They are correlated to $\varepsilon_1(\omega)$ and $\varepsilon_2(\omega)$ as

$$n(\omega) = \left(\frac{\sqrt{\varepsilon_1^2 + \varepsilon_2^2} + \varepsilon_1}{2} \right)^{1/2} \quad k(\omega) = \left(\frac{\sqrt{\varepsilon_1^2 + \varepsilon_2^2} - \varepsilon_1}{2} \right)^{1/2} \quad (5.3)$$

Now, by knowing expression of (2) and (3) absorption coefficient ($\alpha(\omega)$) at normal incidence is defined as,

$$\alpha(\omega) = 2k\omega/(c\hbar) \quad (5.4)$$

where, c represents the speed of light in vacuum and ω is expressed in energy unit.

The absorption coefficient $\alpha(\omega)$, having unit of inverse length, essentially describes the spatial attenuation of the intensity of EM wave passing through the sample. The EELS, denoted by $L(\omega)$, estimates the collective excitation of any structure and defined as,

$$L(\omega) = \text{Im}\left(-\frac{1}{\varepsilon(\omega)}\right) = \frac{\varepsilon_2}{\varepsilon_1^2 + \varepsilon_2^2} \quad (5.5)$$

$R(\omega)$ is related to $n(\omega)$ and $k(\omega)$. To analyze the characteristic fine structure feature of the reflectivity spectrum, calculation of reflectivity modulation ($R_M(\omega)$) [44, 45] is a very convenient way. $R_M(\omega)$ of a material possesses both positive and negative values. $R(\omega)$ (in case of normal incidence) and $R_M(\omega)$ are interpreted as,

$$R(\omega) = \frac{(n-1)^2 + k^2}{(n+1)^2 + k^2}, \quad R_M(\omega) = \frac{1}{R(\omega)} \frac{dR}{d\omega} \quad (5.6)$$

Further, real and imaginary parts of optical conductivity ($\sigma_1(\omega)$ and $\sigma_2(\omega)$) are also calculated via the relations,

$$\sigma_1(\omega) = \frac{\omega\varepsilon_2(\omega)}{4\pi}, \quad \sigma_2(\omega) = \frac{\omega(1-\varepsilon_1(\omega))}{4\pi} \quad (5.7)$$

For comparison purposes, same methodology was used as in previous studies [20, 21].

5.3 Results and discussions

5.3.1 Geometric optimization

Structural optimization is one of the main important task to investigate optical properties of As, Ga, Be adatom added and vacancy induced germanene layers. Buckled FS germanene sheets containing 32 Ge atoms are taken for all calculations in these present investigations. Optimized bond length, buckling and bond angle for relaxed pristine sheet are 2.44 Å, 0.69 Å and 112° respectively which matches with previous studies [46–48]. In case of As and Ga doping concentrations 3.12% and 6.25% are considered. In order to investigate the effect of doping positions, adatoms are incorporated in same and different sub-lattice positions individually of a single hexagonal unit cell of germanene for 6.25% adatom concentration. Co-dopings of As and Ga are

also incorporated. All considered As and Ga doped structures (S1 – S8) are depicted in Figure 5.1. All configurations are optimized successfully with the constraints as mentioned in ‘Computational methodology’ section. It has been already reported by the formation energies calculations in previous studies that, Ga doped and AsGa co-doped systems are unstable while As doped systems are stable compared to bare germanene [20].

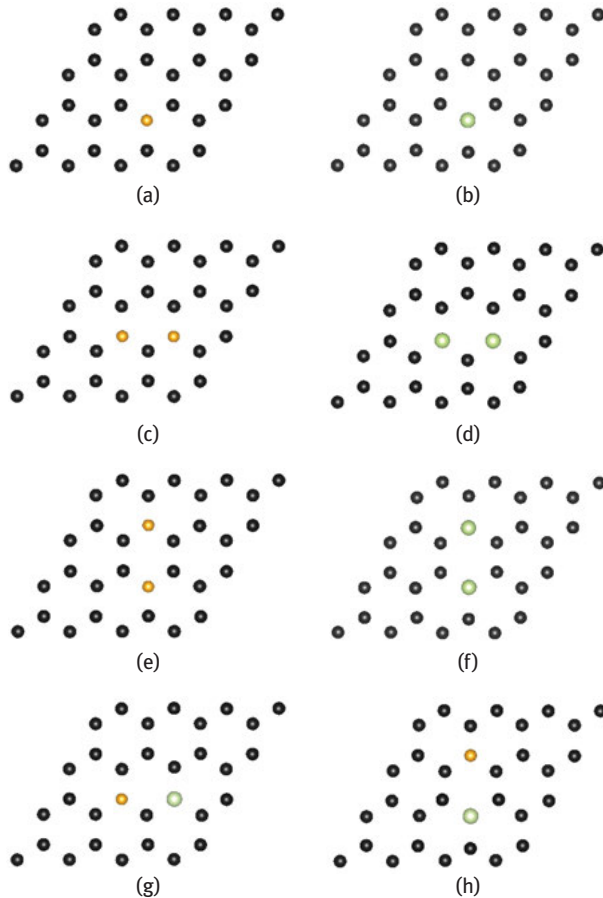


Figure 5.1: Configurations (a) S1, (b) S2, (c) S3, (d) S4, (e) S5, (f) S6, (g) S7, (h) S8; Black colored atoms are Ge, yellow colored atoms are As, light-green colored atom are Ga.

Next, Be is doped in germanene and concentration is increased from 3.12% to 18.75% as shown in Figure 5.2(a) to (f). In addition to this, voids are also incorporated to explore about the effects of vacancies in pristine layer. For this, amount of Be is kept fixed with minimum possible concentration 3.12%. Then void

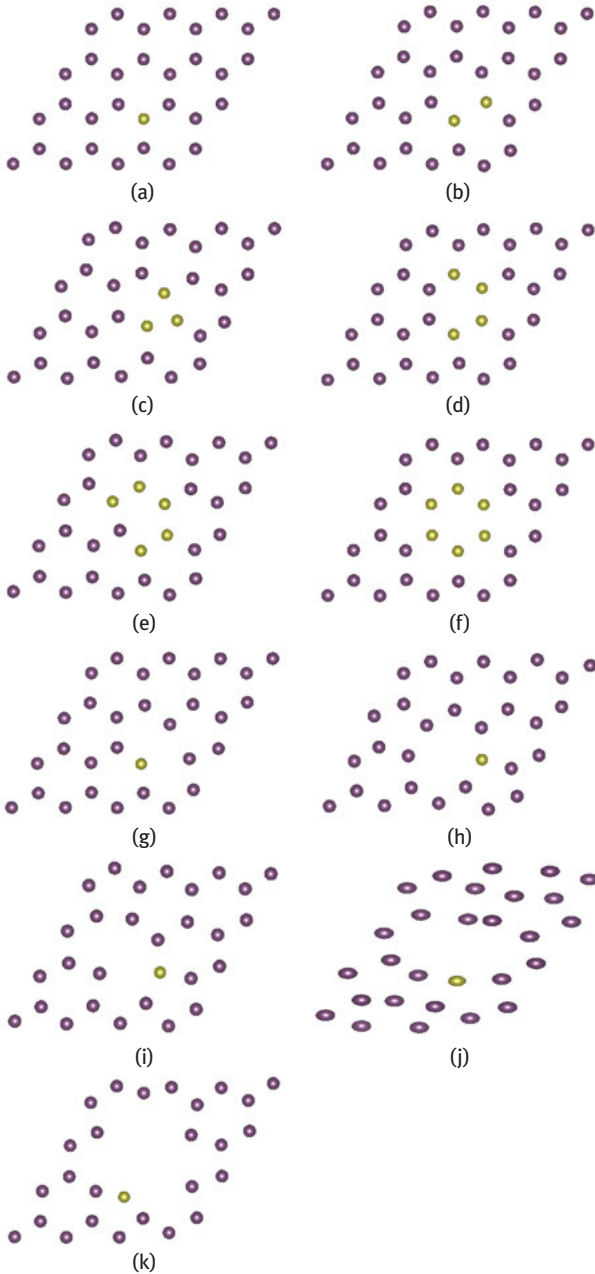


Figure 5.2: Configurations with Be doping concentrations **(a)** 3.12%, **(b)** 6.25%, **(c)** 9.38%, **(d)** 12.50%, **(e)** 15.62%, **(f)** 18.75%; Configurations with Be doping concentration 3.12% and vacancy concentrations **(g)** 3.12%, **(h)** 6.25%, **(i)** 9.38%, **(j)** 12.50%, **(k)** 15.62%. Purple colored atoms are Ge and yellow-green colored atoms are Be.

concentration is increased from 3.12 % to 15.62 % as depicted in Figure 5.2(g) to (k). All adatoms and voids are introduced in same hexagonal cell of pristine germanene, because it has been verified that, incorporation of dopings and vacancies in different hexagonal cell gives higher formation energies.

5.3.2 Optical properties of arsenic and gallium doped germanene

Different optical properties of As and Ga doped structures have already been reported in previous studies [20, 49] in detail. Here, we would like to discuss about some optical properties of these configurations (S1, S2, S3, S4, S5, S6, S7 and S8) briefly which have not been analyzed yet in previous investigations. Some optical properties of these systems are depicted in Figure 5.3 for parallel and perpendicular both types of polarizations. In Figure 5.3(a) imaginary part of dielectric constant ($\epsilon_2(\omega)$) of Ga doped structures are represented. From this figure, it can be observed that, positions of peaks corresponding to maximum of $\epsilon_2(\omega)$ are at 8.21 eV, 8.13 eV and 8.23 eV for S2, S4 and S6 respectively. These peak positions are red shifted compared to the same for pristine Ge-nanosheet. Although infrared (IR) absorbance at zero frequency ($\alpha(0)$) takes finite values in case of pristine germanene and for As and Ga doped structures for parallel polarization [20, 50, 51], but considering perpendicular polarization this $\alpha(0)$ approaches to almost vanishing value for all 8 doped systems. This situation is depicted in table A, Fig. A and Fig. B of “supplementary information”. It can be reflected from Figure 5.3(b) that, in case of co-doped configurations S7 and S8, intensity of peaks of absorption coefficient ($\alpha(\omega)$) are less than pristine germanene, but the same attains higher values than pristine system in some energy regions like 5.30 to 6.84 eV, 7.12 to 8.22 eV, 10.32 to 10.92 eV etc. Thus, values of $\alpha(\omega)$ can be tuned by suitable doping of adatoms in pristine germanene. Analysis of reflectivity of As doped structures in case of perpendicular polarization reveals that, anisotropic oscillations are mainly restricted in 5 to 15 eV which is in ultra-violet (UV) region of energy spectrum (Figure 5.3(c)). In addition, it is noticeable that, in case of Ga doped configurations real part of refractive index ($n(\omega)$) also gets several modifications compared to pristine systems (Figure 5.3(d)). Here, although the peak positions remain almost same with bare structure but, peak intensities are diminished due to doping of foreign element. However, in case of real part of conductivity ($\sigma_1(\omega)$), maximum heighted peak positions are red shifted for As doped configurations compared to bare germanene (Figure 5.3(e)). Moreover, EELS, abbreviated as $L(\omega)$, for parallel polarization of As doped configurations are explored briefly and shown in Figure 5.3(f). A very sharp peak of $L(\omega)$ is observed at 8.90 eV for virgin germanene layer. Second highest intensity peak of $L(\omega)$ appears at 7.70 eV for bare configuration. It can be observed from Figure 5.3(f) that, due to addition of foreign elements the number of peaks as well as peak intensities for

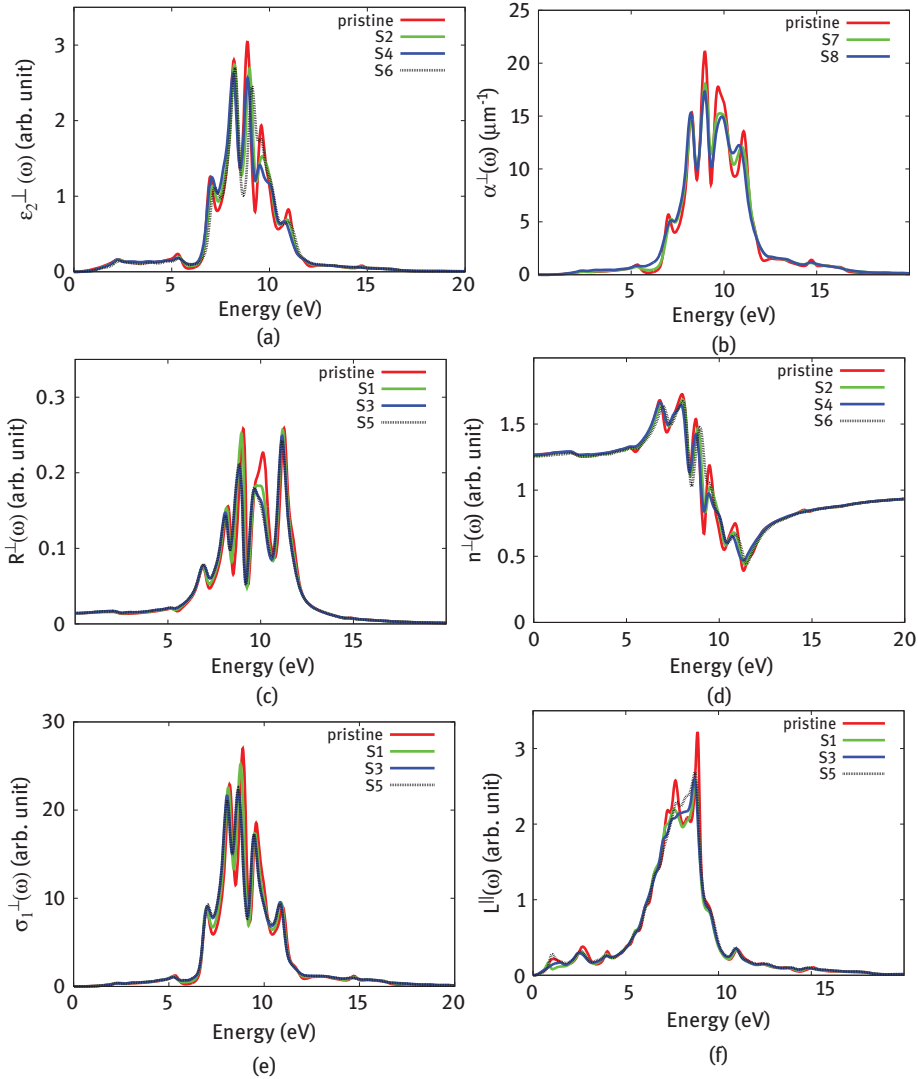


Figure 5.3: (a) Imaginary part of dielectric constant, (b) absorption spectra, (c) reflectivity, (d) real part of refractive index, (e) real part of conductivity of some selected As, Ga and AsGa co-doped structures in case of parallel polarization; (f) EELS for As doped structures for parallel polarization.

the defected structures decrease in contrast to pristine system. At the same time, there are several modifications in $L(\omega)$ due to doping of As than pristine layer which can be applied in future nano-electronics applications. Thus, it is possible to tailor different optical properties of germanene, by varying doping sites crucially (same or different sub-lattice positions) and choosing suitable doping concentrations and doping elements as well.

5.3.3 Optical properties of beryllium doped and vacancy induced germanene

5.3.3.1 Dielectric functions

In this section, real and imaginary parts of dielectric constant, termed as $\epsilon_1(\omega)$ and $\epsilon_2(\omega)$, are investigated for Be doped and vacancy induced germanene layers. It can be elucidated from previous studies that, in case of parallel polarization, static real part of dielectric constant ($\epsilon_1(0)$) exhibits an increasing tendency with increase in doping concentration but the same possesses a decreasing trend with increasing vacancy concentration [21]. In Figure 5.4(a), $\epsilon_1(\omega)$ for a structure with 15.62% Be concentration (arbitrarily chosen) are shown for both types of polarizations. Values of $\epsilon_1(0)$ are ~ 18.20 and 1.60 for parallel and perpendicular polarizations respectively for this system. This value of $\epsilon_1(0)$ is $\sim 15\%$ higher than that of pristine germanene for parallel polarization. Whereas, for perpendicular direction value of $\epsilon_1(0)$ remains almost same with bare germanene. $\epsilon_1(\omega)$ attains maximum intensities at 0.40 and 6.65 eV respectively for parallel and perpendicular direction. There are several plasma frequencies (ω_p) in case of parallel polarization as reflected by this figure. It has been already explored about ω_p of these Be and voids added systems in Ref [21]. critically. In that investigation, it has been clearly indicated that, predicted computational results of ω_p are in well agreement with expected analytical data. However, for perpendicular polarization no ω_p appear for this configuration. In order to analyze $\epsilon_2(\omega)$, this function is depicted in Figure 5.4(b) for a arbitrarily chosen system among all systems. Nature of this function as reported in Ref [20], for pristine germanene is modified significantly due to incorporation of doping and vacancy. Highest intensity peak of $\epsilon_2(\omega)$ appears at 0.60 eV for this configuration (Figure 5.4(b)) for parallel polarization. Second highest intense peak of $\epsilon_2(\omega)$ appears at 1.57 eV for this system. Anisotropic response of $\epsilon_2(\omega)$ for perpendicular direction is very small than parallel direction as reflected from this figure.

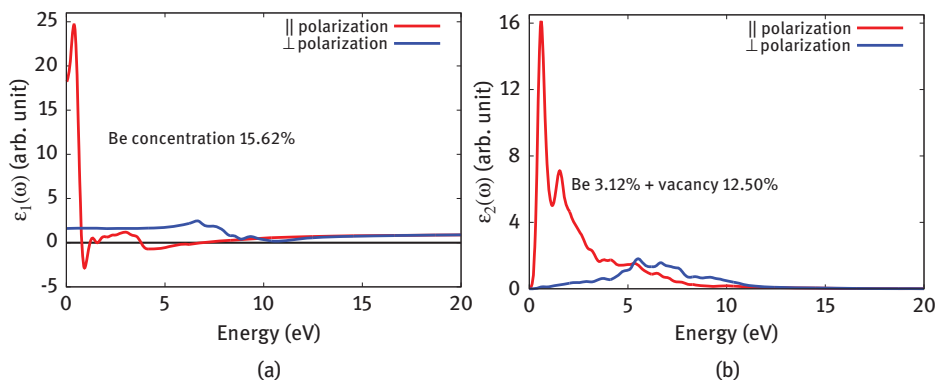


Figure 5.4: (a) Real and (b) imaginary part of dielectric constant for both types of polarization in case of some arbitrarily chosen systems.

Moreover, in case of parallel direction, response is mainly restricted in IR and visible region of energy spectrum, whereas, considering perpendicular direction anisotropic oscillation is mainly in UV region.

5.3.3.2 Absorption spectra

Absorption coefficient ($\alpha(\omega)$) of two arbitrarily chosen configurations are depicted in Figure 5.5 for both parallel and perpendicular polarizations. IR absorbance of these systems have already been estimated in previous studies [21]. It can be elucidated from Figure 5.5(a) and 5(b) that, response of $\alpha(\omega)$ is more significant in case of perpendicular polarization rather than parallel polarization for both defected germanene system. For the configuration with 18.75% Be concentration, maximum heighted peak appears at 8.74 eV and for the configuration with 6.25% vacancy (plus 3.12% Be) the same appears at 10 eV. In case of only Be doped configuration, (18.75%) there exists five prominent peaks in parallel direction and four prominent peaks in perpendicular direction (Figure 5.5(a)). The number of peaks is reduced due to addition of vacancy and peaks also appear to be more broader as can be seen from Figure 5.5(b). It is also noticeable from Figure 5.5(a) that a sharp peak with small intensity arises at 0.69 eV considering parallel polarization. It has been indicated by previous investigations that, this peak appears in case of pristine germanene also due to $\pi \rightarrow \pi^*$ resonant excitations [20]. But interestingly, this peak vanishes when vacancy is introduced in germanene (Figure 5.5(b)). $\alpha(\omega)$ takes exactly same values for both parallel and perpendicular polarizations at 7.32 eV and 7.37 eV for 18.75% Be added and 6.25% void (with 3.12% Be) added systems respectively, as reflected by these figures. So, at these frequencies $\alpha(\omega)$ is independent of polarizations of EM wave. It can be concluded from these investigations that, $\alpha(\omega)$ peaks of pristine germanene appear to be more sharp due to incorporation of dopings and the same become broader while void is introduced in bare germanene.

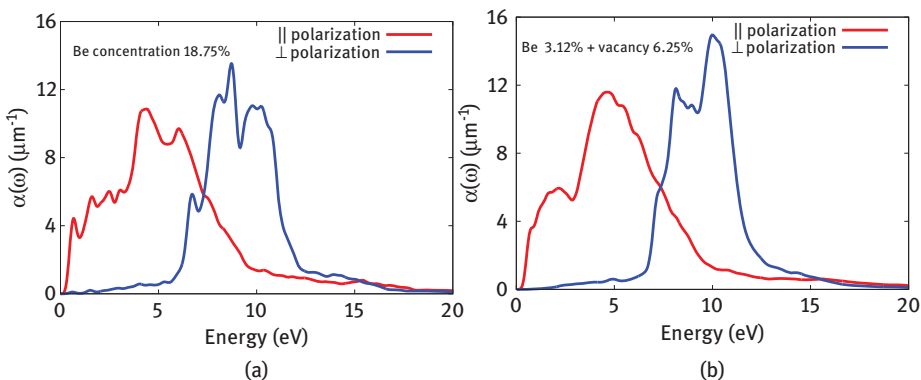


Figure 5.5: (a) and (b) Absorption spectra for both types of polarization in case of some arbitrarily chosen systems.

5.3.3.3 Electron energy loss spectroscopy

How much energy is lost by fast moving electrons through a material is estimated by an important parameter EELS, ($L(\omega)$). $L(\omega)$ for some configurations are indicated in Figure 5.6. Response of $L(\omega)$ is very sharp considering perpendicular polarization. For both systems (Figure 5.6) $L(\omega)$ takes significant value in the energy region 0 to 15 eV in case of parallel polarization. while, for perpendicular polarization $L(\omega)$ is significant within 6 to 15 eV. Peak positions for the system with 9.38 % Be concentration are at 0.97 eV, 2.67 eV, 7.60 eV (parallel polarization) and 8.52 eV, 9.35 eV, 11.35 eV (perpendicular polarization) in energy spectrum. $L(\omega)$ peak positions for the structure with 6.25 % vacancy (plus 3.12% Be) are at 2.76 eV and 7.69 eV (parallel polarization) and 9.10 eV, 11.15 eV (perpendicular polarization). It is evident from this study that, number of EELS peaks is also reduced due to incorporation of vacancy. This same situation arises for absorption spectra as discussed in the previous section. Thus, it is possible to tailor loss function of germanene by increasing doping concentration of Be or increasing void in bare FS germanene mono-layer.

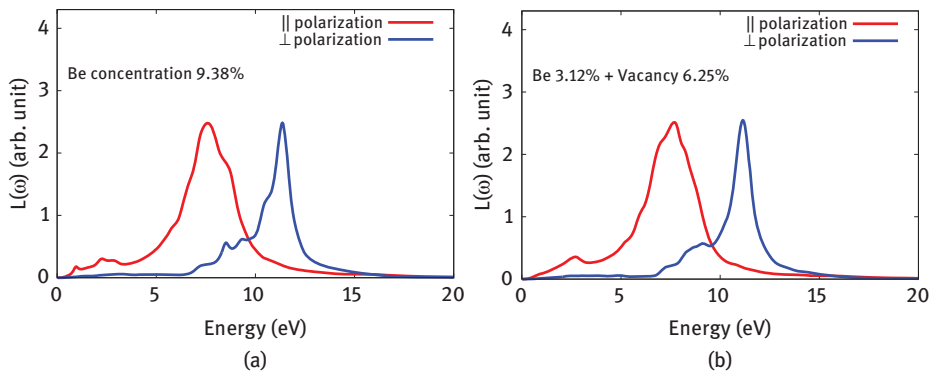


Figure 5.6: (a) and (b) Electron energy loss spectra for both types of polarization in case of some arbitrarily chosen systems.

5.3.3.4 Reflectivity and its modulation

Reflectivity ($R(\omega)$) of these defected germanene layers are analyzed briefly in this section. $R(\omega)$ for the system with 15.62% Be doped germanene is shown in Figure 5.7(a). Values of static reflectivity ($R(0)$) for this configuration are 0.39 and 0.01 for parallel and perpendicular polarization respectively. It can be conjectured from this study that, $R(0)$ approaches almost vanishing value in case of perpendicular direction, while the same is significant when parallel polarization direction is considered. It is clear from Figure 5.7(a) that, response of $R(\omega)$ is significant in case of parallel polarization rather than perpendicular direction. $R(\omega)$ is maximum at 0.81 eV, which is in IR region of energy spectrum. Moreover, it is also noticeable that, at 8.11 eV (UV region) contribution of $R(\omega)$ for both types of polarizations are

exactly the same. So, at this frequency it is not possible to differentiate between parallel and perpendicular polarization by analyzing $R(\omega)$.

Next, reflectivity modulation ($R_M(\omega)$) of this structure is also depicted in Figure 5.7(b) for this configuration in order to study optical properties more crucially. $R_M(\omega)$ is significant for parallel polarization in the region 0–4.10 eV. But, in the energy range 4.10–11 eV values of $R_M(\omega)$ are higher in case of perpendicular polarization than parallel direction. After that, $R_M(\omega)$ is again pronounced for parallel polarization. $R_M(\omega)$ achieves maximum intense peak at energy value 6.52 eV of EM energy spectrum. Second maximum intense peak of $R_M(\omega)$ appears at 9.46 eV for this structure.

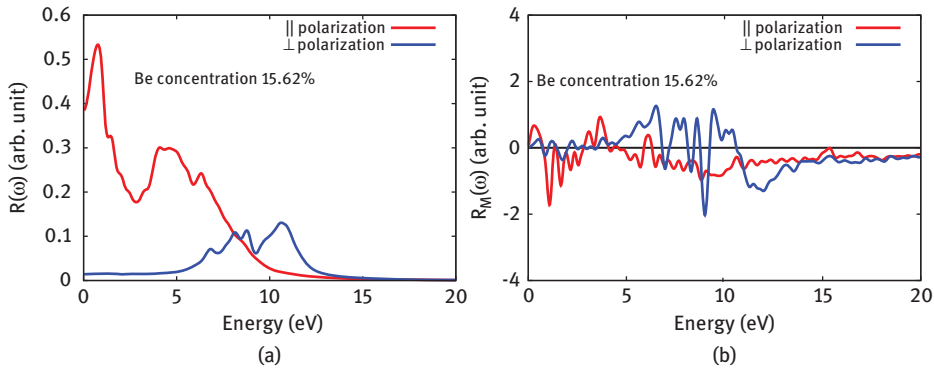


Figure 5.7: (a) Reflectivity and (b) reflectivity modulation for both types of polarization in case of an arbitrarily chosen system.

5.3.3.5 Conductivity

Real and imaginary parts of optical conductivity ($\sigma_1(\omega)$, $\sigma_2(\omega)$ respectively) of two randomly chosen configurations are depicted in Figure 5.8. It can be observed from

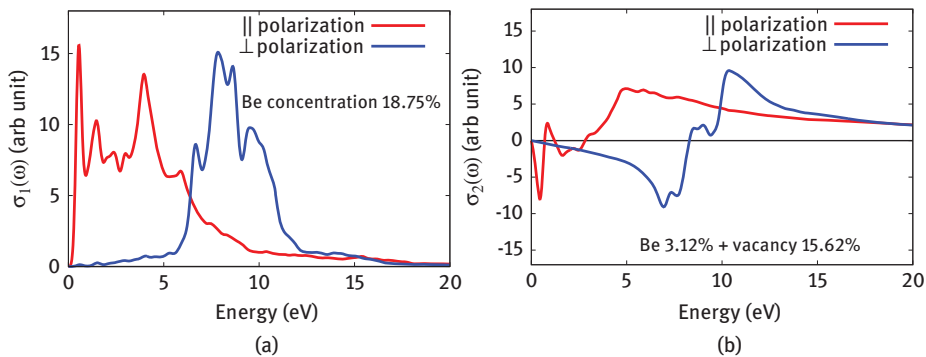


Figure 5.8: (a) Real and (b) imaginary parts of optical conductivity for both types of polarization in case of two arbitrarily chosen systems.

Figure 5.8(a) that, $\sigma_1(\omega)$ exhibits a enormous response in IR region (0.55 eV) for parallel polarization of EM wave. However, considering perpendicular polarization huge response of $\sigma_1(\omega)$ appears in UV region (7.88 eV) of energy spectrum. Rest prominent peaks of $\sigma_1(\omega)$ for this configuration with 18.75% Be concentration are at 1.46 eV, 4 eV (Parallel polarization) and 6.70 eV, 8.64 eV, 9.56 eV (perpendicular polarization). However, at 6.35 eV, $\sigma_1(\omega)$ curves for parallel and perpendicular polarizations crosses which imply that, at this energy position real part of optical conductivity is independent of polarization of EM wave. Oscillating behavior of $\sigma_1(\omega)$ vanishes after 15 eV for both types of polarizations.

Now, $\sigma_2(\omega)$ for 15.62% vacancy (plus 3.12% Be) added Ge-nanosheet is presented in Figure 5.8(b). It is clear from the definition of $\sigma_2(\omega)$ (eq. (5.7)) that, this function can take both positive and negative values depending on the values of $\epsilon_1(\omega)$. From Figure 5.8(b), it can be seen that, maximum intense peak of $\sigma_2(\omega)$ appears at 10.32 eV in perpendicular direction. Other sharp peak positions of $\sigma_2(\omega)$ for this configuration are at 0.85 eV, 5.03 eV (parallel polarization) and 9 eV (perpendicular polarization). $\sigma_2(\omega)$ approaches to vanishing values at 0.76 eV, 1.21 eV, 2.84 eV (parallel polarization) and 8.29 eV (perpendicular polarization). At these frequencies $\epsilon_1(\omega)$ is unity, consistent with eq. (5.7).

5.4 Comparison between As, Ga and Be doped germanene systems

In this section, we are focused to give a comparative discussion of these As, Ga and Be doped germanene layers. Among all these structures Ga doped configuration S6 exhibits maximum response for $\epsilon_1(\omega)$ and $\epsilon_2(\omega)$ in parallel polarization direction of EM wave [20, 49]. $\epsilon_1(0)$ enhances almost 72% than pristine germanene for this structure. Moreover, this structure also exhibits maximum response in $\alpha(\omega)$ and $R(\omega)$ also. So, it can be concluded from our investigation that, 6.25% Ga doped system at non-equivalent sites of germanene nanosheet possesses best opto-electronic properties among all considered systems. Our theoretical study indicates that, formation energies are positive for Ga, AsGa, Be and void incorporated structures. Whereas, the same is negative for As doped structures. So, from experimental point of view, doping of As in pristine germanene may be more practical than other atoms as these structures are stable than bare germanene.

5.5 Conclusions and future directions

A DFT perspective analysis of defected 2D buckled FS germanene mono-layer has been performed in this present theoretical work. In conclusion, addition of foreign elements or void in bare/pristine system modifies optical properties of pristine germanene significantly. As, Ga and Be are chosen as doping elements. Along with

doping elements, doping sites (equivalent sub-lattice positions or non equivalent sub-lattice positions) also play crucial role in modifications of optical properties.

In case of As or Ga doped configurations, modifications in $\epsilon_2(\omega)$, $\alpha(\omega)$, $R(\omega)$ etc. are different for the situations when adatoms are added in same sub-lattice positions and different sub-lattice sites. Increasing Be concentration in germanene lead to a value of $\epsilon_1(0)$, which is even more than pristine case. For Be doped and void added systems, $\alpha(\omega)$ is more significant in perpendicular direction than parallel direction. While, in case of $L(\omega)$, response from both parallel and perpendicular polarization are significant. In contrast, for $R(\omega)$, response is pronounced only in parallel direction. These interesting modulations of optical properties of Ge-nanosheet can be applied to fabricate next generation opto-electronics devices based on germanene. We expect, our current analysis will motivate researchers to carry out more works involving germanene and germanene based technology to enrich applications of this 2D material in device fabrications.

Acknowledgements: This work is supported by DST-FIST, DST-PURSE, Government of India. One of the authors (ND) gratefully acknowledge DST, Government of India for providing financial assistance through DST-INSPIRE Fellowship scheme of grant number IF150670. We are thankful to the anonymous reviewer for critical comments and suggestions in order to improve the scientific quality of this manuscript.

References

- [1] Roome NJ, Carey JD. Beyond Graphene: stable elemental mono-layers of silicene and germanene. *ACS Appl Mater Interfaces USA*. 2014;6:7743–50.
- [2] Balendhran S, Walia S, Nili H, Sriram S, Bhaskaran M. Elemental analogues of graphene: silicene, germanene, stanene, and phosphorene. *Small USA*. 2015;11:640–52.
- [3] Chowdhury S, Jana D. A theoretical review on electronic, magnetic and optical properties of silicene. *Rep Prog Phys UK*. 2016;79(58pp):126501.
- [4] Gupta A, Sakthivel T, Seal S. Recent development in 2D materials beyond graphene. *Prog Mater Sci Netherland*. 2015;73:44–126.
- [5] Asano K, Hotta C. Designing dirac points in two-dimensional lattices. *Phys Rev B USA*. 2011;83(14pp):245125.
- [6] Acun A, Zhang L, Bampoulis P, Farmanbar M, Houselt AV, Rudenko AN, et al. Germanene: the germanium analogue of graphene. *J Phys: Condens Matter UK*. 2015;27(12pp):443002.
- [7] Behera H, Mukhopadhyay G. First principles study of structural and electronic properties of germanene. *AIP Conf Proc USA*. 2011;1349:823–24.
- [8] Miro P, Audiffred M, Heine T. An atlas of two-dimensional materials. *Chem Soc Rev UK*. 2014;43:6537–54.
- [9] Jana D. 2D Materials: future and Perspectives. *J Nanomed Res USA*. 2018;7(1):00169 (4pp).
- [10] Davila ME, Xian L, Cahangirov S, Rubio A, Lay GL. Germanene: a novel two-dimensional germanium allotrope akin to graphene and silicene. *New J Phys UK*. 2014;16(11pp):095002.
- [11] Li L, Lu SZ, Pan J, Qin Z, Wang YQ, Wang Y, et al. Buckled germanene formation on Pt(111). *Adv Mater Germany*. 2014;26:4820–24.

- [12] Madhushankar BN, Kaverzin A, Giouis T, Potsi G, Gournis D, Rudolf P, et al. Electronic properties of germanene field-effect transistors. *2D Mater UK*. 2017;4(6pp):021009.
- [13] Ye XS, Shao ZG, Zhao H, Yang L, Wang CL. Intrinsic carrier mobility of germanene is larger than graphene's: first-principle calculations. *RSC Adv UK*. 2014;4:21216–20.
- [14] Chen X, Sun X, Jiang J, Liang Q, Yang Q, Meng R. Electrical and optical properties of germanene on single-layer BeO substrate. *Phys Chem C USA*. 2016;120:20350–56.
- [15] Kaloni TP, Schwingenschlogl U. Weak interaction between germanene and GaAs(0001) by H intercalation: A route to exfoliation. *J Appl Phys USA*. 2016;114(5pp):184307.
- [16] Chowdhury S, Bandyopadhyay A, Dhar N, Jana D. Computational Sciences. In: Ramasami P, Eds. *Optical and magnetic properties of free-standing silicene, germanene and T-graphene system*. Germany: De Gruyter Publications, 2017:219–27. (Chapter 2). ISBN: 978-3-11-046536-5.
- [17] Schwingenschlogl U, Zhu J, Morishita T, Spencer MJS, Padova PD, Generosi A, et al. Computational Sciences. In: Ramasami P, Eds. *Elemental two-dimensional materials beyond graphene*. Germany: De Gruyter Publications, 2017:23–69. (Chapter 11). ISBN: 978-3-11-046536-5.
- [18] Kaloni TP. Tuning the Structural, Electronic, and magnetic properties of germanene by the adsorption of 3d transition metal atoms. *J Phys Chem C USA*. 2014;118:25200–08.
- [19] Pang Q, Li L, Zhang CL, Wei XM, Song YL. Structural, electronic and magnetic properties of 3d transition metal atom adsorbed germanene: A first-principles study. *Mater Chem Phys Netherland*. 2015;160:96–104.
- [20] Dhar N, Bandyopadhyay A, Jana D. Tuning electronic, magnetic and optical properties of germanene nanosheet with site dependent adatoms arsenic and gallium: A first principles study. *Curr Appl Phys Netherland*. 2017;17:573–83.
- [21] Dhar N, Jana D. Effect of beryllium doping and vacancy in band structure, magnetic and optical properties of free standing germanene. *Curr Appl Phys Netherland*. 2017;17:1589–600.
- [22] S S L, Zhang CW, Ji WX, Li F, Wang PJ, Hu SJ, et al. Tunable electronic and magnetic properties in germanene by alkali, alkaline-earth, group III and 3d transition metal atom adsorption. *Phys Chem Chem Phys UK*. 2014;16:15968–78.
- [23] Dhar N, Jana D. Magnetic and optical properties of carbon and silicon decorated free standing buckled germanene: A DFT approach. *J Phys Chem Solids Netherland*. 2018;115:332–41.
- [24] Liang P, Liu Y, Xing S, Shu H, Tai B. Electronic and magnetic properties of germanene: surface functionalization and strain effects. *Solid State Commun Netherland*. 2016;226:19–24.
- [25] Li SJ, Su Y, Chen G. Patterning germanene into superlattices: an efficient method for tuning conducting properties. *Chem Phys Lett Netherland*. 2015;638:187–90.
- [26] Rupp CJ, Chakraborty S, Ahuja R, Baierle RJ. The effect of impurities in ultra-thin hydrogenated silicene and germanene: a first principles study. *Phys Chem Chem Phys UK*. 2015;17:22210–16.
- [27] Pang Q, Zhang CL, Li L, Fu ZQ, Wei XM, Song YL. Adsorption of alkali metal atoms on germanene: A first-principles study. *Appl Surf Sci Netherland*. 2014;314:15–20.
- [28] Ni Z, Liu Q, Tang K, Zheng J, Zhou J, Qin R, et al. Tunable bandgap in silicene and germanene. *Nano Lett USA*. 2012;12:113–18.
- [29] Matthes L, Pulci O, Bechstedt F. Optical properties of two-dimensional honeycomb crystals graphene, silicene, germanene, and tinene from first principles. *New J Phys UK*. 2014;16(14pp):105007.
- [30] V O O, Kecik D, Durgun E, Ciraci S. Adsorption of group IV elements on graphene, silicene, germanene, and stanene: dumbbell formation. *J Phys Chem C USA*. 2015;119:845–53.
- [31] Walsh KA. Beryllium chemistry and processing. Vidal EE, Goldberg A, Dalder ENC, Olson DL, Mishra B, Eds. USA: The Materials Information Society, ASM International, 2009. ISBN: 978-0-87170-721-5.

- [32] Olaniyan O, Mapasha RE, Momodu DY, Madito MJ, Kahleed AA, Ugbo FU, et al. Exploring the stability and electronic structure of beryllium and sulphur co-doped graphene: first principles study. *RSC Adv UK*. 2016;6:88392–402.
- [33] He X, Chen Z-X, Li Z, Zou Z. Emergence of localized magnetic moment at adsorbed beryllium dimer on graphene. *J Chem Phys USA*. 2010;133(5pp):231104.
- [34] Urias FL, Terrones M, Terrones H. Beryllium doping graphene, graphene-nanoribbons, C60-fullerene, and carbon nanotubes. *Carbon Netherland*. 2015;84:317–26.
- [35] Ran Q, Zhang C-H, Shen J. Silicene-like beryllium encapsulated nanowires. *Chem Phys Netherland*. 2012;397:42–47.
- [36] Perdew JP, Burke K, Ernzerhof M. Generalized gradient approximation made simple. *Phys Rev Lett USA*. 1996;77:3865–68.
- [37] Ordejon P, Artacho E, Soler JM. Self-consistent order-N density-functional calculations for very large systems. *Phys Rev B USA*. 1996;53:R10441–R10444.
- [38] Portal DS, Ordejon P, Artacho E, Soler JM. Density-functional method for very large systems with LCAO basis sets. *Int J Quantum Chem USA*. 1997;65:453–61.
- [39] Soler JM, Artacho E, Gale DJ, Garcia A, Junquera J, Ordejon P, et al. The SIESTA method for ab initio order-N materials simulation. *J Phys: Condens Matter UK*. 2002;14:2745–79.
- [40] Monkhorst HJ, Pack JD. Special points for Brillouin-zone integrations. *Phys Rev B USA*. 1976;13:5188–92.
- [41] Jana D, Sun CL, Chen LC, Chen CH. Effect of chemical doping of boron and nitrogen on the electronic, optical, and electrochemical properties of carbon nanotubes. *Prog Mater Sci Netherland*. 2013;58:565–635.
- [42] Jana D, Chen LC, Chen CW, Chattopadhyay S, Chen KH. A first principles study of optical properties of B_xC_y single wall nanotubes. *Carbon Netherland*. 2007;45:1482–91.
- [43] Jana D, Chakraborty A, Chen LC, Chen CW, Chen KH. First-principles calculations of the optical properties of C_xN_y single walled nanotubes. *Nanotechnology USA*. 2009;20:175701–12.
- [44] Yu PY, Cardona M. *Fundamentals of semiconductors physics and materials properties*. New York, USA: Springer, 2010. ISBN 978-3-642-00709-5.
- [45] Das R, Chowdhury S, Majumdar A, Jana D. Optical properties of P and Al doped silicene: a first principles study. *RSC Adv UK*. 2015;5:41–50.
- [46] Deng Z, Li Z, Wang W. Electron affinity and ionization potential of two-dimensional honeycomb sheets: a first principle study. *Chem Phys Lett Netherland*. 2015;637:26–31.
- [47] Sun M, Ren Q, Wang S, Zhang Y, Du Y, Yu J, et al. Magnetism in transition-metal-doped germanene: a first-principles study. *Comput Mater Sci Netherland*. 2016;118:112–16.
- [48] Padilha JE, Pontes RB. Electronic and transport properties of structural defects in monolayer germanene: an ab initio investigation. *Solid State Commun Netherland*. 2016;225:38–43.
- [49] Dhar N, Jana D. Modifications of optical properties in doped germanene nanosheet. *Int J Nano Biomaterials UK*. 2017;7:29–37.
- [50] Matthes L, Gori P, Pulci O, Bechstedt F. Universal infrared absorbance of two-dimensional honeycomb group-IV crystals. *Phys Rev B USA*. 2013;87(9pp):035438.
- [51] Bechstedt F, Matthes L, Gori P, Pulci O. Infrared absorbance of silicene and germanene. *Appl Phys Lett USA*. 2012;100(4pp):261906.

Supplemental Material: The online version of this article offers supplementary material (<https://doi.org/10.1515/psr-2017-0164>).

Archa Gulati and Rita Kakkar

6 DFT studies on storage and adsorption capacities of gases on MOFs

Abstract: Metal-organic frameworks (MOFs) are highly porous crystalline materials, consisting of metal ions linked together with organic bridging ligands, exhibiting high surface areas. Lately, they have been utilized for gas sorption, storage, sensing, drug delivery, etc. The chemistry of MOFs is expanding with an extraordinary speed, constituting both theoretical and experimental research, and MOFs have proved to be promising candidates so far. In this work, we have reviewed the density functional theory studies of MOFs in the adsorption and separation of the greenhouse gas, CO₂, as well as the storage efficiencies for fuel gases like H₂, CH₄ and C₂H₂. The role of organic ligands, doping with other metal ions and functional groups, open metal sites and hybrid MOFs have been reviewed in brief.

Keywords: adsorption, C₂H₂, CH₄, CO₂, DFT, H₂, MOFs, separation, storage

6.1 Introduction

Over the last decade, there has been a tremendous growth in the synthesis, characterization, theoretical and experimental studies of metal-organic frameworks (MOFs). This is a recently recognized class of porous polymeric material, consisting of metal ions linked together by organic bridging ligands (Figure 6.1). It is a significant development, acting as a bridge between molecular coordination chemistry and material science [1]. It has appeared as a substantial class of crystalline materials with ultrahigh porosity (up to 90% free volume) and immense internal surface areas, extending beyond 6,000 m²/g. As a result of these properties, along with the high degree of flexibility with both the organic and inorganic components of their structure, MOFs bestow wide-ranging applications in clean energy, most importantly as storage materials for gases and high-capacity adsorbents to meet various separation needs [2]. Furthermore, we can know the location and arrangement of the atoms owing to their crystalline nature and can correlate the properties with the structure [3].

The robust porous material is developed by constructing an equivalent “molecular stage” by connecting rigid rod-like organic moieties with inflexible inorganic clusters that act as joints. The self-assembled metal ions act as coordination centers and are linked together with organic bridging ligands, which further give rise to

This article has previously been published in the journal *Physical Sciences Reviews*. Please cite as: Gulati, A., Kakkar, R. DFT studies on storage and adsorption capacities of gases on MOFs. *Physical Sciences Reviews* [Online] **2018**, 3. DOI: 10.1515/psr-2017-0196

<https://doi.org/10.1515/9783110568196-006>

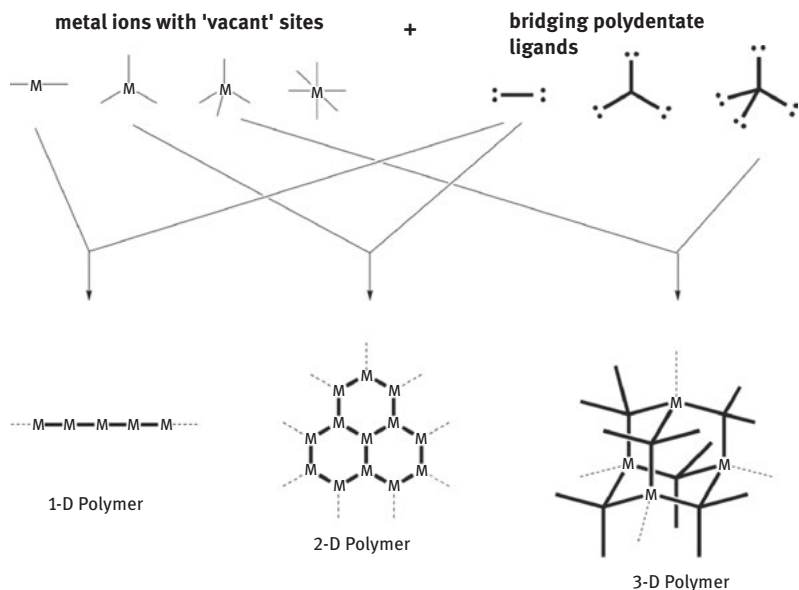


Figure 6.1: The principle of formation of MOFs. Reprinted with permission from ref [1].

nanoporous solid materials with high thermal and mechanical stability [4]. The size and chemical environment of the void spaces are controlled by the length and functional groups of the organic moieties [5]. Varying from other solid matter, e. g. zeolites, carbons and oxides, MOFs show high framework flexibility and shrinkage/expansion because of interaction with guest molecules [6]. Though various metal oxides have been previously reported for gas adsorption and water remediation [7–9], with a rising need for more efficient, energy-saving and environmentally benign methods for gas separation, adsorbents with tailored structures and adjustable surfaces must be found. In this regard, MOFs are worthy candidates for gas separation due to enormous surface areas, adjustable pore size, controllable properties and acceptable thermal stability [10].

The interactions of the electrons and nuclei ultimately decide the properties of materials. As the Schrödinger equation (SE) is analytically barely solvable, numerical approaches for obtaining approximate solutions for multielectron systems is a precious tool for chemists and material scientists. The major breakthrough in these computational calculations came in 1964 when Hohenberg and Kohn [11] and Kohn and Sham [12] reformulated SE (which included $3N$ spatial coordinates of N interacting electrons) into three spatial coordinates by the use of functionals of the electron density, a theory termed as density functional theory (DFT). DFT methods have become a keystone and are a common and indispensable part of various studies in material sciences. For example, classical DFT has been employed for characterization

of pore size distribution and specific surface area of porous materials by gas physisorption. The interaction energies and interatomic distances between adsorbates and MOFs are first obtained using DFT methods, followed by fitting the apt potential functions to get the improved force-field parameters to build first-principles-based force fields. Lately, the conventional and new progress of computational methodologies for MOFs and their application in gas separations have been reviewed by Zhong and co-workers [13]. Lin and co-workers used DFT calculations with periodic boundary conditions to develop force fields that can correctly predict adsorption isotherms, binding geometries and transport properties [14, 15]. Sholl and co-workers reported that an electrostatic potential energy surface computed from a periodic DFT calculation can be applied directly to elucidate the electrostatic interactions for adsorption, and it is not necessary to assign point charges to MOF atoms where the MOF is assumed to be rigid [16]. In addition, the charges extracted from Mulliken population analysis based on DFT calculations have been successfully applied in calculations on periodic structures of some MOFs [17, 18], although the atomic charges obtained by this method depend on the basis set [19]. In this chapter, we have reviewed some of the DFT studies done on MOFs for evaluating their adsorption and storage capacities for gases.

6.2 Water stability of MOFs

For utilizing MOFs in adsorption applications, it becomes important to study their behavior in the presence of water. Water is present in various streams and therefore must be considered while selecting adsorbents for adsorption, separation and purification systems (Figure 6.2).

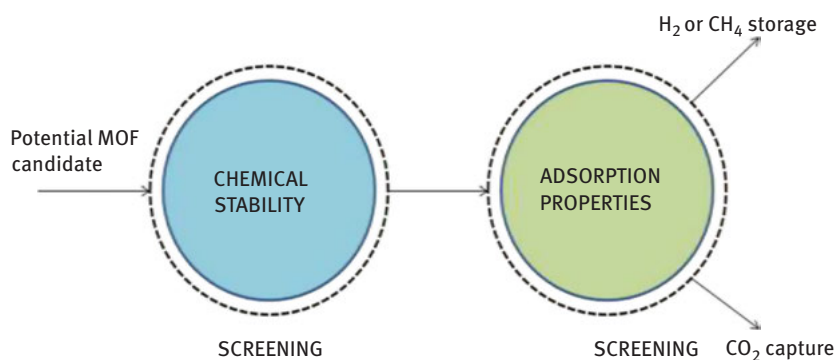


Figure 6.2: Importance of water stability of MOFs.

Natural gas streams usually contain water vapor in large amounts, which must be reduced to ppm levels before use or storage [20]. Water vapors are also present in

considerable amounts (~10%) in industrial flue gas and cannot be ignored when selecting adsorbents for CO₂ capture. They are also a major component of biofuel streams and the energy invested in the dehydration step may be higher than the energy which is finally released by the combustion process [21]. Hence, while selecting an adsorbent, its stability and behavior in humid conditions must also be taken into account.

Several features have been reported which are critical for MOF stability in a humid environment. These are the basicity of the organic ligands, the extent of coordination between metal and ligand and shielding of coordination sites by functional groups [22]. Water stability is a decisive factor in determining whether MOFs can be practically applied for various applications. Since MOFs have a high degree of diversity in their structures, even though some structures are unstable in the presence of water vapors, a large number of stable MOFs do exist.

6.2.1 DFT studies

In the last few years, a lot of importance has been given to exploring the behavior of various MOFs in the presence of water vapors, and a number of experimental and theoretical studies have been performed. Watanabe et al. [23] performed periodic DFT calculations using the PW91-GGA exchange-correlation functional to evaluate the binding of water in CuBTC (or HKUST-1). They found that the interaction energy of the first water molecule and the Cu dimer is -47.3 kJ/mol. For two water molecules, the calculated interaction energy was -75.3 kJ/mol, which is not simply twice the binding energy found for an individual water molecule. They also predicted that, when the relative humidity of the air at room temperature is approximately 2%, then most of the Cu sites are saturated with the water molecules. Sholl et al. [24] found that DFT-derived atomic charges vary significantly, as water molecules move through the framework of HKUST-1. They used plane-wave DFT calculations and calculated the adsorption energies of individual water molecules inside the MOF by using the equation

$$E_{\text{ads}} = (E_{\text{H}_2\text{O}/\text{HKUST-1}}) - (E_{\text{H}_2\text{O}} + E_{\text{HKUST-1}})$$

where E_{ads} , $E_{\text{H}_2\text{O}/\text{HKUST-1}}$, $E_{\text{H}_2\text{O}}$ and $E_{\text{HKUST-1}}$ are the adsorption energy, energy of the adsorption complex, energy of isolated water molecule and energy of isolated HKUST-1, respectively.

DFT calculations were also employed for investigating the formation and stability of water clusters in the hydrophobic pores of FMOF-1. First-principles DFT calculations revealed that larger water clusters (pentamers) are more favorable than the smaller ones (dimers), as shown in Figure 6.3, because of increase in adsorption energy due to more nondirectional dispersive interactions in larger water clusters [25].

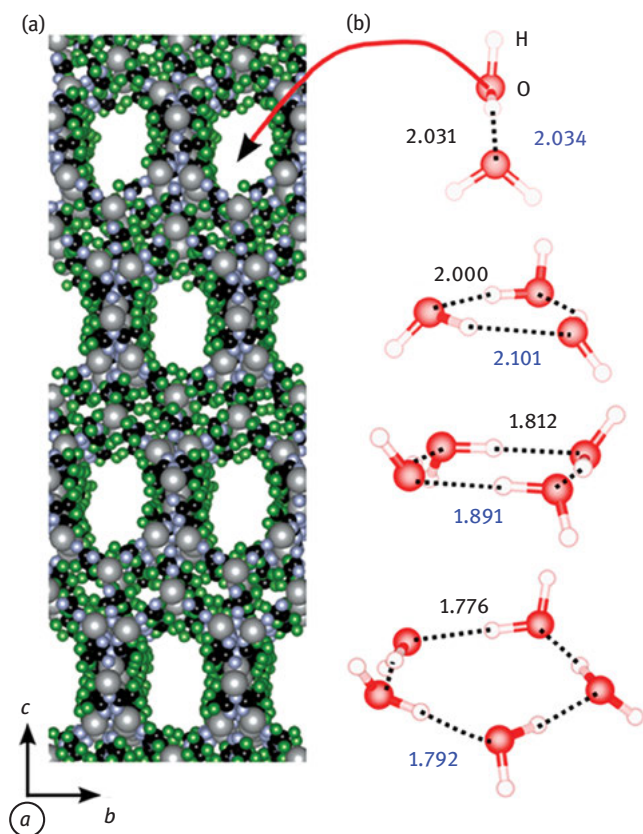


Figure 6.3: The orientation of water clusters in the pores of FMOF-1 after relaxation using density functional theory. Hydrogen bond distances in the gas phase (black) and inside FMOF-1 (blue) are shown in Å. Reprinted with permission from ref [25].

DFT calculations also revealed that water clusters formed in the pores of MOF-1 are energetically more favorable than the same water clusters when present in the water gas phase. Although there exist a limited number of structures which are stable under aqueous conditions, most of the applications will not require such great stabilities. The choice of adsorbent for a particular application depends not only upon the amount of humidity to which it is exposed, but also on the duration and number of cycles for which it remains in these conditions.

6.3 Adsorption and storage of fuel gases in MOFs

Since the concerns over future oil sources, energy security and environmental pollution are not of one particular nation, but global, enormous amount of resources are being spent for finding alternative fuels which are environmentally

acceptable as well as technologically promising. In this facet, the major alternative fuel candidates are H_2 , CH_4 , C_2H_2 , methanol, ethanol, Fischer Tropsch fuel, DME, biomass, biodiesel, biogasoline, etc. [26]. Here, we review DFT studies on adsorption and storage of H_2 , CH_4 and C_2H_2 on MOFs. A lot of work is going on to store these gases. H_2 is a promising fuel because it has a high gravimetric energy density, it is nontoxic and, moreover, its oxidation product is water. However, its small volumetric density is a hurdle in H_2 storage and its application as a fuel. CH_4 burns more cleanly than gasoline, which makes it an attractive alternative fuel. Above all, it has higher hydrogen to carbon ratio (H/C) than any other hydrocarbon fuel [27]. However, it has one-third volumetric energy density than that of gasoline, which is a major disadvantage. C_2H_2 is also a good candidate for being utilized as an alternative fuel, but it is of an explosive nature and, therefore, its storage is limited to pressures below 2 atm. The DFT studies of various MOFs that have been utilized for adsorption of these gases, the major adsorption sites, binding energies and other factors which influence the storage of these gases are discussed below.

6.3.1 Hydrogen (H_2) gas

Since widely used fuels like diesel and petroleum are being extinguished rapidly, an alternate energy resource is the need of the hour. Therefore, considering H_2 as an energy carrier is a vital part of future energy strategies. However, storage problems associated with H_2 limit its usage as an energy carrier in vehicles and portable electronics [28]. Liquefaction of H_2 for storage purposes is also not a lucrative solution because it requires cryogenic temperatures and extremely high pressures. This encouraged a lot of research into finding suitable materials for the efficient storage of H_2 . The various H_2 storage materials which are presently used can be divided into three categories, depending upon the strength of interaction of H_2 with the material which influences H_2 uptake and release [29].

1. *Physisorption materials.* In these materials, H_2 molecules are adsorbed on the surface of pores of materials through van der Waals (vdW) forces. No activation energy is required in this process, and hence the process is reversible and the interaction energy is low. Examples of these kinds of materials are MOFs, zeolites, porous carbons, organic polymers, clathrates, etc. The limitation of these sorbents is that they show low adsorption capacities at ambient temperature and pressure because of weak vdW interaction. The main advantage of these materials is fast adsorption and desorption kinetics.
2. *On-board reversible hydrides.* In this case, there is chemical bond formation between H_2 and these materials. The dissociated H_2 is stored either covalently or interstitially. Also, the release of H_2 is endothermic, which enables exothermic rehydrogenation of these materials. This means that the storage material can be directly recharged with H_2 *in situ* on board the vehicle. This

class includes interstitial metal hydrides such as LaNi_5H_x and covalent metal hydrides like MgH_2 and AlH_3 , but these materials either have very high- or very low-binding energies, metal amides and borohydrides, which include LiBH_4 , NaBH_4 , $\text{Mg}(\text{BH}_4)_2$, LiNH_2 and $\text{Mg}(\text{NH}_2)_2$, which have high dehydrogenation temperature and irreversible adsorption.

3. *Off-board regenerable hydrides.* These materials also store dissociated H_2 covalently, but the release of H_2 is exothermic and involves complex chemical processes for regeneration, which cannot be performed on board a vehicle. Hydrocarbons, alanes (AlH_3) and ammonia boranes belong to this class. Although the hydrocarbons and alane release H_2 endothermically, they require high hydrogenation pressure and complex rehydrogenation processes. Whereas ammonia borane releases H_2 exothermically, the rehydrogenation cannot occur readily at common pressures and temperatures.

The change in enthalpy (ΔH_{ads}) and entropy (ΔS_{ads}) of adsorption are given a lot of consideration while designing an efficient adsorbent. A lot of effort has been made to optimize ΔH_{ads} by controlling the chemical and physical nature of the adsorbing surface [30]. In this context, MOFs are promising H_2 storage materials due to their high porosity and tunable porous surfaces. For example, $\text{Zn}_4\text{O}(\text{BDC})_3$ (MOF-5; $\text{BDC}^{2-} = 1,4\text{-benzenedicarboxylate}$) has the best overall cryogenic H_2 storage performance within a MOF to date, showing a total volumetric adsorption capacity of 66 g/L (10 wt %) at 77 K and 100 bar [31]. Matzger et al. reported that at 60 bar and 77 K, IRMOF-1 stores 5.0 wt% of H_2 and MOF-177 stores 7.5 wt%. However, their H_2 uptake capacity diminishes near room temperature to ~ 0.5 wt%, far too low for practical usage [32]. A lot of research is going on to improve the H_2 storage capacities of MOFs at feasible temperature and pressure conditions. Some of the factors that influence the storage capacity of MOFs are reviewed below.

6.3.1.1 Effect of lithium ion doping

The ideal interaction between the material and H_2 should be intermediate between chemisorption and physisorption. As mentioned above, the H_2 molecule is physisorbed on MOFs [33]. A plausible way to increase the interaction energy is to integrate lightweight metal atoms such as Li. Up to six H_2 molecules can strongly bind with a Li cation, with a mean binding energy of -4.77 kcal/mol per H_2 molecule [34]. Goddard III and co-workers [35] studied MOF-C6, MOF-C10, MOF-C16, MOF-C22 and MOF-C30. For predicting the structure of Li atoms that are bound to aromatic organic linkers containing up to 9 fused aromatic rings (Figure 6.4), they used the X3LYP functional of DFT and found that the preferred site by Li atoms for binding is the center of hexagonal rings, but on adjacent aromatic rings, Li atoms are on opposite sides.

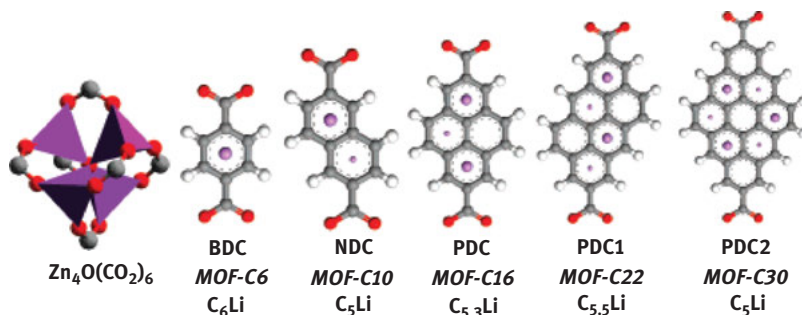


Figure 6.4: Li-doped MOFs. In each case, the $Zn_4O(CO_2)_6$ connector couples to six aromatic linkers through the O-C-O common to each linker. The MOFs are named according to the number of aromatic carbon atoms. The large violet atoms in the linkers represent Li atoms above the linkers, while small violet Li atoms lie below the linkers. The C_xLi ratio considers only aromatic carbon atoms. Reprinted from ref [35] with permission.

Froudakis et al. [36] studied the effect of Li-alkoxide linkers for H_2 storage in various MOFs. To perform quantum mechanical calculations, the model system was decreased in size by separating the organic linker and saturating the carboxylate groups with H ions. This approximation was appropriate for studying the effect of the new modified linker. They used DFT calculations to study interaction energies between one and five H_2 molecules with the two organic linkers of IRMOF-8 and IRMOF-14. Similar results were reported for both the cases, as shown in Table 6.1. The interaction energies of the first two hydrogens are -3.00 and -2.87 kcal/mol per H_2 , which indicate strong adsorption. Also, compared to the most favorable binding sites of any of the unmodified MOFs, these values are two to three times higher.

Table 6.1: Binding energy for one to five H_2 molecules adsorbed on Li atom of Li-alkoxide functionalized IRMOF-8 (naphthalene) and IRMOF-14 (pyrene)*. Reprinted with permission from ref [36].

Number of H_2 molecules	IRMOF-8 (naphthalene)		IRMOF-14 (pyrene)	
	B.E./ H_2 (kcal/mol)	Li- H_2 (Å)	B.E./ H_2 (kcal/mol)	Li- H_2 (Å)
1 H_2	-3.02	2.03	-2.98	2.04
2 H_2	-2.87	2.06	-2.87	2.08
3 H_2	-2.67	2.10	-2.67	2.10
4 H_2	-2.37	2.19	-2.36	2.20
5 H_2	-2.15	2.23/2.34	-2.11	2.24/2.34

*All energies are corrected for BSSE (Basis Set Superposition Error). The distances from Li atoms are measured from the center of mass of the H_2 molecule.

Another group, Ellis et al. [37], investigated MOFs, $Zn_2(BPDC)_2(DNPI)$ and $Zn_2(NDC)_2(BIPY)$, which have a paddle-wheel structure with the Zn_2 corner post surrounded by

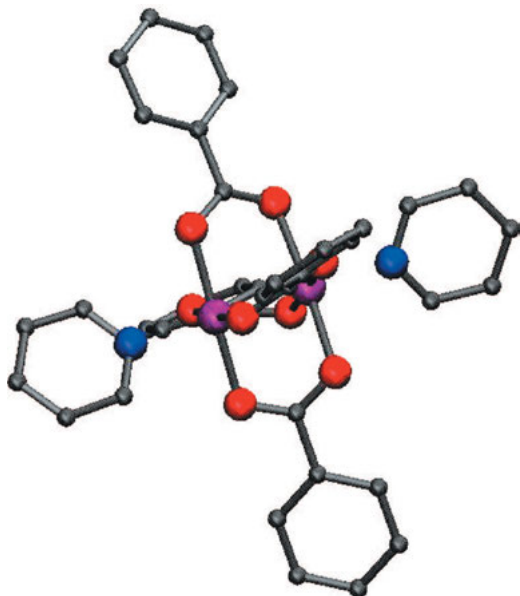


Figure 6.5: Paddle-wheel structure with Zn_2 corner-post surrounded by aromatic struts. Color key: silver, carbon; red, oxygen; purple, zinc; blue, nitrogen. Reprinted from the ref [37] with permission.

aromatic struts, as shown in Figure 6.5. They used DFT on these two MOFs to identify the electronic environment. Furthermore, binding sites and binding energies of H_2 were evaluated for the presence and absence of the Li dopant. It was reported that for both the sites, near the corner postoxygen and on the linking strut ring structure, Li atom increased the binding energy.

6.3.1.2 Effect of doping with other metals

Besides lithium, the effect of other metal atoms on H_2 adsorption by MOFs has also been explored. Venkataramanan et al. [38] examined the introduction of a Li atom on MOFs with the metals Fe, Cu, Ni, Co and Zn. On changing the metal sites, only minute changes in volume occurred before doping with a Li atom. However, upon Li atom doping, a significant change in shape and structure was observed in the DFT studies. No regular trend of adsorption energies with metal atoms was found. These results suggested that the metal centers, as well as volume and structural changes of the system, also influence the adsorption energy of Li, as the volume of the structure was reduced upon introduction of Li in MOFs with metals Fe, Co, Ni and Cu, but very few changes were seen for MOFs with Zn. This implies that only Zn-based MOFs are suitable for lithium doping [38]. Sourav and co-workers [39] employed periodic DFT calculations for predicting binding energies of metal (M) decorated MOF-5, where M = Li, Be, Mg and Al. They reported that the binding energy decreased as the number of H_2 molecules increased, because of increase in repulsions between H_2 molecules,

decrease in sigma donation by H₂ molecules and reduction in effective charge on metal atoms. The authors also stated that only Li and Al atoms enhanced H₂-MOF interactions, since they showed high binding energy. This is because the atomic charge on Li and Al in MOF-5:Li₂ and MOF-5:Al₂ was predicted to be +0.90 and +0.66 a.u., respectively, through DFT, as shown in Table 6.2. This means that the H₂ interacts with the metal ion and not with the neutral metal atom. These metal ions polarize nearby H₂ molecules and, therefore, H₂ adsorption takes place through a charge polarization mechanism.

Table 6.2: Calculated atomic charges of metal atom and interaction energies (ΔE) in MOF5:M₂ systems using GGA-PBE. Reproduced from ref [39] with permission.

Metal	Q(M) (a.u.) GGA-PBE	ΔE (kJ/mol) GGA-PBE
	MOF5:M ₂	MOF5:M ₂
Li	0.90	-151.48
Be	0.45	-4.72
Mg	0.26	-1.35
Al	0.66	-128.32

In another work by the same group [40], the impact of decorating the organic linker in MOF-5 with a metal ion on its H₂ adsorption capacity was studied using DFT. The authors considered MC₆H₆:nH₂ models, where M = Li⁺, Na⁺, Mg²⁺, Be²⁺ and Al³⁺. A common increasing order (Na⁺ < Li⁺ < Mg²⁺ < Be²⁺ < Al³⁺) was reported for the interaction energy of the metal ion M with the benzene ring, binding energy and charge transfer from metal to the benzene ring. H₂-MOF-5 interactions were larger in these metal ion decorated MOFs compared to their pure state. However, among these metal ions, only Mg²⁺ exhibited binding energies in magnitudes which are favorable for H₂ storage at room temperature.

6.3.1.3 Hybrid MOFs

Zeolitic imidazolate framework (ZIFs) is a subfamily of MOFs that consists of tetrahedral clusters of MN₄ (M = Co, Cu, Zn, etc.) linked to imidazolate ligands [41]. Like MOFs, they also have a tunable pore size and chemical functionality as well as they show properties of zeolites, such as exceptional chemical stability and structural diversity [42]. Due to these characteristics, ZIFs are more promising candidates for H₂ storage than MOFs. Yildirim et al. [43] considered ZIF8 for H₂ storage. ZIF8 is a ZIF compound having Zn(MeIM)₂, where MeIM is 2-methylimidazolate with SOD (sodalite), having a nanoporous topology formed by four-ring and six-ring ZnN₄ clusters, as shown in Figure 6.6. They performed DFT calculations using plane-wave implementation of the local density approximation (LDA) to DFT for total energy

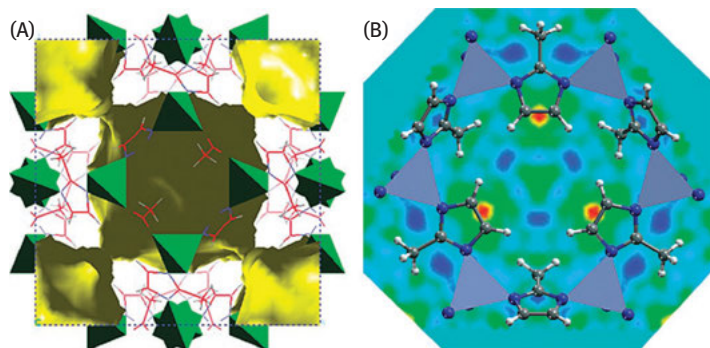


Figure 6.6: (A) (001) view of the refined crystal structure of ZIF8 host lattice from neutron powder diffraction along with the available free space (pore structure) for H_2 occupation, based on van der Waals interactions. (B) A (111) view of the real-space Fourier-difference scattering-length density superimposed with six-ring pore aperture of the ZIF8 structure, indicating the location of the first adsorption sites (red-yellow regions). Reprinted from ref [43] with permission.

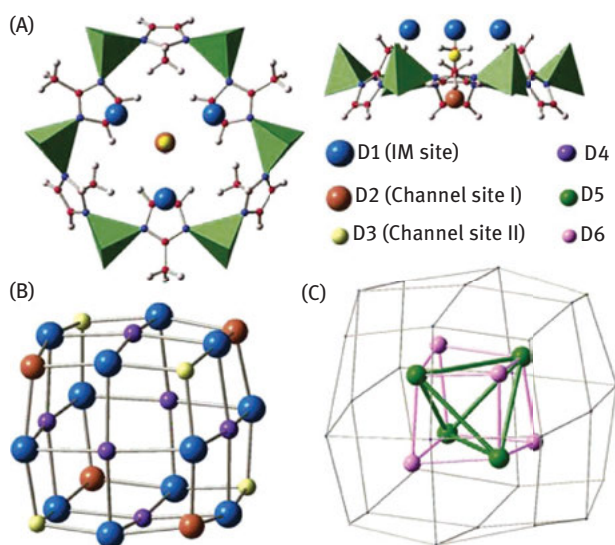


Figure 6.7: The hydrogen adsorption sites obtained from Fourier-difference analysis: (A) top and side views of first three adsorption sites near a Zn hexagon opening; (B) pseudo-cubic nanocage formed by D1, D2 and D3 sites; (C) tetrahedron-like nanocage formed by D5 and D6 sites. Reprinted from ref [43] with permission.

calculations. They found that the energetically most stable adsorption sites are IM and channel site I, as shown in Figure 6.7. The H_2 -binding energies for these two sites are 170 and 147 meV, respectively. The larger value for IM is because of its high population. These theoretical findings are in good agreement with the experimental results also.

6.3.1.4 Effect of open metal sites

In some of the MOFs, guest or solvent molecules can be removed by heating under vacuum without crumbling the framework, when they are coordinatively bound to the metal node. These MOFs are then said to possess open or coordinatively unsaturated metal sites. Lochan et al. [33] performed a combined DFT and simulation study on MOF-505 and reported that the presence of open metal sites enhances the H₂ adsorption capacity in MOFs at low pressures. They also reported that the negative lobe of the quadrupole of H₂ molecule is exposed to Cu atoms, which behave as Lewis acids.

Zhong et al. [44] performed DFT calculations using DMol³ to understand the role of open metal sites in H₂ adsorption on MOF-505. They found that, at low pressure, the open metal sites give impetus to H₂ adsorption in MOFs; on the other hand, the properties of the materials, such as free volume, play a significant role at high pressures. They also suggested that the MOF material should include the benefits of having coordinatively unsaturated sites, along with large free volume, low crystal density and suitable pore size in order to possess high adsorption capacity.

6.3.2 Methane (CH₄)

In the last few years, there has been a pronounced increase in the approachability of natural gas reserves, which has prompted research in using natural gas as a vehicle fuel [27]. Use of natural gas vehicles is aimed to reduce the dependence on petroleum and consequently reduce CO₂ emissions from combustion. Natural gas prior refining consists of 70–90 % CH₄, while the refined natural gas contains almost entirely of CH₄ [45]. It is another alternative gasoline for large-scale transportation applications. At standard temperature and pressure (STP), CH₄ has nearly thousand times less volumetric energy density than gasoline [46]. To increase the density, liquefaction and compression are commonly used, but in these approaches, the efficiency, cost and driving cost are usually compromised. An alternative way of achieving high-density storage for CH₄ is by adsorbing CH₄ on a suitable adsorbent.

Due to their high porosity, surface area and tunable properties, MOFs are suitable adsorbents for CH₄ storage. Significant research has been made in the past decade to improve CH₄ storage capacities to enable its usage as a fuel. A lot of experimental and theoretical studies have been established, out of which, some of the theoretical studies concerning DFT studies are reviewed in this chapter.

Rowell et al. [47] studied CH₄ adsorption and diffusion within alkoxy-functionalized IRMOFs. Isoreticular MOFs (IRMOFs) have the general formula Zn₄OL₃, where L is a linear aromatic dicarboxylate. They are worthy candidates for adsorption due to their large pore volumes and directional organic functionalization. The crystal structures of about 20 IRMOFs have been reported, and they are found to show high symmetry. This really simplifies the construction of computerized models for theoretical studies. For IRMOF-1 and IRMOF-4, crystal structures have been previously

reported and only their relevant structural features were discussed by the authors. They computed single-point energies of various chemically equivalent structures by DFT calculations using the B3LYP functional with a 6-31G(d,p) basis set. Further, they used these results to study the adsorption and diffusion of CH₄ by GCMC (grand canonical Monte Carlo) simulations.

Zhou and co-workers [48] reported a comprehensive study of CH₄ storage in the three MOFs compounds – (1) HKUST-1, (2) PCN-11 and (3) PCN-14. The dicopper paddlewheel secondary unit is common to the three MOFs, but they differ in their organic linkers. This gives them cage-like pores with different sizes and geometries. By using neutron powder diffraction experiments, GCMC simulations and DFT calculations, they located exact locations of CH₄ storage and orientations in these molecules. They found that for HKUST-1 and PCN-11, the DFT-optimized locations and orientations are in complete agreement with the experimental results. This inspired them to consider the results of their DFT studies on PCN-14, for which no experimental structural information of adsorbed CH₄ is available.

Chen and team [49] also performed dispersion-corrected density functional theory (DFT-D) calculations on Cu₃BHB, which they called as UTSA-20 (UTSA = University of Texas at San Antonio), and is formed by self-assembly of a hexacarboxylate organic linker H₆BHB (H₆BHB = 3,3',3'',5,5',5''-benzene-1,3,5-triylhexabenzic acid), to evaluate the static binding energies of CH₄ at the adsorption sites. In DFT-D, vdW interactions are corrected by incorporating an R^{-6} term [50].

$$E_{DFT-D} = E_{DFT} + E_{disp}$$

$$\text{where } E_{disp} = - \sum_{i=1}^{N_{at}-1} \sum_{j=i+1}^{N_{at}} \frac{C_{ij}}{R_{ij}^6} f_{damp}(R_{ij})$$

N_{at} is the number of atoms in the system

C_{ij}^{ij} is the dispersion coefficient for the atom pair ij

R_{ij} is the interatomic distance.

They reported that the binding energy values for open copper sites and linker channel sites are 21.6 and 23.5 kJ mol⁻¹, respectively, which are in agreement with the experimental Q_{st} values. These values also suggested that the CH₄ binding is stronger at the linker channel site, because the binding of CH₄ at the copper site is partly due to electrostatic interactions between the metal ion and the slightly polarized CH₄ molecule, whereas, on the linker channel site, there are van der Waal interactions between CH₄ and the framework. They also reported that the size of the pore in the linker channel site is just appropriate to enable the CH₄ molecules to simultaneously interact with the two BHB linkers.

Yildirim et al. [51] synthesized a new organic linker containing the pyrimidine group, as shown in Figure 6.8, and used it for construction of two MOFs – UTSA-76a and NOTT-101a. They then performed first-principles DFT-D calculations. As a first step, they performed structural optimization of these two MOFs and found that both have

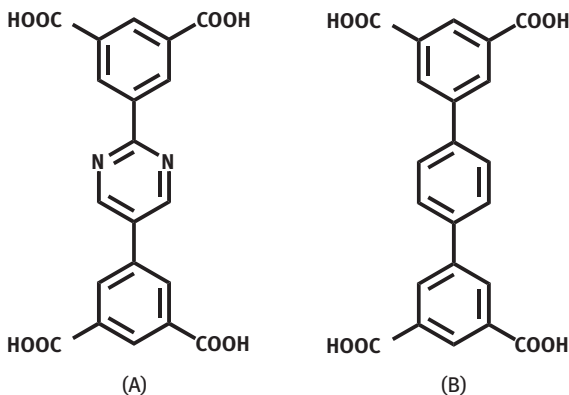


Figure 6.8: Structure of the organic ligands for the construction of (A) UTSA-76 and (B) NOTT-101.

similar static structures. After this, they introduced CH_4 molecules into the MOF structure and found that open copper sites and cage-window sites are the major adsorption sites. However, the adsorption was relatively weak on the linker surfaces. Also, the binding energies of CH_4 molecules adsorbed next to the pyrimidine sites of UTSA-76a were found to be similar to those adsorbed on the central phenyl ring of NOTT-101a.

Siegal and co-workers [52] studied the effect of coordinatively unsaturated metal sites and deep-well pocket sites and referred to them as “enhanced binding sites.” It had been earlier reported that binding at coordinatively unsaturated metal sites is stronger due to coulombic interactions, while at pocket sites, the adsorption emerges from enhanced vdW interactions [53]. They examined 18 metal-substituted variants of M-DOBDC ($M = \text{Metal Organic Framework}$, DOBC = 2,5-oxidobenzene-1,4-dicarboxylate) with $M = \text{Be, Mg, Ca, Sr, Sc, Ti, V, Cr, Mn, Fe, Co, Ni, Zn, Mo, W, Sn}$ and Pb and employed a combination of vdW-augmented DFT (vdW-DFT) and semi-empirical GCMC simulations for studying thermodynamics and CH_4 uptake capacities in the M-DOBDC series. They included the semi-empirical DFT-D2 and vdW-DF method with five different functionals- revPBE (vdW-DF1) [54], optB86b [55], optB88 [56], optPBE [56] and rPW86 (vdW-DF2) [57]. They found that the best agreement with experimental results is obtained with the vdW-DF2 functional and the values obtained are reported in Table 6.3.

Another group, Zhou et al. [53], also investigated the effect of open metal sites on CH_4 adsorption. They studied $\text{M}_2(\text{dhtp})$ compounds, where the open metal $M = \text{Mg, Mn, Co, Ni, Zn}$ and dhtp is 2,5-dihydroxyterephthalate. Since the weak dispersive interactions are not properly accounted in standard DFT, they focused on the results obtained from the LDA. A fair agreement was found between the DFT-LDA-optimized structure of $\text{Mg}_2(\text{dhtp})$ and the structure adsorbed with CH_4 and the experimental data. The binding strengths and the calculated metal-carbon distances are tabulated in Table 6.4, along with the experimental data.

Table 6.3: Calculated and experimental adsorption enthalpies (kJ/mol) from vdW-DF2 for the M-DOBDC^c series. Reprinted with permission from ref [52].

	Be	Mg	Ca	Sr	Sc	Ti	V	Cr	Mn	Fe	Co	Ni	Cu	Zn	Mo	W	Sn	Pb
Calc	18.1	26.3	25.8	26.2	27.1	33.3	29.7	16.4	22.5	19.9	26.0	25.3	22.3	25.4	26.4	22.8	32.0	20.9
Expt		21.2							21.8		22.3	22.9		21.0				

^aExperimental data are taken from refs [53] and [115].

Table 6.4: Summary of data obtained for $M_2(\text{dhtp})^{\text{a,b}}$. Reproduced from ref [53] with permission.

MOF compound	Open M	ρ (g/cm ³)	Maximum CH ₄ ads on open M [cm ³ (STP)/cm ³]	exp CH ₄ ads [cm ³ (STP)/cm ³]	Initial Q_{st} (kJ/mol)	d(M-C) (Å)	E_B (kJ/mol)
Mg ₂ (dhtp)	Mg	0.909	168	149	18.5	2.64	33.8
Mn ₂ (dhtp)	Mn	1.084	160	158	19.1	2.73	29.8
Co ₂ (dhtp)	Co	1.169	168	174	19.6	2.74	29.7
Ni ₂ (dhtp)	Ni	1.206	174	190	20.2	2.58	34.8
Zn ₂ (dhtp)	Zn	1.231	170	171	18.3	2.72	29.7
PCN-11	Cu	0.749	70	170	14.6	2.62	24.7
MOF-5 ^c	(Zn)	0.593	(69)	110	12.2	(3.69)	(20.7)

^aData include the open metal species, crystal density (ρ), the ideal saturated CH₄ adsorption capacity on open metals (max CH₄ ads on open M), experimental excess CH₄ adsorption capacity at 298 K, 35 bar (exp CH₄ ads), the experimental initial isosteric heat of adsorption (Q_{st}) for CH₄, the calculated metal-C distance (d , from LDA), and the calculated static binding energy of CH₄ on the open metal (E_B , also from LDA).

^bAvailable experimental data for PCN-11 and MOF-5 (adopted from refs [116], and [117], respectively) are also shown for comparison purposes. The metal ion in MOF-5 is fully coordinated (not open metal); thus the corresponding values are shown in parentheses.

In Figure 6.9, the partial structures of DFT-optimized PCN-11 and MOF-5 with adsorbed CH₄ are shown. The calculated CH₄-binding energy on the copper site in PCN-11 is smaller than those on $M_2(\text{dhtp})$, which is compatible with the relatively low initial Q_{st} of PCN-11 (14.6 kJ mol⁻¹) compared to that of $M_2(\text{dhtp})$ (>18 kJ mol⁻¹) obtained experimentally. For PCN-14, exceedingly high initial Q_{st} (30 kJ mol⁻¹) indicates that some other CH₄-binding sites also exist. MOF-5 has the lowest binding energy, which is again in agreement with its lowest experimental Q_{st} .

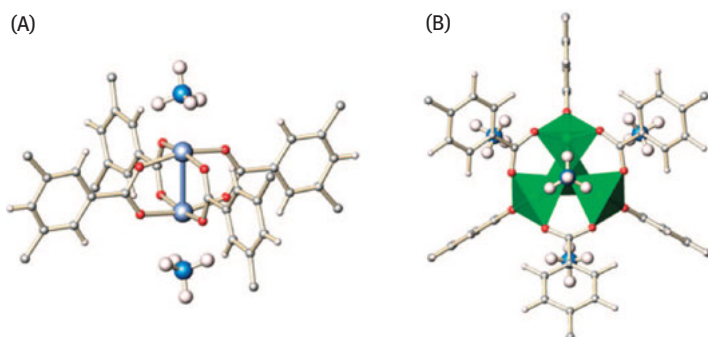


Figure 6.9: (A) Partial structure of the DFT-optimized PCN-11 crystal with CH₄ molecules adsorbed on the open Cu metal sites. (B) Partial structure of the DFT-optimized MOF-5 crystal with CH₄ molecules adsorbed on the “cup” sites of the $\text{OZn}_4(\text{CO}_2)_6$ cluster. Reprinted from ref [53] with permission.

6.3.3 Acetylene (C₂H₂)

C₂H₂ is one of the major components of organic chemistry. It is an unstable and highly reactive hydrocarbon. Other products, such as benzene and vinylacetylene, are formed when sufficiently high concentration of C₂H₂ is present. Moreover, these reactions are exothermic, which makes it risky to store C₂H₂ in vessels at a pressure greater than 2 atm because of fear of explosion [58]. Hence, recently many porous, high surface-area sorbents for storing C₂H₂ at low pressures are being studied.

Many groups considered MOFs with small pores for increasing C₂H₂ adsorption enthalpies, but this limited their uptake capacities. The highest uptake capacity ever reported was 106 cm³/g [59–67]. Xiang et al. [68] made use of the open metal sites of HKUST-1 for evaluating interactions with C₂H₂ molecules and reported C₂H₂ uptake up to 201 cm³/g at 295 K and 1 atm. They further investigated the binding properties of open Cu²⁺ sites by first-principles calculations based on DFT. They used both the LDAs and generalized gradient approximations (GGA) and the binding energies of C₂H₂ molecules were obtained by first introducing the C₂H₂ molecule at the various adsorption sites, followed by structural relaxation. They elucidated that the open Cu²⁺ site and cage-window site are the most energetically favorable sites for C₂H₂ adsorption in HKUST-1 (Table 6.5) which is in agreement with experimental observations from neutron powder diffraction.

Table 6.5: Binding energies (kJ/mol) obtained with LDA and GGA approximations for the two sites.

Site name	Binding energies (kJ/mol)	
	LDA	GGA
Open Cu ²⁺	44.8	15.8
Cage window	29.2	9.3

As per expectations, GGA underestimates the binding strength, whereas LDA overestimates it. Therefore, the calculated binding strength matches well with the experimentally reported results, which state that the open Cu²⁺ site interacts with C₂H₂ molecules with greater strength and is therefore populated first. The interactions of C₂H₂ with the framework at the cage-window site are typically vdW in nature, while at the open Cu²⁺ site, the interactions are coulombic in nature.

6.4 Capture and separation of the carbon dioxide (CO₂) gas in MOFs

With an increase in global population and industrialization, energy consumption is shooting up. At present, most of the energy demand of the world is fulfilled by

burning fossil. The combustion of fossil fuels, such as natural gas, coal and petroleum has produced an enormous amount of the greenhouse gas (GHG) CO₂ [69]. This increased concentration of CO₂ in the environment has led to adverse effects, such as air pollution and global warming [70]. Increased concentration of CO₂ disturbs the balance of incoming and outgoing energy from the earth's atmosphere, which leads to a rise in the average surface temperature of the earth. Thus, CO₂ has often been cited as a primary anthropogenic GHG.

Coal-fired power plants generate about one-third of the CO₂ released to the atmosphere [71]. Gases in the combustion exhaust (flue gas) from fossil fuel-fired power plants have 15 to 16 % CO₂ by volume at ambient conditions [72, 73]. The low partial pressures and high flow rate make it a tremendous challenge to capture and seize CO₂ from the exhaust streams of fossil fuel combustion to reduce GHG emission [74]. Adsorption processes are a suitable solution owing to their low-energy requirements, cost-effectiveness and satisfactory results, which have triggered recent research in finding suitable adsorbents for separating CO₂ from flue gas [75].

The necessity for material that can be used for CO₂ capture in fossil fuel-fired power plants has elicited study of several classes of material. A material must possess the following traits in order to be a successful adsorbent: (1) High selectivity for CO₂. This is required so that the CO₂ component of the flue gas is completely removed. (2) The affinity of the material towards CO₂. If the interaction of the material with CO₂ is very strong, then high energy will be required to cause desorption, whereas weak interactions between the material and CO₂ would mean lower selectivity. (3) The material should be highly stable under the conditions of capture and regeneration. (4) The material should adsorb CO₂ at high density so that volume of the adsorbent can be minimized.

The main existing materials in context with these above-mentioned qualities used for CO₂ capture are discussed below:

Aqueous Alkanolamine Adsorbents: Aqueous alkanolamine solutions have been vastly studied for CO₂ capture. The mechanism of CO₂ adsorption in the case of alkanolamines is chemisorptive, and the enthalpy of adsorption is in the range of 50 to 100 kJ/mol at 298 K [76]. Commonly used alkanolamines are monoethanolamine alone or in mixtures with secondary or tertiary alkanolamines, such as diethanolamine and triethanolamine [77], 2-amino-2-methyl-1-propanol (AMP) and N-methyl-diethanolamine. Recently, some new amine-type solvents, piperazine [78] and imidazolium-based ionic liquids [79], have gained attention. They exhibit enhanced absorption properties with higher chemical and thermal stability, but aqueous alkanolamine solutions have several disadvantages as adsorbents for large-scale CO₂ adsorption. First of all, the solutions are relatively unstable towards heating, which limits the temperatures required for regenerating the captured material. The lifetime of the solutions is not much, because amines decompose with time, which decreases the adsorption capacities. The amine solutions also corrode the vessels in which they are contained; this is prevented by limiting the concentration of the alkanolamine species to below 40 wt%.

Zeolites: These are porous aluminosilicate materials that show high chemical and thermal stability. They have been studied extensively for CO₂ capture from post-combustion flue gas [80–83]. For example, zeolite 13X, which has a large surface area ($SA_{\text{BET}} = 726 \text{ m}^2/\text{g}$) and micropore volume ($0.25 \text{ cm}^3/\text{g}$), exhibits good capacities for CO₂ adsorption at room temperature (16.4 wt% at 0.8 bar and 298 K) [84, 85]. However, many of the zeolites become easily saturated with the water vapor present in the flue gas stream, which diminishes the CO₂ adsorption capacity [86, 87].

Activated Carbon: These materials are amorphous porous forms of carbon prepared by pyrolysis of carbon containing resins, fly ash or biomass [88]. They are implemented for CO₂ capture in high-pressure flue gas. It has been reported in one study that the upper limit for the CO₂ adsorption capacity within activated carbon materials is approximately 10–11 wt% under post-combustion CO₂ capture conditions and 60–70 wt% under pre-combustion CO₂ capture conditions [89]. Although their hydrophobic nature reduces the effect of water, and therefore they do not undergo any decomposition or show decreased adsorption capacities in the presence of water [90], the surfaces of activated carbons have relatively uniform electrical potential, which leads to a lower enthalpy of adsorption for CO₂, and hence lower capacities for CO₂ as compared with zeolites at lower pressures.

As we have seen, none of the materials fulfill all of the criteria which were mentioned above, and hence there is an urgent need for new materials to emerge that upgrade the characteristics of these materials. In this regard, MOFs have an edge over other materials.

Metal-Organic Frameworks: The expansive surface areas [91] and tunable pore properties [92–94] have made these materials worthy candidates for adsorption studies. For CO₂ capture applications, the materials must possess high mechanical strengths to enable dense packing of the adsorbent bed without any deterioration of the network structure. For temperature swing adsorption processes (in which regeneration of the adsorbent is attained by a temperature increase), small heat capacity of the adsorbent is an important parameter, and the solid porous adsorbents are known to have lower heat capacities [95]. Thus, large CO₂ adsorption capacities can be achieved by using MOFs. For example, at 35 bar pressure, the volumetric CO₂ adsorption capacity for MOF-177 reaches a storage density of $320 \text{ cm}^3 \text{ (STP)}/\text{cm}^3$ which is higher than the adsorption capacities of conventional materials used, namely, zeolite 13X and MAXSORB [96].

6.4.1 Computational modeling for CO₂ capture

Kawakami and co-workers [97] made the first attempts to simulate CO₂ adsorption on MOFs. They studied the influence of framework changes, and the adsorption amount found by their simulations was three times greater than the experimental result. They

ascribed this discrepancy to the unsaturated adsorption in the experiment because of irregular stacking of the crystal cells.

6.4.1.1 Effects of CUM and metal doping on CO₂ adsorption

DFT studies can provide an insight into the influence of different structural properties of MOFs on CO₂ adsorption. These correlations are beneficial in predicting the CO₂ uptake capacity and for the rational design of MOFs for enhancing CO₂ adsorption capacities. MOFs containing a high degree of CUMs, like M-MOF-74, HKUST-1, UMCM-150 and UMCM-150(N)₂, are the best adsorbents for CO₂ [98, 99]. Hou and co-workers [100] used a combination of DFT and GCMC to study the significance of CUMs in M-MOCF-74 (M = Mg and Zn) in CO₂ adsorption. They established that the strong Lewis acid and base interactions between metal ions and oxygen atoms of CO₂, as well as between the carbon atom of CO₂ and the oxygen atoms in organic linkers, are responsible for the high CO₂ adsorption capacities of M-MOF-74. Nachtigall et al. [101] studied CO₂ adsorption on HKUST-1 at various coverages using the DFT/CC method. They found that the adsorption sites are heterogeneous and CUMs are the most favorable sites for CO₂ adsorption. Ha and co-workers [102] elucidated the effect of alkali-metal (Li, Na, K) doping in MOF-5s on CO₂ adsorption. They reported that doping can increase the CO₂ adsorption capacity, owing to the strong interactions between CO₂ and the metals. The largest increase in adsorption capacity was shown by Li doping.

6.4.1.2 CO₂ adsorption in MILs and ZIFs

Matériaux Institut Lavoisier (MILs) display an unusual structural transformation, known as “breathing,” caused by interactions with guest molecules or temperature and pressure stimuli. Maurin et al. [103] studied CO₂ adsorption on a hybrid MOF of MIL-53(Al). It has two structural forms – MIL-53np (Al) and MIL-53lp (Al) (np is narrow pore and lp is large pore) – which have the same chemical composition, but different pore widths. They used DFT calculations to derive the charges of the adsorbent frameworks. In another work, Maurin and co-workers [104] performed DFT calculations to find the CO₂ adsorption geometries in the MIL-53(Al,Cr) and MIL-47 frameworks. Bell et al. [105] performed DFT calculations in MIL-53(Al) to evaluate the effect of various functional groups – –OH, –COOH, –NH₂ and –CH₃ on CO₂ adsorption. The binding energies for each were calculated using DFT calculations. They reported that, for COOH-MIL-53(lp), the adsorption site geometry of CO₂ is the same as that observed in the cluster calculations, with a similar hydrogen bond length (2 Å) between the oxygen atom of CO₂ and the hydrogen atom of –COOH. The additional interactions present from C=O groups of neighboring ligands enhance the lone pair polarization of the CO₂ electron density. This indicates the effect of the specific pore size of MIL-53(lp) and the resulting geometry. Similar cooperative effects were also observed in NH₂, (OH)₂ and (CH₃)₂-MIL-53(lp), as shown in Figure 6.10.

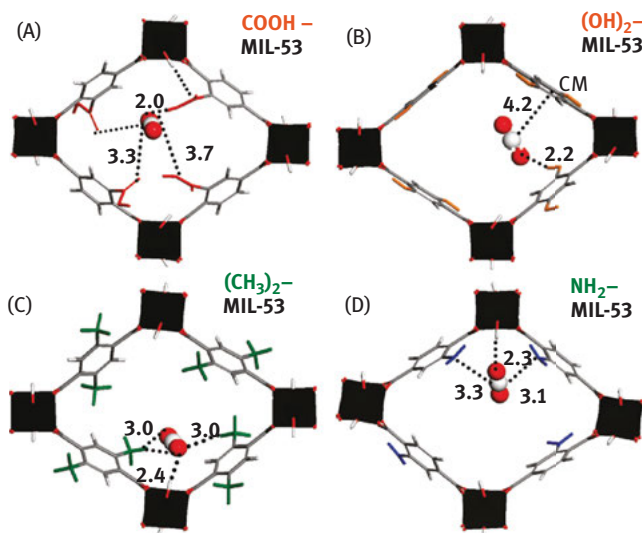


Figure 6.10: Most stable adsorption site for CO₂ in substituted 1p forms of MIL-53(Al_{3p}), calculated by DFT at 0 K: (A) COOH⁻; (B) (OH)₂⁻; (C) (CH₃)₂⁻; (d) NH₂⁻. Distances are reported in Å. Reprinted from ref [105] with permission.

Soujanya and co-workers [106] investigated the influence of substitution of -CH₃, -Cl, -CN, -OH, -NH₂ and -NO₂ functional groups at the C2, C4 and C5 positions of the imidazolate (Im) linkers of ZIFs using DFT calculations. They reported that the CO₂ adsorption is influenced by both the nature and position of the functional group. The asymmetrical substitution of Im linkers with NO₂/OH, CN/OH and Cl/OH combinations leads to very favorable linkers of ZIFs for CO₂ adsorption.

6.4.2 CO₂ separation in MOFs

The most vital parameter in CO₂ separation is the selectivity. Selectivity can be predicted by classical DFT studies for mixtures [107]. In classical DFT, the thermodynamic grand potential of an inhomogeneous fluid is expressed as a function of the molecular density. The equilibrium density profile is obtained by minimizing this functional. The grand potential is expressed as a sum of the Helmholtz-free energy and the contributions of the bulk chemical potential and the external potential which cause the inhomogeneity. For mixtures, the grand potential is taken as a functional of the density of each of the components. The selectivities are easily calculated by estimating the adsorption isotherms for individual components at equilibrium. Jiang et al. [108] applied DFT to CO₂/CH₄ and CO₂/N₂ mixtures in ZIF-8 and Zn₂(BDC)₂(ted). The excess free energy was broken into repulsive and attractive terms, which were dealt with by weighted density approximations. A good agreement was found between the theoretical results and GCMC simulations.

It was inferred that the two MOFs have similar separation capacities, even though the adsorption in $\text{Zn}_2(\text{BDC})_2(\text{ted})$ is stronger than that in ZIF-8.

6.4.2.1 Specific MOF design to enhance selectivity

The feasibility of specific designs improving the selectivity is one of the main benefits of MOFs. Doping of MOFs with alkali metals is known to enhance the adsorptive selectivity of CO_2 - CH_4 mixtures [109]. Combined GCMC and DFT simulations demonstrated the importance of the electrostatic terms in accounting for the adsorbent-metal interactions. The low first ionization potential of the added alkali metals and longer distances to the aromatic rings of the linkers enhance the electrostatic interactions and steric effects. These further boost the selectivity for CO_2 adsorption. Another group, Zhong et al. [110], studied a Li-modified MOF-5, named chem-4Li MOF, in which all of the hydrogen atoms were substituted by O-Li groups. A combination of DFT and GCMC simulations showed that the strength and gradient of the electrostatic potential in the pores are modified by Li doping. Therefore, there is a change in the preferential adsorption sites of the mixture components, which causes molecular level segregation in the aromatic rings of MOF-5. In another study done on MIL-53, the effects of ligand functionalization (tested with -OH, -COOH, - NH_2 , and - CH_3 functional groups) on gas separation from the mixture were studied [105]. The investigation was conducted using three methods: DFT in small clusters to assess CO_2 adsorption in the hybrid framework, periodic DFT and GCMC simulations. Good consistency was obtained from this set of techniques. Small polar groups such as $(\text{OH})_2$ -MIL-53(lp) and $(\text{COOH})_2$ -MIL53(lp) were found to be the most advantageous additions to MIL-53 for achieving CO_2 adsorption and selectivity enhancement in CO_2/CH_4 mixtures. Maurin et al. [111] recently reported a DFT and GCMC study of CO_2 adsorption and selectivity in MIL102 consisting of small one-dimensional channels. Their models contain two terminal water molecules, which would be removed at temperatures above 500 K, and they are reported to be the preferential sites for CO_2 adsorption. This highlights the importance of considering the structural water in the simulation analysis.

6.4.2.2 Effects of linkers on selectivity

Jiang et al. [112] studied the role of linkers for separating nonpolar and polar binary mixtures in the very hydrophobic $\text{Zn}(\text{BDC})(\text{TED})_{0.5}(\text{BDC})$. Their experimental and theoretical study emphasized the mechanical differences in the segregation properties of polar versus nonpolar mixtures in these MOFs. DFT and GCMC simulations showed good accord with experiment for the CO_2 - CH_4 mixture. At low pressure, CO_2 is preferentially adsorbed near the BDC linkers, and at higher pressures, it is adsorbed at the oxide and TED linkers as well as to the small windows, where the adsorbed CO_2 - CO_2 cooperative interactions enhance the adsorption. The role of functional groups in organic linkers has

also been studied [113]. It has been reported that the presence of electron-donating groups in the linkers leads to a distribution of the electrostatic field that elevates the CO₂ selectivity, although the introduction of multiple substituents may produce negative steric effects. These effects were tested by introducing four types of functional groups (-CH₃, -F, -OH and -NH₂) into the organic linker in MOF-5 for the mixtures of CO₂/CH₄. Enhancements of gas mixture separations by the electrostatic field were also reported by Yang et al. [114], who conducted a computational study to examine binary and ternary mixtures containing CO₂, CH₄ and C₂H₆ in HKUST-1. The separation of mixtures having very unlike electrostatic interactions with the framework sites was strengthened by the development of ordered microdomains with various electrostatic field strengths.

6.5 Conclusions

MOFs are better adsorbents than other available porous materials, due to their high surface areas, adjustable pore sizes and a vast range of modifications possible in their structure. The incorporation of organic ligands has enabled rational design and functionalization of the structure. This further allows us to tune the properties of the MOFs as per our requirements, depending upon the adsorbate. Furthermore, chiral MOFs can be utilized for enantioselective separations, whereas the conventional adsorbents like zeolites do not possess this quality due to the difficulty in synthesis of chiral zeolites. Also, since MOFs consist of a polar part (metal ion) and a nonpolar part (organic ligands) as well, both polar and nonpolar adsorbates can be adsorbed on their surfaces.

DFT studies of MOFs have been performed to evaluate molecular adsorption, stability and diffusion in MOFs. DFT studies will play an increasingly vital role, because as the number of newly reported structures increases, it will be cumbersome to experimentally evaluate the performance of all the materials in the laboratory. Above all, classical and quantum chemistry approaches provide us with mechanistic insights into water diffusion and reaction events that are beyond the reach of experimentalists. The evaluation of thousands of adsorption configurations in periodic structures with complex calculations using MP2 or coupled cluster calculations is not feasible. However, this can be achieved using DFT. Moreover, working experimentally with some systems such as H₂ gas and C₂H₂ gas is both difficult and dangerous. For such systems, performing theoretical studies first on various MOFs and then limiting the options on the basis of these results for experimental studies can be very helpful. Furthermore, exploring the possibilities with DFT is in a way a greener approach, as no chemicals are actually used in this study and also, the results are reliable and can guide us further for performing the experimental studies.

References

- [1] James SL. Metal-organic frameworks. *Chem Soc Rev.* 2003;32:276–88.
- [2] Zhou H-C, Long JR, Yaghi OM. Introduction to metal-organic frameworks. *Chem Rev.* 2012;112:673–4.
- [3] Long JR, Yaghi OM. The pervasive chemistry of metal-organic frameworks. *Chem Soc Rev.* 2009;38:1213–4.
- [4] Czaja AU, Trukhan N, Müller U. Industrial applications of metal-organic frameworks. *Chem Soc Rev.* 2009;38:1284–93.
- [5] Rowsell JLC, Yaghi OM. Metal-organic frameworks: a new class of porous materials. *Microporous Mesoporous Mater.* 2004;73:3–14.
- [6] Kitagawa S, Kitaura R, Noro S. Functional porous coordination polymers. *Angew Chem Int Ed.* 2004;43:2334.
- [7] Kakkar R, Kapoor PN. Theoretical study of the adsorption of formaldehyde on magnesium oxide nanosurfaces:- Size effects and the role of low-coordinated and defect sites. *J Phys Chem B.* 2004;108:18140–8.
- [8] Kakkar R, Kapoor PN, Klabunde KJ. First principles density functional study of the adsorption and dissociation of carbonyl compounds on magnesium oxide nanosurfaces. *J Phys Chem B.* 2006;110:25941–9.
- [9] Sharma L, Kakkar R. Hierarchical porous magnesium oxide (Hr-MgO) microspheres for adsorption of an organophosphate pesticide: kinetics, isotherm, thermodynamics, and DFT studies. *ACS Appl Mater Interfaces.* 2017;9:38629–42.
- [10] Li J-R, Kuppler RJ, Zhou H-C. Selective gas adsorption and separation in metal-organic frameworks. *Chem Soc Rev.* 2009;38:1477–504.
- [11] Hohenberg P, Kohn W. Inhomogeneous electron gas. *Phys Rev.* 1964;136:B864.
- [12] Kohn W, Sham LJ. Self-consistent equations including exchange and correlation effects. *Phys Rev.* 1965;140:A1133.
- [13] Yang Q, Liu D, Zhong C, Li J-R. Development and computational methodologies for metal-organic frameworks and their application in gas separations. *Chem Rev.* 2013;113:8261–323.
- [14] Lin L-C, Lee K, Gagliardi L, Neaton JB, Smit B. Force-field development from electronic structure calculations with periodic boundary conditions: applications to gaseous adsorption and transport in metal-organic frameworks. *J Chem Theory Comput.* 2014;10:1477–88.
- [15] Mercado R, Vlasisavljević B, Lin L-C, et al. Force field development from periodic density functional theory calculations for gas separation applications using metal-organic frameworks. *J Chem Phys C.* 2016;120:12590–604.
- [16] Watanabe T, Manz TA, Sholl DS. Accurate treatment of electrostatics during molecular adsorption in nanoporous crystals without assigning point charges to framework atoms. *J Phys Chem C.* 2011;115:4824–36.
- [17] Sirjoosingh A, Alavi S, Woo TK. Grand-canonical monte carlo and molecular-dynamics simulations of carbon-dioxide and carbon-monoxide adsorption in zeolitic imidazolate framework materials. *J Phys Chem C.* 2010;114:2171–8.
- [18] Liu D, Zheng C, Yang Q, Zhong C. Understanding the adsorption and diffusion of carbon dioxide in zeolitic imidazolate frameworks: a molecular simulation study. *J Phys Chem C.* 2009;113:5004–9.
- [19] Philips JJ, Hudspeth MA, Browne PM, Peralta JE. Basis set dependence of atomic spin populations. *Chem Phys Lett.* 2010;495:146–50.
- [20] Ribeiro AM, Sauer TP, Grande CA, Moreira RF, Loureiro JM, Rodrigues AE. Adsorption equilibrium and kinetics of water vapor on different adsorbents. *Ind Eng Chem Res.* 2008;47:7019–26.

- [21] Kanchanalai P, Lively RP, Realff M, Kawajiri Y. Cost and energy savings using an optimal design of reverse osmosis membrane pretreatment for dilute bioethanol purification. *Ind Eng Chem Res.* 2013;52:11132–41.
- [22] Burtch NC, Jasuja H, Walton KS. Water stability and adsorption in metal–organic frameworks. *Chem Rev.* 2014;114:10575–612.
- [23] Watanabe T, Sholl DS. Molecular chemisorption on open metal sites in Cu_3 (benzenetricarboxylate)₂: A spatially periodic density functional theory study. *J Chem Phys.* 2010;133:094509.
- [24] Zang J, Nair S, Sholl DS. Prediction of water adsorption in copper-based metal-organic frameworks using force fields derived from dispersion-corrected DFT calculations. *J Phys Chem C.* 2013;117:7519–25.
- [25] Nijem N, Canepa P, Kaipa U, et al. Water cluster confinement and methane adsorption in the hydrophobic cavities of a fluorinated metal-organic framework. *J Am Chem Soc.* 2013;135:12615–26.
- [26] Semelsberger TA, Borup RL, Greene HL. Dimethyl ether (DME) as an alternative fuel. *J Power Sources.* 2006;156:497–511.
- [27] Burchell T, Roggers M. Low pressure storage of natural gas for vehicular applications. SAE technical paper, 2000, 2000-01-2205.
- [28] Schlapbach L. Züttel. Hydrogen-storage materials for mobile applications. *Nature.* 2001;414:353–8.
- [29] Suh MP, Park HJ, Prasad TK, Lim D-W. Hydrogen storage in metal-organic frameworks. *Chem Soc Rev.* 2009;38:1294–314.
- [30] Sumida K, Stück D, Mino L, et al. Impact of metal and anion substitution on the hydrogen storage properties of M-BTT metal-organic frameworks. *J Am Chem Soc.* 2013;135:1083–91.
- [31] Kaye SS, Dailly A, Yaghi OM, Long JR. Impact of preparation and handling on the hydrogen storage properties of $\text{Zn}_4\text{O}(1,4\text{-benzenedicarboxylate})_3$ (MOF-5). *J Am Chem Soc.* 2007;129:14176–7.
- [32] Wong-Foy AG, Matzger AJ, Yaghi OM. Exceptional H_2 saturation uptake in microporous metal-organic frameworks. *J Am Chem Soc.* 2006;128:3494–5.
- [33] Lochan RC, Head-Gordon M. Computational studies of molecular hydrogen binding affinities: the role of dispersion forces, electrostatics, and orbital interactions. *Phys Chem Chem Phys.* 2006;8:1357–70.
- [34] Barbatti M, Jalbert G. The effects of the presence of an alkaline atomic cation in a molecular hydrogen environment. *J Chem Phys.* 2001;114:2213.
- [35] Han SS, Goddard III WA. Lithium-doped metal-organic frameworks for reversible H_2 storage at ambient temperature. *J Am Chem Soc.* 2007;129:8422–3.
- [36] Klontzas E, Mavrandonakis A, Tylianakis E, Froudakis GE. Improving hydrogen capacity of MOF by functionalization of the organic linker with lithium atoms. *Nano Lett.* 2008;8:1572–6.
- [37] Dalach P, Frost H, Snurr RQ, Ellis DE. Enhanced hydrogen uptake and the electronic structure of lithium doped metal-organic frameworks. *J Phys Chem C.* 2008;112:9278–84.
- [38] Venkataramanan NS, Sahara R, Mizuseki H, Kawazoe Y. Probing the structure, stability and hydrogen adsorption of lithium functionalized isorecticular MOF-5 (Fe, Cu, Co, Ni and Zn) by density functional theory. *Int J Mol Sci.* 2009;10:1601–8.
- [39] Dixit M, Maark TA, Pal S. Ab initio and periodic DFT investigation of hydrogen storage on light metal-decorated MOF-5. *Int J Hydrogen Energy.* 2011;36:10816–27.
- [40] Maark TA, Pal S. A model study of effect of $\text{M} = \text{Li}^+, \text{Na}^+, \text{Be}^{2+}, \text{Mg}^{2+}$, and Al^{3+} ion decoration on hydrogen adsorption of metal-organic framework-5. *Int J Hydrogen Energy.* 2010;35:12846–57.

- [41] Huang X-C, Lin -Y-Y, Zhang J-P, Chen X-M. Ligand-directed strategy for zeolite-type metal-organic frameworks: zinc(II) imidazolates with unusual zeolitic topologies. *Angew Chem, Int Ed.* 2006;45:1557–9.
- [42] Park KS, Ni Z, Cote AP, et al. Exceptional chemical and thermal stability of zeolitic imidazolate frameworks. *Pnas.* 2006;103:10186–91.
- [43] Wu H, Zhou W, Yildirim T. Hydrogen storage in a prototypical zeolitic imidazolate framework-8. *J Am Chem Soc.* 2007;129:5314–5.
- [44] Yang Q, Zhong C. Understanding hydrogen adsorption in metal-organic frameworks with open metal sites: a computational study. *J Phys Chem B.* 2006;110:655–8.
- [45] NaturalGas.org. Available at: <http://www.naturalgas.org/overview/background.asp>. Accessed: June 2013.
- [46] IOR Energy. Available at: <http://web.archive.org/web/20100825042309/>, <http://www.ior.com.au/ecflist.html>. Accessed June 2013.
- [47] Jhon YH, Cho M, Jeon HR, et al. Simulations of methane adsorption and diffusion with alkoxy-functionalized IRMOFs exhibiting severely disordered crystal structures. *J Phys Chem C.* 2007;111:16618–25.
- [48] Wu H, Simmons JM, Liu Y, et al. Metal-organic frameworks with exceptionally high methane uptake: where and how is methane stored? *Chem Eur J.* 2010;16:5205–14.
- [49] Gou Z, Wu H, Srinivas G, et al. A metal-organic framework with optimized open metal sites and pore spaces for high methane storage at room temperature. *Angew Chem Int Ed.* 2011;50:3178–81.
- [50] Chai J-D, Head-Gordon M. Long-range corrected hybrid density functional with damped atom-atom dispersion corrections. *Phys Chem Phys Chem.* 2008;10:6615–20.
- [51] Li B, Wen H-M, Wanh H, et al. A porous metal-organic framework with dynamic pyrimidine groups exhibiting record high methane storage working capacity. *J Am Chem Soc.* 2014;136:6207–10.
- [52] Rana MK, Koh HS, Zuberi H, Siegel DJ. Methane storage in metal-substituted metal-organic frameworks: thermodynamics, usable capacity, and the impact of enhanced binding sites. *J Phys Chem C.* 2014;118:2929–42.
- [53] Wu H, Zhou W, Yildirim T. High-capacity methane storage in metal-organic frameworks M_2 (dhpt): the important role of open metal sites. *J Am Chem Soc.* 2009;131:4995–5000.
- [54] Dion M, Rydberg H, Schröder E, Langreth DC, Lundqvist BI. Van der Waals density functional for general geometries. *Phys Rev Lett.* 2004;92:246401.
- [55] Klimeš J, Bowler DR, Michaelides A. Van der Waals density functional applied to solids. *Phys Rev B.* 2011;83:195131.
- [56] Klimeš J, Bowler DR, Michaelides A. Chemical accuracy for the van der Waals density functional. *J Phys: Condens Matter.* 2010;22:022201.
- [57] Lee K, Murray ED, Kong L, Lundqvist BI, Langreth DC. Higher-accuracy van der Waals density functional. *Phys Rev B.* 2010;82:081101.
- [58] Getman RB, Bae Y-S, Wilmer CE, Snurr RQ. Review and analysis of molecular simulations of methane, hydrogen, and acetylene storage in metal-organic frameworks. *Chem Rev.* 2012;112:703–23.
- [59] Reid CR, Thomas M. Adsorption kinetics and size exclusion properties of probe molecules for the selective porosity in a carbon molecular sieve used for air separation. *J Phys Chem B.* 2001;105:10619–29.
- [60] Matsuda R, Kitaura R, Kitagawa S, et al. Highly controlled acetylene accommodation in a metal-organic microporous material. *Nature.* 2005;436:238–41.
- [61] Thallapally PK, Dobrzańska L, Gingrich TR, Wirsing TB, Barbour LJ, Atwood JL. Acetylene absorption and binding in a nanoporous crystal lattice. *Angew Chem, Int Ed.* 2006;45:6506–9.

- [62] Samsonenko DG, Kim H, Sun Y, Kim G-H, H-S L, Kim K. Microporous magnesium and manganese formats for acetylene storage and separation. *Chem Asian J.* 2007;2:484–8.
- [63] Tanaka D, Higuchi M, Horike S, Matsuda R, Kinoshita Y, Yanai N, et al. Storage and sorption properties of acetylene in jungle-gym-like open frameworks. *Chem Asian J.* 2008;3:1343–9.
- [64] J-P Z, Kitagawa S. Supramolecular isomerism, framework flexibility, unsaturated metal center, and porous property of Ag(I)/Cu(I) 3,3',5,5'-tetramethyl-4,4'-bipyrazolate. *J Am Chem Soc.* 2008;130:907–17.
- [65] Zhang C, Lan Y, Gou X, Yang Q, Zhong C. Materials genomics-guided ab initio screening of MOFs with open copper sites for acetylene storage. *AIChE J.* 2018;64:1389–98.
- [66] Hu Y, Xiang S, Zhang W, et al. A new MOF-505 analog exhibiting high acetylene storage. *Chem Commun.* 2009;0:7551–3.
- [67] Zhang JP, Chen X-M. Optimized acetylene/carbon dioxide sorption in a dynamic porous crystal. *J Am Chem Soc.* 2009;131:5516–21.
- [68] Xiang S, Zhou W, Gallegos JM, Liu Y, Chen B. Exceptionally high acetylene uptake in a microporous metal-organic framework with open metal sites. *J Am Chem Soc.* 2009;131:12415–9.
- [69] Royer DL, Berner RA, Park J. Climate sensitivity constrained by CO₂ concentrations over the past 420 million years. *Nature.* 2007;446:530–2.
- [70] Heinberg R. *The party's over: oil, war and the fate of industrial societies.* Gabriola Island, Canada: New Society Publishers, 2005.
- [71] Eli K. Making dirty coal plants cleaner. *Science.* 2007;317:184–6.
- [72] Granite EJ, Pennline HW. Photochemical removal of mercury from flue gases. *Ind Eng Chem Res.* 2002;41:5470–6.
- [73] Lee KB, Sircar S. Removal and recovery of compressed CO₂ from flue gas by a novel thermal swing chemisorptions process. *AIChE J.* 2008;54:2293–302.
- [74] Karl TR, Trenberth KE. Modern global climate change. *Science.* 2003;302:1719–23.
- [75] Willis RR, Benin A, Snurr RQ, Yazaydın Ö. *Nanotechnology for carbon dioxide capture.* In: García-Martínez J, editor. *Nanotechnology for the energy challenge*, 2nd ed. Weinheim: Wiley-VCH, press, 2009:517–53.
- [76] Le Bouhelec EB, Mougín P, Barreau A, Solimando R. Rigorous modeling of the acid gas heat of absorption in alkanolamine solutions. *Energy Fuels.* 2007;21:2044–55.
- [77] Rochelle GT. Amine scrubbing for CO₂ capture. *Science.* 2009;325:1652–4.
- [78] Fine NA, Goldman MJ, Nielsen PT, Rochelle GT. Managing n-nitrosopiperazine and dinitrosopiperazine. *Energy Procedia.* 2013;37:273–84.
- [79] Karadast F, Atilhan M, Aparicio S. Review on the use of ionic liquids (ILs) as alternative fluids for CO₂ capture and natural gas sweetening. *Energy Fuels.* 2010;24:5817–28.
- [80] Cavenati S, Grande CA, Rodrigues AE. Adsorption equilibrium of methane, carbon dioxide, and nitrogen on zeolite 13X at high pressures. *J Chem Eng Data.* 2004;49:1095–101.
- [81] Cavenati S, Grande CA, Rodrigues AE. Separation of CH₄/CO₂/N₂ mixtures by layered pressure swing adsorption for upgrade of natural gas. *Chem Eng Sci.* 2006;61:3893–906.
- [82] Hendrix Y, Lazaro A, Yu Q, Brouwers J. Titania-silica composites: A review on the photocatalytic activity and synthesis methods. *Wjnse.* 2015;5:161–77.
- [83] Ghoufi A, Gaberova L, Rouquerol J, Vincent D, Llewellyn P, Maurin G. Adsorption of CO₂, CH₄ and their binary mixture in Faujasite NaY: A combination of molecular simulations with gravimetry-manometry and microcalorimetry measurements. *Micropor Mesopor Mater.* 2009;119:117–28.
- [84] Lee J-S, Kim J-H, Kim J-T, Suh J-K, Lee J-M, Lee C-H. Adsorption equilibria of CO₂ on zeolite 13X and zeolite X/activated carbon composite. *J Chem Eng Data.* 2002;47:1237–42.
- [85] Wang Y, LeVan MD. Adsorption equilibrium of carbon dioxide and water vapor on zeolites 5A and 13X and silica gel: pure components. *J Chem Eng Data.* 2009;54:2839–44.

- [86] Li G, Xiao P, Webley P, Zhang J, Singh R, Marshall M. Capture of CO₂ from high humidity flue gas by vacuum swing adsorption with zeolite 13X. *Adsorption*. 2008;14:415–22.
- [87] Li G, Xiao P, Webley PA, Zhang J, Singh R. Competition of CO₂/H₂O in adsorption based CO₂ capture. *Energy Procedia*. 2009;1:1123–30.
- [88] Choi S, Drese JH, Jones CW. Adsorbent materials for carbon dioxide capture from large anthropogenic point sources. *Chem Sus Chem*. 2009;2:796–854.
- [89] Martín CF, Plaza MG, Pis JJ, Rubiera F, Pevida C, Centeno TA. On the limits of CO₂ capture capacity of carbons. *Sep Purif Technol*. 2010;74:225–9.
- [90] Plaza MG, García S, Rubiera F, Pis JJ, Pevida C. Post-combustion CO₂ capture with a commercial activated carbon: comparison of different regeneration strategies. *Chem Eng J*. 2010;63:41–7.
- [91] Furukawa H, Ko N, Go YB, et al. Ultrahigh porosity in metal-organic frameworks. *Science*. 2010;329:424–8.
- [92] Rowsell JLC, Yaghi OM. Effects of functionalization, catenation, and variation of the metal oxide and organic linking units on the low-pressure hydrogen adsorption properties of metal-organic frameworks. *J Am Chem Soc*. 2006;128:1304–15.
- [93] Wang Z, Cohen SM. Postsynthetic modification of metal-organic frameworks. *Chem Soc Rev*. 2009;38:1315–29.
- [94] Tanabe KK, Cohen SM. Postsynthetic modification of metal-organic frameworks—a progress report. *Chem Soc Rev*. 2011;40:498–519.
- [95] Sumida K, Rogow DL, Mason JA, et al. Carbon dioxide capture in metal-organic frameworks. *Chem Rev*. 2012;112:724–81.
- [96] Millward AR, Yaghi OM. Metal-organic frameworks with exceptionally high capacity for storage of carbon dioxide at room temperature. *J Am Chem Soc*. 2005;127:17998–9.
- [97] Kawakami T, Takamizawa S, Kitagawa Y, Maruta T, Mori W, Yamaguchi K. Theoretical studies of spin arrangement of adsorbed organic radicals in metal-organic nanoporous cavity. *Polyhedron*. 2001;20:1197–206.
- [98] Yazaydin AÖ, Snurr RQ, Park, T-H, et al. Screening of metal-organic frameworks for carbon dioxide capture from flue gas using a combined experimental and modeling approach. *J Am Chem Soc*. 2009;131:18198–9.
- [99] Valenzano L, Cavalleri B, Chavan S, Palomino GT, Areán CO, Bordiga S. Computational and experimental studies on the adsorption of CO, N₂, and CO₂ on Mg-MOF-74. *J Phys Chem C*. 2010;114:11185–91.
- [100] Hou X-J, He P, Li H, Wang X. Understanding the adsorption mechanism of C₂H₂, CO₂, and CH₄ in isostructural metal-organic frameworks with coordinatively unsaturated metal sites. *J Phys Chem C*. 2013;117:2824–34.
- [101] Grajciar L, Wiersum AD, Llewellyn PL, Chang J-S, Nachtigall P. Understanding CO₂ adsorption in CuBTC MOF: comparing combined DFT-ab initio calculations with microcalorimetry experiments. *J Phys Chem C*. 2011;115:17925–33.
- [102] Ha NT, Lafedova OV, Ha NN. Theoretical study on the adsorption of carbon dioxide on individual and alkali-metal doped MOF-5s. *Russ J Phys Chem A*. 2016;90:220–5.
- [103] Ramsahye NA, Maurin G, Bourrelly S, Llewellyn P, Loiseau T, Ferey G. Charge distribution in metal organic framework materials: transferability to a preliminary molecular simulation study of the CO₂ adsorption in the MIL-53 (Al) system. *Phys Chem Chem Phys*. 2007;9:1059–63.
- [104] Ramsahye NA, Maurin G, Bourelly S, et al. Probing the adsorption sites for CO₂ in metal organic framework materials MIL-53 (Al,Cr) and MIL-47 (V) by density functional theory. *J Phys Chem C*. 2008;112:514–20.
- [105] Torrisi A, Bell RG, Mellot-Draznieks C. Functionalized MOFs for enhanced CO₂ capture. *Cryst Growth Des*. 2010;10:2839–41.

- [106] Hussain MA, Soujanya Y, Sastry GN. Computational design of functionalized imidazolate linkers of zeolitic imidazolate frameworks for enhanced CO₂ adsorption. *J Phys Chem C*. 2015;119:23607–18.
- [107] Roth R. Fundamental measure theory for hard-sphere mixtures: a review. *J Phys: Condens Matter*. 2010;22:063102.
- [108] Liu Y, Liu H, Hu Y, Jiang J. Density functional theory for adsorption of gas mixtures in metal-organic frameworks. *J Phys Chem B*. 2010;114:2820–7.
- [109] Mu W, Liu D, Zhong C. A computational study of the effect of doping metals on CO₂/CH₄ separation in metal-organic frameworks. *Micropor Mesopor Mat*. 2011;143:66–72.
- [110] Wu D, Xu Q, Liu D, Zhong C. Exceptional CO₂ capture capability and molecular-level segregation in a Li-modified metal-organic framework. *J Phys Chem C*. 2010;114:16611–7.
- [111] Borges DD, Prakash M, Ramsahye NA, et al. Computational exploration of the gas adsorption on the iron tetracarboxylate metal-organic framework MIL-102. *Mol Simul*. 2015;41:1357–70.
- [112] Chen YF, Lee JY, Babarao R, Li J, Jiang JW. A highly hydrophobic metal-organic framework Zn(BDC)(TED)_{0.5} for adsorption and separation of CH₃OH/H₂O and CO₂/CH₄: an integrated experimental and simulation study. *J Phys Chem C*. 2010;114:6602–9.
- [113] Mu W, Liu D, Yang Q, Zhong C. Computational study of the effect of organic linkers on natural gas upgrading in metal-organic frameworks. *Micropor Mesopor Mat*. 2010;130:76–82.
- [114] Yang Q, Zhong C. Electrostatic-field-induced enhancement of gas mixture separation in metal-organic frameworks: a computational study. *Chem Phys Chem*. 2006;7:1417–21.
- [115] Bloch ED, Queen WL, Krishna R, Zadrozny JM, Brown CM, Long JR. Hydrocarbon separations in a metal-organic framework with open iron(II) coordination sites. *Science*. 2012;335:1606–10.
- [116] Yan Y, Juríček M, Coudert F-X, et al. Non-interpenetrated metal-organic frameworks based on copper(II) paddlewheel and oligoparaxylene-isophthalate linkers: synthesis, structure, and gas adsorption. *J Am Chem Soc*. 2016;138:3371–81.
- [117] Zhou W, Wu H, Hartman MR, Yildirim T. Hydrogen and methane adsorption in metal-organic frameworks: A high-pressure volumetric study. *J Phys Chem C*. 2007;111:16131–7.

Cecil NM Ouma and Walter E Meyer

7 Metastability of the boron-vacancy complex in silicon: Insights from hybrid functional calculations

Abstract: Using four distinct configurations of the boron-vacancy (BV) complex in silicon, we investigate the experimentally observed defect metastability of the BV complex in silicon using the HSE06 hybrid functional within the density functional theory formalism. We identify the experimentally observed metastable configurations of the defect complex when the substitutional boron is in the nearest neighbor position with respect to silicon vacancy and when the two defects are in the next (second) nearest neighbor position with respect to each other. The next (second) nearest neighbor position consists of two configurations that almost degenerate with C_1 and C_{1h} symmetry.

Keywords: c-center defect complex, defects in semiconductors, metastability, hybrid functionals, DFT

7.1 Introduction

The c-center defect complex in silicon comprises a substitutional boron and a silicon vacancy and hence the boron-vacancy (BV) complex. It is one of the experimentally well-known metastable defects in silicon; however, even though it has attracted the attention of experimental [1–5] and theoretical investigations [6, 7], its identity has been the subject of intense debate both experimentally and theoretically and there is still no consensus on the atomic configuration of its respective metastable states and in what charge states is the metastability observed [1–4]. Sprenger et al. [3] and Watkins [5] associated the Si-G10 EPR spectrum to the BV complex with B_{Si} and V_{Si} in the nearest and next-nearest neighbor positions with respect to each other. However, using deep-level transient spectroscopy (DLTS), Bains *et al.* [8], Londos [4] and Zangenberg et al. [2] observed metastable defect peaks in electron-irradiated boron-doped silicon, which they also associated with the c-center defect complex in silicon and their identification was in part supported by theoretical studies that used density functional theory (DFT) [6, 7].

This article has previously been published in the journal *Physical Sciences Reviews*. Please cite as: Ouma, C. NM., Meyer, W. E. Metastability of the boron-vacancy-complex in silicon: Insights from hybrid functional calculations. *Physical Sciences Reviews* [Online] **2018**, 3. DOI: 10.1515/psr-2018-0001

<https://doi.org/10.1515/9783110568196-007>

Theoretical studies have also been carried on the isolated B_{Si} and V_{Si} as well as the $B_{\text{Si}}V_{\text{Si}}$ complex (referred to as BV in this manuscript) in Si [6, 7, 9–11]. Adey et al. [6] while investigating the theory of BV complex in silicon using DFT found that the BV complex had two different minimum energy (stable) configurations in different charge states. In their study, the configuration of the BV complex with B_{Si} and V_{Si} in the second nearest position with respect to each other was found to be degenerate and this configuration was stable in the 0 and +1 charge state; the configuration with B_{Si} and V_{Si} in the third nearest neighbor configuration was found to be stable in the –1 charge state. Another study [7] that used DFT with the B3LYP [12] hybrid functional to investigate the electronic structure of boron-interstitial clusters in silicon found the configuration with B_{Si} and V_{Si} in the first nearest neighbor positions to be the minimum energy configuration; however, even using hyperfine interactions they were still not able to give a clear-cut assignment of any configuration to the experimentally observed Si-G10 center.

In this study, we use the screened hybrid functional Heyd–Scuseria–Ernzerhof (HSE06) [13, 14] within DFT to investigate the metastability of the BV complex in silicon with the aim of identifying the possible metastable atomic configurations of the BV complex. DFT with and without hybrid functionals has to some extent complimented experimental observations of charge state-controlled metastability in the case of substitutional europium vacancy complex ($\text{Eu}_{\text{Ga}}\text{-V}_{\text{N}}$) in GaN [15] and carbon-substitutional–carbon-interstitial (CsCi) defect pair in silicon [16].

7.2 Computation details

Using the projector-augmented wave method [17, 18] with the screened hybrid functional of HSE06 [13, 14] within DFT formalism as implemented in the VASP code [19, 20], we investigated the nature of the BV complex in silicon, in different configurations, and compared our results to experimentally observed metastability of this BV complex. A lattice constant of 5.43 Å and a band gap of 1.13 eV were obtained using HSE06 functional when the unit cell was optimized using an energy cutoff of 500 eV, a Γ centered $8 \times 8 \times 8$ Monkhorst-Pack (MP) grid of k -points and the optimized unit cell used to construct the supercells. For the systems, the electronic energies were converged to 10^{-6} eV and the force per atom was converged to 0.02 eV/Å. For defect calculations, a 64-atom Si supercells constructed from the optimized unit cell were used with a kinetic energy cutoff of 500 eV. A $3 \times 3 \times 3$ Monkhorst-Pack [21] grid of k -points was used to sample the Brillouin zone and the defect supercells. A similar supercell with the same k -point sampling has been used to investigate the VO (A-center), VV and VO_2 defect in silicon [22]. The electronic energies of the defect systems were also converged to an accuracy of 10^{-6} eV, keeping the volume of the supercell constant, and the finite supercell correction was done according to Freysoldt et al [23, 24]. Defect formation energies were calculated according to the Zhang and Northup formalism [25]. Within this

formalism, the formation energy of the defect in this case, the $B_{\text{Si}}V_{\text{Si}}$ at charge state q , is given by,

$$E_{B_{\text{Si}}V_{\text{Si}}}^q = E_{\text{tot}}(B_{\text{Si}}V_{\text{Si}}^q) - E_{\text{tot}}(\text{Si}) + 2\mu_{\text{Si}} - \mu_{\text{B}} + q(E_{\text{V}} + E_{\text{F}} + \Delta V) \quad (7.1)$$

where $E_{\text{tot}}(B_{\text{Si}}V_{\text{Si}}^q)$ is the total energy of the defect containing supercell at charge state q , $E_{\text{tot}}(\text{Si})$ is the total energy of the pristine Si supercell, μ_{Si} and μ_{B} are the chemical potentials for Si and B, respectively, E_{F} is the Fermi level, referenced to the valence band maximum (VBM) E_{V} and ΔV is the potential alignment term [26–28] needed to align the VBM of the defect lattice to that of the host lattice. We considered four different configurations of the BV complex where the relative positions of V_{Si} with respect to B_{Si} were used to distinguish between the configurations (see Figure 7.1). These configurations were labeled C1 to C4.

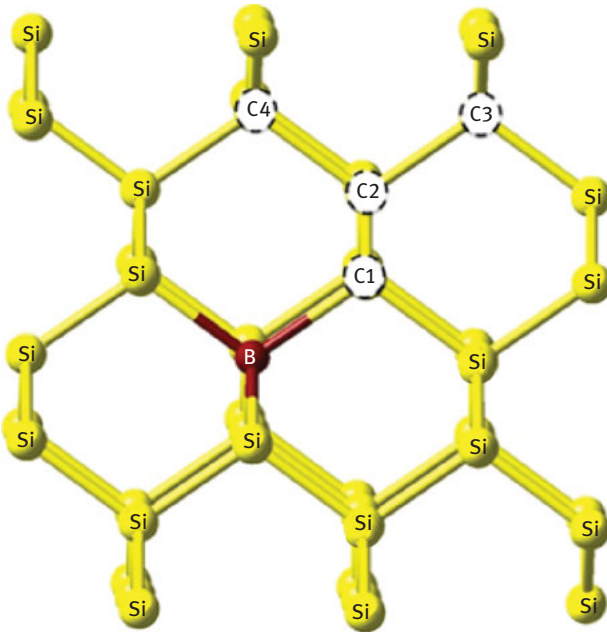


Figure 7.1: (Color online) Figure showing the V_{Si} positions (white spheres) with respect to B_{Si} .

7.3 Results and discussion

B_{Si} is a shallow acceptor in silicon and V_{Si} is known to be highly mobile in silicon. When these two defects are close to each other they form the BV complex. The calculated formation energies relative to the minimum energy configuration at various charge states as well as the binding energies and thermodynamic transitions for the different configurations of the BV complex are presented in Table 7.1. In all cases,

Table 7.1: Calculated formation energies (eV) relative to the most stable defect configuration of the B-V complex in each charge state and the binding energy (eV).

Configuration	Charge state			Thermodynamic transitions		Binding energy
	-1	0	-1	0/-1	1/0	
C1	0.00	0.00	0.36	0.15	0.03	1.00
C2	0.64	0.09	0.00	0.70	0.48	0.91
C3	0.80	0.33	0.42	0.62	0.30	0.67
C4	0.72	0.25	0.17	0.63	0.46	0.75

the atomic positions were relaxed, keeping the supercell volume equal to that of the pristine supercell. The binding energy of a defect pair (complex) is the energy needed to dissociate the defect pair into its constituent defects; therefore, at 0K the defect complex exists as stable compound since all configurations have small but positive binding energies. Since the binding energies are small, it is possible that at ≤ 0 K the defect complex will dissociate.

From the table, it can be seen that the C1 configuration (configuration with B_{Si} and V_{Si} in the nearest neighbor position) was the minimum energy configuration in the -1 and neutral charge states, while the C2 configuration (configuration with B_{Si} and V_{Si} in the next-nearest neighbor position) was the minimum energy configuration in the +1 charge state. This observation contradicts that of [6] that used spin-polarized DFT with the Hartwigsen, Goedecker and Hutter pseudopotentials [29] where the C2 configuration was found to be the minimum energy configuration in the +1 and neutral (0) charge states and C3 (configuration with B_{Si} and V_{Si} in the third (next next) nearest neighbor position) as the minimum energy configuration in the -1 charge state. Initially, we attributed the source of this discrepancy to the choice of the exchange-correlation functional within DFT; however, we also did similar calculations with standard generalized gradient approximation (GGA) also within the DFT formalism and still we were not able to observe what was reported in [6]. GGA predicted the C2 configuration as the minimum energy configuration in all charge states. As a further step, we used gamma point-only sampling on a 216-atom supercell with the defect complex embedded for both the GGA and HSE06 case, but still the results were consistent to that of the 64-atom supercell with a $3 \times 3 \times 3$ Monkhorst-Pack [21] grid of k -points. When the minimum energy configuration of defect complex is different in two different charge states, the defect complex is said to possess charge-state-controlled metastability. Other instances where analogous charge-state-controlled metastability has been observed from DFT calculations include the Eu-vacancy complex in GaN where one of two configurations (basal configuration) was found to be stable in the neutral and +1 charge states, with the other (axial configuration) being stable in the -1 charge state [15]. The carbon-substitutional-carbon-interstitial pair in Si has also been investigated using DFT where charge-state-controlled

metastability was only observed in the neutral and -1 charge states [16]. Configuration metastability due to impurity position has also been reported in GaAs in the case of As-vacancy–Si-impurity ($V_{As}As_{Ga}$) and the As-vacancy–As-anti-site complexes ($V_{As}Si_{Ga}$). For these complexes, $V_{As}As_{Ga}$ was found to be the stable configuration in the $+1$ charge state, while $V_{As}Si_{Ga}$ was the stable configuration in the neutral charge state [30].

Figure 7.2 shows the formation energies of the defect complex in various configurations at various charge states as a function of the Fermi level. Several observations can be made from Figure 7.2. In Figure 2a, C1 is the minimum energy configuration for both the -1 and 0 charge states; however this is not the case for 0 and $+1$ charge state in Figure 2b. It can be seen in Figure 2b that from $E_F = 0.00 \rightarrow 0.39$ eV, C2 in the $+1$ charge state is the minimum energy configuration. Beyond $E_F = 0.39$ eV, C1 is the minimum energy configuration. This confirms that the BV complex exhibits charge-state-controlled metastability. Defect levels obtained using DLTS are analogous to the thermodynamic transition levels obtained from DFT calculations. A thermodynamic transition level is the Fermi level position at which a defect in two different charge states will have the same formation energy. This can be obtained from the intersection points of the charge state lines in Figure 7.2. These intersection points of the defect in two different charge states are indicated by arrows in the figure and also presented in Table 7.1. The energy difference between the C2 and C4 configurations is the order of 0.15 eV and their respective thermodynamic transitions levels are also relatively close to each other as can be seen in Figure 2(a) and (b). The symmetry of

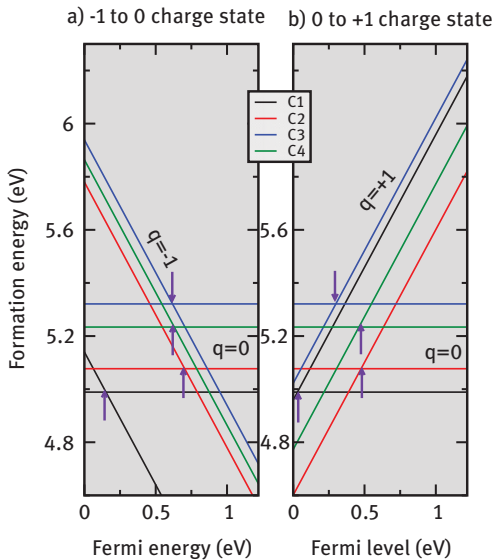


Figure 7.2: (Color online) Formation energy as function of the Fermi level (eV) at various charge states for all the BV complex configurations investigated. Arrows indicate thermodynamic transition levels.

these configurations was C_1 and C_{1h} for C2 and C4 configurations, respectively, which was consistent to what was observed by [6] where they concluded that these two configurations are almost degenerate. This makes it likely that defect levels associated to these two configurations are experimentally observable as levels originating from one defect center with two peaks that are of different heights. A similar observation has been made when DFT was used to investigate vacancies and E-centers in silicon, where $As_{Si}V_{Si}$ and $Sb_{Si}V_{Si}$ were found to exist as multisymmetry defects, i. e. defects that can coexist in several metastable configurations with notably different relaxation patterns which have very similar formation energies [31]. If this is the case, then according to Figure 2(a), only the C1 peak will be experimentally observable at lower temperatures while two peaks associated to another configuration which in our case will be C2 and C4 will be observable at higher temperatures and the charge states responsible will be the -1 and 0 charge states. In the case of the 0 and $+1$ charge states, low-temperature peak associated with C1 configurations is not likely to be experimentally observable due to the fact that it lies very close to the valence band. However, the higher temperature peaks associated with the C2 and C4 configuration will be observable either as a single peak or as two peaks. As can be seen in Table 7.1, the $0/+1$ thermodynamic transition levels are very close in energy, within 0.02 eV of each other, and hence not likely distinguishable from DLTS experiments.

In a semiconductor, the Fermi level position usually spans from the top of the VBM to the bottom of conduction band minimum (CBM) that is, $VBM \leftarrow E_F \rightarrow CBM$. When the Fermi level is shifted such that it approaches CBM from VBM, $E_F \rightarrow CBM$, the process is analogous to applying a reverse bias voltage on a Schottky barrier diode. The reverse process $E_F \rightarrow VBM$ is analogous to applying a zero bias to the diode. Using this analogy, it can be seen that for the -1 to 0 charge state case that, as $E_F \rightarrow CBM$ (forward bias), the $-1/0$ thermodynamic transition level associated with the C1 configuration is observed at $E_{VBM} + 0.15$ eV followed by those associated to the C2, C3 and C4 configurations at $E_{VBM} + 0.70$ eV, $E_{VBM} + 0.62$ eV and $E_{VBM} + 0.63$ eV, respectively. C3 will, however, not be accessible experimentally because its formation energy is relatively higher compared to the C1, C2 and C4 formation energies. Since the C1 configuration has the lowest formation energy, its associated thermodynamic transition level can be assigned to the low-temperature peak while the almost degenerate thermodynamic transition levels associated with the C2 and C4 configurations can be assigned to the high-temperature peaks of [2]. According to Zangenberg et al. [2], a shallow trap at $E_{VBM} + 0.105$ eV that corresponded to a low-temperature peak was observed and when a reverse bias of 5V is applied after annealing at 215 K. They also observed two new peaks that corresponded to traps at $E_{VBM} + 0.31$ eV and $E_{VBM} + 0.37$. This transformation was found to be reversible.

Experimentally, in order for two configurations of single defect complex in the same charge state to have similar occupations, their formation energy difference ought to be at least approximately kT at room temperature. However, if the formation energy difference between the two configurations is approximately $3kT$ (approximately 0.1 eV

at room temperature) or greater, then the occupation ratio of the two configurations will be in the order of 1:10 assuming that there is no degeneracy. This results in one configuration being dominant over the other. When $E_F \rightarrow \text{VBM}$ (zero biasing), for the 0 and -1 charge state, the formation energy difference between C1 and both the C2 and C4 configurations was 0.64 eV and 0.72 eV respectively, which is greater than $3kT$ at 215 K (temperature at which the annealing was done in the cited experimental work [2]), implying that, a majority of the defects will be in the C1 configuration (i. e. the minimum energy configuration). If this system is quenched, this configuration will be frozen in, and if a DLTS spectrum is recorded, its two relatively deep energy levels are likely to be observed experimentally at higher temperatures. This is in agreement with Configuration A as described by Zangenberg et al [2]. Both Zangenberg et al. [2] and Lodos [4] determined the energies of the two DLTS peaks to be $E_{\text{VBM}} + 0.31$ eV and $E_{\text{VBM}} + 0.37$ eV, while our calculations predict the $-1/0$ thermodynamic transition levels of the configurations to be $E_{\text{VBM}} + 0.63$ eV and $E_{\text{VBM}} + 0.70$ eV. We therefore identify Configuration A of Zangenberg et al. [2] as one with V_{Si} and B_{Si} at next-nearest neighbor positions with respect to each other. This identification is consistent with the DFT work of [6].

As $E_F \rightarrow \text{CBM}$ (reverse biasing), the minimum energy configuration is the C1 in the neutral charge state. As previously, the formation energy difference between the C1 and both C2 and C4 configurations was 0.09 eV and 0.25 eV which is also significantly greater than $3kT$, implying a complete conversion to the C1 configuration. This is consistent with experimental observations [2, 4, 8]. The $-1/0$ thermodynamic transition level of the C1 was found at $E_{\text{VBM}} + 0.15$ eV configuration and was much shallower (closer to the VBM) than those of the C2 configuration, implying that the DLTS peaks associated with C1 will be observed at a much lower temperature. Zangenberg et al. [2] as well as few other authors [4, 8] observed only a single low-temperature peak after reverse-bias annealing at $E_{\text{VBM}} + 0.105$ eV, and we therefore tentatively propose that the identity of Configuration B of Zangenberg et al. [2] is the one with V_{Si} and B_{Si} at the nearest neighbor positions with respect to each other. In the case of 0 and $+1$ charge states, only the two defect levels associated with the almost degenerate C2 and C4 configurations are experimentally observable. Although the C1 in the neutral charge state is the minimum energy configuration when one is close to the CBM, the $0/+1$ thermodynamic transition level lies too close to the CBM, making it not likely observable experimentally. Thus, metastability is less likely to be observed in this case.

Using a nudged elastic band calculation, we found the transition state (transformation) energy from C1 to C2 and C1 to C4, in the neutral charge state, to be approximately 1.1 eV. The experimental transformation kinetics of this defect has not been published yet. Theoretically, the transformation rate of the defect may be estimated by the Arrhenius equation taking the calculated transition state energy of 1.1 eV and assuming a pre-exponential constant of 10^{12}S^{-1} , which is consistent with an atomic jump [32]. This leads to a rate of 10^{-12}S^{-1} which is much lower than the

experimental observations where complete transformation was observed in 15 minutes at 220 K. This discrepancy may be explained by the fact that the transition state calculations are done at 0 K and do not take barrier height changes due to lattice vibrations into account.

7.4 Conclusion

We have investigated the metastability of the BV complex in silicon using HSE06 and compared our predictions to experimentally observed metastability. HSE06 gave the correct qualitative prediction of the observed changes in the DLTS spectrum due to the metastability of the defect complex. These predictions were in part consistent with experimental observations, and from our study, we assign configurations of the BV complex with V_{Si} and B_{Si} in the nearest and next-nearest neighbor positions with respect to each other to the experimentally observed configurations [2].

Funding: This work is based on the research supported in part by the National Research Foundation of South Africa (Grant specific unique reference number (UID) 76938). The grant holder acknowledges that opinions, findings and conclusions or recommendations expressed in any publication generated by the NRF supported research are that of the author(s), and that the NRF accepts no liability whatsoever in this regard.

References

- [1] Chantre A. Configurationally bistable C center in quenched Si: B:possibility of a boron-vacancy pair. *Phys Rev B*. 1985;32:3687–94.
- [2] Zangenberg NR, Nylandsted Larsen A. On-line DLTS investigations of vacancy related defects in low-temperature electron irradiated, boron-doped Si. *Appl Phys*. 2005;80:1081–86.
- [3] Sprenger M, Van Kemp R, Sieverts E, Ammerlaan C. Electronic and atomic structure of the boron-vacancy complex in silicon. *Phys Rev B Condens Matter*. 1987;35:1582–92.
- [4] Londos CA. Investigation of a new metastable defect in boron-doped Cz-Si. *Phys Status Solidi*. 1992;133:429.
- [5] Watkins G. EPR of a trapped vacancy in boron-doped silicon. *Phys Rev B*. 1976;13:2511–18.
- [6] Adey J, Jones R, Palmer D, Briddon P, Öberg S. Theory of boron-vacancy complexes in silicon. *Phys Rev B*. 2005;71:165211.
- [7] Deák P, Gali A, Sólyom A, Buruzs A, Frauenheim T. Electronic structure of boron-interstitial clusters in silicon. *J Phys Condens Matter*. 2005;17:S2141–S2153.
- [8] Bains SK, Banbury PC. A bistable defect in electron-irradiated boron-doped silicon. *J Phys C*. 1985;18:L109–L116.
- [9] Nichols C, Van De Walle C, Pantelides S. Mechanisms of dopant impurity diffusion in silicon. *Phys Rev B*. 1989;40:5484–96.
- [10] Windl W, Stumpf R. Charge of self-interstitials and boron-interstitial pairs as a function of doping concentration. *Mater Sci Eng B*. 2008;155:198–201.
- [11] Cowren DJGB, Janssen KTF, Van De Walle GFA. Impurity Diffusion via intermediate species: the B:Si system. *Phys Rev Lett*. 1990;65:2434–37.

- [12] Becke AD. Density-functional thermochemistry. III. The role of exact exchange. *J Chem Phys.* 1993;98:5648.
- [13] Heyd J, Scuseria GE, Ernzerhof M. Hybrid functionals based on a screened Coulomb potential. *J Chem Phys.* 2003;118:8207.
- [14] Heyd J, Scuseria GE, Ernzerhof M. Erratum: “Hybrid functionals based on a screened Coulomb potential”. *J Chem Phys.* 2006;124:219906. [*J. Chem. Phys.* 118, 8207 (2003)]. DOI: 10.1063/1.2204597
- [15] Ouma CNM, Meyer WE. Ab initio study of metastability of Eu³⁺ Defect complexes in GaN. *Phys B Condens Matter.* 2013. DOI: <http://dx.doi.org/10.1016/j.physb.2013.11.004>
- [16] Ouma CNM, Meyer WE. The carbon-substitutional–carbon-interstitial (CsCi) defect pair in silicon from hybrid functional calculations. *Comput Mater Sci.* 2016;118:338–41.
- [17] Blöchl PE. Projector augmented-wave method. *Phys Rev B.* 1994;50:17953–79.
- [18] Kresse G, Joubert D. From ultrasoft pseudopotentials to the projector augmented-wave method. *Phys Rev B.* 1999;59:1758–75.
- [19] Kresse G, Furthmüller J. Efficiency of ab-initio total energy calculations for metals and semi-conductors using a plane-wave basis set. *Comp Mat Sci.* 1996;6:15–50.
- [20] Kresse G, Hafner J. Ab initio molecular dynamics for open-shell transition metals. *Phys Rev B.* 1993;48:13115–18.
- [21] Monkhorst HJ, Pack JD. Special points for Brillouin-zone integrations. *Phys Rev B.* 1976;13:5188–92.
- [22] Christopoulos S-R, Wang H, Chroneos A, Londos CA, Sgourou EN, Schwingenschlögl U. VV and VO₂ defects in silicon studied with hybrid density functional theory. *J Mater Sci Mater Electron.* 2015;26:1568–71.
- [23] Freysoldt C, Neugebauer J, Van De Walle CG. Electrostatic interactions between charged defects in supercells. *Phys Status Solidi.* 2011;248:1067–76.
- [24] Freysoldt C, Neugebauer J, Van De Walle C. Fully Ab initio finite-size corrections for charged-defect supercell calculations. *Phys Rev Lett.* 2009;102:16402.
- [25] Zhang S, Northrup J. Chemical potential dependence of defect formation energies in GaAs: application to Ga self-diffusion. *Phys Rev Lett.* 1991;67:2339–42.
- [26] Van De Walle CG. First-principles calculations for defects and impurities: applications to III-nitrides. *J Appl Phys.* 2004;95:3851.
- [27] Lany S, Zunger A. Accurate prediction of defect properties in density functional supercell calculations. *Model Simul Mater Sci Eng.* 2009;17:84002.
- [28] Lany S, Zunger A. Assessment of correction methods for the band-gap problem and for finite-size effects in supercell defect calculations: case studies for ZnO and GaAs. *Phys Rev B.* 2008;78:235104.
- [29] Hartwigsen C, Goedecker S, Hutter J. Relativistic separable dual-space Gaussian pseudo-potentials from H to Rn. *Phys Rev B.* 1998;58:3641–62.
- [30] Pöykkö S, Puska MJ, Alatalo M, Nieminen RM. Metastable defect complexes in GaAs. *Phys Rev B.* 1996;54:7909–16.
- [31] Ganchenkova MG, Oikkonen LE, Borodin VA, Nicolaysen S, Nieminen RM. Vacancies and E-centers in silicon as multi-symmetry defects. *Mater Sci Eng B.* 2009;159:107–11.
- [32] Lanoo M, Bourgoin J. Point defects in semiconductors I. *Theo Asp Springer Ser Solid-State Sci.* 1981;22:2.

Supplementary Material: The online version of this article offers supplementary material (DOI: <https://doi.org/10.1515/psr-2018-0001>).

Helen P. Kavitha, Lydia Rhyman and Ponnadurai Ramasami

8 Molecular structure and vibrational spectra of 2-(4-bromophenyl)-3-(4-hydroxyphenyl) 1,3-thiazolidin-4-one and its selenium analogue: Insights using HF and DFT methods

Abstract: 2-(4-Bromophenyl)-3-(4-hydroxyphenyl)-1,3-thiazolidin-4-one and its selenium analogue were studied in the gas phase using HF and DFT methods. The functionals considered were B3LYP, BP86 and M06. The basis set for all the atoms was 6-311++ G(d,p). Molecular parameters such as bond lengths, bond angles, rotational constants, dipole moments, electronic energies, and vibrational parameters namely harmonic vibrational frequencies and relative intensities were computed for these compounds. Atomization energies, HOMO-LUMO gaps and natural charges on the atoms were also calculated. The molecular parameters and the vibrational spectra of sulfur compound are in good agreement with the experimental data. Therefore, the data for the selenium analogue should be helpful in its future characterization.

Keywords: 2-(4-bromophenyl)-3-(4-hydroxyphenyl)-1, 3-thiazolidin-4-one, HF, DFT, selenium, vibrational spectroscopy

8.1 Introduction

Heterocyclic compounds containing sulfur are extensively studied because of their medicinal and pharmaceutical importance [1–3]. 4-Thiazolidinone ring system contains sulfur and nitrogen at positions 1 and 3, respectively, and keto group at position 4. They are well known for their diverse pharmacological activities. The thiazolidinone nucleus is considered as wonder nucleus because it forms different derivatives which possess different biological activities [4]. Their derivatives are found to possess antiviral [5], antimicrobial [6], anti-inflammatory [7], anticancer [8], antitubercular [9], anticonvulsant [10] and anti-HIV activities [11]. The presence of N-C-S linkage in the thiazolidinone derivatives are known to possess hypnotic [12] and anticancer [13] activities. It has also been proved that discrete modifications in the chemical structure of the thiazolidinone agonists produces derivatives with diverse pharmacological properties

This article has previously been published in the journal *Physical Sciences Reviews*. Please cite as: Kavitha, H., Rhyman, L., Ramasami, P. Molecular structure and vibrational spectra of 2-(4-bromophenyl)-3-(4-hydroxyphenyl) 1,3-thiazolidin-4-one and its selenium analogue: Insights using HF and DFT methods. *Physical Sciences Reviews* [Online] **2018**, 3. DOI: 10.1515/psr-2018-0031

<https://doi.org/10.1515/9783110568196-008>

[14]. Some of the thiazolidinone compounds were evaluated for their inhibitory effects on the replication on yellow fever virus in green monkey kidney by means of a cytopathic effect reduction assay [15]. Thiazolidinone amides, carboxylic acids and serine amides were synthesized and tested for possible anticancer activity [16].

Selenium pathology is a subject of a new scientific discipline – geomedicine – dealing with the influence of natural factors on the geographical distribution of problems in human and veterinary medicine [17]. For the biological effects of selenium, its chemical form is also very important. However, different chemical forms of selenium have different toxic potentials and effects. Organic compounds of selenium are more effective in comparison with inorganic compounds [18]. Selenium reagents have been extensively used in a variety of organic reactions. Other major applications are: (i) ligand chemistry, (ii) precursors for the preparation of thin films in metal-organic chemical vapour deposition and (iii) biochemistry [19, 20].

In view of the biological applications of thiazolidinone compound, one of us synthesized 2-(4-bromophenyl)-3-(4-hydroxyphenyl)-1,3-thiazolidin-4-one and reported the crystal structure of the compound [21]. In continuation with the previous report [21], the molecular and spectroscopic parameters of the sulfur-based compound were investigated using Hartree-Fock (HF) and density functional theory (DFT) methods. We extended this research work to include the selenium analogue of the title compound for which experimental data is not available.

8.2 Computational method

All computations were performed with the Gaussian 09 software [22]. The HF and DFT methods were used to optimize the title compound and its selenium analogue. The gradient-correlated functionals used were B3LYP, BP86 and M06. The basis set for all atoms was 6-311++ G(d,p). Frequency computations based on the same geometry optimization method were used to confirm the nature of the stationary points. The compounds were subjected to normal coordinate analysis for the assignment of some of the computed vibrational frequencies. The electronic energies, geometrical parameters, atomic charges, energy of the highest occupied molecular orbital (HOMO), energy of the lowest unoccupied molecular orbital (LUMO), uncorrected harmonic frequencies and infra-red intensities were computed. We also evaluated the performance of the HF/6-31G (d) method for the sulfur based compound. GaussView (Gaussian, Inc., USA) [23] was used for visualizing the structure.

8.3 Results and discussion

8.3.1 Structural parameters

The atoms labelling of the two compounds studied are given in Figure 8.1.

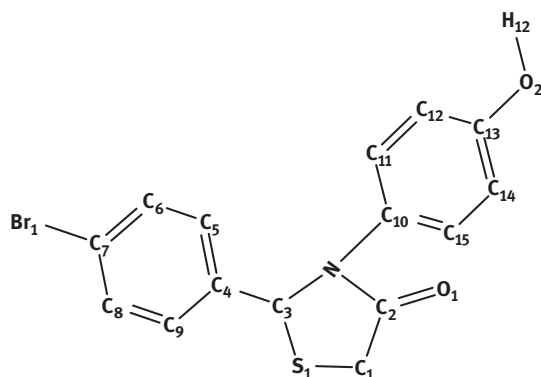


Figure 8.1: Atoms labelling of 2-(4-bromophenyl)-3-(4-hydroxyphenyl)-1,3-thiazolidin-4-one and its selenium analogue ($S_1 = Se_1$).

Selected bond lengths and the bond angles of the title compound and its selenium analogue are collected in Table 8.1 and Table 8.2. The experimental structural parameters are also included for the sulfur-based compound [21] for comparison purposes. There are no experimental data for the selenium analogue but we have tried to compare with related compounds available in literature. From Table 8.1, it is

Table 8.1: Selected bond lengths and bond angles of the optimized structure of 2-(4-bromophenyl)-3-(4-hydroxyphenyl)-1,3-thiazolidin-4-one.

Level of theory	HF	B3LYP	M06	BP86	HF	Experimental [21]
Basis set	6-31G(d)		6-311++ G(d,p)			
Bond length/Å						
C1-C2	1.507	1.524	1.514	1.530	1.516	1.503
C1-S1	1.863	1.824	1.816	1.829	1.810	1.791
C2-O1	1.221	1.213	1.207	1.225	1.190	1.226
C2-N1	1.364	1.382	1.372	1.393	1.361	1.385
C3-N1	1.459	1.467	1.452	1.472	1.453	1.463
C3-S1	1.902	1.862	1.851	1.870	1.840	1.832
C7-Br1	1.929	1.917	1.898	1.920	1.900	1.897
C13-O2	1.373	1.368	1.355	1.376	1.348	1.371
N1-C10	1.434	1.434	1.426	1.435	1.431	1.438
C3-C4	1.508	1.511	1.504	1.513	1.517	1.502
O2-H12	0.950	0.963	0.961	0.973	0.941	0.820
Bond angle/°						
C2-C1-S1	107.8	107.6	108.5	107.6	107.6	108.0
N1-C2-C1	113.7	112.2	111.7	111.9	112.4	112.2
N1-C3-S1	105.0	105.2	105.4	105.1	105.6	105.1
C2-N1-C3	120.6	118.2	119.5	117.8	119.6	117.8
C1-S1-C3	92.2	92.0	92.7	91.7	93.6	91.9

Table 8.2: Selected bond lengths and bond angles of the optimized structure of selenium analogue of 2-(4-bromophenyl)-3-(4-hydroxyphenyl)-1,3-thiazolidin-4-one.

Level of theory	HF	B3LYP	M06	BP86	HF	Literature
Basis set	6-31G(d)		6-311++ G(d,p)			
Bond length/Å						
C1-C2	1.509	1.523	1.513	1.523	1.517	
C1-Se1	1.963	1.966	1.949	1.966	1.943	1.944 ^a
C2-O1	1.222	1.215	1.208	1.215	1.190	
C2-N1	1.365	1.379	1.373	1.379	1.364	
C3-N1	1.467	1.460	1.453	1.460	1.453	
C3-Se1	1.984	2.019	1.988	2.019	1.980	1.978 ^b
C7-Br1	1.929	1.917	1.898	1.917	1.900	
C13-O2	1.374	1.367	1.355	1.367	1.348	
N1-C10	1.432	1.439	1.428	1.439	1.433	
C3-C4	1.514	1.510	1.502	1.510	1.515	
O2-H12	0.950	0.963	0.961	0.963	0.941	
Bond angle/°						
C2-C1-Se1	106.8	108.6	108.8	108.6	107.8	108.8 ^c
N1-C2-C1	114.3	114.4	113.5	114.4	114.3	
N1-C3-Se1	104.2	105.5	105.3	105.5	105.5	
C2-N1-C3	120.5	122.2	121.8	122.2	121.7	
C1-Se1-C3	87.7	88.8	88.6	88.8	89.2	

observed that the bond length and the bond angle determined by the *ab initio* methods are comparable with the largest deviations in bond length and bond angle being 0.153 Å and 0.8°, respectively. It is worth pointing out that the HF/6-31G method is also performing well with the largest deviations in bond length and bond angle being 0.143 Å and 0.4°, correspondingly. On comparing the bond lengths of the heterocyclic ring, significant variation occurs due to the electronegativity of the atoms. The longest bond length C3-S1 (1.862 Å) is due to the attachment of phenyl ring with the electronegative bromine atom to C3. The longest C3-S1 bond length is also attributed to its pure single bond character. The shortest bond length C2-O1 (1.213 Å) can be attributed due to the ring strain. Due to ring strain the C2-N1 (1.467 Å) bond length is shorter than C2-C1 (1.524 Å). The longest C7-Br1 (1.917 Å) bond length is due to the electronegativity of the bromine atom [24, 25].

Other structural parameters such as dipole moment, rotational constants, free energy, enthalpy, atomization energy, HOMO-LUMO gap, chemical potential and chemical hardness are reported in Table 8.3 and Table 8.4 for the title compound and its selenium analogue, respectively. The chemical potential (μ) and chemical hardness (η) were calculated from the HOMO and LUMO energies as $\mu = 1/2 (E_{\text{LUMO}} + E_{\text{HOMO}})$ and $\eta = 1/2 (E_{\text{LUMO}} - E_{\text{HOMO}})$.

The lower rotational constants of selenium analogue may be understood in terms of the larger reduced mass and longer bond lengths involved [26]. Similarly, the

Table 8.3: Dipole moment, rotational constants, electronic energy, enthalpy, free energy and HOMO-LUMO gap of 2-(4-bromophenyl)-3-(4-hydroxyphenyl)-1,3-thiazolidin-4-one.

Level of theory	B3LYP	BP86	M06	HF	HF
Basis set		6-311++ G(d,p)			6-31G
Dipole moment (Debye)	0.735	0.705	1.581	1.472	1.535
A (GHz)	0.311	0.310	0.305	0.319	0.314
B (GHz)	0.149	0.148	0.157	0.144	0.145
C (GHz)	0.111	0.110	0.117	0.110	0.110
Atomization energy (kJ/mol)	14,951.1	15,656.3	15,144.3	10,709.3	10,026.1
HOMO-LUMO gap (eV)	4.98	3.37	5.43	9.84	11.68
μ (kJ/mol)	-437.8	-475.9	-453.9	-345.2	-174.6
η (kJ/mol)	174.2	58.1	197.8	517.7	692.8

Table 8.4: Dipole moment, rotational constants, electronic energy, enthalpy, free energy and HOMO-LUMO gap of 2-(4-bromophenyl)-3-(4-hydroxyphenyl)-1,3-selenazolidin-4-one.

Level of theory	B3LYP	BP86	M06	HF	HF
Basis set		6-311++ G(d,p)			6-31G
Dipole moment (Debye)	1.629	1.295	1.550	1.397	1.630
A (GHz)	0.240	0.234	0.237	0.241	0.240
B (GHz)	0.139	0.140	0.150	0.138	0.139
C (GHz)	0.096	0.096	0.102	0.097	0.096
Atomization energy (kJ/mol)	14,884.2	14,288.8	15,075.3	10,636.7	140,815.5
HOMO-LUMO gap (eV)	4.84	4.85	5.32	9.80	4.43
μ (kJ/mol)	-149.2	-447.4	-448.2	-343.0	-288.8
η (kJ/mol)	708.0	163.0	192.6	516.0	296.6

smaller atomization energy of the selenium compound can be explained in terms of longer and hence weaker C-Se bond. The decrease in hardness from the title compound to its Se analogue can be interpreted in terms of increasing size of sulfur to selenium. The larger value of chemical potential in selenium analogue indicates that the charge transfer processes are more predominant and this leads to stabilization through hyper conjugative interactions [27, 28].

The HOMO-LUMO energy gap is an important index of the stability of a molecule [27]. HOMO-LUMO energy gap is 4.98 eV and for the selenium analogue it is 4.52 eV by B3LYP method. The smaller energy gap indicates the greater reactivity of the compounds. It has been found from the literature that the HOMO-LUMO energy gap for ethyl-4-formyl-3,5-dimethyl-1H-pyrrole-2-carboxylate thiosemicarbazone obtained from B3LYP/6-31G(d,p) is 4.16 eV [29]. This reflects the chemical stability of the title compound [30].

8.3.2 Vibrational frequencies

Selected stretching frequencies of 2-(4-bromophenyl)-3-(4-hydroxyphenyl)-1,3-thiazolidin-4-one and its selenium analogue are collected in the Table 8.5. The carbonyl stretching C = O vibration [31] is expected to occur in the region 1765–1680 cm^{-1} . The band observed at 1621 cm^{-1} in FT-IR is attributed to C = O stretching vibration and for the selenium analogue the computed value for C = O vibration matches with the literature value [32]. C-Br stretching vibration usually occurs in the region 650–485 cm^{-1} [33]. C-Br vibration in thioxanthone appears at 650 cm^{-1} . For compound 1, the peak observed at 693 cm^{-1} is assigned to C-Br stretching vibration and it matches with the theoretical value 680.7 cm^{-1} obtained by BP86 method. O-H stretching vibration appears in the region 3750–3900 cm^{-1} [34]. The band observed at 3835.1 cm^{-1} in FT-IR is attributed to O-H stretching vibration and for the selenium analogue the computed value for O-H vibration matches with the literature value.

Table 8.5: Stretching frequencies of the carbonyl, C-Br and C-OH linkages of 2-(4-bromophenyl)-3-(4-hydroxyphenyl)-1,3-thiazolidin-4-one and its selenium analogue.

Level of theory	B3LYP	BP86	M06	HF	HF	Experimental [21]
Basis set		6-311++ G(d,p)			6-31G	
2-(4-bromophenyl)-3-(4-hydroxyphenyl)-1,3-thiazolidin-4-one						
C = O	1757	1697	1807	1802	1852	1621
O-H	3835	3706	3893	4186	4047	3864
C-Br	668	681	667	673	661	693
2-(4-bromophenyl)-3-(4-hydroxyphenyl)-1,3-selenazolidin-4-one						
C = O	1848	1743	1798	1925	1848	
O-H	4047	3834	3890	4186	4047	
C-Br	708	652	660	701	708	

8.3.3 Atomic charges

Atomic charges influence properties like molecular polarizability, dipole moment, electronic structure and other properties of molecular systems. Hence, quantum mechanical calculation plays an important role in analysing structures at molecular level [35]. From Table 8.6, it is observed that N1, C2, S1, C3 and H12 atoms have positive charges except for HF/6-31G(d) method and they act as electron acceptor atom. It is also observed that C1, O1, Br1 and O2 atoms have negative charges and they act as electron donor atoms. Similarly, from Table 8.7, it is observed that for the selenium compound, N1, C2, Se1 and H12 atoms have positive charges and act as electron acceptor atoms and atoms like C1, C3, O1, Br1 and O2 have negative charge and act as electron donor atoms.

Table 8.6: Mulliken charges (e) on the atoms of 2-(4-bromophenyl)-3-(4-hydroxyphenyl)-1,3-thiazolidin-4-one.

Level of theory	B3LYP	BP86	M06	HF	HF
Basis set	6-311++ G(d,p)			6-31G(d)	
Atom					
N1	0.295	0.388	0.107	0.391	-0.923
C2	0.199	0.187	0.191	0.503	0.797
C1	-0.781	-0.892	-0.825	-0.867	-0.657
S1	-0.152	-0.137	0.102	0.009	0.319
C3	0.203	0.241	0.187	0.185	-0.267
O1	-0.269	-0.235	-0.246	-0.343	-0.575
Br1	-0.178	-0.192	-0.273	-0.264	0.162
O2	-0.225	-0.181	-0.246	-0.295	-0.790
H12	0.261	0.261	0.285	0.275	0.419

Table 8.7: Atomic charges (e) on the atoms of 2-(4-bromophenyl)-3-(4-hydroxyphenyl)-1,3-selenazolidin-4-one.

Level of theory	B3LYP	BP86	M06	HF	HF
Basis set	6-311++ G(d,p)			6-31G(d)	
Atom					
N1	0.443	0.443	0.276	0.522	0.904
C2	0.143	0.143	0.0635	0.383	0.821
C1	-0.516	-0.516	-0.512	-0.564	-0.712
Se1	0.00156	0.00156	0.0712	-0.102	0.395
C3	-1.223	-1.223	-0.469	-0.461	-0.370
O1	-0.248	-0.248	-0.239	-0.329	-0.578
Br1	-0.177	-0.179	-0.197	-0.265	0.159
O2	-0.223	-0.223	-0.234	-0.296	-0.790
H12	0.262	0.262	0.284	0.275	0.418

8.3.4 Molecular orbitals surfaces

The HOMO-LUMO surfaces are given in Figure 8.2. The energy of the HOMO is directly related to the ionization potential and LUMO energy is related to the electron affinity [36]. Energy difference between HOMO and LUMO orbital explains the stability of structures [37]. The highest molecular orbitals of the compounds are on the heterocyclic ring and the phenyl rings with the -OH group. This implies that they are the most active parts of the molecule. The electron density is therefore transferred from these rings to the phenyl ring containing bromine. A similar trend is observed for the selenium analogue too.

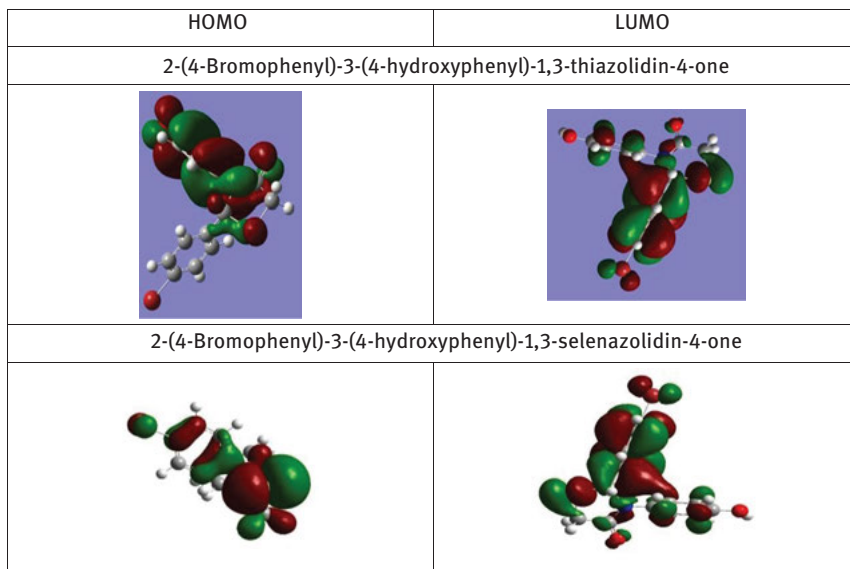


Figure 8.2: Highest occupied molecular orbital (HOMO) and the lowest occupied molecular orbital (LUMO) surfaces [B3LYP/6-311++ G(d,p)] of (a) 2-(4-bromophenyl)-3-(4-hydroxyphenyl)-1,3-thiazolidin-4-one and its (b) selenium analogue.

8.3.5 Natural bond orbital analysis (NBO)

The useful aspect of NBO is that it provides an accurate method for studying charge transfer or conjugative interaction in various molecular systems [38, 39]. The selected Lewis (bond or lone pair) NBO of the title compound and selenium analogue are presented in the Table 8.8 and Table 8.9. The valence hybrids analysis of NBO show

Table 8.8: Selected Lewis NBO orbitals of 2-(4-bromophenyl)-3-(4-hydroxyphenyl)-1,3-thiazolidin-4-one.

Bond	NBO hybrid orbitals	s (%)	p (%)
σ_{C1-S1}	0.7257 ($sp^{3.64}$) C1 +	21.53	78.31
	0.6880 ($sp^{5.69}$) S1	14.87	84.57
σ_{C2-N1}	0.6000 ($sp^{2.20}$) C2 +	31.25	68.64
	0.8000 ($sp^{1.98}$) N1	33.53	66.43
σ_{C2-O1}	0.5852 ($sp^{2.91}$) C2 +	25.49	74.28
	0.8109 ($sp^{2.24}$) O1	30.80	69.09
σ_{C3-N1}	0.6119 ($sp^{3.19}$) C3 +	23.83	76.04
	0.7909 ($sp^{2.16}$) N1	31.60	68.37
σ_{C3-S1}	0.7361 ($sp^{4.21}$) C3 +	19.16	80.70
	0.6769 ($sp^{6.26}$) S1	13.70	85.74
σ_{C10-N1}	0.6077 ($sp^{2.78}$) C10 +	26.40	73.51
	0.7942 ($sp^{1.93}$) N1	34.14	65.83

that the C-S bond is polarized towards sulfur (85 %) whereas the C-N bond and C-O bond orbitals are polarized towards carbon (76 % and 74 %, respectively). For the selenium analogue, C-Se and C-Br bonds are polarized towards selenium (85 %) and bromine (85 %), respectively, whereas the C-O bond orbital is polarized towards carbon (74 %).

Table 8.9: Selected Lewis NBO orbitals 2-(4-bromophenyl)-3-(4-hydroxyphenyl)-1,3-selenazolidin-4-one.

Bond	NBO hybrid orbitals	s (%)	p (%)
σ_{C1-}	0.7679 ($sp^{3.38}$) C1 +	22.84	77.16
$Se32$	0.6405 ($sp^{5.30}$) Se1	15.88	84.12
σ_{C4-}	0.5786 ($sp^{2.85}$) C4 +	25.97	74.03
$O28$	0.8156 ($sp^{1.98}$) O28	31.94	68.06
σ_{C4-}	0.5994 ($sp^{2.17}$) C4 +	31.50	68.50
$N27$	0.8005 ($sp^{1.96}$) N27	33.75	66.25
σ_{C5-}	0.7762 ($sp^{3.78}$) C5 +	20.90	79.10
$Se32$	0.6304 ($sp^{5.78}$) Se1	14.74	85.26
σ_{C12-}	0.7063 ($sp^{3.86}$) C12 +	21.92	78.08
$Br31$	0.7069 ($sp^{6.04}$) Br	14.20	85.80

8.4 Conclusions

In the present work, theoretical quantum chemical calculations was carried out for 2-(4-bromophenyl)-3-(4-hydroxyphenyl)-1,3-thiazolidin-4-one and its selenium analogue. The calculated geometrical parameters and vibrational frequencies obtained from density functional theory calculations are in good agreement with the experimental values obtained for the investigated molecule. HOMO–LUMO energy gap explains the eventual charge transfer interactions taking place within the compound. NBO analysis confirms the hyperconjugative interactions within the molecule. Various thermodynamic parameters were evaluated to study the stability of the compounds.

Acknowledgements: HPK acknowledges the University Grants Commission of India and Tertiary Education Commission for the financial assistance. The authors thank their respective universities for the facilities provided.

References

- [1] Srivastava SK, Srivastava SL, Srivastava SD. Synthesis of 5-Arylidene-2-aryl-3-(2-chloropheno-thiazinoacetamidyl)-1,3-thiazolidin-4-ones as Antifungal and Anticonvulsant Agents. J Indian Chem Soc. 2000;39B:464–7
- [2] Gomtsyan A. Heterocycles in Drugs and Drug Discovery. Chem Heterocycl Compd. 2012;48:7–10.
- [3] Dua R, Shrivastava S, Sonwane SK, Srivastava SK. Pharmacological Significance of Synthetic Heterocycles Scaffold : A Review. Adv Biol Res (Rennes). 2011;5:120–44.

- [4] Solankee AN, Patel KP, Patel RB. Efficient Synthesis and Pharmacological Evaluation of some New 4-Thiazolidinones and 5-Arylidenes. *Arch Appl Sci Res.* 2012;4:72–7.
- [5] Ravichandran V, Jain A, Kumar KS, Rajak H, Agrawal RK. Design, Synthesis, and Evaluation of Thiazolidinone Derivatives as Antimicrobial and Antiviral Agents. *Chem Biol Drug Des.* 2011;78:464–70.
- [6] Devappa SL, Reddy KRV, Govinda Raju Reddy KB, Sahana KN, Smitha NC. A Simple and Efficient Carbodiimide Mediated One-Pot Synthesis of Novel 2-(2-hydroxynaphthalen-1-yl)-3-phenyl-1,3-thiazolidin-4-one Derivatives: A Potent Antimicrobial Agent. *Int J ChemTech Res.* 2010;2:1220–8.
- [7] Bhati SK, Kumar A. Synthesis of New Substituted Azetidinoyl and Thiazolidinoyl-1,3,4-thiazidino (6,5-b) Indoles as Promising Anti-Inflammatory Agents. *Eur J Med Chem.* 2008;43:2323–30.
- [8] Voss ME, Carter PH, Tebben AJ, Scherle PA, Brown GD, Thompson LA, Xu M, Lo YC, Yang G, Liu R-Q, Strzemienski P, Everlof JG, Trzaskos JM, Decicco CP. Both 5-Arylidene-2-thioxodihydropyrimidine-4,6(1H,5H)-diones and 3-Thioxo-2,3-dihydro-1H-imidazo[1,5-a]indol-1-ones are Light-Dependent Tumor Necrosis Factor- α Antagonists. *Bioorg Med Chem Lett.* 2003;13:533–8.
- [9] Karthikeyan SV, Perumal S, Shetty KA, Yogeewari P, Sriram D. A Microwave-Assisted Facile Regioselective Fischer Indole Synthesis and Antitubercular Evaluation of Novel 2-Aryl-3,4-dihydro-2H-thieno[3,2-b]indoles. *Bioorg Med Chem Lett.* 2009;19:3006–9.
- [10] Agarwal A, Lata S, Saxena KK, Srivastava VK, Kumar A. Synthesis and Anticonvulsant Activity of some Potential Thiazolidinonyl 2-Oxo/Thiobarbituric Acids. *Eur J Med Chem.* 2006;41:1223–9.
- [11] Ravichandran V, Prashantha Kumar BR, Sankar S, Agrawal RK. Predicting Anti-HIV Activity of 1,3,4-Thiazolidinone Derivatives: 3D-QSAR Approach. *Eur J Med Chem.* 2009;44:1180–7.
- [12] Chaudhari SK, Verma M, Chaturvedi AK, Parmar SS. Substituted Thiazolidones: Selective Inhibition of Nicotinamide Adenine Dinucleotide-Dependent Oxidations and Evaluation of their CNS Activity. *J Pharma Sci.* 1975;64:614–7.
- [13] Jain AK, Vaidya A, Ravichandran V, Kashaw SK, Agrawal AK. Recent Developments and Biological Activities of Thiazolidinone Derivatives: A Review. *Bioorg Med Chem.* 2012;20:3378–95.
- [14] Jaya Preethi P, Bindu Sree K, Pavan Kumar K, Rajavelu R, Sivakumar T. Synthesis, Characterization and its Biological Evaluation of some Novel 4-Thiazolidinone and 2-Azetidinone Derivatives. *Asian J Pharm Res.* 2012;2:63–70.
- [15] Sriram D, Yogeeshwari P, Ashok Kumar TG. Microwave-Assisted Synthesis and Anti-YFV Activity of 2,3-Diaryl-1,3-thiazolidin-4-ones. *J Pharm Pharm Sci.* 2005;8:426–9.
- [16] Gupta R, Chaudhary RP. X-ray, NMR and DFT Studies on Benzo[h]thiazolo[2,3-b]quinazoline Derivatives. *J Mol Struct.* 2013;1049:189–197.
- [17] Ostadalova I. Biological Effects of Selenium Compounds with a Particular Attention to the Ontogenetic Development. *Physiol Res.* 2012;61:S19–S34.
- [18] Iwaoka M, Arai K. From Sulfur to Selenium. A New Research Arena in Chemical Biology and Biological Chemistry. *Curr Chem Biol.* 2013;7:2–24.
- [19] Kaur R, Singh HB, Patel RP, Kulshreshtha SK. Syntheses, Characterization and Molecular Structures of Monomeric Selenolato Complexes of Mercury with Nitrogen-Containing Chelating Ligands. *J Chem Soc Dalton Trans.* 1996;461–7
- [20] Bochmann M. Metal Chalcogenide Materials: Chalcogenolato complexes as “single-source” precursors. *Chem Vap Deposition.* 1996;2:85–96.
- [21] Vennila JP, John Thiruvadigal D, Kavitha HP, Chakkaravarthi G, Manivannan V. 2-Chloro-4,6-bis(piperidin-1-yl)-1,3,5-triazine. *Acta Cryst.* 2011;67:1902.
- [22] Frisch MJ, Trucks GW, Schlegel HB, Scuseria GE, Robb MA, Cheeseman JR. Gaussian 03, Revision C.02, Wallingford, CT: Gaussian Inc., 2004.

- [23] Dennington II R, Keith T, Milliam J, Eppinnett K, Hovell WL, Gilliland R. GaussView, version 3.09, Shawnee Mission, KS: Semichem, Inc., 2003.
- [24] Arjunan V, Arushma R, Santhanam R, Marchewka MK, Mohan S. Structural, Vibrational, Electronic Investigations and Quantum Chemical Studies of 2-Amino-4-methoxybenzothiazole. *Spectrochim Acta A Mol Biomol Spectrosc.* 2013;102:327–40.
- [25] Hodage AS, Phadnis PP, Wadawale A, Priyadarsini KI, Jain VK. Crystal Structure of 2,2,4-Diselenobis(acetic acid). *X-Ray Struct Anal Online.* 2009;25:101. © The Japan Society for Analytical Chemistry.
- [26] Kandasamy K, Kumar S, Singh HB, Butcher RJ, Holman T. Synthesis, Structural Characterization and Fluorescence Properties of Organoselenium Compounds Bearing a Ligand Containing both Bulky and Nonbonding Groups – The First Observation of both Intramolecular Se...N and Se...O Interactions in a Diselenide Structure. *Eur J Inorg Chem.* 2004;2004:1014–23
- [27] Rhyman L, Abdallah HH, Ramasami P. Quantum Mechanical Study of the Syn-Anti Isomerisation of 2-Tellurophenecarbaldehyde: Vive la Différence. *Spectrochim Acta A Mol Biomol Spectrosc.* 2011;78:258–63.
- [28] Rhyman L, Abdallah HH, Ramasami P. Theoretical Study of the Structural, Spectroscopic and Energetic Properties of Difluoro(germylthio)phosphine and Difluoro(germylseleno)phosphine in the Gas Phase. *Polyhedron.* 2010;29:220–5.
- [29] Singh RN, Amit K, Tiwari RK, Poonam R, Divya V, Baboo V. Synthesis, Molecular Structure and Spectral Analysis of Ethyl 4-Formyl-3,5-dimethyl-1H-pyrrole-2-carboxylate Thiosemicarbazone: A Combined DFT and AIM Approach. *J Mol Struct.* 2012;1016:97–108.
- [30] Rhyman L, Abdallah HH, Ramasami P. Quantum Mechanical Study of the Structure and Spectroscopic Characterisation of the Novel Trisilylsilylcyanide and Trigermylgermylcyanide in the Gas Phase. *Polyhedron.* 2010;29:1168–74.
- [31] Roeges NPG. A guide to the complete interpretation of infrared spectra of organic structures. New York: Wiley, 1981.
- [32] Barthes M, De Nunzio G, Ribet M. Polarons or proton transfer in chains of peptide groups?. *Synth Met.* 1996;76:337–40.
- [33] Bahgat K, Ragheb AG. Analysis of Vibrational Spectra of 8-Hydroxyquinoline and its 5,7-Dichloro, 5,7-Dibromo, 5,7-Diiodo and 5,7-Dinitro Derivatives Based on Density Functional Theory Calculations. *Cent Europ J Chem.* 2007;5:201–21.
- [34] Singh RN, Amit K, Tiwari RK, Rawat P. A Combined Experimental and Theoretical (DFT and AIM) Studies on Synthesis, Molecular Structure, Spectroscopic Properties and Multiple Interactions Analysis in a Novel Ethyl-4-[2-(thiocarbamoyl)hydrazinylidene]-3,5-dimethyl-1H-pyrrole-2-carboxylate and its Dimer. *Spectrochim Acta A Mol Biomol Spectrosc.* 2013;112:182–90.
- [35] Jensen JN. Vibrational Frequencies and Structural Determination of Tetraazidogermane. *Spectrochim Acta A Mol Biomol Spectrosc.* 2003;59:2805–14.
- [36] Gece G. The Use of Quantum Chemical Methods in Corrosion Inhibitor Studies. *Corros Sci.* 2008;50:2981-2992.
- [37] Fukui K. Role of Frontier Orbitals in Chemical Reactions. *Science.* 1987;218:747–54.
- [38] Jensen JN. Vibrational Frequencies and Structural Determination of Triethynylmethylgermane. *Spectrochim Acta A Mol Biomol Spectrosc.* 2004;60:2819–24.
- [39] Gupta R, Chaudhary RP X-ray, NMR and DFT Studies on Benzo[h]thiazolo[2,3-b]quinazoline Derivatives. *J Mol Struct.* 2013;1049:189–97.

Aleksey E. Kuznetsov

9 Complexes between core-modified porphyrins $ZnP(X)_4$ ($X = P$ and S) and small semiconductor nanoparticle Zn_6S_6 : are they possible?

Abstract: The synthetic approach of the anchoring of porphyrins to the surface of semiconductor nanoparticles (NPs) has been realized to form very promising organic/inorganic nanocomposites. They have been of considerable scientific and a wide practical interest including such areas as material science, biomedical applications, and dye-sensitized solar cells (DSSCs). Macrocyclic pyrrole-containing compounds, such as phthalocyanines and porphyrins, can bind to the NP surface by a variety of modes: as monodentate ligands oriented perpendicular to the NP surface, parallel to the NP surface, or, alternatively, in a perpendicular orientation bridging two adjacent NPs. Also, non-covalent (coordination) interactions may be realized between the NP via its metal centers and appropriate *meso*-attached groups of porphyrins. Recently, we showed computationally that the prominent structural feature of the core-modified $MP(X)_4$ porphyrins ($X = P$) is their significant distortion from planarity. Motivated by the phenomenon of numerous complexes formation between tetrapyrroles and NPs, we performed the density functional theory (DFT) studies of the complex formation between the core-modified $ZnP(X)_4$ species ($X = P$ and S) *without any substituents or linkers* and semiconductor NPs, exemplified by small NP Zn_6S_6 . The complexes formation was investigated using the following theoretical approaches: (i) B3LYP/6-31G* and (ii) CAM-B3LYP/6-31G*, both in the gas phase and with implicit effects from C_6H_6 considered. The calculated binding energies of the complexes studied were found to be significant, varying from ca. 29 up to ca. 69 kcal/mol, depending on the complex and the approach employed.

Keywords: core-modified metalloporphyrins, semiconductor quantum dots, complexes formation, density functional theory

This article has previously been published in the journal *Physical Sciences Reviews*. Please cite as: Kuznetsov, A. E. Complexes between core-modified porphyrins $ZnP(X)_4$ ($X = P$ and S) and small semiconductor nanoparticle Zn_6S_6 : are they possible?. *Physical Sciences Reviews* [Online] **2018**, 3. DOI: 10.1515/psr-2017-0187

<https://doi.org/10.1515/9783110568196-009>

9.1 Introduction

Porphyrins and their versatile derivatives, including metal-containing forms of those, have attracted the researchers' attention because their stable aromatic core can be functionalized at *meso*- or pyrrolic β -positions and the central metal can tune their chemical, electronic, and photophysical properties broadly. Chemists have incorporated metalloporphyrins and their derivatives in numerous molecular architectures for various fields of applications [1–3], e. g., artificial photosynthesis [4, 5], molecular electronics [6, 7], molecular machines [8, 9], catalysis [10, 11], therapy [12], and surface engineering [13]. The use of porphyrins as a host structure in the design of nanoassemblies offers several attractive opportunities [1]: porphyrin molecule as a large structural element will define the shape of the molecular cavity, and its metal-containing core can coordinate various ligands within the cage.

The synthetic approach of the anchoring of various functional organic molecules, including porphyrins and other heteromacrocycles and even proteins, to the surface of semiconductor nanoparticles (often referred to as quantum dots, QD, e. g., CdSe, CdTe or CdSe/ZnS and other II–VI systems) has been realized to form very promising organic/inorganic nanocomposites [14]. They have been of considerable scientific and a wide practical interest including such areas as material science [14–20], biomedical applications [21, 22], and dye-sensitized solar cells (DSSCs) [23–35]. With respect to the formation and potential applications of the porphyrin-QD nanoassemblies in liquid or solid phase several factors were considered to be of essential importance [14]: (i) attachment/detachment of dye molecules to QD, (ii) the interplay between dye molecule attachment and capping ligand exchange, and (iii) the presence and formation of various surface trap states in the QD bandgap whose properties may be tuned by interface reconstruction or competing ligand/dye exchange dynamics.

Macrocyclic pyrrole-containing compounds, such as phthalocyanines and porphyrins, can bind to the QD surface by variety of modes. Thus, so-called subphthalocyanines (the lowest phthalocyanines homologues composed of three diiminoisoindole rings N-fused around a boron core) [36] possess a *cup-shaped structure*, suggesting a good geometric match with NPs having diameters in the 2–3 nm range; in addition, they contain a functional group (e. g., -OPh) perpendicular to the macrocycle which offers the possibility of connecting to other NPs by covalent bonds [37]. Porphyrins with four phenyl substituents attached to the tetrapyrrole macrocycle in *meso*-positions (tetraphenylporphyrins, TPP) bearing one -COOH group and three long-chained alkoxide (or other similar groups) attached to these phenyls were shown to act as monodentate ligands oriented perpendicular to the NP surface [37]. On the other hand, when all the four phenyls bear -COOH or -SH groups, these compounds are able to attach themselves to QDs in the flat-on mode, i. e., parallel to the NP surface, or, alternatively, these ligands may adopt a perpendicular orientation bridging between two adjacent quantum dots [37]. Computationally, two

possibilities for binding of ZnTPP with the CdTe QDs were found by Rajbanshi and Sarkar in 2016: through the amide linkage connected to the *meso*-phenyl group of ZnTPP and through the $-S-(CH_2)_3-NH_2$ ligands of the QD bound to the Zn center of ZnTPP [23]. Also, non-covalent (coordination) interactions may be realized between the QD via its metal centers and appropriate *meso*-attached groups of porphyrins [14]. It is also worthwhile to mention some more details of the previous experimental studies of the nanohybrids composed of porphyrins and CdTe QDs. Thus, Jhonsi and Renganathan in 2010 [24] showed that for the positively charged porphyrin electron transfer from thioglycolic acid (TGA) capped CdTe QDs to porphyrin occurs, whereas negatively charged porphyrin moieties were involved in the energy transfer mechanism. 2012 work by Amelia and Credi [25] demonstrated the energy transfer from a Zn-phenylporphyrin noncovalently bound to 5.6 nm CdTe QD in chloroform. Keane et al. [26] reported the donor–acceptor composite of *meso*-tetrakis(4-*N*-methylpyridyl) zinc porphyrin (ZnTMPyP₄) and TGA coated CdTe QD to exhibit very rapid photoinduced electron transfer. In 2015, Aly et al [27]. reported the experimental observations of controlled ultrafast electron transfer at cationic porphyrin-CdTe QD interfaces.

In spite of the fact that in general various porphyrin-QD nanocomposites have drawn the great attention of experimentalists, their theoretical investigations are still rather limited. Recently, we reported the computational studies of the structures and electronic properties of the series of metalloporphyrins with all the four pyrrole nitrogens replaced with P-atoms, MP(P)₄, M = Sc-Zn [38–40]. We showed that the prominent structural feature of all the MP(P)₄ compounds studied is their significant distortion from planarity leading to the bowl-like shape [38–40]. Moreover, motivated by the phenomenon of stack formation by regular metalloporphyrins, we performed the computational check of the stack formation between the MP(P)₄ species without any linkers or substituents, choosing the ZnP(P)₄ species as the simplest MP(P)₄ compound [41]. Three modes of binding or coordination were shown to be possible between the monomeric ZnP(P)₄ units. The “convexity-to-convexity” dimer was shown to be the most stable compound with the highest binding energy calculated among the three types of dimers studied. Of course, it would be extremely significant and interesting to further advance into the understanding of the potential significance of core-modified MP(X)₄ compounds and their future application areas. Computational studies, without any doubts, can be of great help here.

Thus, motivated by both the numerous examples of the formation of complexes/nanoassemblies between various QDs and regular metalloporphyrins and their derivatives and relative scarcity of their computational studies, we decided to investigate computationally if the complex formation between core-modified MP(X)₄ porphyrins and semiconductor quantum dots, exemplified by small NP Zn₆S₆, *without any substituents or linkers* would be possible (for computational details of the research see Supporting Information, [44–58]). For this study, we chose two core-modified Zn-porphyrins, Zn^{II}P(P)₄ and Zn^{II}P(S)₄. We decided to focus on these species because they are relatively simple representatives of the core-modified MP(X)₄ compounds,

with relatively “inactive” d-electrons. Moreover, these compounds were quite intensively investigated earlier, both by us and other researchers [38–43]. The paper is organized as follows: in the following section, we address binding details and structural features of the calculated $\text{Zn}_6\text{S}_6\text{-ZnP(X)}_4$ complexes; next, we address the $\text{Zn}_6\text{S}_6\text{-ZnP(X)}_4$ complexes electronic properties; finally, we summarize the research findings and discuss further research perspectives.

9.2 Results and discussion

9.2.1 Structural features of the $\text{Zn}_6\text{S}_6\text{-ZnP(X)}_4$ complexes

The $\text{Zn}_6\text{S}_6\text{-ZnP(X)}_4$ complexes calculated at the CAM-B3LYP/6-31G* level with the effects from implicit C_6H_6 are shown in Figure 9.1. Comparison of their structures along with considering the structures of the free ZnP(X)_4 species and Zn_6S_6 NP (see Figs. S1–S3) shows the following. For both $X = \text{P}$ and S , similar mode of the NP coordination to the core-modified Zn-porphyrin was found, with one of the S-centers of the NP forming relatively short bond with the Zn-center of the porphyrin, 2.29 and 2.18 Å for $X = \text{P}$ and S , respectively. It is worthwhile to notice that using the B3LYP/6-31G* approach in the gas phase for $X = \text{P}$ gave just slightly longer bond distance between the NP and the Zn-center of the porphyrin, 2.32 Å (see Fig. S3). We can consider this bond as formed by donation of the S-center free electron pair to the Zn-center. Upon the complex formation, the NP undergoes slight structural changes: the interlayer Zn-S bond

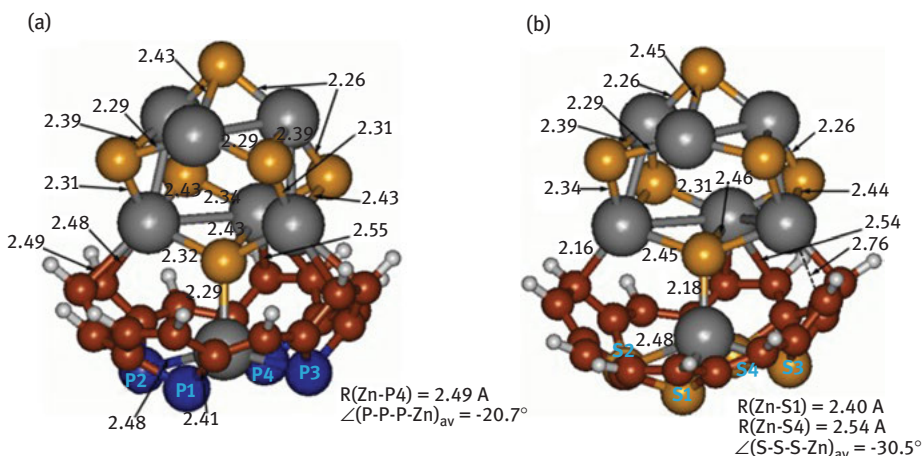


Figure 9.1: The structures of the complexes $\text{Zn}_6\text{S}_6\text{-ZnP(X)}_4$, $X = \text{P}$ (a) and S (b), calculated at the CAM-B3LYP/6-31G* level with implicit C_6H_6 . The color coding is as follows: dark grey corresponds to Zn, yellow corresponds to S, greyish white corresponds to H, brown corresponds to C, and dark blue corresponds to P. Distances are given in Å.

distances become slightly elongated, by up to 0.05–0.06 Å (cf. Supporting Information, Fig. S1). The interlayer Zn-S bond distances of the NP are elongated in the part of the NP bound to the Zn-porphyrin, up to 0.07 Å for X = P (cf. Figure 9.1a) and up to 0.18 Å for X = S (cf. Figure 9.1b). But, generally, the NP is not noticeably distorted and essentially keeps its shape.

However, the situation is noticeably different for the $\text{ZnP}(X)_4$ species. First of all, it is interesting to notice that the free $\text{ZnP}(S)_4$ compound was calculated to have a triplet as a ground state at the B3LYP/6-31G* and CAM-B3LYP/6-31G* levels of theory, both in the gas phase and with effects from implicit benzene taken into account (the triplet being more stable than the singlet by 3.6/0.9 and 5.8/2.9 kcal/mol for B3LYP/6-31G* and CAM-B3LYP/6-31G*, gas phase/ C_6H_6 , respectively, Table S2). But for the Zn_6S_6 - $\text{ZnP}(S)_4$ complex, the singlet structure was calculated to be significantly more stable than the triplet: thus, at the B3LYP/6-31G* level in the gas phase the energy difference was computed to be ca. 25 kcal/mol, and at the CAM-B3LYP/6-31G* level it is just a little smaller, being 21.3/19.6 kcal/mol in the gas phase and benzene, respectively (see Table S1). Next, the core-modified porphyrin species become noticeably distorted upon the complex formation. Thus, in the $\text{ZnP}(P)_4$ species, the Zn-P bond distances are elongated compared to the free species by 0.05–0.13 Å and the average dihedral angle P-P-P-Zn becomes much more negative compared to the free species. This means that the Zn-center significantly protrudes inside the “bowl” made by the molecular framework due to the interaction with the S-center of the coordinated NP (cf. Fig. S2). The whole structure of the $\text{ZnP}(P)_4$ moiety generally changes from approximately C_{4v} symmetry to approximately C_s symmetry. In the $\text{ZnP}(S)_4$ moiety within the complex, the Zn-S bond distances are shortened compared to the free species by 0.17–0.32 Å, the average dihedral angle S-S-S-Zn is decreased by ca. 16° compared to the free species, which means that now the Zn-center protrudes less inside the “bowl” made by the molecular framework compared to the free porphyrin (cf. Fig. S3). In this case, the free $\text{ZnP}(S)_4$ has approximate C_{2v} symmetry whereas within the complex it attains approximate C_s symmetry.

In both complexes, the NP forms relatively short, ca. 2.5 Å, bonds by coordination of the Zn-center with the α -carbon atoms on the one side of the porphyrin macrocycle. Also, in the case of $\text{ZnP}(P)_4$ the NP coordinates by its Zn-centers to two other pairs of the α -carbon atoms of the porphyrin macrocycle, forming even shorter bonds, 2.48–2.49 Å. For $\text{ZnP}(S)_4$, the situation is different: the NP coordinates by its Zn-centers only to one of the pairs of the α -carbon atoms of the porphyrin macrocycle (see Figure 9.1b) but forms quite short bond, 2.16 Å. These interactions between the NP Zn-centers and carbon atoms of the porphyrin macrocycle could be ascribed to van der Waals/dispersion interactions between those. We suppose that they would need further analysis to understand why and how they are formed. In general, both complexes studied possess approximate C_s symmetry, as can be seen from their structures (Figure 9.1).

9.2.2 Binding energies in the Zn_6S_6 -MP(X)₄ complexes

Calculations results presented in Table 9.1 show that the both complexes studied are quite strongly bound. Interestingly, the Zn_6S_6 -ZnP(S)₄ is more stable than the Zn_6S_6 -ZnP(P)₄ compound by more than 23 kcal/mol in the gas phase and almost twice more stable in the solvent phase. With the BSSE corrections in the gas phase the binding energies become noticeably more moderate: 15.2 and 33.2 kcal/mol for Zn_6S_6 -ZnP(P)₄ and Zn_6S_6 -ZnP(S)₄, respectively. Our data fall in the range of the BEs calculated by Rajbanshi and Sarkar [24] for their ZnTPP-Cd₁₇Te₁₇ nanocomposites, with the BE for the axially coordinated nanocomposite being 45.4 kcal/mol and BE for the amide-linked composite being 3 kcal/mol (without BSSE correction). However, it is necessary to take into account here both the significant difference between the systems studied and the methods employed (PBE approach with the Slater-type orbitals in the Rajbanshi and Sarkar [24] study). We were not able to find any other computational studies of complexes between QDs and porphyrins or their derivatives in order to compare BEs.

Table 9.1: Binding energies of the Zn_6S_6 -ZnP(X)₄ complexes computed at the CAM-B3LYP/6-31G* level, in the gas phase and with implicit effects from benzene, kcal/mol.

Complex	Gas phase	Benzene
Zn_6S_6 -ZnP(P) ₄	45.4	29.4
Zn_6S_6 -ZnP(S) ₄	68.7	52.8

The higher stability of the Zn_6S_6 -ZnP(S)₄ complex can be explained by easier interactions between the ZnP(S)₄ porphyrin Zn-center due to its significant protruding inside the “bowl” (cf. Fig. S3) and the S-center of the NP (shorter Zn-S distances in the final complex, cf. Figure 9.1a and 1b), and, possibly, by slightly higher NBO charges on the α -carbons of the ZnP(S)₄ porphyrin macrocycle (cf. Figs. S2 and S3) which could lead to stronger interactions between the α -carbons and the Zn-centers of the NP. Apparently, in general, the shape of the ZnP(S)₄ porphyrin macrocycle is more favorable for the stronger binding between the NP and core-modified porphyrin.

9.2.3 NBO charges in the Zn_6S_6 -MP(X)₄ complexes

Analysis of the gas-phase calculated NBO charges (see Fig. S4) for the both complexes shows the following (we use the gas-phase calculated NBO charge values because they are very close to the charges calculated in the solvent phase).

Some negative charge accumulation occurs at the NP S-center bound to the Zn-center of the core-modified porphyrin, ca. $-0.17 - -0.18$ e (cf. Fig. S1). Generally, the

charge redistribution occurs in the bound NP, its S-centers become slightly more negatively charged and its Z-centers become slightly more positively charged (cf. Figs. S4 and S1). The positive charge on the Zn-center of the core-modified porphyrin slightly *decreases* for the $\text{ZnP}(\text{P})_4$ case (by 0.04e, cf. Figs. S4 and S2), but noticeably *increases* for the $\text{ZnP}(\text{S})_4$ case (by 0.25e, cf. Figs. S4 and S3). The charges on the X-centers of the core-modified porphyrins generally become more positive within the complexes (cf. Fig. S4 and S2-S3). Finally, the negative charges on the α -carbons of the $\text{ZnP}(\text{X})_4$ porphyrin macrocycles bound to the Zn-centers of the NP become somewhat increased, by $-0.08 - -0.09\text{e}$ (cf. Figs. S2-S4).

We can conclude that there is some charge transfer both from the $\text{ZnP}(\text{X})_4$ porphyrin macrocycles to the Zn_6S_6 NP and within the $\text{ZnP}(\text{X})_4$ porphyrin macrocycles and the NP itself. Its detailed picture would require more profound analysis.

9.3 Conclusions and perspectives

Motivated by the numerous examples of the formation of complexes/nanoassemblies between various QDs and regular metalloporphyrins and their derivatives and relative scarcity of their computational studies, we decided to investigate computationally *if the complex formation between core-modified $\text{MP}(\text{X})_4$ porphyrins and semiconductor quantum dots, exemplified by small NP Zn_6S_6 , without any substituents or linkers would be possible*. For this, we chose two core-modified Zn-porphyrins, $\text{Zn}^{\text{II}}\text{P}(\text{P})_4$ and $\text{Zn}^{\text{II}}\text{P}(\text{S})_4$. Using two computational approaches, B3LYP/6-31G* and CAM-B3LYP/6-31G*, in the gas phase and with implicit effects from benzene, we have shown that indeed the Zn_6S_6 - $\text{ZnP}(\text{X})_4$ complexes ($\text{X} = \text{P}$ and S) are possible. We investigated structural features and charges in these two complexes, and our findings are summarized below.

For both $\text{X} = \text{P}$ and S , similar mode of the NP coordination to the core-modified Zn-porphyrin was found, with one of the S-centers of the NP forming relatively short bond with the Zn-center of the porphyrin. We can consider this bond as formed by donation of the S-center free electron pair to the Zn-center. Upon the complex formation the NP undergoes slight structural changes and essentially keeps its shape. However, the situation is noticeably different for the $\text{ZnP}(\text{X})_4$ species. First of all, the free $\text{ZnP}(\text{S})_4$ compound was calculated to have a triplet as a ground state, both in the gas phase and with effects from implicit benzene taken into account (the triplet being more stable than the singlet by 3.6/0.9 and 5.8/2.9 kcal/mol for B3LYP/6-31G* and CAM-B3LYP/6-31G*, gas phase/ C_6H_6 , respectively, cf. Table S2). But for the Zn_6S_6 - $\text{ZnP}(\text{S})_4$ complex, the singlet structure was calculated to be considerably more stable than the triplet.

Next, the core-modified porphyrin species become noticeably distorted upon the complex formation. Thus, in the $\text{ZnP}(\text{P})_4$ species, the Zn-P bond distances are elongated

compared to the free species by 0.05–0.13 Å, the average dihedral angle P-P-P-Zn becomes much more negative compared to the free species, which means that the Zn-center significantly protrudes inside the “bowl” made by the molecular framework due to the interaction with the S-center of the coordinated NP (cf. Fig. S2). In the ZnP(S)_4 moiety within the complex, the Zn-S bond distances are shortened compared to the free species by 0.17–0.32 Å, the average dihedral angle S-S-S-Zn is decreased by ca. 16° compared to the free species, which means that now the Zn-center protrudes less inside the “bowl” made by the molecular framework compared to the free porphyrin (cf. Fig. S3). In the both complexes, the NP forms relatively short, ca. 2.5 Å, bonds by coordination of the Zn-center with the α -carbon atoms on the one side of the porphyrin macrocycle. Also, in the case of ZnP(P)_4 the NP coordinates by its Zn-centers to two other pairs of the α -carbon atoms of the porphyrin macrocycle, forming even shorter bonds, 2.48–2.49 Å. For ZnP(S)_4 , the situation is different: the NP coordinates by its Zn-centers only to one of the pairs of the α -carbon atoms of the porphyrin macrocycle (see Figure 9.1b) but forms quite short bond, 2.16 Å. These interactions between the NP Zn-centers and carbon atoms of the porphyrin macrocycle could be ascribed to van der Waals/dispersion interactions between those.

The both complexes are quite strongly bound, with binding energies varying from ca. 29 up to ca. 69 kcal/mol. With the BSSE corrections in the gas phase the binding energies become 15.2 and 33.2 kcal/mol for $\text{Zn}_6\text{S}_6\text{-ZnP(P)}_4$ and $\text{Zn}_6\text{S}_6\text{-ZnP(S)}_4$, respectively. The higher stability of the $\text{Zn}_6\text{S}_6\text{-ZnP(S)}_4$ complex can be explained by easier interactions between the ZnP(S)_4 porphyrin Zn-center due to its significant protruding inside the “bowl” and the S-center of the NP, and, possibly, by slightly higher NBO charges on the α -carbons of the ZnP(S)_4 porphyrin macrocycle. Apparently, in general, the shape of the ZnP(S)_4 porphyrin macrocycle is more favorable for the stronger binding between the NP and core-modified porphyrin.

Some negative charge accumulation occurs at the NP S-center bound to the Zn-center of the core-modified porphyrin, ca. $-0.17 - -0.18 e$. There is some charge transfer both from the ZnP(X)_4 porphyrin macrocycles to the Zn_6S_6 NP and within the ZnP(X)_4 porphyrin macrocycles and the NP itself. Its detailed picture would require more profound analysis.

Thus, we have obtained quite interesting and intriguing results showing that the complex formation between semiconductor NPs and *core-modified metalloporphyrins* is possible without any linkers or substituents connecting the both components of the complex. It would be really good if these findings would be checked experimentally. Meanwhile, based on the obtained results, we can formulate for ourselves the following research questions to consider (some of them are being under consideration currently):

- i. Detailed analysis of the bonding between the components of these complexes. Investigation of possibilities for other coordination modes between the NP and core-modified porphyrin.

- ii. Detailed electronic features of these complexes (molecular orbitals picture, ionization potentials and electron affinities). Optical and charge-transfer properties of these complexes.
- iii. Dependence of structures and electronic properties and strength of binding between the components on different metals included in the core-modified porphyrins and on various core-modifying elements (X = O, Se, Te, etc.).
- iv. Possibility of the complex formations for larger NPs and NPs of other types – for instance, Zn₉S₉, Zn₁₂S₁₂, Zn₃₃S₃₃, Cd₆Se₆, Cd₃₃Se₃₃, Cd₆Te₆, etc.

Funding: This work was partially supported by the Conselho Nacional de Desenvolvimento Científico e Tecnológico (CNPq) grant “Estudo Teórico Computacional de Sistemas Nanoestruturados com Potencial Aplicação Tecnológica”, number 402313/2013-5, approved in the call N° 70/2013 Bolsa de Atração de Jovens Talentos – BJT – MEC/MCTI/CAPES/CNPq/FAPs/Linha 2 – Bolsa de Atração de Jovens Talentos – BJT. Partial support comes also from the University of São Paulo – SP. The computational resources of the Centro Nacional de Processamento de Alto Desempenho – UFC are highly appreciated.

References

- [1] Durot S, Taesch J, Heitz V. Multiporphyrinic cages: Architectures and functions. *Chem Rev.* 2014;114:8542–78.
- [2] Kim D. Multiporphyrin arrays: Fundamentals and applications. Singapore: Pan Stanford Publishing, 2012:828.
- [3] Kadish KM, Smith KM, Guillard R. Handbook of porphyrin science, vol. 1. London: World Scientific Publishing, 2010.
- [4] Aratani N, Kim D, Osuka A. Discrete cyclic porphyrin arrays as artificial light-harvesting antenna. *Acc Chem Res.* 2009;42:1922–34.
- [5] Wasielewski MR. Self-assembly strategies for integrating light harvesting and charge separation in artificial photosynthetic systems. *Acc Chem Res.* 2009;42:1910–21.
- [6] Kang BK, Aratani N, Lim JK, Kim D, Osuka A, Yoo K-H. Electrical transport properties and their reproducibility for linear porphyrin arrays. *Mater Sci Eng, C.* 2006;26:1023.
- [7] Jurow M, Schuckman AE, Batteas JD, Drain CM. Porphyrins as molecular electronic components of functional devices. *Coord Chem Rev.* 2010;254:2297.
- [8] Ogi S, Ikeda T, Wakabayashi R, Shinkai S, Takeuchi M. A bevel-gear-shaped rotor bearing a double-decker porphyrin complex. *Chem Eur J.* 2010;16:8285.
- [9] Lang T, Graf E, Kyritsakas N, Hosseini MW. An oscillating molecular turnstile. *Dalton Trans.* 2011;40:5244.
- [10] To W-P, Liu Y, Lau T-C, Che C-M. A robust palladium(II)–Porphyrin complex as catalyst for visible light induced oxidative C-H functionalization. *Chem Eur J.* 2013;19:5654.
- [11] Meunier B, Robert A, Pratviel G, Bernardou J. In Kadish KM, Smith KM, Guillard R, editors. *The porphyrin handbook*, vol. 4. San Diego, CA: Academic Press, 2010:119–88.
- [12] Therrien B. Chemistry of nanocontainers. In: Albrecht M., Hahn E., editors. *Topics in current chemistry*. Vol. 319. Berlin, Heidelberg: Springer, 2012:35–55.

- [13] Drain CM, Varotto A, Radivojevic I. Self-organized porphyrinic materials. *Chem Rev.* 2009;109:1630.
- [14] Zenkevich EI, Von Borczyskowski C. Self-organization principles in the formation of multi-porphyrin complexes and “semiconductor quantum dot-porphyrin” nanoassemblies. *J Porphyrins Phthalocyanines.* 2014;18:1–19.
- [15] Stewart MH, Huston AL, Scott AM, Efros AL, Melinger JS, Gemmill KB, Trammell SA, et al. Complex Förster energy transfer interactions between semiconductor quantum dots and a redox-active osmium assembly. *ACS Nano.* 2012;6:5330–47.
- [16] Lee JR, Whitley HD, Meulenberg RW, Wolcott A, Zhang JZ, Prendergast D, Lovingood DD, et al. Ligand-mediated modification of the electronic structure of CdSe quantum dots. *Nano Lett.* 2012;12:2763–7.
- [17] Kilina S, Velizhanin KA, Ivanov S, Prezhdo OV, Tretiak S. Surface ligands increase photo excitation relaxation rates in CdSe quantum dots. *ACS Nano.* 2012;6:6515–24.
- [18] Zenkevich EI, Von Borczyskowski C. Assembly principles and relaxation processes in nanosized heterogeneous complexes: multiporphyrin structures and CdSe/ZnS nanocrystals. *High Energy Chem.* 2009;43:570–6.
- [19] Kowerko D, Krause S, Amecke N, AbdelMottaleb M, Schuster J, Von Borczyskowski C. Identification of different donor-acceptor structures via Förster resonance energy transfer (FRET) in quantum-dot-perylene bisimide assemblies. *Int J Mol Sci.* 2009;10:5239–56.
- [20] McArthur EA, Godbe JM, Tice DB, Weiss EA. A study of the binding of cyanine dyes to colloidal quantum dots using spectral signatures of dye aggregation. *J Phys Chem C.* 2012;116:6136–42.
- [21] Blanco-Canosac JB, Wud M, Susumub K, Eleonora Petryayeva TL, Jennings PE, Russ Algar DW, Medintz IL. Recent progress in the bioconjugation of quantum dots. *Coord Chem Rev.* 2014;263–264:101–37.
- [22] Bradburne CE, Delehanty JB, Gemmill KB, Mei BC, Mattoussi H, Susumu K, et al. Cytotoxicity of quantum dots used for in vitro cellular labeling: Role of QD surface ligand, delivery modality, cell type, direct comparison to organic fluorophores. *Bioconjug Chem.* 2013;24:1570–83.
- [23] Rajbanshi B, Sarkar P. Optimizing the photovoltaic properties of CdTe quantum dot – porphyrin nanocomposites: A theoretical study. *J Phys Chem C.* 2016;120:17878–86.
- [24] Jhonsi MA, Renganathan R. Investigations on the photoinduced interaction of water soluble thioglycolic acid (TGA) capped CdTe quantum dots with certain porphyrins. *J Colloid Interface Sci.* 2010;344:596–602.
- [25] Amelia M, Credi A. Photosensitization of the luminescence of CdTe nanocrystals by noncovalently bound Zn tetraphenylporphyrin. *Inorg Chim Acta.* 2012;381:247–50.
- [26] Keane PM, Gallagher SA, Magno LM, Leising MJ, Clark IP, Greetham GM, Towrie M, et al. Photophysical studies of CdTe quantum dots in the presence of a zinc cationic porphyrin. *Dalton Trans.* 2012;41:13159–66.
- [27] Aly SM, Ahmed GH, Shaheen BS, Sun J, Mohammed OF. Molecular-structure control of ultrafast electron injection at cationic porphyrin-CdTe quantum dot interfaces. *J Phys Chem Lett.* 2015;6:791–5.
- [28] Ahmed GH, Aly SM, Usman A, Eita MS, Melnikov VA, Mohammed OF. Quantum confinement-tunable intersystem crossing and the triplet state lifetime of cationic porphyrin–CdTe quantum dot nano-assemblies. *Chem Commun.* 2015;51:8010–3.
- [29] Imahori H, Umeyama T, Ito S. Large π -aromatic molecules as potential sensitizers for highly efficient dye-sensitized solar cells. *Acc Chem Res.* 2009;42:1809–18.
- [30] Li -L-L, Diao EW. Porphyrin-sensitized solar cells. *Chem Soc Rev.* 2013;42:291–304.
- [31] Imahori H, Kurotobi K, Walter MG, Rudine A, Wamser C. Porphyrin-and phthalocyanine-based solar cells. *Handb Porphyrin Sci.* 2012;18:57.

- [32] Wang C-L, Shiu J-W, Hsiao Y-N, Chao P-S, Wei-Guang Diao E, Lin C-Y. Co-sensitization of zinc and free-base porphyrins with an organic dye for efficient dye-sensitized solar cells. *J Phys Chem C*. 2014;118:27801–7.
- [33] Hart AS, Kc CB, Gobeze HB, Sequeira LR, D'Souza F. Porphyrin-sensitized solar cells: Effect of carboxyl anchor group orientation on the cell performance. *ACS Appl Mater Interfaces*. 2013;5:5314–23.
- [34] Mandal B, Sarkar S, Sarkar P. Theoretical studies on understanding the feasibility of porphyrin-sensitized graphene quantum dot solar cell. *J Phys Chem C*. 2015;119:3400–07.
- [35] Chakravarty C, Ghosh P, Mandal B, Sarkar P. Understanding the electronic structure of graphene quantum dot/fullerene nanohybrids for photovoltaic applications. *Z Phys Chem*. 2016;230:777–90.
- [36] Claessens CG, González-Rodríguez D, Salomé Rodríguez-Morgade M, Medina A, Torres T. Subphthalocyanines, subporphyrines, and subporphyrins: Singular nonplanar aromatic systems. *Chem Rev*. 2014;114:2192–277.
- [37] Chambrier I, Banerjee C, Remiro-Buenamante S, Chao Y, Cammidge AN, Bochmann M. Synthesis of porphyrin–CdSe quantum dot assemblies: Controlling ligand binding by substituent effects. *Inorg Chem*. 2015;54:7368–80.
- [38] Barbee J, Kuznetsov AE. Revealing substituent effects on the electronic structure and planarity of Ni-porphyrins. *Comp Theor Chem*. 2012;981:73–85.
- [39] Kuznetsov AE. Metalloporphyrins with all the pyrrole nitrogens replaced with phosphorus atoms, $MP(P)_4$ ($M = Sc, Ti, Fe, Ni, Cu, Zn$). *Chem Phys*. 2015;447:36–45.
- [40] Kuznetsov AE. How the change of the ligand from $L = porphine, P^2-$, to $L = P_4$ -substituted porphine, $P(P)_4^{2-}$, affects the electronic properties and the M-L binding energies for the first-row transition metals $M = Sc-Zn$: Comparative study. *Chem Phys*. 2016;469-470:38–48.
- [41] Kuznetsov AE. Computational design of $ZnP(P)_4$ stacks: Three modes of binding. *J Theor Comput Chem*. 2016;15:1650043.
- [42] Kuznetsov AE. Can $MP(P)_4$ compounds form complexes with C_{60} ? *J Appl Solution Chem Modeling*. 2017;6:91–7.
- [43] Kuznetsov AE. Design of novel classes of building blocks for nanotechnology: Core-modified metalloporphyrins and their derivatives, descriptive inorganic chemistry researches of metal compounds, Dr. Takashiro Akitsu (Ed.), InTech, Available at: <https://www.intechopen.com/books/descriptive-inorganic-chemistry-researches-of-metal-compounds/design-of-novel-classes-of-building-blocks-for-nanotechnology-core-modified-metalloporphyrins-and-th>. 2017.
- [44] Frisch MJ, Trucks GW, Schlegel HB, Scuseria GE, Robb MA, Cheeseman JR, et al. Gaussian 09: ES64L-G09RevD.01 24-Apr-2013. Wallingford CT: Gaussian, Inc., 2013
- [45] Parr RG, Yang W. Density-functional theory of atoms and molecules. Oxford: Oxford University Press, 1989.
- [46] Ditchfield R, Hehre WJ, Pople JA. Self-consistent molecular-orbital methods. IX. An extended Gaussian-type basis for molecular-orbital studies of organic molecules. *J Chem Phys*. 1971;54:724–8.
- [47] Hehre WJ, Ditchfield R, Pople JA. Self-consistent molecular orbital methods. XII. Further extensions of Gaussian-type basis sets for use in molecular orbital studies of organic molecules. *J Chem Phys*. 1972;56:2257–61.
- [48] Hariharan PC, Pople JA. Accuracy of AH_n equilibrium geometries by single determinant molecular orbital theory. *Mol Phys*. 1974;27:209–14.
- [49] Gordon MS. The isomers of silacyclopropane. *Chem Phys Lett*. 1980;76:163–8.
- [50] Hariharan PC, Pople JA. The influence of polarization functions on molecular orbital hydrogenation energies. *Theo. Chim. Acta*. 1973;28:213–22.

- [51] Yanai T, Tew D, Handy N. A new hybrid exchange-correlation functional using the Coulomb-attenuating method (CAM-B3LYP). *Chem Phys Lett.* 2004;393:51–7.
- [52] Kozłowski PM, Bingham JR, Jarzecki AA. Theoretical analysis of core size effects in metallo-porphyrins. *J Phys Chem A.* 2008;112:12781–8.
- [53] Myradalyev S, Limpanuparb T, Wang X, Hirao H. Comparative computational analysis of binding energies between several divalent first-row transition metals (Cr^{2+} , Mn^{2+} , Fe^{2+} , Co^{2+} , Ni^{2+} , and Cu^{2+}) and ligands (porphine, corrin, and TMC). *Polyhedron.* 2013;52:96–101.
- [54] Cancès E, Mennucci B, Tomasi J. A new integral equation formalism for the polarizable continuum model: Theoretical background and applications to isotropic and anisotropic dielectrics. *J Chem Phys.* 1997;107:3032–41.
- [55] Barone V, Cossi M, Tomasi J. A new definition of cavities for the computation of solvation free energies by the polarizable continuum model. *J Chem Phys.* 1997;107:3210–21.
- [56] Reed AE, Curtiss LA, Weinhold F. Intermolecular interactions from a natural bond orbital, donor-acceptor viewpoint. *Chem Rev.* 1988;88:899–926.
- [57] Reed AE, Weinstock RB, Weinhold F. Natural-population analysis. *J Chem Phys.* 1985;83:735–46.
- [58] Schaftenaar G, Noordik JH. Molden: A pre- and post-processing program for molecular and electronic structures. *J Comput-Aided Mol Design.* 2000;14:123–34.

Supplemental Material: The online version of this article offers supplementary material (DOI: <https://doi.org/10.1515/psr-2017-0187>).

M. Alcolea Palafox

10 DFT computations on vibrational spectra: Scaling procedures to improve the wavenumbers

Abstract: The performance of *ab initio* and density functional theory (DFT) methods in calculating the vibrational wavenumbers in the isolated state was analyzed. To correct the calculated values, several scaling procedures were described in detail. The two linear scaling equation (TLSE) procedure leads to the lowest error and it is recommended for scaling. A comprehensive compendium of the main scale factors and scaling equations available to date for a good accurate prediction of the wavenumbers was also shown. Examples of each case were presented, with special attention to the benzene and uracil molecules and to some of their derivatives. Several DFT methods and basis sets were used. After scaling, the X3LYP/DFT method leads to the lowest error in these molecules. The B3LYP method appears closely in accuracy, and it is also recommended to be used. The accuracy of the results in the solid state was shown and several additional corrections are presented.

Keywords: density functional theory, scaling, vibrational wavenumbers

10.1 Introduction

Density functional theory (DFT) has become very popular today. This is justified based on the pragmatic observation that it is less computationally intensive than other methods with similar accuracy, or even better in some cases, such as the theoretical prediction of vibrational spectra [1]. Because the most accurate of the quantum chemical methods are still too expensive to apply as routine research, the present paper shows an overview of the different procedures to improve this accuracy in the calculated wavenumbers but using a lower theoretical level.

Vibrational spectroscopy is one of the most powerful techniques for the characterization of medium-size molecules, but proper assignment of spectra is often not straightforward. For this reason, the last two decades have been highly productive in the interpretation of vibrational experimental spectra by means of quantum chemical methods, especially by DFT methods [2, 3]. The accurate determination of vibrational frequencies through the use of computational quantum chemistry is essential to many fields of chemistry and has become an important part of spectrochemical and quantum chemical investigations. For example, computed wavenumbers can be

This article has previously been published in the journal *Physical Sciences Reviews*. Please cite as: Palafox, M. A. DFT computations on vibrational spectra: Scaling procedures to improve the wavenumbers. *Physical Sciences Reviews* [Online] **2018**, 3. DOI: 10.1515/psr-2017-0184

<https://doi.org/10.1515/9783110568196-010>

used: (i) for the identification of known and unknown compounds; (ii) in synthetic and natural product chemistry to calculate the expected spectra of proposed structures, confirming the identity of a product or of a completely new molecule; (iii) to guide spectroscopic measurements by predicting or refining the spectral regions in which transitions of interest might occur [2]; (iv) to identify and characterize transient species, such as molecular radicals, van der Waals complexes, and reactive intermediates, and; (v) for the calculation of vibrational zero-point energies and vibrational partition functions, which are also important for thermochemical kinetics.

DFT methods can also be used to help in the assignment of the bands of the spectra. Until recently, chemical spectroscopists have attempted to interpret the vibrational spectra of more complex molecules by a transposition of the results of normal coordinate analysis of simpler molecules, often aided by qualitative comparisons of the spectra of isotopically substituted species, and the polarizations of the Raman bands. Thus, it has become an accepted practice to include tables of these “vibrational assignments” in publications on the infrared and Raman spectra of larger molecules [4–6]. However, to make such “assignments” for all the bands in the spectra is risky, owing to the fact that while some of the assignments may be credible, others can be highly speculative. Further, the modes assigned to these vibrations are often grossly oversimplified in an attempt to describe them as group wavenumbers in localized bond systems. The use of suitable DFT quantum chemical methods and scaling procedures remarkably reduces the risk in the assignment and can accurately determine the contribution of the different modes in an observed band. Now this procedure appears to be used extensively in the journals of vibrational spectroscopy.

The computation of the vibrational spectrum of a polyatomic molecule of even modest size is lengthy despite the tremendous advances made in both, in the theoretical methods, especially with DFT methods, and in computer hardware. One may be forced to work at a low level, and consequently, one must expect a large overestimation of the calculated vibrational wavenumbers. This overestimation (which may be due to many different factors that are usually not even considered in the theory, such as anharmonicity, errors in the computed geometry, Fermi resonance, solvent effects, etc.) can be significantly reduced with the use of transferable empirical parameters for the force fields, or for the calculated wavenumbers. The scale factor is therefore designed to correct the calculated harmonic wavenumbers to be compared with the anharmonic wavenumbers found by the experiment. The scale factor is a consequence of the deficiency of the theoretical approach and potentially allows vibrational wavenumbers (and thermochemical information) of useful accuracy to be obtained from procedures of modest computational cost only. Widespread application to molecules of moderate size is then possible.

Due to the importance of the scaling in vibrational spectroscopy, it is a hot research field today with many publications recently [7–14], and with a computer program created [15]. However, most of these studies are focused on only one

procedure of scaling which is not the best. Also these studies focus the attention on the improvement of the calculated wavenumbers only through the increase of the theoretical level used, and after that the use of a single overall scale factor (OSF). However, we think that it is better to improve the scaling procedure instead of only incrementing the theoretical level with the corresponding computational cost. Thus, the main goal of the present work was try to resume the different procedures used for scaling and the accuracy reached with them, with special attention to the procedures less known but more accurate. As examples, we show the results with several benzene and uracil derivatives, as well as with other molecules.

10.2 DFT methods

DFT has emerged during the past decades as a powerful methodology for the simulation of chemical systems. DFT methods are less computationally demanding than other computational methods with a similar accuracy, being able to include electron correlation in the calculations at a fraction of time of post-Hartree–Fock methodologies [10]. Therefore, these DFT methods have a widespread application, and in the present work we focus the attention only on them.

Figure 10.1 represents in schematic form the accuracy/hierarchy [16] of the seven main types of density approximations with indication of some of the most common DFT functionals:

- i. the local density approximation (LDA), with the functional SPWL (Slater Perdew–Wang local)
- ii. the generalized gradient approximation (GGA), with the pure functionals such as BLYP, BP86, BPW91, G96LYP, HCTC, HCTH93, OLYP, PBE, and PBEPBE

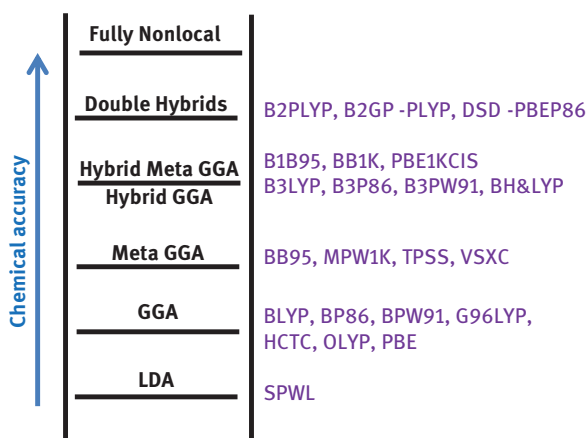


Figure 10.1: Representation of the accuracy in the five generations of DFT functionals, with indication of some of the most common DFT functional within each rung.

- iii. the meta generalized gradient approximation (M-GGA), with the functionals such as BB95, MPW1K, TPSS, and VSXC
- iv. the hybrid generalized gradient approximation (H-GGA), with hybrid functionals with Hartree–Fock exchange such as B3LYP, B3P86, B3PW91, PBE1PBE, mPW1K, BH&LYP, and BH&HLYP
- v. the hybrid meta generalized gradient approximation (MH-GGA), in which the energy depends on the occupied orbitals not only through the HF exchange terms (as in hybrid-GGAs) but also through the noninteracting spin-component kinetic energy densities (as in M-GGAs). It includes the functionals such as B1B95, BB1K, and PBE1KCIS
- vi. the Minnesota Hybrid meta functionals with the kinetic energy density gradient such as M05, M06, M05-2X, M06-2X, M08-HX, and M08-SO,
- vii. the double-hybrid (DH-DFT) functionals with Møller–Plesset correlation such as B2PLYP, B2GP-PLYP, and DSD-PBEP86 and a dispersion-corrected functional B97-D.

When moving from the lower to the higher rungs, a noticeable improvement in the quality/accuracy of the results is obtained and there is an increase in the computational cost associated. Among these methods, hybrid functionals have allowed a significant improvement over GGAs for many molecular properties. For this, they have become a very popular choice in quantum chemistry and widely used, and thus they are the main DFT functionals considered in the present work. Table 10.2 gives a resume of some of the most commons density functionals, with the indication of the functional type. The accuracy of results from DFT calculations can be poor to fairly good, depending on the choice of basis set and density functional [1]. The accuracy of results tends to degrade significantly with the use of small basis sets. For accuracy considerations, the smallest basis set to be used is generally 6–31G(d) or the equivalent. The observation that there is only a small increase in the accuracy obtained by using very large basis sets is interesting. This is probably due to the fact that the density functional is limiting accuracy more than the basis set limitations.

The choice of density functional is difficult because creating new functionals is still an active area of research. In DFT methods, the most used functionals are B-LYP and B3-LYP. The B-LYP method uses a combination of the Becke exchange functional (B) coupled with the correlation functional of Lee, Yang and Parr (LYP), while the hybrid B3-LYP procedure uses Becke's three-parameter exchange functional [17] (B3), in combination with the LYP correlation functional [18]. The B and B3 exchange functional can be used with other correlation functionals [19, 20] such as P86 and PW91 [21] to compute vibrational wavenumbers, although they have received less attention in the recent literature. The B3LYP hybrid functional (also called Becke3LYP) is the most widely used today for molecular calculations by a fairly large margin. This is due to the high accuracy of the B3LYP results obtained for a large range of compounds, particularly organic molecules. Thus, particular attention

is dedicated here to the relative performance of this popular B3LYP method. Other DFT methods of interest for calculating the wavenumbers are O3LYP [22] and X3LYP [23] and those developed by Zhao et al. are M06L, M052X and M062X [24, 25]. The meaning of the notation used for some of the functionals is shown in Table 10.1.

Table 10.1: Notation for the density functionals used in the present work.

Acronyms	Name	Type
PW91	Perdew and Wang 1991	Gradient corrected (GGA)
P86	Perdew 1986	Gradient corrected (GGA)
B96	Becke 1996	Gradient corrected (GGA)
BLYP	Becke correlational with Lee–Yang–Parr exchange	Gradient corrected (GGA)
B3LYP	Becke 3 term with Lee–Yang–Parr correlation	Hybrid (H-GGA)
B3P86	Becke exchange, Perdew correlation	Hybrid (H-GGA)
B3PW91	Becke exchange, Perdew and Wang correlation	Hybrid (H-GGA)
O3LYP	OpX with Lee, Yang, Parr correlation	Hybrid (H-GGA)
X3LYP	Becke88+PW91 with Lee–Yang–Parr	Hybrid (H-GGA)
M052X	Minnesota 2005	HM-GGA

With the development of new functionals, the performance of DFT methods is not completely known and continues changing. At the present time, DFT results have been very good for organic molecules, particularly those with closed shells [26, 27]. Results have not been so encouraging for heavy elements, highly charged systems, or systems known to be very sensitive to electron correlation. Also, most of the functionals do not perform well for problems dominated by dispersion forces. Unfortunately, there is no systematic way to improve DFT calculations, thus making them unusable for very-high-accuracy work. A detailed analysis of the performance of many DFT methods in the reproduction of a large variety of chemical properties, including bond lengths and angles, barrier heights, atomization energies, etc., has been reviewed [16], but the wavenumbers have not been analyzed, which is focused in the present work.

Mainly, three levels of theory were used for geometry optimizations of the monomer form of the molecules studied, B3LYP/6–31G(d,p), B3LYP/6–311++G(3df, pd), and MP2/6–31G(d,p), while for optimizations and vibrational wavenumbers of their dimer forms were B3LYP/6–31G(d,p), X3LYP/6–31G(d,p), and M062X/6–31G(d, p). The vibrational wavenumbers obtained by these DFT methods appear very accurate and they are available in the Gaussian 09 [28] program package. Although several basis sets were used, in the present work, the results with 6–31G(d,p) basis set are mainly discussed, due to the small improvement reached with its increment. The B3LYP functional is better than the M06L functional, in accordance to a previous work carried out by us in a benzene derivative [29]. In general, DFT methods have been applied properly in many studies of drug design [30–34] and in other

nucleosides [35]. In the present work, the B3LYP/DFT method was chosen mainly because of following three reasons: (i) this method is one of the most accurate and most used today, i. e. it is the most standard method [36–41]; (ii) many studies have reported that the wavenumbers obtained with this method are better than those determined by other more costly computational ones, especially the vibrational wavenumbers of nucleic bases calculated with this method are better than those with MP2 and HF methods [42–44]; and (iii) scaling equations are available with this method to reduce the error between theory and experiment [29, 42–44].

Without imposing molecular symmetry constraints in the optimization process, the final geometry was obtained by minimizing the energy with regard to all geometrical parameters. The Broyden algorithm in redundant internal coordinates under the tight convergence criterion was used for this optimization. The default fine integration grid was employed. All the computed structures are true minimum proved by no negative wavenumbers. The optimized structural parameters were used in the vibrational wavenumber calculations within the harmonic approximation at the same level of theory used for the optimized geometry. The vibrational assignments were interpreted by using the animation option of GaussView 5.1 graphical interface for Gaussian 09 program [45]. All quantum chemical calculations have been carried out on the Quipu computer of the “Centro de Cálculo de la Universidad Complutense de Madrid.”

10.3 Wavenumber calculation

Because of the nature of the computations involved, wavenumber calculations are valid only at stationary points on the potential energy surface. Thus, they must be performed on optimized structures. For this reason, it is necessary to run a geometry optimization prior to making a wavenumber calculation. To ensure that a real minimum is located on the potential energy surface, imaginary values should not appear among the calculated harmonic wavenumbers.

A wavenumber job must use the same theoretical model and basis set as employed in the optimized geometry step. Wavenumbers computed with different basis sets or procedures have no validity. A wavenumber job begins by computing the energy of the input structure. It then goes on to minimize this energy and recalculate a new geometry. The process is successively repeated until the change in the forces and in the displacements of the atoms of the molecule is lower than a certain fixed threshold. When it is reached, the geometry corresponds to an optimum structure and then the wavenumbers can be computed. The wavenumbers, intensities, Raman depolarization ratios and scattering activities for each spectral line are therefore predicted. However, calculated values of the intensities should not be taken too literally, due to the high error in their computation, although relative values of the intensities for each wavenumber may be reliably compared.

In addition to the wavenumbers and intensities, the output of the free and commercial quantum chemical programs also displays the atomic displacements for each computed wavenumber. These displacements are presented as XYZ coordinates, in the standard orientation, which can be plotted to identify each vibration [43].

The accuracy of calculated vibrational wavenumbers is affected more by the quality of the calculated potential than by the inclusion of anharmonicity. π -Self-consistent-field (SCF) calculations are known to give a good account of the energy hypersurface only in the region close to the equilibrium molecular geometry. At larger deviations from the minimum, the SCF potential curve starts to depart considerably from the experimental curve because of the neglect of electron correlation. The simplest case with a diatomic molecule is schematically illustrated in Figure 10.2 for three levels of calculations [46]. As it is observed, the SCF curve is too steep, giving rise to a force constant and to a computed vibrational wavenumber too high. The smaller the basis set, the more profound is this effect. With electron correlation the curve is lowered toward the almost exact solid curve (blue color). However, even with the exact curve, if replaced by a harmonic approximation, the calculated wavenumbers are yet too high, since the approximating parabola rises too steeply at large distances. These arguments concern the potential curves for stretching vibrations, but it has been found that the same trends hold for bending modes. The use of the scaling corrects these deficiencies.

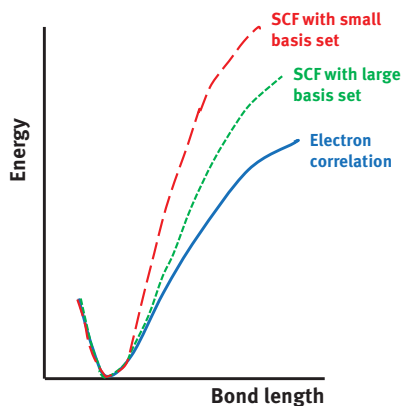


Figure 10.2: Schematic representation of the potential curves obtained by *ab initio* calculations for a diatomic molecule at three levels of computation.

10.3.1 Error in the calculated wavenumbers

The vibrational wavenumbers are usually calculated using the simple harmonic oscillator model. Therefore, they are typically larger than the fundamentals observed experimentally [47]. This overestimation in the wavenumbers also depends on the

type of vibrational mode and the range considered. The possible reasons for the deficiency in the calculations are:

- An approximate method is used to solve the Schrödinger equation.
- The overall neglect of anharmonicity in the vibrational potential energy surface.
- The incomplete description of electron correlation due to the use of an incomplete basis set (they are too small).
- The Hartree–Fock potential is too steep and therefore wavenumbers are too high.

The third factor arises because the computational cost for methods including electron correlation increases rapidly as the number of base functions increases. In general, the calculated *ab initio* wavenumbers are overestimated, at the Hartree–Fock level by about 10–20 %, and at the MP2 level by about 5–10 %. This overestimation in the wavenumbers also depends on the type of vibrational mode and on the wavenumber range, varying between 1 and 12 %. Thus, for modes that appear at high wavenumber, the difference between the harmonic oscillator prediction and the exact or Morse potential-like behavior is about 10 %. However, below a few hundred wavenumbers, this difference can be off by a large amount.

The relative accuracy of the results obtained, at some chosen computational level, is better than the absolute accuracy [48, 49]. On this basis, Figure 10.3 shows how the error is in the calculated wavenumbers as computed in a variety of molecular environments, with different methods and sized basis sets. The vertical axis shows the difference between the computed wavenumbers with different methods and various sizes of SCF basis sets in the normal modes of the benzene molecule, and the experimental values in gas phase [43]. The error is more or less found to fall within the area of the two orange curves of the diagram. For small basis sets (or semiempirical calculations), the error, or range of uncertainty about the “true” value obtained from experiment, is largely increased. The convergence limit, approached by very large basis sets, still differs from the true value, but this residual error has been found empirically to be significantly constant for a given parameter, and it is very nearly independent of the molecule studied. Thus, the calculations can be done efficiently at the point marked as “scaling” in Figure 10.3, and the residual error can be removed with the use of a scaling, and therefore gives rise to an accurate predicted wavenumber. High *ab initio* methods, such as CCD (coupled cluster theory with double substitutions), CCSD (coupled cluster theory with both single and double substitutions), CCSD(T) (including triple corrections), and QCISD (Quadratic configuration interaction using single and double substitutions) when used in conjunction with large basis sets, produce almost correct harmonic wavenumbers for most systems, so no scaling is necessary. However, they are rather expensive methods in time and computer memory, and general application of them has been limited to considerable small molecules. For larger molecules, computations are prohibitively expensive, even with small basis set, and other methods should be used.

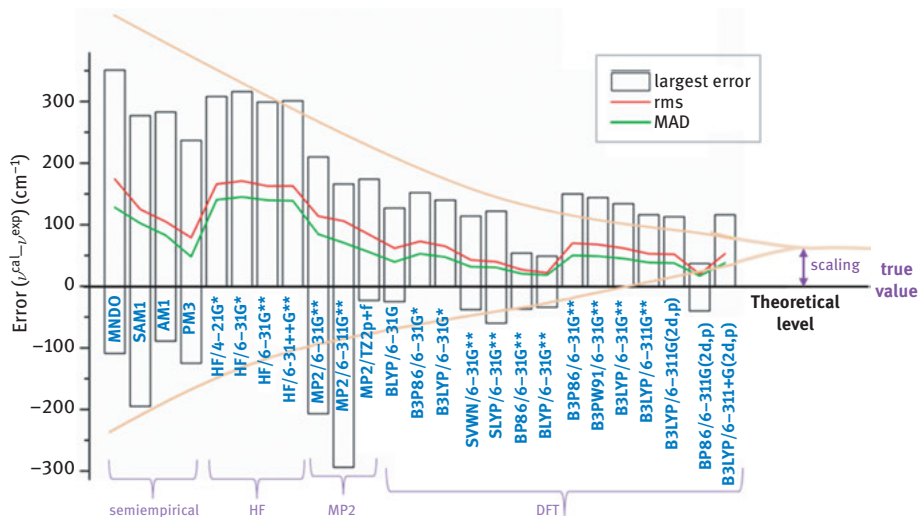


Figure 10.3: The largest $\Delta(v^{cal} - v^{exp})$, rms, and MAD errors obtained by the different methods and basis set, in increased form, in the calculated wavenumbers of the ring modes of the benzene molecule. The point to do the calculations is indicated and the corresponding scaling factor to be used.

10.3.1.1 Definition of the different errors

The root mean square (rms) error for the calculated wavenumbers is defined as:

$$\text{rms} = \left(\sum_{i=1}^N \frac{(v_i^{cal} - v_i^{exp})^2}{N} \right)^{1/2}$$

where v_i^{cal} is the i th calculated vibrational harmonic wavenumber, v_i^{exp} is the corresponding experimentally determined i th vibrational wavenumber, and the parameter N denotes the total number of harmonic wavenumbers considered.

The mean absolute deviation (MAD) is defined as: $\text{MAD} = \sum_{i=1}^N \frac{|v_i^{cal} - v_i^{exp}|}{N}$

where the sum is over all the absolute errors (Δv_i) in the calculated wavenumbers $\Delta v_i = |v_i^{cal} - v_i^{exp}|$

Finally, the standard deviation (Std.Dev.) is defined as: $\text{Std.Dev.} =$

$$\left(\frac{1}{N} \sum_{i=1}^N (\Delta v_i - \overline{\Delta v})^2 \right)^{1/2} \quad \text{where } \Delta v_i \text{ is the absolute error in every calculated wavenum-}$$

ber $|v_i^{cal} - v_i^{exp}|$, and $\overline{\Delta v}$ is the MAD.

Similar definition is used for the error in the scaled wavenumbers, v_i^{scal} :

$$\text{rms} = \left(\sum_{i=1}^N \frac{(v_i^{scal} - v_i^{exp})^2}{N} \right)^{1/2}, \quad \text{MAD} = \sum_{i=1}^N \frac{|v_i^{scal} - v_i^{exp}|}{N}, \quad \text{Std.Dev.} = \left(\frac{1}{N} \sum_{i=1}^N (\Delta v_i^s - \overline{\Delta v^s})^2 \right)^{1/2}$$

where $v^{scal} = \lambda \cdot v^{cal}$, $\Delta v_i^s = |v_i^{scal} - v_i^{exp}|$, and $\overline{\Delta v^s}$ is the MAD for the scaled values.

10.3.1.2 Examples

In aniline molecule, the errors obtained in the calculated theoretical harmonic wavenumbers with *ab initio* and DFT methods as compared to the experimental values are collected in Table 10.2. The second and third columns list the rms and MAD errors, respectively, while the fourth column shows the standard deviation of the values. The largest ($v^{cal}-v^{exp}$) positive and negative errors are indicated in the fifth to sixth columns. As in benzene molecule, HF and MP2 methods clearly fail in the calculated wavenumbers, and DFT methods appear to be the best, especially the B3LYP functional.

The uracil molecule was also studied in detail [42, 44] by different DFT and *ab initio* methods and the errors obtained in the calculated wavenumbers are shown in the second to fourth columns of Table 10.3. It is noted again that the calculations at the HF level fail to give the observed experimental pattern. Inclusion of electron correlation (MP2) slightly improves the computed wavenumbers, but they are still incorrect. Only with DFT methods, the wavenumbers are close to the experimental values. However, these results do not reproduce well all the experimental pattern of wavenumbers and intensities, but the use of scale factors solves this problem.

Several benzene and uracil derivatives were optimized at the B3LYP/6-31G(d,p) level and the calculated wavenumbers were compared to the experimental ones. The rms errors obtained are shown in the second column of Table 10.4. These errors are larger than those expected for an accurate assignment of the experimental bands. Thus, it is necessary to correct these calculated wavenumbers, i. e. the scaling.

10.4 Scaling procedures for the wavenumbers

The wavenumbers calculated with the most accurate/expensive quantum chemical methods and with the largest basis set do not need to be corrected (scaling). However, these methods are expensive to be applied for the calculation of the vibrational spectrum of a polyatomic molecule of even modest size. Thus, one may be forced to work at small level, with the consequence of the deficiency of the theoretical approach, and thus a large overestimation of the calculated vibrational wavenumbers is expected. However, this error can be significantly reduced/avoided with the use of transferable empirical parameters/corrections for the computed wavenumbers/force constants, i. e. the scaling. This feature is based on the assumption that the values of the wavenumbers/force constants are close among similar molecules and characteristic groups. Therefore, with the scaling, it is possible to determine the vibrational wavenumbers of useful accuracy to be obtained from procedures of only modest computational cost.

The scaling of the theoretical wavenumbers can be used to obtain:

- I. Accurate fundamental wavenumbers, which can be directly compared to the observed experimental values and

Table 10.2: Errors obtained in the calculated and scaled wavenumbers of the aniline ring modes by the different procedures, methods, and levels.

Method	Calculated wavenumbers						Scaled wavenumbers with an overall factor						Scaled wavenumbers with the scaling equations						Scaled wavenumbers with specific scale factors						
	rms		MAD		stdDev		Largest error		rms		MAD		stdDev		Largest error		rms		MAD		stdDev		Largest error		
	Positive	Negative	Positive	Negative	Positive	Negative	Positive	Negative	Positive	Negative	Positive	Negative	Positive	Negative	Positive	Negative	Positive	Negative	Positive	Negative	Positive	Negative	Positive	Negative	
SCF																									
HF/6-31G(d)	164	138.5	88.7	320 (7b)	-	-	30.9	21.5	22.2	25 (5)	-104 (14)	23.9	16.6	17.3	39 (8a)	-87 (14)	8.5	6	6	18 (7b)	-28 (20b)				
HF/6-31G(d,p)	158	132.8	83	307 (7b)	-	-	31.2	21.8	22.3	28 (5)	-105 (14)	24.3	16.8	17.5	40 (8b)	-90 (14)	9.7	6.9	6.8	23 (7b)	-27 (20b)				
HF/6-31++G(d,p)	156	130.7	84.6	309 (7b)	-	-	-	-	-	-	-	24.3	16.7	17.7	47 (5)	-90 (14)	9.2	6.6	6.3	22 (7b)	-27 (20b)				
Post-SCF																									
MP2/6-31G(d)	96	73.2	62.5	185 (7b)	-234 (4)	-212(4)	62	40.6	47.2	67 (14)	-212(4)	54	38.9	38	99 (14)	-192 (4)	25	19.1	16.3	19 (12)	-62 (11)				
Density functional																									
B3P86/6-31G(d)	69	49	49.1	160 (7b)	-9 (10b)	-50 (17a)	18.2	13.7	11.9	19 (7b)	-50 (17a)	13.1	10.3	8	24 (18b)	-33 (17a)	11.1	8	7.6	27 (8a)	-27 (20b)				
B3P86/6-31G(d,p)	67	46.2	48.4	159 (7b)	-5 (15)	-45 (17a)	19.1	14.8	12	18 (7b)	-45 (17a)	13.4	11.3	7.2	26 (8a)	-26 (17a)	10.1	7.6	6.6	20 (8a)	-27 (20b)				
B3LYP/6-31G(d)	61	43.4	42.5	145 (7b)	-10 (17a)	-46 (17a)	16.9	13.8	9.7	23 (7b)	-46 (17a)	11.8	8.5	8.2	29 (18b)	-32 (17a)	10.8	7.7	7.6	28 (18b)	-30 (20b)				
B3LYP/6-31G(d,p)	59	41.3	41.8	143 (7b)	-4 (15,17a)	-45 (10a)	18.6	15.5	10.1	21 (7b)	-45 (10a)	11.2	8.5	7.2	22 (18b)	-26 (17a)	12.5	9	8.7	37 (8a)	-27 (20b)				
B3LYP/6-311G(2d,p)	49.2	34.6	35	124 (7b)	-9 (17a)	-	-	-	-	-	-	11.5	8.8	7.3	25 (18b)	-27 (17a)	10.7	7.7	7.4	27 (18b)	-26 (20b)				
B3LYP/6-311+G(2d,p)	49.7	33.6	36.6	128(7b)	-4(15)	-	-	-	-	-	-	10.4	8.5	6.1	23(7b)	-16(20b)	11.1	7.8	7.9	25(18b)	-31(20a)				
B3LYP/6-311++G(2d,p)	49.6	33	37	128 (7b)	-11 (5a)	-	-	-	-	-	-	12.4	10	7.3	26 (18b)	-24 (5a)	11.9	8.5	8.6	25 (18b)	-31 (20a)				
B3PW91/6-31G(d,p)	64.7	44.5	47	155 (7b)	-5 (15)	-44 (17a)	18.8	14.9	11.5	19 (7b)	-44 (17a)	12.8	10.4	7.4	25 (8a)	-26 (17a)	10.2	7.7	6.7	20 (7b,8a)	-2.6 (20b)				

Table 10.3: Errors obtained in the calculated and scaled wavenumbers of the uracil modes by the different procedures and methods.

Method	Calculated wavenumbers		Scaled wavenumbers with an overall factor (OSF)		Scaled wavenumbers with the scaling equations (LSE)	
	Largest error (cm^{-1})		Largest error (cm^{-1})		Largest error (cm^{-1})	
	rms	Negative	rms	Negative	rms	Negative
HF/6-31G(d,p)	184	427	6	23	22.6	46
HF/6-31++G(d,p)	177	418	11	37	16.7	27
MP2/6-31G(d)	82	187	44	37	25.4	50
BP86/6-31G(d,p)	35	86	44	33	18.1	34
BLYP/6-31G(d,p)	34	73	49	34	19.6	34
B3P86/6-31G(d,p)	77	207	14	24	15.0	32
B3LYP/6-31G(d,p)	66	184	15	21	13.8	24
B3LYP/6-311 + G(2d,p)	54	156	20	25	13.7	21
B3PW91/6-31G(d,p)	75	206	14	25	14.9	30
M06-2X/6-31G(d,p)	79	192	13	13	19.1	53
M06-L/6-31G(d,p)	70	190	13	13	19.0	49

Table 10.4: RMS errors obtained in the calculated and scaled wavenumbers of several benzene and uracil derivatives at the B3LYP/6-31G(d,p) level.

Molecules	(a)	(b)	(c)	(d)
Benzene	62	17	8.8	–
Aniline	60	19	12.4	11.0
Benzoic acid	55.9	19.7	13.9	10.7
Phenylsilane	60.1	17.0	10.7	10.5
<i>p</i> -Aminobenzoic acid	47.8	19.3	13.7	11.3
<i>p</i> -Methoxybenzoic acid	46.3	18.6	13.4	12.5
1,4-Dicyanobenzene	56.5	23.1	17.7	13.4
2,4-Difluorobenzonitrile	64.1	20.2	16.5	14.2
Phenothiazine	75.0	24.2	17.6	17.1
Uracil	66.4	21.4	13.8	–
5-Fluorouracil	70.3	29.8	23.5	14.7
5-Bromouracil	76.2	29.2	18.5	13.7
5-Methyluracil	59.8	21.5	18.4	13.1
5-Nitouracil	71.7	26.1	16.5	13.0
1-Methyluracil	69.2	27.0	17.9	15.8
2-Thiouracil	79.0	26.5	15.5	11.5
3-Methyluracil	63.2	22.8	15.6	11.0
1,3-Dimethyluracil	49.4	23.1	16.5	12.1

(a) Calculated wavenumbers, (b) scaled wavenumbers with an overall factor (OSF), (c) scaled wavenumbers with the scaling equations (LSE), and (d) scaled wavenumbers with specific scale factors (SCFEM).

II. The corresponding true harmonic analogs. These wavenumbers are just conceptual, and in practice, these are obtained from experiment by extrapolating a vibrational progression to the experimentally inaccessible vibrationless state.

Most of the works are only interested in the accurate fundamental wavenumbers, point (I). Because, it is the most interesting point, the present study undertakes only to this point. As reference of point (II), we can show the studies reported by Alecu et al. [2] and Kesharwani et al. [50], with a large set of scaling factors displayed to obtain the true harmonic wavenumbers.

The wavenumbers can be calculated: (i) by a generic internal coordinate system created by the computer program, e. g. Gaussian 09 or (ii) by specific internal coordinates defined by us in the molecule, and in general standardized to permit the transferability of scale factors among related molecules. The choice depends on whether the wavenumbers (case (i)) are scaled or the force constants are scaled previously to compute the vibrational wavenumbers (case (ii)). Thus, for the calculation of the fundamental wavenumbers, point (I), two main groups of procedures can be used for an accurate scaling [51–53]:

(Ia) Procedures based on scaling the calculated force constant to get scaled wavenumbers and

(Ib) Procedures based on scaling the wavenumbers directly.

10.4.1 Procedures based on scaling the force constants

These procedures are based on the transferability of the force constants and dipole moment derivatives among similar molecules. The procedure does not assume that the force constants are similar in related molecules, but makes the weaker assumption that the error in calculating the force field is similar for related types of vibrational motions in analogous molecules as determined by the identical computational procedure.

Due to the complementarity between *ab initio* and empirical sources of information [54], this empirical scaling technique was introduced in 1971 [55]. However, the first systematic application of mixed *ab initio* with empirical techniques was done in the pioneering work of Blom and Altona [56].

A set of force constants represents a quantitative expression of the forces binding the atoms in a molecule. The valence force field is generally accepted as the most plausible representation of the intramolecular forces from a physical point of view. However, the complete force field cannot be obtained from experiment alone, even within the harmonic oscillator approximation, except for the simplest molecules. Thus, the force constants for different types of vibrations need to be computed, expressed in internal coordinates, and corrected with a small set of scaling factors. Such coordinates, often referred to as local symmetry coordinates, are linear combinations of primitive coordinates [57]. These empirically corrected *ab initio* force constants and dipole moment derivatives for a variety of basic organic compounds are assembled in a database [54], from which it is possible to predict the spectra of unknown substances with a modest effort, utilizing the transferability of these quantities.

The purely empirical determination of force constants and thus the development of transferable force fields for larger molecules, have been unsuccessful for a long time, except for small molecules. *Ab initio* methods and molecular mechanics methods have been used for this purpose. However, molecular mechanics appears rather inaccurate for calculated wavenumbers, because the determination of force constants suffers, as other empirical methods, problems of insufficient data and uncertain assignment.

In the SQM or SQMFF (scaled quantum mechanical force field) approach [58] for determining *ab initio*/empirical force fields, a small number of scale factors are used to correct the deficiencies of the *ab initio* force fields, and the effects of anharmonicity in the observed wavenumbers. The off-diagonal force constants (F_{ij}) are scaled by $(C_i C_j)^{1/2}$, $F_{ij} = (C_i C_j)^{1/2} F_{ij}^{\text{th}}$ where C_i and C_j are the scale factors for F_{ii} and F_{jj} . The force constants calculated by this method are not the harmonic force constants but effective constants for the fundamental 0→1 transition. The fact that the SQM force

constants include part of the anharmonicity makes comparison with accurate *ab initio* values. In the SQM technique, usually several molecules are treated together, and a number of chemically analogous coordinates share the same scale factor. This makes the optimization of the scale factors very stable. The scale factors are in general much more transferable than the force constants themselves.

The SQM method can be used in two ways: in the refinement and in the predictive modes. For molecules which contain new structural elements, the scale factors have to be refined. This requires a careful analysis of the experimental data. The fitting procedure is somewhat iterative, as the identity of the fundamentals is often uncertain. Therefore, first a prediction is made using tentative scale factors, and the predicted results are carefully compared to experiment. This usually allows the identification of more fundamentals. The latter are used to refine the scale factors further, until a complete assignment is achieved.

In the simple predictive mode, the calculated force constants are combined with scale factors transferred from analogous molecules to produce force fields. The predictive mode is used for molecules which contain structural elements already studied, and the results usually agree with experiment without further refinement.

The SQM method can be used with several quantum mechanical force fields: semiempirical, density functional, SCF level, and high-level correlated wave functions. At higher level of calculations, the less empirical correction is required. Transformation of the force field and the subsequent normal coordinate analysis including the least-square refinement of the scaling factors are carried out with the MOLVIB program written by Sundius [59, 60].

A pioneering study on benzene [61] produced a small set of scaling factors which was transferred with minor modifications to scale the computed force fields of several derivatives, such as fluorobenzene [62], aniline [63], toluene [64], phenylsilane [65], etc. Similar force fields have been derived for other rings [66] and acyclic compounds [67]. However, these calculations have been done at the modest HF/4–21G level. Actually many other systems have been reported [68–70]. Table 10.5 shows the reference of three selected studies reported at different levels of computation. Actually, the basis for the SQM method [71] has been reformulated, and the standard commercial implementation of this method [72] scales directly the primitive valence force constants. An alternative multiparameter scaling method, called an effective scaling

Table 10.5: SQM studies with scale factors for the force constants.

Year	Number of species studied	Methods	Reference
1995	31	B3LYP	[74]
2010	30	B3LYP	[11]
2012	18	B3LYP with VDZ, VTZ, 6-31G (d) basis sets	[9]

frequency factor (ESFF) method, has been proposed [73]. A further modification of the ESFF procedure (called ESFF2) consists in replacing ordinary potential energy distribution coefficients by the contributions calculated on the basis of amplitudes only rather than amplitudes and force constants [11]. Therefore, the problem of ambiguity of the force field in terms of the redundant coordinates can be avoided.

10.4.1.1 Disadvantages

In spite of the superior results provided by methods using several scale factors, in particular SQM, many calculations are performed by its simplified version which uses only a single OSF for the wavenumbers, ca. 0.9 [47]. The advantage of this last method is its extreme simplicity. In particular, scaling with several scale factors requires the transformation of the force field to a chemically reasonable local internal coordinate system, called *natural internal coordinates*, which requires significant effort. This is not necessary if only a single-scale factor is used. However, the accuracy of the single OSF method is less than that of the SQM method.

The main advantage of scaling the force constants as compared to scale the wavenumbers directly is the higher accuracy reached. However, this procedure has many disadvantages, such as:

- High complexity, especially for large systems.
- Previous definition of the internal coordinates (the definition is not unique).
- Some manual intervention or huge programming effort for nonstandard situations.
- The necessity of a computer program to apply the set of scale factors.
- Low transferability of the scale factors corresponding to the out-of-plane modes, the torsion of conjugated systems, and the torsions of single-bonded systems [74].
- The force constants are not physically observable, and therefore the improvement appears difficult.

Although with this procedure excellent results are obtained, we feel that the introduction of scaling factors for the wavenumbers themselves is preferable to the more indirect approach of scaling the force constants. First, the wavenumbers are visually observable and the force constants are not. Second, the definition of the force constant matrix is not unique because the number of matrix elements is usually much larger than the number of known wavenumbers. The third argument is the pragmatic observation that we may be primarily interested only in a few major characteristic wavenumbers and not in the whole spectrum, which requires much more effort.

10.4.2 Procedures based on scaling the wavenumbers directly

It is based on the regularity of the error produced in the wavenumber calculation with each theoretical level used. With this procedure of scaling is reached a slight lower

accuracy than with the procedure based on scaling the force constants. However, scaling the wavenumbers directly has many advantages, such as:

- Simplicity: it does not require the previous definition of the internal coordinates, neither an additional computer program to scale the values.
- It can be used for a single vibration: it is not necessary to scale the entire spectrum as it is required with the scale force constant procedure. It is especially useful when studying the shifts of a specific mode in different spectra.
- The wavenumbers are physically observable, and therefore the scale factors can be improved for specific systems.

Therefore, in the present study, we will focus the attention on the procedures that scale the computed wavenumbers directly [42–44, 75]. Four procedures can be carried out satisfactorily, and they are described below. Its use depends on the accuracy required:

- By an OSF: $v^{scal} = \lambda \cdot v^{cal}$

or two overall factors: from 4,000–800 cm^{-1} and from 800–0 cm^{-1} , or similar ranges.

- By a linear scaling equation (LSE): $v^{scal} = a + b \cdot v^{cal}$

or two linear scaling equations (TLSEs): From 4,000–1,500 cm^{-1} and from 1,500–0 cm^{-1} , or similar ranges.

- By a polynomial scaling equation (PSE): $v^{scal} = a + b_1 \cdot v^{cal} + b_2 \cdot (v^{cal})^2$
- By specific scale factors for each mode (SCFEM): $v_i^{scal} = \lambda_i \cdot v_i^{cal}$

10.4.2.1 By a single overall scale factor (OSF)

With this procedure, all the computed harmonic wavenumbers of a molecule at a specific level of theory are scaled with a unique scale factor (correction factor, global multiplicative scaling factor [7], or uniform scaling [76]) or two scale factors, which is common for all the molecules with the same level of calculation. The scaling factors are different for distinct levels of theory, and at low level of calculation, the scale factors differ from the value 1.

The procedure to determine this scale factor is complicated, because the scale factor depends upon not only the basis set or theoretical method used but also on the group of molecules used for comparison and whether or not the comparisons are made with only harmonic wavenumbers or with all fundamentals. The procedure for calculating the scale factor [77] is as follows: With a full set of calculated wavenumbers, v_i^{cal} , for different molecules, and with their corresponding experimental fundamental wavenumbers, v_i^{exp} , the scale factors λ are those which minimize the residuals, Δ :

$$\Delta = \sum_i^N (\lambda v_i^{cal} - v_i^{exp})^2 \text{ and thus, } \lambda = \frac{\sum_i^N (v_i^{cal} v_i^{exp})}{\sum_i^N (v_i^{cal})^2}.$$

The parameter N denotes the total number of harmonic wavenumbers, and the scaling factor determined is for a particular level of theory.

Following this procedure of scaling, a host of scale factors for various levels of theory and basis sets can be found on the Computational Chemistry Comparison and benchmark database (CCCBDB) from the National Institute of Standards and Technology (NIST) [78], as well as in ref [79]. Others scale factors have been reported [2, 80] and some references with them are collected in Table 10.6 for many DFT levels. Only Kashinski et al. [7], Irikura et al. [81], and Teixeira et al. [82] report the scale factors including the standard uncertainties associated, and they conclude that the scale factors calculated at most of the levels have an accuracy of only two decimal places (e.g. 0.98), but for the basis sets cc-pVTZ, 6–311G(d,p), and SPK-TZP, the accuracy is three decimal places [7] (e.g. 0.985).

Table 10.6: Studies with sets of scale factors to be used for the OSF procedure.

Year	Number of systems studied	Methods	Reference
1993	41	AM1	[83]
1996	122	HF, MP2, DFT	[77]
2001	111	HF, SVWN, BLYP, B3LYP, B3PW91, MP2 with pVTZ	[76]
2003	82 diatomic	DFT: TPSS with 6–311++G(3df,3pd)	[84]
2004	41	HF, MP2, B3LYP	[85]
2005	125	DFT with triple- ζ basis set	[86]
2005	358	<i>Ab initio</i>	[81]
2006	122	DFT	[87]
2007	122	HF, MP2, DFT: B3LYP, BMK, EDF2, M052X, MPWB1K	[88]
2010	143	X3LYP	[82]
2010	145	MPWLYP1M, BB95, BLYP, BP86, B3LYP, MPW3LYP, VSXC	[2]
2011	41 ^a	HCTH93, B3LYP, B3PW91, PBE1PBE, mPW1K, M052X, M062X	[3]
2012	41 ^a	HCTH93, B3LYP, B3PW91, PBE1PBE, mPW1K, M052X, M062X	[8]
2014		CC2, MP2	[89]
2015	HFREQ2014 ^b	Double hybrids: B2PLYP, B2GP-PLYP, DSD-PBEP86	[50]
2016	122	Double hybrids: DuT-D3, DSD-type	[90]
2017	26	DFT: TPSS, M06, M11, B3LYP, B3PW91, PBE, PBE0	[7]

^aTwo scaling factors are calculated, for high and low wavenumbers. ^bDataset from ref [91].

It has been suggested that the scale factors have a stronger dependence on the DFT functional choice than on the choice of basis set [7, 89], and that significantly increasing the size of the basis sets does not necessarily lead to improved results.

If it is used two scale factors (TOSF) (or dual scaling [80]), one is for wavenumbers in the 4,000–1,000 cm^{-1} range (or >1,800 cm^{-1}), and another for wavenumbers

lower than $1,000\text{ cm}^{-1}$ (or $<1,800\text{ cm}^{-1}$). In this case, to minimize the large errors in wavenumbers at the low end of the wavenumber range, an inverse wavenumber scaling factor, λ' , is used to minimize the residuals:

$$\Delta = \sum \left(\frac{1}{\lambda \cdot v_i^{\text{cal}}} - \frac{1}{v_i^{\text{exp}}} \right)^2 \text{ and thus, } \lambda' = \sum \left(\frac{1}{v_i^{\text{cal}}} \right)^2 / \sum \frac{1}{v_i^{\text{cal}} v_i^{\text{exp}}}$$

10.4.2.1.1 Sets of scale factors

Following this procedure of scaling, sets of scale factors at different levels have been published by many authors. Some of them are collected in Table 10.6. The references appear distributed in chronological way, with the last values for the double-hybrid methods. A selection of the two scale factors reported by Scott et al. [77] for the different levels of theory has been collected in Table 10.7, one for high wavenumbers and another one for low values. They have been obtained from a dataset containing 122 molecules and 1,066 wavenumbers. This set of scale factors is one of the most used today.

Table 10.7: Scale factors reported [77] for different levels for the (OSF) procedure.

Level of theory	Scale factor		Level of theory	Scale factor	
	λ	λ'^a		λ	λ'^a
HF/ 3–21G	0.9085	1.0075	QCISD-fc/6-31G(d)	0.9538	1.0147
HF/ 6-31G(d)	0.8953	0.9061			
HF/6-31 + G(d)	0.8970	0.9131	SVWN/ 6-31G(d)	0.9833	1.0079
HF/6-31G(d,p)	0.8992	0.9089	B-LYP/ 6-31G(d)	0.9945	1.0620
HF/6–311G(d,p)	0.9051	0.9110	B-LYP/6–311G(df,p)	0.9986	1.0667
HF/6-31G(df,p)	0.9054	0.9085	B-P86/6-31G(d)	0.9914	1.0512
			B3-LYP/ 6-31G(d)	0.9614	1.0013
MP2-fu/ 6-31G(d)	0.9427	1.0214	B3-P86/6-31G(d)	0.9558	0.9923
MP2-fc/ 6-31G(d)	0.9434	1.0485	B3-PW91/6-31G(d)	0.9573	0.9930
MP2-fc/6-31G(d,p)	0.9370	1.0229			
MP2-fc/6–311G(d,p)	0.9496	1.0127			

^aSuitable for the prediction of low-wavenumber vibrations $\equiv 1/\lambda$.

Another selection of scale factors with the newest DFT methods and several basis sets is collected in Table 10.8. For comparison purposes, the popular B3LYP and B3PW91 methods have been included. All these factors have been reported by Kashinski et al. [7], but only one factor is determined for all the spectrum range, the OSF procedure.

This OSF (or TOSF) procedure is the simplest and easiest way to scale the wavenumbers, and thus it is the procedure generally used in the bibliography. However, with this procedure, the error is something large in the scaled values,

Table 10.8: Scale factors reported [7] for different levels for the (OSF) procedure.

Method	6-311G (d,p)	6-311+ +G (2d,2p)	6-311+ +G (3df,3pd)	aug-cc- pVDZ	aug-cc- pVTZ	cc- pVTZ	SPK- TZP	Sadlej- TZP
M06	0.960	0.961	0.961	0.962	0.963	0.960	0.961	0.968
M06-2X	0.946	0.947	0.947	0.950	0.949	0.948	0.948	0.952
M06-HF	0.931	0.929	0.927	0.937	0.932	0.931	0.930	0.934
M06-L	0.963	0.963	0.965	0.963	0.965	0.963	0.963	0.968
M11	0.958	0.954	0.954	0.961	0.954	0.953	0.954	0.960
B3LYP	0.964	0.963	0.964	0.967	0.965	0.965	0.965	0.970
B3PW91	0.959	0.958	0.959	0.962	0.961	0.960	0.960	0.963
CAM-B3LYP	0.953	0.952	0.953	0.956	0.954	0.954	0.954	0.959
PBE	0.990	0.990	0.989	0.993	0.992	0.991	0.991	0.996
PBE0	0.953	0.953	0.953	0.956	0.955	0.954	0.954	0.957

although much lower than without scaling, but this error can make assignment difficult and in some cases a clear and nonaccurate assignment.

10.4.2.1.2 Example with aniline molecule

This procedure of scaling with two scale factors, for high- and low-wavenumber ranges, was applied to the aniline ring modes [92, 93]. The final rms, MAD and Std.Dev. results are shown in Table 10.2, where the sum is over all the modes of the aniline molecule, $N = 30$. The greatest positive and negative deviations from experiment by different methods and basis sets are also listed. An analysis of this table gives rise to the following conclusions: In the fundamental wavenumbers, the most cost-effective procedures found for predicting vibrational wavenumbers are the B3-based/6-31G(d) DFT procedures, with the lowest rms values. The B-based DFT procedures are not performing quite as well as the corresponding B3-based procedures, and for this reason, they were omitted in Table 10.2. MP2/6-31G(d) does not appear to offer a significant improvement in performance over HF/6-31G(d) and occasionally it shows a high degree of error. While the QCISD method yields wavenumbers (not shown in Table 10.2) that are more reliably predicted than those computed at the MP2 level, the improvement comes at a significant additional computational cost and the results are generally not better than those for the much less expensive B3-based DFT procedures. With low-wavenumber vibrations, the DFT methods also yield the lowest errors, while HF performs slightly worse.

An overall conclusion is that B3-based DFT procedures provide a very cost-effective means of determining harmonic vibrational wavenumbers and derived thermochemical quantities. They show fewer poorer cases than do HF- and MP2-based procedures. With *ab initio* methods, although the error is remarkably reduced using the OSF procedure, as compared to the calculated wavenumbers, in several ring modes of the aniline molecule, the error is large. With DFT procedures, however,

the errors are in general small and they are improved efficiently with the OSF procedure.

10.4.2.1.3 Example with other molecules

The ring modes of the benzene molecule were scaled with the OSF procedure. In Figure 10.4 was plotted the largest $\Delta(v^{scal} - v^{exp})$, rms and MAD errors obtained by the same methods and basis set of those of Figure 10.3. Because scale factors have not been reported yet at several levels, some bars in the histogram appear empty. As compared to Figure 10.3, a remarkable reduction of the error can be

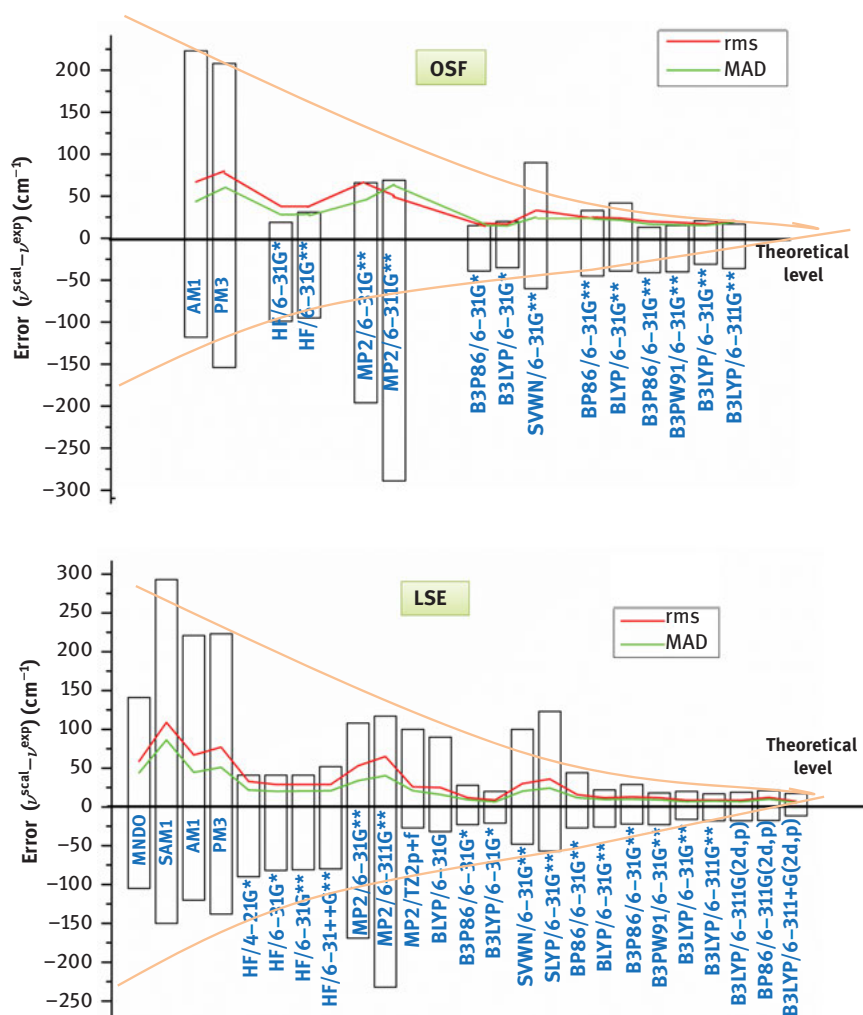


Figure 10.4: The largest $\Delta(v^{scal} - v^{exp})$, rms, and MAD errors obtained by the different methods and basis set in the scaled wavenumbers using an overall scale factor (OSF) and scaling equation (LSE) of the ring modes of the benzene molecule.

observed in Figure 10.4, with the exception of the semiempirical and MP2 methods that are still large. Table 10.3 and Table 10.4 show the errors obtained with this scaling procedure in the uracil ring modes and in several of their derivatives as well as in benzene derivatives. The rms error obtained is ca. 2–3 times lower than without scaling, but in several molecules and DFT methods this error is large for an accurate assignment of some bands. Thus, it is recommended to use a better scaling procedure than OSF.

Twenty-six gas-phase organic and nonorganic molecules typically found in detonated solid propellant residue have been studied by Kashinski et al. [7] with the OSF procedure. These authors found that the M06HF functional showed a weaker performance than all other functionals used, and the 6–311G and cc-CpVTZ basis sets have a weak performance when employed across all functionals.

Alecu et al. [2] found that upon scaling, the most reliable results were obtained with the BMC-CCSD multilevel method, which had an average rms deviation of 20 cm^{-1} , and the best performance of the DFT tested was obtained for VSXC, with an average rms deviation of 32 cm^{-1} . In the Minnesota functionals, the best performance was for M06-L, with an average rms deviation of $39\text{--}40\text{ cm}^{-1}$, depending on the basis set used. By contrast, HF, HFLYP, and M06-HF (all with 100% Hartree–Fock exchange) are much less reliable than the other methods. These authors also found that increasing the size of the one-electron basis set for a given DFT did not significantly alter the ensuing values for λ nor lead to more accurate results. In fact, increasing the basis set generally resulted in a slight loss of accuracy with regard to the prediction of both the harmonic and fundamental wavenumbers.

10.4.2.2 By a linear scaling equation (LSE)

This procedure uses a scaling equation to correct the computed wavenumbers of a molecule at a specific level of theory. The use of an equation instead of one factor leads to a slight improvement in the predicted wavenumbers, as it is expected, especially in the low-wavenumber region, i. e. it is better than the OSF procedure. The scaling equation can also refer to a group or to a kind of molecules for a specific level of theory, which greatly improves the accuracy in the predicted wavenumbers.

This procedure is based in the linear relationship that can be established between the calculated and experimental wavenumbers of a molecule:

$$\nu^{\text{exp}} = a + b \cdot \nu^{\text{cal}}$$

For example, Figure 10.5 shows this linear relationship for the ring modes of the benzene molecule. If the coefficients “*a*” and “*b*” are known, the relationship can be established as:

$$\nu^{\text{scal}} = a + b \cdot \nu^{\text{cal}}$$

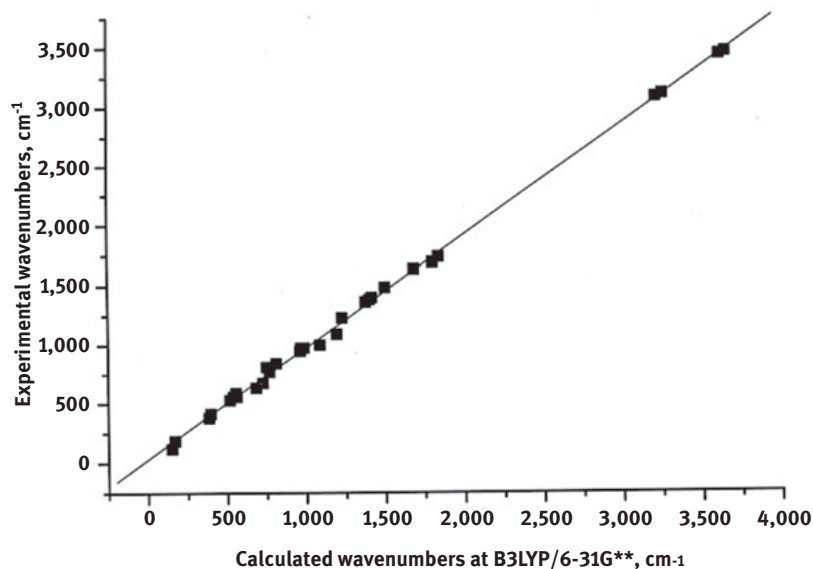


Figure 10.5: Linear regression distribution of the calculated wavenumbers by B3LYP/6-31G(d,p) versus experimental ones in benzene molecule.

Therefore, with the theoretical calculated wavenumbers (ν^{cal}) of a molecule of interest can be obtained their scaled values (ν^{scal}).

For the calculation of the “ a ” and “ b ” coefficients, this procedure requires the previous computed wavenumbers of a simple and related structure in which the gas-phase vibrational wavenumbers have been reported. This fitting can be done to the values of a model molecule, or a group of molecules, to be used in related molecules or in their derivatives. The LSE procedure developed by the author represents a compromise between accuracy and simplicity, especially for DFT methods, and therefore it is one of the methods recommended for scaling the wavenumbers. However, only scaling equations have been reported for benzene, uracil, and cytosine molecules, to be used in their derivatives. Although, we are in the way to get general equations determined from several database, as it is reported with the OSF procedure. Following this procedure, Table 10.9 collects the calculated scaling equations obtained in the benzene [43] and uracil [42, 44] molecules, as well as in the amino modes, at several *ab initio* and DFT levels. These scaling equations can be used in related molecules and in their derivatives at the same theoretical level. It is because of the large transferability of these equations to related molecules.

Table 10.10 collects the scaling equations obtained with different DFT methods in uracil molecule, to be used in their derivatives. The error in the coefficients “ a ” and “ b ” is included, as well the correlation coefficient “ r .” The X3LYP method appears to be the best, with the lowest error in these coefficients and with the value of “ r ” closest to 1.

Table 10.9: Scaling equations $v^{scal} = a + b \cdot v^{cal}$ for the ring modes of benzene and uracil derivatives, and for the amino modes using the OSF procedure.

Methods	Benzene		Uracil		Amino modes	
	a	b	a	b	a	b
HF/6-31G(d)	-4.0	0.9103	4.6	0.8924	22.7	0.8934
HF/6-31G(d,p)	-8.6	0.9162	5.7	0.8867	40.3	0.8846
HF/6-31++G(d,p)	-6.2	0.9153	10.5	0.8938	45.9	0.8833
MP2/6-31G(d,p)	83.4	0.9088				
MP2/6-311G(d,p)	97.3	0.9156				
BP86/6-31G(d,p)	32.7	0.9752	46.0	0.9678	44.3	0.9699
BP86/6-311G(2d,p)	28.8	0.9819				
BLYP/6-31G(d,p)	27.2	0.9791	46.4	0.9718	31.3	0.9791
B3P86/6-31G(d)	25.0	0.9473	29.9	0.9412	33.0	0.9434
B3P86/6-31G(d,p)	27.2	0.9476	34.1	0.9389	57.4	0.9318
B3LYP/6-31G(d)	23.3	0.9519	30.8	0.9468	21.3	0.9555
B3LYP/6-31G(d,p)	22.1	0.9543	34.6	0.9447	44.5	0.9441
B3LYP/6-311G(2d,p)	18.6	0.9616			24.5	0.9572
B3LYP/6-311+G(2d,p)	20.8	0.9601	30.8	0.9538	45.0	0.9484
B3LYP/6-311++G(2d,p)	28.5	0.9574			45.6	0.9482
B3LYP/6-311++G(3df,pd)			31.9	0.9512		
B3LYP/aug-cc-pVDZ			28.6	0.9543		
B3LYP/dgdzvp			39.2	0.9472		
B3PW91/6-31G(d,p)	24.8	0.9501	34.9	0.9393	56.8	0.9325
B3PW91/6-311+G(2d,p)	25.2	0.9554				
MPW1PW91/6-311+G(2d,p)	24.6	0.9499				

Table 10.10: Scaling equations for the ring modes of uracil derivatives with the 6-31G(d,p) basis set for the OSF procedure.

Levels	a	b	r
B3LYP	29.4 ± 5.3	0.9475 ± 0.0033	0.9996
O3LYP	35.7 ± 6.3	0.9424 ± 0.0039	0.9995
X3LYP	27.9 ± 5.2	0.9462 ± 0.0033	0.9997
B97D	41.7 ± 7.0	0.9643 ± 0.0045	0.9994
M05	38.2 ± 8.1	0.9299 ± 0.0050	0.9992
M052X	28.3 ± 5.4	0.9310 ± 0.0033	0.9996
M06	29.1 ± 7.5	0.9458 ± 0.0047	0.9992
M06L	29.7 ± 6.0	0.9446 ± 0.0037	0.9995
M062X	22.7 ± 6.0	0.9417 ± 0.0037	0.9995

The two next methods in accuracy are B3LYP and M052X. This feature is found in the normal modes of uracil molecule, but it is also expected to be found in their derivatives. Thus, these methods are those recommended to be used.

Table 10.11 lists other scaling equations determined for cytosine and uracil molecules, to be used in their derivatives. In DFT methods, with the increment of the basis set, the value of “*r*” tends to 1, especially when diffuse functions are added.

Table 10.11: Scaling equations for the ring modes of cytosine and uracil derivatives for the (OSF) procedure.

Levels of computation	a	b	Correlation coefficient, r
Cytosine molecule:			
HF/6-31 + G(d,p)	-4.1	0.8965	0.9997
HF/6-31 + G(2d,p)	-14.3	0.9053	0.9997
B3LYP/6-31 + G(d,p)	16.3	0.9560	0.9999
B3LYP/6-31 + G(2d,p)	6.2	0.9631	0.9999
B3LYP/6-311 + G(2d,p)	4.8	0.9671	0.9999
Uracil molecule:			
HF/6-31G(d,p)	5.7	0.8928	0.9997
MP2/6-31G(d)	34.5	0.9372	0.9996
B3PW91/6-31G(d)	30.1	0.9421	0.9999

10.4.2.2.1 Examples

The calculated wavenumbers of the ring modes in the benzene molecule were scaled using the LSE procedure (Figure 10.4). In DFT methods, a significant improvement (ca. 30 %) is reached over those with the OSF procedure. Semiempirical methods as well as HF and MP2 *ab initio* methods fail, and although the error is reduced it is still large.

The calculated wavenumbers of the aniline ring modes were also scaled with LSE at different levels, and the rms errors, MAD, Std. Dev., and the greatest positive and negative deviations from experiment have been determined and included in the 12th to 16th columns, respectively, of Table 10.2. A general reduction of ca. 30 % in the error over the use of the OSF procedure was obtained. The rms error by HF is ca. twice larger than by B3LYP, but by MP2 is twice worse than by HF. The use of the B3LYP/6-31G(d) level leads to the best result. In contrast to that expected, the increment of the basis set leads to slight worse results.

The LSE procedure was also applied to the calculated wavenumbers of uracil molecule (Table 10.3). The best result was obtained at the B3LYP/6-311 + G(2d,p) level. Closely in accuracy appears the B3LYP/6-31G(d,p) level. The rms errors are slight larger than those obtained in the aniline molecule. The LSE procedure at the B3LYP/6-31G(d,p) level was also applied to several benzene and uracil derivatives [94–96] (Table 10.4). As it is expected, the rms error increments with the complexity of the molecule studied. Also it increments with the difference between its molecular structure and that structure in which the scale equation has been obtained. Thus, the rms error is largest in 1,4-dicyanobenzene and phenothiazine molecules, because

these molecules are more different than benzene molecule (in which the scaling equations were obtained) than the remaining benzene derivatives listed. A similar feature appears in 5-fluorouracil, with the largest error, because its molecular structure is more different to uracil molecule (in which the scaling equations were obtained) than the remaining uracil derivatives listed in the table. In general, the errors obtained in the predicted wavenumbers of the present investigation were very small, and the mean deviation was 10 cm^{-1} (1%). These errors are very close to those obtained in other molecules studied earlier by us [27, 92, 93, 97]. This scaling procedure has been also used by other authors in different molecules [98].

In the normal modes of an acetamide derivative, Srivastava et al. [99] have compared the results obtained using OSF (also called “uniform scaling”) vs. LSE (also called “nonuniform scaling”) and they concluded that in high-frequency region (above $1,400\text{ cm}^{-1}$) where most of the stretching modes occur, LSE provides more accurate vibrational bands as compared to OSF. Thus, it is recommended to use the LSE procedure over OSF.

10.4.2.2.2 By using two linear scaling equations (TLSE)

With the use of the scaling equation approach, the low-wavenumber vibrations are usually predicted fairly accurately while stretching wavenumbers appear overestimated. It is because the OSF and the LSE procedures do not take into account how the distribution of the error is in the calculated wavenumbers. Figure 10.6 shows this distribution in the calculated wavenumbers of benzene molecule at the B3LYP/6-31G(d,p) level according to their experimental values. As can be observed, two linear regressions/tendencies appear in the figure. By dividing the wavenumber range into two parts, and using one scaling equation for the $0\text{--}1,000\text{ cm}^{-1}$ (or $0\text{--}1,500\text{ cm}^{-1}$) range and another one for the $1,000\text{--}4,000\text{ cm}^{-1}$ (or $1,500\text{--}4,000\text{ cm}^{-1}$) range, the error in the stretching region is slightly reduced. Thus, a small improvement over LSE procedure can be reached. Thus, it is recommended to use two scale factors/scaling equations for the $0\text{--}4,000\text{ cm}^{-1}$ range of the vibrational spectra. Figure 10.7 shows the distribution of the error in the scaled wavenumbers of the uracil molecule using the LSE procedure at the B3LYP/6-31G(d,p) level according to their experimental values. As can be observed, a linear regression/tendency appears below $1,500\text{ cm}^{-1}$, which indicated that below $1,500\text{ cm}^{-1}$ the calculated wavenumbers have not been scaled adequately. Thus, it is necessary to use two scaling equations to reduce the error. The range of wavenumbers to use the two scaling equations depends on how is the distribution of the error at each level of theory. Thus, in Figure 10.7, this range can be established as $0\text{--}1,500\text{ cm}^{-1}$ and $1,500\text{--}4,000\text{ cm}^{-1}$, but it can be changed depending on the theoretical level. The most used is $0\text{--}1,000\text{ cm}^{-1}$ and $1,000\text{--}4,000\text{ cm}^{-1}$ ranges. The distribution of the error after scaling should be as that shown in Figure 10.8, which is random. This figure has been plotted using the TLSE procedure for the uracil molecule at the B3LYP/6-31G(d,p) level, and with one scaling equation for the $0\text{--}1,500\text{ cm}^{-1}$ range, and another one for the $1,500\text{--}4,000\text{ cm}^{-1}$ range. If some tendency appears, it means that the scaling has not

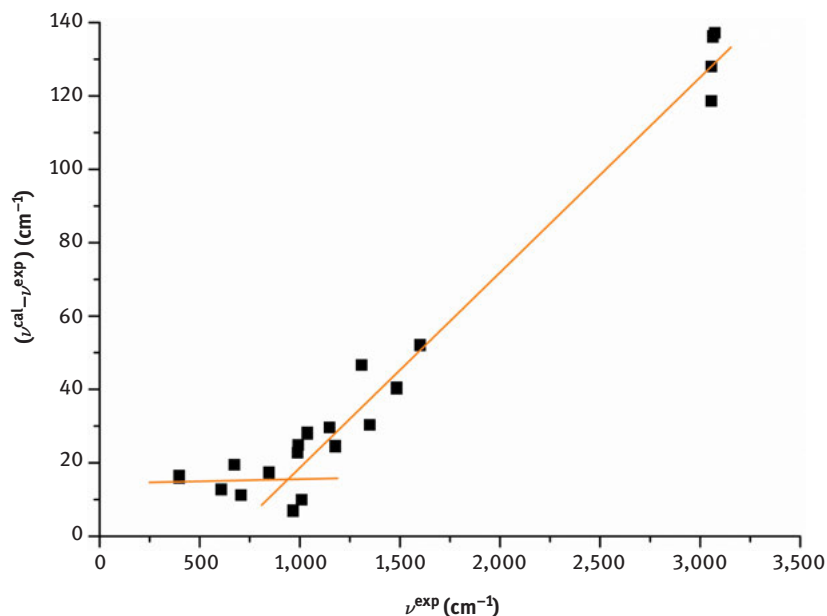


Figure 10.6: Distribution of the error in the calculated wavenumbers of benzene molecule at the B3LYP/6-31G(d,p) level according to their experimental values. Two linear regressions/tendencies appear in the figure.

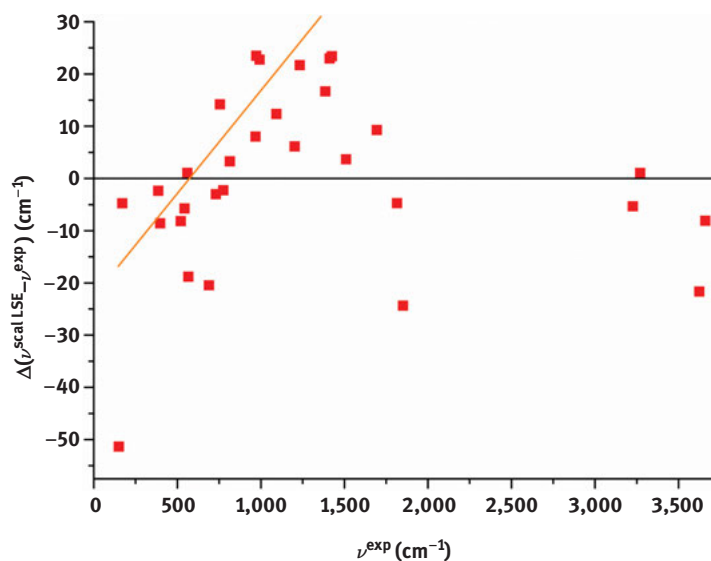


Figure 10.7: Distribution of the error in the scaled wavenumbers of the uracil molecule using the LSE procedure at the B3LYP/6-31G(d,p) level according to their experimental values. A linear regression/tendency appears below $1,500 \text{ cm}^{-1}$.

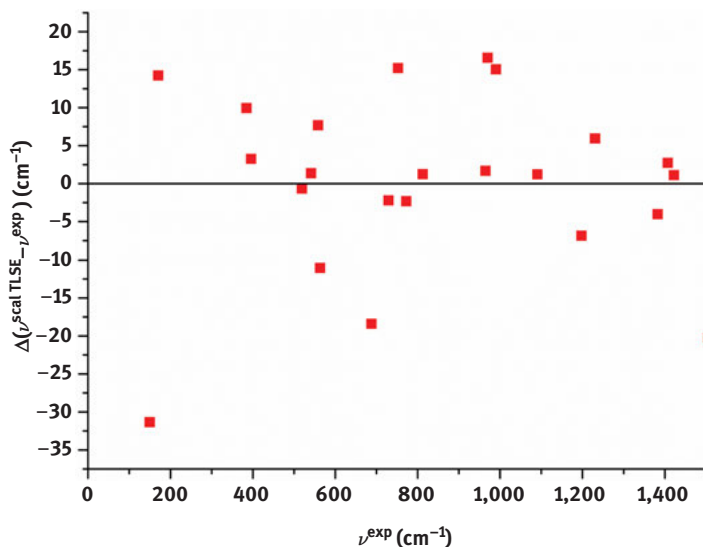


Figure 10.8: Nonuniform distribution of the error in the scaled wavenumbers of uracil molecule using the TLSE procedure at the B3LYP/6-31G(d,p) level according to their experimental values below 1,500 cm^{-1} .

been carried out suitably, but in the present figure it is not observed. Thus, two scaling equations, from 0 to 1,500 cm^{-1} and 1,500 to 4,000 cm^{-1} ranges, were determined in the uracil molecule to be used in their derivatives (Table 10.12). The error in the coefficients “*a*” and “*b*” is included, as well as the correlation coefficient “*r*.” The B3LYP functional appears to be the best in both ranges, with the lowest error in these coefficients and with the value of “*r*” closest to 1. The two next methods in accuracy are X3LYP and M062X. Similar feature was also found with the LSE procedure. Thus, these methods are recommended to be used.

Table 10.12: Scaling equations for the TLSE procedure and for the ring modes of uracil derivatives with the 6-31G(d,p) basis set.

Levels	0–1,500 cm^{-1}			1,500–4,000 cm^{-1}		
	<i>a</i>	<i>b</i>	<i>r</i>	<i>a</i>	<i>b</i>	<i>r</i>
B3LYP	3.3 ± 5.9	0.9813 ± 0.0064	0.9990	34.7 ± 16.0	0.9429 ± 0.0056	0.9998
O3LYP	4.3 ± 6.8	0.9829 ± 0.0074	0.9988	49.6 ± 22.4	0.9345 ± 0.0078	0.9996
X3LYP	3.1 ± 6.0	0.9787 ± 0.0065	0.9990	27.3 ± 16.6	0.9436 ± 0.0058	0.9998
B97D	3.5 ± 6.9	1.0144 ± 0.0078	0.9987	70.4 ± 19.3	0.9507 ± 0.0069	0.9997
M05	0.3 ± 6.9	0.9808 ± 0.0075	0.9987	4.5 ± 38.6	0.9365 ± 0.0133	0.9988
M052X	5.7 ± 6.2	0.9613 ± 0.0066	0.9990	3.6 ± 17.7	0.9363 ± 0.0061	0.9997
M06	1.4 ± 6.7	0.9851 ± 0.0073	0.9988	−39.3 ± 36.1	0.9646 ± 0.0126	0.9990
M06L	8.0 ± 7.0	0.9744 ± 0.0076	0.9987	−3.8 ± 25.4	0.9528 ± 0.0089	0.9995
M062X	5.7 ± 6.0	0.9670 ± 0.0064	0.9990	−51.4 ± 22.0	0.9633 ± 0.0076	0.9996

10.4.2.3 By using a polynomial scaling equation (PSE)

This procedure is based on the fact that the relationship established between the calculated and experimental wavenumbers is a second-order polynomial form:

$$\nu^{\text{exp}} = a + b_1 \cdot \nu^{\text{cal}} + b_2 \cdot (\nu^{\text{cal}})^2$$

If the “ a ,” “ b_1 ,” and “ b_2 ” coefficients are known, the relationship can be established as:

$$\nu^{\text{scal}} = a + b_1 \cdot \nu^{\text{cal}} + b_2 \cdot (\nu^{\text{cal}})^2$$

Therefore, with the theoretical calculated wavenumbers (ν^{cal}) of a molecule of interest can be obtained their scaled values (ν^{scal}). Similar to the LSE and TLSE procedures, the calculation of the “ a ,” “ b_1 ,” and “ b_2 ” coefficients needs to be calculated previously by fitting the experimental and theoretical wavenumbers of a model molecule, or group of molecules. This PSE procedure has also been developed by us, and it represents a compromise between accuracy and simplicity, and therefore it is one of the methods recommended for scaling the wavenumbers.

Table 10.13 collects the values of the coefficients obtained with different DFT methods in uracil molecule, to be used in their derivatives. The error in the coefficients is included, as well the correlation coefficient “ r .” The B3LYP and X3LYP methods appear to be the best, with the lowest error in these coefficients and with the value of “ r ” closest to 1, as it was found in LSE and TLSE procedures.

Table 10.13: Polynomial scaling equation $y = a + b_1x + b_2x^2$ determined in uracil molecule at different DFT methods using the 6-31G(d,p) basis set. The standard deviations in the polynomial coefficients a , b_1 and b_2 are also included, as well as the correlation coefficient “ r .”

Levels	a	b_1	$b_2 \times 10^6$	r
B3LYP	3.2 ± 7.4	0.9904 ± 0.0103	-11.2 ± 2.6	0.9998
O3LYP	2.8 ± 8.5	0.9962 ± 0.0118	-14.0 ± 3.0	0.9997
X3LYP	3.9 ± 7.6	0.9856 ± 0.0106	-10.3 ± 2.7	0.9998
B97D	0.7 ± 8.4	1.0332 ± 0.0120	-18.3 ± 3.1	0.9997
M05	8.2 ± 12.9	0.9786 ± 0.0178	-12.5 ± 4.4	0.9993
M052X	9.6 ± 8.6	0.9611 ± 0.0119	-7.7 ± 2.9	0.9997
M06	13.1 ± 13.1	0.9720 ± 0.0183	-6.8 ± 4.6	0.9993
M06L	13.1 ± 10.0	0.9717 ± 0.0140	-7.1 ± 3.5	0.9996
M062X	17.3 ± 10.8	0.9506 ± 0.0150	-2.3 ± 3.8	0.9995

10.4.2.4 With a specific scale factor for each mode (SCFEM)

This procedure requires two actions: (i) the previous characterization of the calculated wavenumbers and (ii) the use of a specific scaled factor for each specific mode.

These specific factors need to be deduced from a related structure in which the gas phase wavenumbers have been reported. This procedure leads to the lowest errors, but it requires much more effort, and with large basis sets the improvement is very small. This procedure is recommended only for modes with large anharmonicity.

It is well known that in organic molecules, many of the vibrational modes are localized and that many functional groups have characteristic wavenumbers that do not vary much between different molecules. Therefore, considering groups of similar molecules can be calculated the scaling factor λ_i of a specific mode as: $\lambda_i = \nu_i^{\text{exp}}/\nu_i^{\text{cal}}$ that brings the computed wavenumbers in line with the available experimental data. That is, the procedure is based on the assumption that the ratios between experimental and computed wavenumbers are fairly constant for each type of characteristic wavenumber, such as C-H stretch, C-Cl stretch, NH_2 torsion, etc. It is then possible to derive for known experimental spectra a correction factor for each characteristic wavenumber by taking the average of the ratios between the experimental and computed wavenumbers, λ , and to use them for predicting or assigning unknown spectra. Therefore, the scaled value can be calculated as: $\nu_i^{\text{scal}} = \lambda_i \cdot \nu_i^{\text{cal}}$.

The introduction of different scale factors for distinct types of vibrational modes significantly improves the accuracy of the predicted wavenumbers. The introduction of a scaling factor for a single characteristic wavenumber is capable of accounting for all the deficiencies of the quantum chemical methods and leads to a more precise prediction for specific characteristic wavenumbers that are of special interest.

It should be noted that certain types of vibrational modes are much more readily identified than others, e. g. the stretchings. On the other hand, many of the torsion and out-of-plane modes are delocalized throughout a wide low-wavenumber range, and it is difficult to identify these modes or to differentiate between them. Thus, the scale factors obtained with these modes produce many errors, and should be considered with caution.

To our knowledge, the first specific scale factors reported with this procedure are for tertiary amines [100, 101] and for toluene molecule [102]. Actually, the specific scale factors of other molecules have been reported. We have collected in Table 10.14 the factors obtained at several levels in the benzene [43] molecule to be used in their derivatives. The first column lists the normal ring modes according to the Wilson notation [103].

With these specific scale factors were scaled the wavenumbers of the ring modes of the aniline molecule (Figure 10.9). The largest positive and negative errors by HF and MP2 methods are remarkably reduced, ca. half, as compared to LSE procedure. The rms and MAD are also drastically reduced by these methods (Table 10.2). By DFT methods, the reduction of the error is only ca. 20–30%. With this SCFEM procedure, the rms error by HF appears lower than by the DFT methods, i. e. if the calculation of the wavenumbers is carried out at the HF level, the scaling procedure must be SCFEM. Table 10.15 collects the specific scale factors determined in the NH_2 group that were calculated in the aniline molecule [92, 93] to be used in compounds with this amino group. By the same methodology, we have determined the scale factors of other model molecules, as those

Table 10.14: Calculated specific scale factors (λ) for each normal mode of the benzene molecule [43].

Ring mode ^a	B3P86/6-31G(d,p)	B3LYP/6-31G(d)	B3LYP/6-31G(d,p)	B3PW91/6-31G(d,p)
1	0.9651	0.9726	0.9736	0.9679
2	0.9535	0.9564	0.9582	0.9552
3	0.9825	0.9733	0.9775	0.9818
4	0.9819	0.9846	0.9846	0.9833
5	0.9764	0.9802	0.9773	0.9754
6	0.9841	0.9777	0.9792	0.9840
7	0.9558	0.9591	0.9609	0.9576
8	0.9604	0.9662	0.9780	0.9621
9	0.9798	0.9750	0.9790	0.9790
10	0.9805	0.9804	0.9793	0.9782
11	0.9753	0.9725	0.9712	0.9711
12	0.9960	0.9902	0.9922	0.9970
13	0.9589	0.9619	0.9638	0.9607
14	0.9468	0.9642	0.9656	0.9502
15	0.9768	0.9702	0.9743	0.9760
16	0.9660	0.9590	0.9590	0.9660
17	0.9908	0.9979	0.9929	0.9888
18	0.9685	0.9712	0.9730	0.9694
19	0.9731	0.9693	0.9731	0.9737
20	0.9537	0.9567	0.9585	0.9552

^aAccording to the Wilson notation [103].

of uracil [42, 44]. With these specific scale factors of the uracil molecule and those of the benzene molecule were calculated the rms errors of several benzene and uracil derivatives at the B3LYP level (Table 10.4). About 10–20 % of improvement was obtained as compared to LSE procedure.

10.4.2.5 Comparison of the different methods

A comparison of the errors obtained by the LSE, TLSE, and PSE scaling procedures on the wavenumbers of uracil molecule, and by different DFT methods and the 6-31G(d,p) basis set, is shown in Table 10.16. The lowest error in all the DFT methods was obtained with the TLSE procedure, with the exception of X3LYP. The PSE procedure appears better than LSE. The best functional was B3LYP, but the M052X functional shows similar accuracy. The scaled values by M052X are better by LSE and TLSE than by M062X. The majority of the published works with *ab initio* and DFT methods use a single overall correction value for the wavenumbers, with no consideration for the different modes. Sometimes, a simplification is used with only two or three scale factors for the modes, e. g. 0.9 for stretches and bends and 1.0 for torsion. However, the best accuracy is obtained if SCFEM is applied for each mode and level of calculation, although it requires more effort and the previous assignment of the modes. This feature hinders the standard use of SCFEM, and for this reason we recommend the second best procedure, the TLSE.

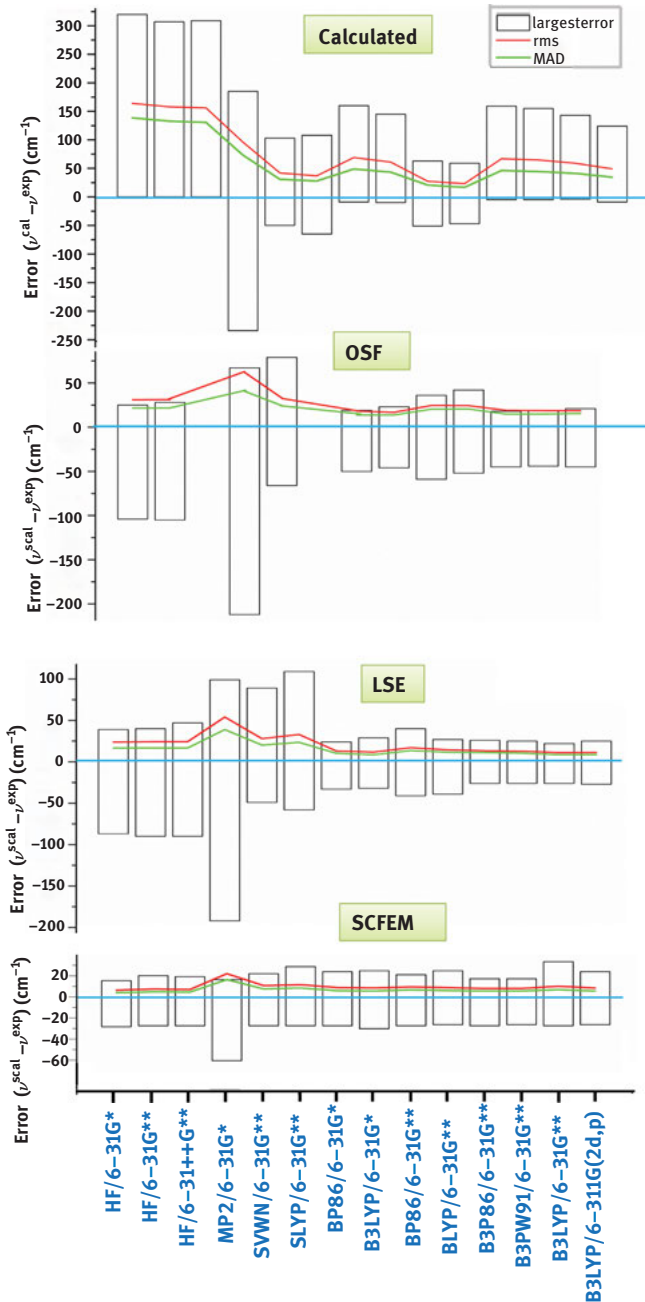


Figure 10.9: Comparison of the largest $\Delta(v^{cal} - v^{exp})$, rms, and MAD errors obtained by the different methods and basis set in the calculated wavenumbers and in the scaled values using the overall scale factor (OSF), the scaling equation (LSE), and the specific scale factor for each mode procedure of the ring modes of the aniline molecule.

Table 10.15: Specific scale factors (λ_i) to be used for the amino group vibrations [92, 93].

Mode	B3P86/6-31G(d,p)	B3LYP/6-31G(d)	B3LYP/6-31G(d,p)	B3PW91/6-31G(d,p)
ν_{as}	0.9431	0.9606	0.9529	0.9436
ν_s	0.9494	0.9640	0.9582	0.9500
β_s	0.9753	0.9549	0.9765	0.9753
r	0.9805	0.9761	0.9823	0.9814
ω	1.1267	1.0405	1.0912	1.1248
τ	0.9337	0.9699	0.9497	0.9337

Table 10.16: Errors in the calculated and scaled wavenumbers of uracil.

Method	Calculated					Scaled (LSE)				
	rms	MAD	stanDev	Large error		rms	MAD	StanDev	Large error	
				Negative	Positive				Negative	Positive
B3LYP	65.16	39.50	54.08	-14.4	183.4	16.81	12.93	17.10	-24.3	52.3
O3LYP	70.25	41.01	60.17	-15.9	205.7	20.14	15.90	20.49	-29.7	56.6
X3LYP	67.98	42.23	55.24	-14.0	188.6	16.60	12.65	16.88	-23.5	51.3
B97D	40.54	29.19	41.15	-38.0	115.8	22.40	19.15	22.78	-32.8	58.0
M05	90.02	53.89	74.53	-16.8	253.1	25.88	20.70	26.33	-41.0	59.5
M052X	92.76	62.30	70.71	-13.4	241.0	17.03	12.10	17.32	-28.6	51.1
M06	70.12	42.57	58.37	-16.1	187.0	23.97	17.84	24.38	-34.0	65.5
M06L	70.09	43.83	57.61	-13.1	190.1	18.97	14.50	19.29	-25.5	49.2
M062X	79.43	53.49	60.53	-13.2	192.4	19.07	12.56	19.40	-31.1	53.2

Method	TLSE					PSE				
	rms	MAD	StanDev	Large error		rms	MAD	StanDev	Large error	
				Negative	Positive				Negative	Positive
B3LYP	11.34	8.46	11.53	-16.6	31.3	12.96	9.63	13.2	-18.5	36.4
O3LYP	13.60	10.74	13.80	-18.7	31.3	14.96	11.41	15.2	-20.4	43.5
X3LYP	18.06	13.72	16.87	-41.7	31.4	13.37	9.97	13.6	-19.0	37.9
B97D	13.36	10.47	13.59	-22.5	27.3	14.79	11.00	15.0	-22.3	43.8
M05	16.88	12.93	17.16	-37.4	36.5	22.75	15.65	23.1	-29.3	75.0
M052X	11.94	8.85	12.15	-20.8	33.1	31.39	23.63	22.3	-12.2	78.3
M06	15.93	12.48	16.20	-31.8	32.7	23.05	16.03	23.4	-26.8	74.7
M06L	14.38	11.48	14.62	-20.2	33.9	17.70	13.28	18.0	-20.3	54.1
M062X	12.23	8.92	12.44	-25.9	33.0	18.94	12.32	19.3	-29.9	56.4

DFT methods with the 6-31G(d,p) basis set shows a more reliable prediction for the calculated wavenumbers (with scale factors closer to the unit) than with more expensive HF and MP2 methods (Figure 10.9).

With B3LYP, Andersson et al. [86] found that the convergence of the vibrational wavenumbers with respect to the addition of diffuse and polarization functions was

generally met already at the 6-311G(d,p) level. Thus, vibrational wavenumbers calculated with B3LYP/6-311G(d,p) typically agreed to within 10 cm^{-1} with those obtained from B3LYP/6-311++G(3df,3pd). This convergence criteria proposed by Andersson et al. [86] and confirmed by Alecu et al. [2] in the case of B3LYP can be applicable to DFT in general.

DH-DFT procedures have been reported to be highly potential to obtain vibrational wavenumbers [3]. Thus, Kesharwani et al. [50] showed that the basis sets 6-31G(d) and N07D are clearly inferior to def2-SVP and CBSB7. After scaling, B2PLYP, B2GP-PLYP, and DSD-PBEP86 deliver similar performances, with a slight edge for DSD-PBEP86. For unscaled harmonic wavenumbers, B2GP-PLYP was clearly inferior to the two other double hybrids. In another study, Chan and Radom [90] found that DuT-D3- and DSD-type procedures lead to a slightly improved overall performance compared to B3LYP. The best was the DSD-PBE-P86/aug'-cc-pVTZ+d combination, and thus this level was recommended by these authors for its use for geometry optimization and vibrational frequency calculations.

10.4.3 Anharmonic calculation of the wavenumbers

To improve the calculated wavenumbers, a viable alternative is to include anharmonic terms. Calculating the anharmonicity requires higher-order (e. g. cubic and quartic) force constants and information about torsional barriers or full potential energy surfaces, and this additional data is often unavailable or even unaffordable. For small molecules, perturbative approaches may be affordable and can yield accurate anharmonic vibrational wavenumbers provided that these approaches are not significantly affected by the problem of Fermi resonances [2]. However, linear species cannot be treated with this formalism, and for large systems, the associated computational cost may not be affordable since analytic second derivatives are required for such calculations.

The introduction in the Gaussian code of an effective algorithm based on finite-difference evaluations of third and semidiagonal fourth derivatives paves the route for a more systematic investigation of larger molecules [104]. Thus, a number of studies [105, 106] have demonstrated the reliability of this approach using in most of them an anharmonic calculation of the wavenumbers by means of the second-order perturbative method (PT2) elaborated by Barone [107]. The VPT2 approach appears available in Gaussian 09 [10], and the VSCF and VSCF-PT2 are implemented in Gamess-US software [108].

The inclusion of anharmonicity requires a larger computational effort, but the improvement reached is similar that some of the scaling procedures for the wavenumbers explained above. The exception can be in the modes involved in a large anharmonicity, such as the inversion/rotation motion of the amino groups, which requires a specific treatment, but even in these modes, the use of the SCFEM procedure for the wavenumbers leads to low errors, and it has similar accuracy.

10.4.4 Wavenumber corrections for the experimental solid state sample

The theoretical methods predict the vibrational spectra of molecules in the isolated state. Thus, if these predicted/scaled spectra are compared to the experimental gas phase/Ar matrix spectra, the agreement is good. For example, Figure 10.10 shows the good accordance between the experimental IR spectrum in gas phase versus the scaled one in the general anesthetic halothane [109]. However, if we have the experimental values in the solid state, the difference between theory and experiment can be very large, especially in the modes involved in intermolecular H-bonds. Thus, to avoid a mistake in the assignment of these modes it is necessary/recommended to carry out these two points:

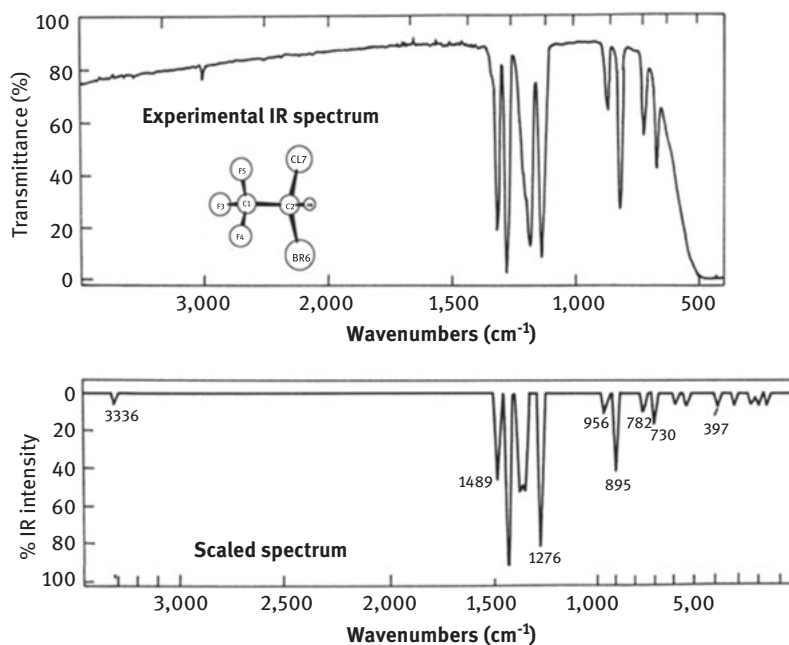


Figure 10.10: Comparison of the experimental IR spectrum in gas phase and the scaled one at the HF/6-311G(d,p) level of halothane molecule [109].

(i) To simulate with a theoretical model this solid state. In a simple way, in many cases, it is enough with the simulation of the crystal unit cell. Many structures have been optimized following this procedure [27, 94–96, 110–115]. For example Figure 10.11 shows the spectrum simulated/scaled considering a monomer (isolated stated) and a tetramer form (the crystal unit cell) of 5-iodouracil at the B3LYP/DGDZVP level as compared to the corresponding experimental IR spectrum in the

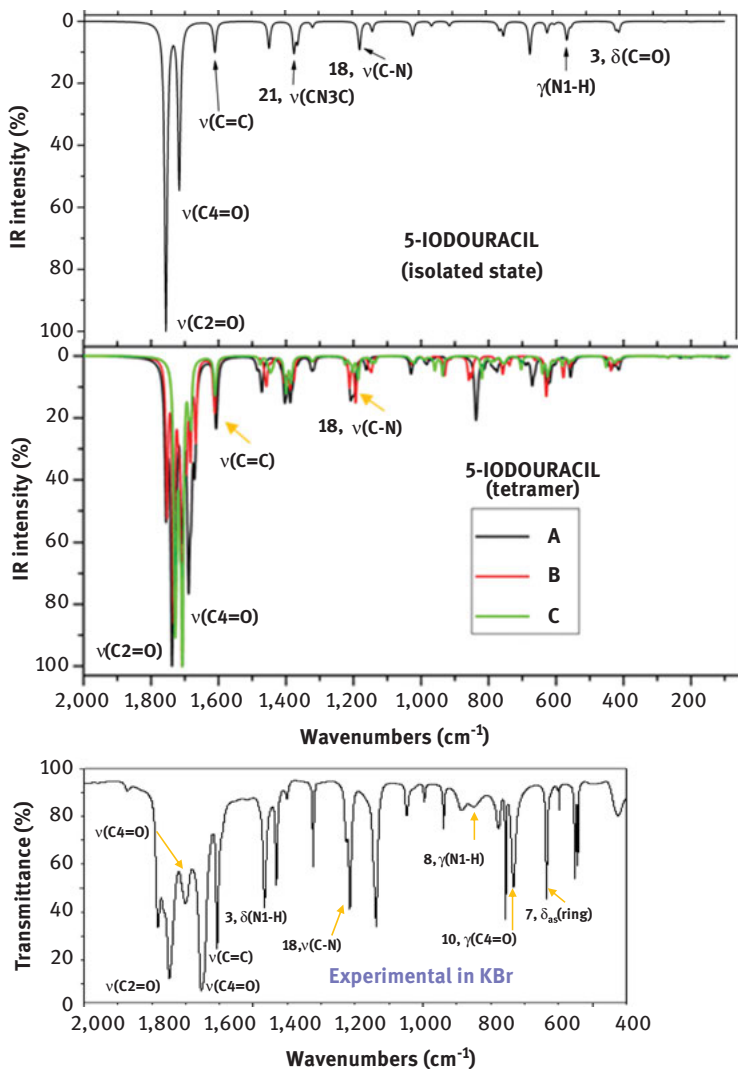


Figure 10.11: Comparison of the experimental IR spectrum of 5-iodouracil in the solid state with those spectra simulated (scaled theoretically) considering a monomer (isolated state) and a tetramer form, at the B3LYP/DGDZVP level. Three kinds of tetramer forms were simulated, named A, B and C [110].

solid state [110]. Three kinds of tetramer forms were simulated, named A, B and C. The spectra of these tetramer forms appear more in accordance to the experimental one than that of the isolated state.

(ii) To carry out an additional correction/scaling in the modes involved in H-bonds. Because the simulation of the solid state by a dimer/trimer/tetramer form is a simplification, some discrepancies with the experimental values can be

expected in the modes with groups involved in H-bonds. The H-bonds can rise to a blue-shift of ca. 300 cm^{-1} in the stretching region and consequently a red-shift of similar value in the in-plane bending range. The rms errors obtained with the OSF, LSE, TLSE, and PSE procedures in the calculated wavenumbers of d4T and by three DFT methods with the 6-31G(d,p) basis set are shown in Table 10.17. The TLSE procedure appears the best by B3LYP, X3LYP, and M062X/DFT methods, in accordance to other examples discussed above. The B3LYP method has a similar accuracy than X3LYP. Thus, both methods are recommended. The simulation of a dimer form reduces the error, as compared to the values of the monomer form. The lowest error were obtained in dimer V, which corresponds to that present in the solid-state sample.

Table 10.17: Rms errors obtained after scaling the calculated wavenumbers of d4T by different DFT methods.

Structure	Method	Scaling procedure			
		OSF	LSE	TLSE	PSE
Monomer C1	B3LYP	24.0	15.9	10.5	13.6
	X3LYP	–	14.2	10.5	13.2
	M062X	–	19.6	11.7	18.9
Dimer V	B3LYP	21.9	12.6	8.2	11.2
	X3LYP	–	12.5	8.1	11.2
	M062X	–	18.1	11.5	18.0
Dimer I	B3LYP	22.6	16.3	14.5	15.2
Dimer G	B3LYP	21.8	16.0	14.1	15.2

10.5 Summary and conclusions

A compressible compendium of the scaling procedures available today is described, with special attention to those that scales the wavenumbers directly. Several accurate procedures and examples are presented.

The procedure selected for scaling depends on: (i) the size of the organic molecule, (ii) the type of compound, and (iii) the accuracy required for the predicted wavenumbers.

(i) This point can be a limitation depending on the computer facilities. For larger organic molecules with less than 50 atoms, DFT methods and large basis sets can be used for calculating wavenumbers. Among the procedures for scaling the wavenumber, the CCD, CCSD(T), and QCISD methods and large basis sets give rise

to almost corrected harmonic wavenumbers. Thus, it is not necessary to use scaling procedures. However, these methods are very demanding in time and memory computer consuming, and they are limited to small molecules with less than 10 atoms.

For large systems, DFT methods with small basis sets can be used for calculating wavenumbers. However, the cost/effective ratio with DFT methods is something high versus semiempirical methods, and therefore their use is not recommended. In contrast, the AM1 and SAM1 semiempirical methods, when the SCFEM procedure is used, lead to scaled wavenumbers with errors lower than 7%.

(ii) When the empirically corrected *ab initio* force constant of the different groups of a molecule is known, or at least in the majority of the groups, the use of the procedure which requires the scaling of the geometry and the force constant produces excellent results. In other cases or with “exotic” molecules, previous computational work is required to get satisfactory scale factors. Another disadvantage of the procedure which scales the force constant is the additional effort that in general is necessary for a good description of the internal coordinates and the scaling process.

(iii) If the accuracy required is not high (the errors in the predicted wavenumbers can be ca. 5–10%), the use of a unique scale factor with the calculated wavenumbers (or two, for the high- and for the low-wavenumbers vibrations) is the simplest and easiest procedure. In this case, among the DFT methods, the most cost-effective ones are the B3-based/6-31G(d). If the accuracy required is higher, then, at the same level can be used the LSE, TLSE and PSE procedures. For the lowest error, previous scale factors should be calculated for each mode from related and simpler molecules, the SCFEM procedure.

When the comparisons theory-experiment are carried out with experimental gas phase values, a good concordance is obtained. However, for experimental values in the solid state, it is recommended to simulate the crystal unit cell of the system.

Benzene and uracil molecules were used as examples, and scaling factors obtained in them are shown in the present article. The predicted wavenumbers for the ring modes using B3LYP and X3LYP methods lead to the smallest errors. Thus, these methods are recommended to be used. HF and MP2 methods lead to large errors, and thus they are not recommended to be used for calculating the wavenumbers, with the exception of the use of the SCFEM scaling procedure. The scaling equations procedures (LSE, TLSE) give rise to a remarkably improvement in the predicted wavenumbers, than when OSF is used. However, few scaling equations have been reported and therefore these procedures have not been so standardized as the OSF procedure.

Note: MAP wishes to thank to BSCH-UCM PR26/16 for financial support.

References

- [1] Alcolea Palafox M. The prediction of vibrational spectra: the use of scale factors. *Recent Res Devel in Physical Chem. Transworld Research Network: Trivandrum, India*, 1998;2:213–32.
- [2] Alecu IM, Zheng J, Zhao Y, Truhlar DG. Computational thermochemistry: scale factor databases and scale factors for vibrational frequencies obtained from electronic model chemistries. *J Chem Theory & Comput.* 2010;6(9):2872–87.
- [3] Laury ML, Boesch SE, Haken I, Sinha P, Wheeler RA, Wilson AK. Harmonic vibrational frequencies: scale factors for pure, hybrid, hybrid meta, and double-hybrid functionals in conjunction with correlation consistent basis sets. *J Comput Chem.* 2011;32(11):2339–47.
- [4] Alcolea Palafox M. Infrared study of some solid local anesthetics. *Spectrochim Acta A.* 1988;44:1465–71.
- [5] Alcolea Palafox M. Raman spectra and vibrational analysis for benzocaine. *J Raman Spectrosc.* 1989;20:765–71.
- [6] Alcolea Palafox M. Infrared and Raman spectra, vibrational assignment and barrier to torsion and inversion in the *p*-amino group of procaine hydrochloride. *Ind J Pure Appl Phys.* 1993; 31(2):90–101.
- [7] Kashinski DO, Chase GM, Nelson RG, Di Nallo OE, Scales AN, VanderLey DL, et al. Harmonic vibrational frequencies: approximate global scaling factors for TPSS, M06, and M11 functional families using several common basis sets. *J Phys Chem A.* 2017;121:2265–73.
- [8] Laury ML, Carlson MJ, Wilson AK. Vibrational frequency scale factors for density functional theory and the polarization consistent basis sets. *J Comput Chem.* 2012;33 (30): 2380–87.
- [9] Borowski P, Ruiz TP, Barczak M, Pilorz K, Pasieczna-Patkowska S. Application of the multi-parameter SQM harmonic force field, and ESFF harmonic frequencies scaling procedures to the determination of the vibrational spectra of silicon- and sulfur(II)-containing compounds. *Spectrochim Acta A.* 2012;86:571–85.
- [10] Borowski P, Pilorz K, Pitucha M. An effective scaling frequency factor method for scaling of harmonic vibrational frequencies: application to 1,2,4-triazole derivatives. *Spectrochim Acta A.* 2010;75(5):1470–75.
- [11] Borowski P. An effective scaling frequency factor method for scaling of harmonic vibrational frequencies The use of redundant primitive coordinates. *J Molec Spectrosc.* 2010;264(1): 66–74.
- [12] Johnson RDIII, Irikura KK, Kacker RN, Kessel R. Scaling factors and uncertainties for ab initio anharmonic vibrational frequencies. *J Chem Theory & Comput.* 2010;6(9):2822–28.
- [13] Borowski P, Fernández-Gómez M, Fernández-Liencreas M-P, Peña Ruiz T, Quesada Rincón M An effective scaling frequency factor method for scaling of harmonic vibrational frequencies: application to toluene, styrene and its 4-methyl derivative. *J Molec Struct.* 2009;924–926: 493–503.
- [14] Kabelac M, Hobza P, Spirko V. The *ab initio* assigning of the vibrational probing modes of tryptophan: linear shifting of approximate anharmonic frequencies vs. multiplicative scaling of harmonic frequencies. *Phys Chem Chem Phys.* 2009;11(20):3921–26.
- [15] Yu HS, Fiedler LJ, Alecu IM, Truhlar DG. Computational thermochemistry: automated generation of scale factors for vibrational frequencies calculated by electronic structure model chemistries. *Comp Phys Commun.* 2017;210:132–38.
- [16] Sousa SF, Fernandes PA, Ramos MJ. General performance of density functionals. *J Phys Chem A.* 2007;111:10439–52.
- [17] Becke AD. Density-functional thermochemistry. 3. The role of exact exchange. *J Chem Phys.* 1993;98(7):5648–52.

- [18] Lee C, Yang W, Parr RG. Development of the Colle–Salvetti correlation-energy formula into a functional of the electron-density. *Phys Rev.* 1988;B37(2):785–89.
- [19] Perdew JP. Density-functional approximation for the correlation energy of the inhomogeneous electron gas. *Phys Rev.* 1986;B33(12):8822–24.
- [20] (a) Perdew JP, Wang Y. Accurate and simple analytic representation of the electron-gas correlation energy. *Phys Rev.* 1992;B45(23):13244–49. (b) Perdew JP, Chevary JA, Vosko SH, Jackson KA, Pederson MR, Singh DJ, Fiolhais C. Atoms, molecules, solids, and surfaces: applications of the generalized gradient approximation for exchange and correlation. *Phys Rev.* 1992; B46(11):6671–87.
- [21] (a) Zhao Y, Schultz NE, Truhlar DG. Design of density functionals by combining the method of constraint satisfaction with parametrization for thermochemistry, thermochemical kinetics, and noncovalent interactions. *J Chem Theory Comput.* 2006;2(2):364–82. (b) Becke AD. Density-functional thermochemistry. IV. A new dynamical correlation functional and implications for exact-exchange mixing. *J Chem Phys.* 1996;104(3):1040–46.
- [22] Schultz NE, Zhao Y, Truhlar DG. Density functionals for inorganometallic and organometallic chemistry. *J Phys Chem A.* 2005;109(49):11127–43.
- [23] Xu X, Goddard WAIII. The X3LYP extended density functional for accurate descriptions of nonbond interactions, spin states, and thermochemical properties. *Proc Natl Acad Sci USA.* 2004;101(9):2673–77.
- [24] Zhao Y, Truhlar DG. A new local density functional for main-group thermochemistry, transition metal bonding, thermochemical kinetics, and noncovalent interactions. *J Chem Phys.* 2006; 125(19):194101–06.
- [25] Zhao Y, Truhlar DG. Applications and validations of the Minnesota density functionals. *Chem Phys Lett.* 2011;502(1–3):1–13.
- [26] Alcolea Palafox M, Kattan D, Afseth NK. FT-IR spectra of the anti-HIV nucleoside analogue d4T (Stavudine). Solid state simulation by DFT methods and scaling by different procedures. *J Molec Struct.* 2018;1157:587–601.
- [27] Alcolea Palafox M, Rastogi VK, Singh SP. FT-IR and FT-Raman spectra of 5-chlorocytosine: solid state simulation and tautomerism. Effect of the chlorine substitution in the Watson-Crick base pair 5-chlorodeoxycytidine-deoxyguanosine. *Spectrochim Acta A.* 2018;188:418–35.
- [28] Frisch MJ, Trucks GW, Schlegel HB, Scuseria GE, Robb MA, Cheeseman JR, et al. Gaussian 09, Revision D.01. Wallingford CT: Gaussian, Inc., 2009.
- [29] Alcolea Palafox M, Rastogi R, Anupama, Jane Alam M, Bhat D, Rastogi VK. The accuracy of the M06L DFT method in the prediction of the vibrational spectra of 4-amino-2-chlorobenzonitrile: a detailed interpretation of the molecular structure and vibrational IR and Raman spectra and other molecular properties using several DFT methods. *Asian J Phys.* 2016;25(2):189–219.
- [30] El-Sayed AA, Tamara Molina A, Álvarez-Ros MC, Alcolea Palafox M. Conformational analysis of the anti-HIV Nikavir prodrug: comparisons with AZT and Thymidine, and establishment of structure–activity relationships/tendencies in other 6′-derivatives. *J Biomol Struct Dyn.* 2015;33(4):723–48.
- [31] Alcolea Palafox M. Structure–activity relationships/tendencies found in several anti-HIV Nicavir derivatives using DFT quantum chemical methods. *Chem Informatics.* 2015;1(2:11):1–13.
- [32] Alcolea Palafox M, Posada-Moreno P, Villarino-Marín AL, Martínez-Rincon C, Ortuño-Soriano I, Zaragoza-García I. DFT Calculation of four new potential agents muscarinic of bispyridinium type: structure, synthesis, biological activity, hydration, and relations with the potents W84 and DUO-30. *J Comput Aided Mol Des.* 2011;25(2):145–61.
- [33] Alcolea Palafox M, Iza N. Structure–activity relationships of the antiviral D4T and seven 4′-substituted derivatives using MP2 and DFT methods. *Struct Chem.* 2013;24(3):967–80.

- [34] Hoffmann M, Rychlewski J. Density functional theory (DFT) and drug design. *Rev Modern Quantum Chem.* 2002;2:1767–803.
- [35] Yurenko YP, Zhurakivsky RO, Ghomi M, Samijlenko SP, Hovorun DM. Comprehensive conformational analysis of the nucleoside analogue 2'- β -deoxy-6-azacytidine by DFT and MP2 calculations. *J Phys Chem B.* 2007;111(22):6263–71.
- [36] Balachandran V, Murugan M, Nataraj A, Karnan M, Ilango G. Comparative vibrational spectroscopic studies, HOMO–LUMO, NBO analyses and thermodynamic functions of p-cresol and 2-methyl-p-cresol based on DFT calculations. *Spectrochim Acta A.* 2014;132: 538–49.
- [37] Arjunan V, Thirunarayanan S, Devi GD, Mohan S. Substituent influence on the structural, vibrational and electronic properties of 2,5-dihydrothiophene-1,1-dioxide by experimental and DFT methods. *Spectrochim Acta A.* 2015;150:641–51.
- [38] Arjunan V, Marchewka MK, Raj A, Yang H, Mohan S. Structural and vibrational spectral investigations of melaminium glutarate monohydrate by FTIR, FT-Raman and DFT methods. *Spectrochim Acta A.* 2015;135:540–50.
- [39] Szafran M, Komasa A, Anioła M, Katrusiak A, Dega-Szafran Z. Structure of the complex of dimethylphenyl betaine with dichloroacetic acid studied by X-ray diffraction, DFT calculations, infrared and Raman spectra. *Vib Spectrosc.* 2016;84:92–100.
- [40] Singh JS. FT-IR and Raman spectra, ab initio and density functional computations of the vibrational spectra, molecular geometries and atomic charges of uracil and 5-halogenated uracils (5-X-uracils; X=F, Cl, Br, I). *Spectrochim Acta A.* 2013;117:502–18.
- [41] Szafran M, Katrusiak A, Dega-Szafran Z, Kowalczyk I. Structure of 4-(trimethylammonium) benzoate hydrate studied by X-ray diffraction, DFT calculations, NMR and FTIR spectra. *J Molec Struct.* 2011;1005(1–3):144–51.
- [42] Alcolea Palafox M, Rastogi VK. Quantum chemical predictions of the vibrational spectra of polyatomic molecules. The uracil molecule and two derivatives. *Spectrochim Acta A.* 2002; 58(3):411–40.
- [43] Alcolea Palafox M. Scaling factors for the prediction of vibrational spectra. I. Benzene molecule. *Int J Quantum Chem.* 2000;77:661–84.
- [44] Alcolea Palafox M, Iza N, Gil M. The hydration effect on the uracil wavenumbers: an experimental and quantum chemical study. *J Molec Struct (Theochem).* 2002;585(1–3):69–92.
- [45] GaussView 5.1. Wallingford CT: Gaussian Inc., 2009.
- [46] Hess JBA, Schaad LJ, Cársky P, Zahradnik R. Ab initio calculations of vibrational spectra and their use in the identification of unusual molecules. *Chem Rev.* 1986;86(4):709–30.
- [47] Hehre WJ, Radom L, Schleyer PvR, Pople JA. Ab initio molecular orbital theory. New York, USA: Wiley & Sons, 1986.
- [48] Boggs JE. Accurate determination of molecular structure and vibrational force constants by computation. *Phys Chem Minerals.* 1987;14(5):407–12.
- [49] Boggs JE. Accurate computational prediction of molecular structure and spectra. *Pure & Appl Chem.* 1988;60(2):175–1982.
- [50] Kesharwani MK, Brauer B, Martin JML. Frequency and zero-point vibrational energy scale factors for double-hybrid density functionals (and other selected methods): can anharmonic force fields be avoided?. *J Phys Chem A.* 2015;119:1701–14.
- [51] Alcolea Palafox M, Rastogi VK. Some procedures for predicting the wavenumbers of the spectra: the scaling. In: Joseph J, Sharma A, Rastogi VK, editor(s). *Perspectives in modern optics & optical instrumentation.* India: Anita Publications, 2002:91–8.
- [52] Alcolea Palafox M, Núñez JL, Gil M, Rastogi VK. Scaling procedures for the prediction vibrational spectra: the benzene and aniline molecules, and some derivatives. In: Singh K, Rastogi VK, editors. *Perspectives in engineering optics.* Anita Publications, 2002: 356–91.

- [53] Alcolea Palafox M. Computational chemistry applied to vibrational spectroscopy: a tool for characterization of nucleic acid bases and some of their 5-substituted derivatives. In: Ramasami P, editors. Computational sciences. 121 High Street, Boston: Walter de Gruyter, Inc., 2017;5: 118–51.
- [54] (a) Pulay P, Zhou X, Fogarasi G. Recent experimental and computational advances in molecular spectroscopy. Fausto R, editor. Netherlands: Kluwer Acad. Publishers, 1993: 99. (b) Pulay P, Fogarasi G, Zhou X, Taylor PW. Ab initio prediction of vibrational spectra: a database approach. *Vibrational Spectrosc.* 1990;1(2):159–165.
- [55] Pulay P, Meyer W. Ab initio calculation of the force field of ethylene. *J Molec Spectrosc.* 1971; 40(1):59–70.
- [56] Blom CE, Altona C. Application of self-consistent-field ab initio calculations to organic molecules. V. Ethene: general valence force field scaled on harmonic and anharmonic data, infra-red and Raman intensities. *Mol Phys.* 1977;34(1):177–92.
- [57] Pulay P, Fogarasi G, Pang F, Boggs JE. Systematic ab initio gradient calculation of molecular geometries, force constants, and dipole moment derivatives. *J Am Chem Soc.* 1979;101(10): 2550–60.
- [58] Pulay P, Fogarasi G, Pongor G, Boggs JE, Vargha A. Combination of theoretical ab initio and experimental information to obtain reliable harmonic force constants. Scaled quantum mechanical (QM) force fields for glyoxal, acrolein, butadiene, formaldehyde, and ethylene. *J Am Chem Soc.* 1983;105:7037–47.
- [59] Sundius T. Scaling of ab initio force fields by MOLVIB. *Vib Spectrosc.* 2002;29(1–2):89–95.
- [60] Sundius T. MOLVIB (V.7.0): calculation of harmonic force fields and vibrational modes of molecules. 2002. QCPE program No. 807.
- [61] Pulay P, Fogarasi G, Boggs JE. Force-field, dipole-moment derivatives, and vibronic constants of benzene from a combination of experimental and ab initio quantum chemical information. *J Chem Phys.* 1981;74(7):3999–4014.
- [62] Fogarasi G, Császár AG. Theoretical prediction of vibrational-spectra - scaled quantum-mechanical (SQM) force-field for fluorobenzene. *Spectrochim Acta A.* 1988;44(11):1067–77.
- [63] Niu Z, Dunn KM, Boggs JE. Theoretical prediction of vibrational spectra. III. The harmonic force field and vibrational spectra of aniline, aniline-NHD, and aniline-ND₂. *Mol Phys.* 1985;55: 421–32.
- [64] Xie Y, Boggs JE. The computed force constants and vibrational spectra of toluene. *J Comput Chem.* 1986;7(2):158–64.
- [65] Alcolea Palafox M, Boggs JE. Theoretical prediction of the vibrational spectrum, geometry, and scaled quantum mechanical (SQM) force field of phenylsilane, C₆H₅SiH₃. *J Molec Struct (Theochem).* 1993;284(1–2):23–35.
- [66] Xie Y, Fan K, Boggs JE. The harmonic force field and vibrational spectra of pyrrole. *Mol Phys.* 1986;58:401–11.
- [67] Fan K, Boggs JE. Rotational isomerism of acrylic acid. *J Molec Struct.* 1987;157(1–3):31–41.
- [68] Xavier RJ, Gobinath E. Density functional theory study on characterization of 3-chloro-1,2-benzisothiazole. *Spectrochim Acta A.* 2012;91:248–55.
- [69] Xavier RJ, Gobinath E. FT-IR, FT-Raman, ab initio and DFT studies, HOMO-LUMO and NBO analysis of 3-amino-5-mercapto-1,2,4-triazole. *Spectrochim Acta A.* 2012;86:242–51.
- [70] Murugan M, Balachandran V, Karnan M. Vibrational spectra and electrostatic potential Surface of 2-fluoro-6-methoxybenzonitrile base don quantum chemical calculations. *J Chem Pharmaceutical Res.* 2012;4(7):3400–13.
- [71] Baker J, Jarzecki AA, Pulay P. Direct scaling of primitive valence force constants: an alternative approach to scaled quantum mechanical force fields. *J Phys Chem A.* 1998;102(8):1412–24.

- [72] SQM version 1.0, Scaled quantum mechanical force field, 2013 Green Acres Road, Fayetteville, Arkansas 72703.
- [73] Borowski P, Fernández-Gómez M, Fernández-Liencreas MP, Peña Ruiz T. An effective scaling frequency factor method for scaling of harmonic vibrational frequencies: theory and preliminary application to toluene. *Chem Phys Lett.* 2007;446:191–98.
- [74] Rauhut G, Pulay P. Transferable scaling factors for density functional derived vibration force fields. *J Phys Chem.* 1995;99(10):3093–100.
- [75] Alcolea Palafox M. Scaling factors for the prediction of the wavenumbers of the ring modes in benzene derivatives. *J Phys Chem A.* 1999;103:11366–77.
- [76] Halls M, Velkovski J, Schlegel H. Harmonic frequency scaling factors for Hatree-Fock, S-VWN,B-LPY, B3-LYP, B3-PW91,and MP2 with the Sadlej pVTZ electric property basis set. *Theor Chem Acc.* 2001;105(6):413–421.
- [77] Scott AP, Radom L. Harmonic vibrational wavenumbers: an evaluation of Hartree–Fock, Møller–Plesset, quadratic configuration interaction, density functional theory, and semiempirical scale factors. *J Phys Chem.* 1996;100(41):16502–13.
- [78] NIST computational chemistry comparison and benchmark database, <http://cccbdbnist.gov>, 2013;First Accessed 2015.
- [79] Database of frequency scale factors for electronic model chemistries: Version3Beta2. <https://comp.chem.umn.edu/freqscale/version3b2.htm>, First Accessed 2016.
- [80] <http://comp.chem.umn.edu/freqscale/version3b2.htm>
- [81] Irikura K, Johnson RIII, Kacker RN. Uncertainties in scaling factors for ab initio vibrational frequencies. *J Phys Chem A.* 2005;109(37):8430–8437.
- [82] Teixeira F, Melo A, Natalia M, Cordeiro S. Calibration sets and the accuracy of vibrational scaling factors: a case study with the X3LYP Hybrid Functional. *J Chem Phys.* 2010;133(11):114109–16.
- [83] Healy E, Holder A. An evaluation of AM1 calculated vibrational frequencies. *J Molec Struct (Theochem).* 1993;281:141–156.
- [84] Staroverov VN, Scuseria GE, Tao J, Perdew JP. Comparative assessment of a new nonempirical density functional: molecules and hydrogen-bonded complexes. *J Chem Phys.* 2003;119:12129–37.
- [85] Sinha P, Boesch S, Gu C, Wheeler R, Wilson A. Harmonic vibrational frequencies: scaling factors for HF, B3LYP, and MP2 methods in combination with correlation consistent basis sets. *J Phys Chem A.* 2004;108:9213–17.
- [86] Andersson M, Uvdal P. New scale factors for harmonic vibrational frequencies using the B3LYP density functional method with the triple- ζ basis set 6-311+G(d,p). *J Phys Chem A.* 2005;109:2937–41.
- [87] Roddecha S, Surawatanawong P, Sutthikhum V, Limtrakul J. Scaling factors for vibrational frequencies and zero-point vibration energies of some recently developed exchange-correlation functionals. *J Molec Struct Theochem.* 2006;760:189–92.
- [88] Merrick JP, Moran D, Radom L. An evaluation of harmonic vibrational frequency scale factors. *J Phys Chem A.* 2007;111(45):11683–700.
- [89] Friese DH, Törk L, Hättig C. Vibrational frequency scaling factors for correlation consistent basis sets and the methods CC2 and MP2 and their spin-scaled SCS and SOS variants. *J Chem Phys.* 2014;141(19):194106–12.
- [90] Chan B, Radom L. Frequency scale factors for some double-hybrid density functional theory procedures: accurate thermochemical components for high-level composite protocols. *J Chem Theory Comput.* 2016;12:3774–80.
- [91] Martin JML, Kesharwani MK. Assessment of CCSD(T)-F12 approximations and basis sets for harmonic vibrational frequencies. *J Chem Theory Comput.* 2014;10:2085–90.

- [92] Alcolea Palafox M, Núñez JL, Gil M. Accurate scaling of the vibrational spectra of aniline and several derivatives. *J Molec Struct (Theochem)*. 2002;593:101–31.
- [93] Alcolea Palafox M, Gil M, Núñez JL, Rastogi VK, Mittal L, Sharma R. Scaling factors for the prediction of vibrational spectra. II. The aniline molecule and several derivatives. *Int J Quantum Chem*. 2005;103(4):394–421.
- [94] Ortiz S, Alcolea Palafox M, Rastogi VK, Akitsu T, Joe IH, Kumar S. Simulation of a tetramer form of 5-chlorouracil: the vibrational spectra and molecular structure in the isolated and in the solid state by using DFT calculations. *Spectrochim Acta A*. 2013;110:404–18.
- [95] Ortiz S, Alvarez-Ros MC, Alcolea Palafox M, Rastogi VK, Balachandran V, Rathor SK. FT-IR and FT-Raman spectra of 6-chlorouracil: molecular structure, tautomerism and solid state simulation. A comparison between 5-chlorouracil and 6-chlorouracil. *Spectrochim Acta A*. 2014;130:653–68.
- [96] Kattan D, Alcolea Palafox M, Rathor SK, Rastogi VK. A DFT analysis of the molecular structure, vibrational spectra and other molecular properties of 5-nitrouracil and comparison with uracil. *J Molec Struct*. 2016;1106:300–15.
- [97] Alcolea Palafox M, Kattan D, Afseth NK. FT-IR spectra of the anti-HIV nucleoside analogue d4T (Stavudine). Solid state simulation by DFT methods and scaling by different procedures. *J Molec Struct*. 2017;1157:587–601.
- [98] Alcolea Palafox M. Computational chemistry applied to vibrational spectroscopy: a tool for characterization of nucleic acid bases and some of their 5-substituted derivatives. In: Ramasami P, editor. *Computational sciences*. Phys Sci Rev. 2017;5:117–51.
- [99] Srivastava AK, Pandey AK, Pandey S, Nayak PS, Narayana B, Sarojini BK, et al. Uniform versus nonuniform scaling of normal modes predicted by ab initio calculations: a test on 2-(2,6-dichlorophenyl)-n-(1,3-thiazol-2yl) acetamide. *Inter J Spectrosc*. 2014;ID 649268: 1–7.
- [100] Hameka HF, Famini GR, Jensen JO, Newhouse EI. *Gov Rep Announce Index*. 1990;90:13.
- [101] Hameka HF, Famini GR, Jensen JO, Jensen JL. *Gov Rep Announce Index*. 1991;91:15.
- [102] Hameka HF, Jensen JO. Theoretical studies of the methyl rotational barrier in toluene. *J Molec Struct (Theochem)*. 1996;362(3):325–30.
- [103] Wilson EB. The normal modes and frequencies of vibration of the regular plane hexagon model of the benzene molecule. *Phys Rev*. 1934;45(10):706–14.
- [104] Barone V, Festa G, Grandi A, Rega N, Sanna N. Accurate vibrational spectra of large molecules by density functional computations beyond the harmonic approximation: the case of uracil and 2-thiouracil. *Chem Phys Letts*. 2004;388:279–83.
- [105] Alam MJ, Ahmad S. Molecular structure, anharmonic vibrational analysis and electronic spectra of o-, m-, p-iodonitrobenzene using DFT calculations. *J Molec Struct*. 2014;1059:239–54.
- [106] Alam MJ, Bhat SA, Ahmad S. Molecular structure and vibrational analysis of 5-nitro-6-methyluracil molecule based on monomer, dimer and trimer calculations. *Indian J Phys*. 2016;90(5): 503–18.
- [107] Barone V. Anharmonic vibrational properties by a fully automated second-order perturbative approach. *J Chem Phys*. 2005;122(1):14108–18.
- [108] The general atomic and molecular electronic structure system (GAMESS program). <http://molecularmodelingbasics.blogspot.com/search/label/gamess>
- [109] Meléndez FJ, Alcolea Palafox M. Geometry and frequencies of the halothane molecule. *J Molec Struct (Theochem)*. 1999;493(1–3):179–85.
- [110] Alcolea Palafox M, Rastogi VK, Guerrero-Martínez A, Tardajos G, Joe H, Vats JK. Simulation of a tetramer form of 5-iodouracil. The vibrational spectra and molecular structure in the isolated and in the solid state by using DFT calculations. *Vibrat Spectrosc*. 2010;52(2): 108–21.

- [111] Ortiz S, Alcolea Palafox M, Rastogi VK, Tomer R. Solid state simulation in the tetramer form of 5-aminoorotic acid: the vibrational spectra and molecular structure by using MP2 and DFT calculations. *Spectrochim Acta A*. 2012;97:948–62
- [112] Rastogi VK, Alcolea Palafox M, Tomar R. 2-Amino-3, 5-dichlorobenzonitrile: DFT calculations in the monomer and dimer forms, FT-IR and FT-Raman spectra, molecular geometry, atomic charges and thermodynamical parameters. *Spectrochim Acta A*. 2013;110:458–70.
- [113] Alcolea Palafox M, Rastogi VK, Kumar S, Joe H. The biomolecule of 5-bromocytosine: FT-IR and FT-Raman spectra and DFT calculations. Identification of the tautomers in the isolated state and simulation the spectra in the solid state. *Spectrochim Acta A*. 2013;111:104–22.
- [114] Cuellar A, Alcolea Palafox M, Rastogi VK, Kiefer W, Schlücker S, Rathor SK. FT-IR and FT-Raman spectra of 5-fluoroorotic acid with solid state simulation by DFT methods. *Spectrochim Acta A*. 2014;132:430–45.
- [115] Alcolea Palafox M, Rastogi VK. 6-aminouracil: geometries and spectra in the isolated state and in the solid state simulation. A comparison with 5-aminouracil. *J Molec Struct*. 2016;1108: 482–95.

Siddheshwar D. Jadhav, Ponnadurai Ramasami
and Nagaiyan Sekar

11 Substituent effects on linear and nonlinear optical properties of fluorescent (E)-2-(4-halophenyl)-7-arylstyrylimidazo[1,2-A] pyridine: spectroscopic and computational methods

Abstract: Effects of alkylamino and bromo substituents on imidazo[1,2-a]pyridines containing donor- π -acceptor type groups were comprehensively investigated for their linear and nonlinear optical properties by solvatochromic and DFT (CAM-B3LYP and BHandHLYP) methods. The difference between the ground and excited dipole moments as well as their ratios obtained by solvatochromic analysis indicate that the excited state is more polar than the ground state for both the bromo and diethyl amino derivative. More than twofold enhancement in the excited state dipole moments was observed as revealed by the difference and ratio of dipole moment upon the introduction of alkylamino donor group and these suggest large intramolecular charge transfer in the dyes. Stabilization energy above 20 kJ/mol was observed for large number of electron donor-acceptor interactions in Natural Bonding Orbital (NBO) analysis. Bond length alternation (BLA) and Bond order alternation (BOA) values tend to zero suggesting a high degree of polarization in the dyes. Enhancement in mean polarizability (α_0), first hyperpolarizability (β_0) and second static hyperpolarizabilities ($\bar{\gamma}$) were observed by the introduction of alkylamino and bromo group in place of chloro in spite of the fact that Hammett constant of chloro and bromo are the same. The dyes have fundamental and intrinsic properties within the Hamiltonian limits. The two-photon absorption cross section value ($\approx 100 \text{ GM}$) is comparable with LDS-698, a commercial TPA dye. This investigation is important for understanding the electronic structure of imidazo[1,2-a]pyridine with active functional groups and extending the potential for optical applications.

Keywords: Imidazo[1,2-a]pyridine, DFT, TDDFT, fundamental limits, two photon absorption, NLO properties

This article has previously been published in the journal *Physical Sciences Reviews*. Please cite as: Jadhav, S. D., Ramasami, P., Sekar, N. Substituent effects on linear and nonlinear optical properties of fluorescent (E)-2-(4-halophenyl)-7-arylstyrylimidazo[1,2-A] pyridine: spectroscopic and computational methods. *Physical Sciences Reviews* [Online] **2018**, 3. DOI: 10.1515/psr-2018-0032

<https://doi.org/10.1515/9783110568196-011>

11.1 Introduction

Imidazo [1,2-a]pyridines are isosteres of indoles and azaindoles [1], which have diverse range of applications in material chemistry [2–5]. They have luminescent properties unlike the analogous imidazo [1,5-a]pyridines [6] which are non-luminescent. Imidazo[1,2-a]pyridine derivatives are utilized as the emitting layer in OLEDs [7], dopamine D3 receptors ligands [8], mercury ion detector [9], peripheral benzodiazepine receptors and microglia cell visualization [10]. Some of the derivatives show characteristic luminescence in the blue region in solution and in the solid state with excited-state intramolecular proton transfer (ESIPT) [11–13].

Usually, styryl dyes show an increase in quantum yield on interaction with biomolecules such as DNA and RNA [14–16]. Styryl dyes have good photostability, structural diversification and enhancement in fluorescence intensity after binding with biomolecules. Enhancement in dipole moment is possible by modification in the D- π -A system containing delocalized π -electrons. Due to excellent optoelectronic properties, styryl dyes have good potentials as advanced materials in dye lasers, optical or electro-optical devices or sensors [17–24] because nowadays optics is overtaking areas of applications previously dominated by electronics [25].

The use of solvatochromic shifts for the estimation of the dipole moments of the ground and electronically excited state of a molecule is important to understand their structure in that state, which gives the information about optoelectronic properties of the material. Increase in transition dipole moment, increase in the polarity of the microenvironment, a red shift in absorption wavelength and twisted intramolecular charge transfer (TICT) in the molecule are responsible for enhancing the molecular hyperpolarizability [26–29]. It has been shown that the bromo substituted polyimides exhibit a higher optical transparency and macroscopic nonlinear optical coefficient (d_{33}) than the common reference polyimides containing the strong electron accepting nitro or cyano groups [30]. In poled polymeric films, chromophores with large ground state dipole moment (μ) will not arrange in parallel fashion, and hence consequently the optical coefficient (d_{33}) of the film is reduced. Therefore, the dyes with small dipole moment (μ) in the ground state and higher dipole moment (μ) in the excited state would be the desired fluorophore for obtaining a polymer with large optical coefficient for applications [30, 31].

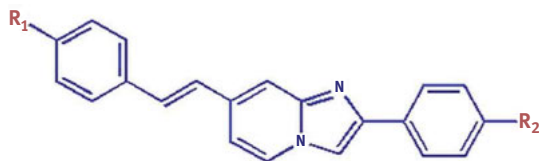
In this paper, our study was focused to calculate the ratio and difference in excited and ground state dipole moment of imidazo[1,2-a]pyridine styryl dyes. Nonlinear Optical (NLO) properties were compared with the electron donating alkylamino and weak electron withdrawing bromo substitutions with the unsubstituted dye. NLO and related properties estimated by solvatochromic and DFT methods were correlated with the structural modifications. In this context, the difference in ground state and excited state dipole moments of styryl dyes were studied using the well-known Bilot–Kawski, Liptay, Lippert and Mataga and Reichardt solvatochromic shift methods and the ratio of dipole moment by Bilot–Kawski, Bakshiev and McRae methods as well as by

computational method. Looking at the large difference in the singlet ground state and excited state dipole moments, we evaluated nonlinear optical properties of the molecules in different solvent polarity media [32]. Typically, 500–800 GM values of two-photon absorption (TPA) cross-section for bisimidazo[1,2-a]pyridines inspired us for studying mono derivatives [33], especially, employing effective substituents and their theoretical assessment to improve NLO properties. Quantum mechanical investigation plays an important role to investigate the relationship between electronic structure and linear and nonlinear optical properties in designing effective fluorophores [34–36]. The NLO properties of the molecules can be defined by parameters like mean polarizability (α_0), mean first hyperpolarizability (β_0), static second hyperpolarizability ($\bar{\gamma}$), upper limit of polarizability (α_0^{max}), upper limit of first hyperpolarizability (β_0^{max}), upper negative ($\bar{\gamma}^{min}$) and positive ($\bar{\gamma}^{max}$) limit of second hyperpolarizability, intrinsic polarizability (α_0^{int}), intrinsic first hyperpolarizability (β_0^{int}), static negative intrinsic second hyperpolarizability ($\bar{\gamma}_{int}^{min}$) and static positive intrinsic second hyperpolarizability ($\bar{\gamma}_{int}^{max}$). These parameters were obtained using experimental and computational methods for the arylstyrylimidazo[1,2-a]pyridine (E)-2-(4-chlorophenyl)-7-(4-fluorostyryl)imidazo[1,2-a]pyridine dyes as illustrated in Figure 11.1.

11.2 Materials and methods

11.2.1 Material and theoretical methods

All the computations were performed with the Gaussian 09 package [37]. Density Functional Theory (DFT) method was used for ground state (S_0) geometries optimization, while time-dependent density functional theory (TDDFT) for the excited state optimization of all the extended styryl dyes (**P1-P10**) [38]. The popular hybrid functional B3LYP was used, which combines Becke's three parameter exchange functional (B3) [39] with the nonlocal correlation functional by Lee, Yang and Parr (LYP) [40]. The 6-31G(d) basis set was used for all the atoms, which seems to be sufficient for this type of molecules [41, 42]. Polarizable Continuum Model (PCM) as implemented in Gaussian 09 was used for computations in all solvents [43] and the results were visualized with GaussView 5.0 [44]. TDDFT calculations were used to determine molecular orbital (MO) transitions for various excited states and to determine the most likely transitions. The photophysical properties reported earlier [45] were used in the calculation of dipole moment and hyperpolarizability of arylstyrylimidazo[1,2-a]pyridine in the solvents dichloromethane (DCM), dimethylsulphoxide (DMSO), dimethylformamide (DMF), acetonitrile (ACN) and tetrahydrofuran (THF). For the Stokes shift calculation, highest intensity absorption (λ_{max}) was considered and it increases as the polarity of the solvent increases for all dyes. The methods for calculating dipole moment were explained very first in the supporting information under the title "Theoretical Methods for calculation of difference and ratio in dipole moment".



Dye	R ₁	R ₂	Dye	R ₁	R ₂
P1		H	P6		Br
P2		C1	P7		H
P3		Br	P8		C1
P4		H	P9		Br
P5		C1	P10	H	H

Figure 11.1: Substituted arylstyrylimidazo[1,2-a]pyridine (E)-2-(4-chlorophenyl)-7-(4-fluorostyryl)imidazo[1,2-a]pyridine.

11.3 Results and discussion

11.3.1 Absorption, vertical excitation and computed emission

Vertical excitations were estimated using TD-B3LYP/6-31G(d) method for the first 20 states. The computed energies of the vertical excitations, oscillator strength and their orbital contributions and computed emission for dyes **P1–P10** are listed in Table 11.1.

All dyes show a large red shifted absorption and emission wavelength in comparison with the unsubstituted dye **P10** using both methods. The computed vertical excitation for the dyes **P1–P10** range from 393 to 441 nm whereas experimental values of absorption maximum range from 372 to 394 nm. Experimental, DFT and TDDFT results suggest that there was no influence of solvent polarity on the absorption of dyes **P1–P10**. Based on DFT method, red shift was observed in the

Table 11.1: Observed absorption and computed vertical excitation for dyes P1-P10 in various solvents.

Dye	Solvent	Expt λ_{abs}^a nm	Vertical excitation		Oscillator strength (f)	Orbital contribution	Expt λ_{emi}^b nm	TD-B3LYP/ 6-311G(d) λ_{emi}^c nm
			eV					
			nm					
P1	Toluene	379	429.93	2.8838	1.4039	L→H (98.67 %)	431	479.13
	THF	379	432.48	2.8668	1.3748	L→H (98.73 %)	459	481.30
	DCM	379	433.43	2.8605	1.3799	L→H (98.76 %)	467	484.00
	ACN	376	433.14	2.8624	1.3557	L→H (98.73 %)	482	483.76
	DMSO	386	435.26	2.8485	1.3774	L→H (98.81 %)	490	487.17
P2	Toluene	384	432.51	2.8667	1.3976	L→H (98.57 %)	459	482.18
	THF	380	435.24	2.8487	1.3646	L→H (98.62 %)	464	486.31
	DCM	381	436.16	2.8427	1.3697	L→H (98.65 %)	469	487.77
	ACN	377	435.90	2.8443	1.3443	L→H (98.61 %)	485	487.33
	DMSO	389	437.94	2.8311	1.3665	L→H (98.70 %)	494	490.64
P3	Toluene	384	433.02	2.8633	1.4114	L→H (98.51 %)	455	482.78
	THF	382	435.84	2.8447	1.3774	L→H (98.56 %)	461	486.98
	DCM	379	436.77	2.8387	1.3824	L→H (98.60 %)	471	488.44
	ACN	384	436.57	2.8400	1.3571	L→H (98.56 %)	486	488.04
	DMSO	384	438.59	2.8269	1.3797	L→H (98.65 %)	492	491.31
P4	Toluene	387	432.47	2.8669	1.431	L→H (98.70 %)	456	481.05
	THF	384	435.5	2.8469	1.4045	L→H (98.76 %)	462	485.07
	DCM	387	436.45	2.8407	1.4096	L→H (98.79 %)	466	486.53
	ACN	384	436.29	2.8418	1.3869	L→H (98.76 %)	486	486.10
	DMSO	391	438.35	2.8284	1.4078	L→H (98.83 %)	489	489.40

(continued)

Table 11.1 (continued)

Dye	Solvent	Expt λ_{abs}^a nm	TD-B3LYP/6-31G(d)			Expt λ_{emi}^b nm	TD-B3LYP/ 6-311G(d) λ_{emi}^c nm	
			Vertical excitation		Oscillator strength (f)			Orbital contribution
			nm	eV				
P5	Toluene	388	436.03	2.8434	1.4287	439	482.56	
	THF	386	438.65	2.8265	1.3978	475	487.98	
	DCM	389	439.54	2.8208	1.4029	475	490.07	
	ACN	383	439.25	2.8226	1.3794	491	489.10	
	DMSO	391	441.22	2.8100	1.4009	494	492.31	
P6	Toluene	388	436.43	2.8409	1.4404	434	484.32	
	THF	384	439.14	2.8233	1.4093	417	488.63	
	DCM	386	440.03	2.8176	1.4139	475	489.00	
	ACN	383	439.77	2.8193	1.3912	488	489.81	
	DMSO	392	441.74	2.8067	1.4124	495	492.99	
P7	Toluene	378	422.59	2.9339	1.4673	435	480.42	
	THF	374	423.95	2.9245	1.4483	463	484.87	
	DCM	372	424.72	2.9192	1.4529	434	486.39	
	ACN	376	424.13	2.9232	1.4329	482	486.22	
	DMSO	380	426.02	2.9103	1.4524	491	489.58	
P8	Toluene	380	426.08	2.9099	1.4709	459	483.65	
	THF	376	427.26	2.9019	1.4465	460	488.58	
	DCM	373	427.98	2.8970	1.4514	476	490.11	
	ACN	371	427.33	2.9014	1.4306	484	490.11	
	DMSO	383	429.22	2.8886	1.4512	497	493.39	

P9	Toluene	376	426.81	2.9049	1.4882	L→H (98.40 %)	459	484.22
	THF	374	428.14	2.8959	1.4638	L→H (98.45 %)	467	489.38
	DCM	374	428.86	2.8910	1.4687	L→H (98.48 %)	479	490.90
	ACN	373	428.27	2.8950	1.4492	L→H (98.45 %)	490	490.97
	DMSO	382	430.08	2.8828	1.469	L→H (98.53 %)	497	494.22
P10	Toluene	380	397.11	3.1222	1.1411	L→H (97.62 %)	397	451.74
	THF	377	394.7	3.1412	1.1263	L→H (97.62 %)	416	452.92
	DCM	376	395.03	3.1386	1.1326	L→H (97.67 %)	416	453.99
	ACN	372	393.08	3.1542	1.1107	L→H (97.58 %)	418	452.60
	DMSO	379	394.6	3.1421	1.1328	L→H (97.73 %)	425	455.49

$\lambda_{\text{abs}}^{\text{a}}$ = experimental wavelength maxima, $\lambda_{\text{em}}^{\text{b}}$ = experimental emission maxima, $\lambda_{\text{em}}^{\text{c}}$ = computed emission maxima using TD B3LYP/6-311G(d).

excitation and emission wavelength by replacement of H with bromine and similar replacement of chlorine with bromine. In all the solvents for the imidazo[1,2-a]pyridine dyes **P1–P10**, the vertical excitations are associated with the HOMO-LUMO transitions with the major contribution >97.58% and oscillator strength ranges from 1.1107 to 1.4882. A general trend of longer absorption-emission wavelength was observed for chloro derivatives by experimental method while a higher absorption-emission wavelength was observed for the bromo derivatives by DFT method.

11.3.2 Estimation of difference in dipole moments ($\mu_e - \mu_g$)

To understand the effects of substituted amines, absorption and emission spectra of the dyes were analysed using the Bilot–Kawski [46, 47] and MacRae [48] equations S1 to S9. Dipole–dipole, hydrogen bonding and solvation interactions stabilize the excited state of the molecule in polar solvents [49]. The bulk solvent polarity functional values were obtained using the relative permittivity and refractive index for mixtures by Equations (11.1)–(11.9) for respective functions. Solvent polarity function values of $f_{BK}(\epsilon, n)$, $\varphi_{BK}(\epsilon, n)$, $f_L(\epsilon, n)$, $\varphi_L(\epsilon, n)$ and molecular microscopic solvent function E_T^N for the various solvents and solvent mixtures used in this paper are summarized in Table S1. The absorption and emission maxima wavenumbers (in nm), Stokes shift and the summation of absorption and emission wavelength (in cm^{-1}) determined for the dyes **P1–P10** in different solvents are collected in Table S2 in the supporting information. The same f_{BK} , f_L and f_{BS} functions were used on the Y-axis to plot two different functions of Bilot–Kawski, Liptay and Bakshie using Equation S1 and Equation S2. Polarity graphs of Stoke shift ($\bar{\nu}_{abs} - \bar{\nu}_{em}$) against $f(\epsilon, n)$ and ($\bar{\nu}_{abs} + \bar{\nu}_{em}$) against $\varphi(\epsilon, n)$ were plotted by using above polarity functions in Equation S1 and S2 and they are represented in Figure S1. Slope and regression coefficients were obtained and representative graphs for McRae function (similar to Liptay Equation S1) are represented in Figure 11.2.

Substantial charge transfer in alkylamino substituted dyes is indicated by the steeper line and regression coefficients closer to unity for all the dyes except for the unsubstituted dye **P10**. Fluctuations in regression coefficient and slope are observed in different derivatives but both values are higher when compared to ($R^2 = 0.7724$ and slope = 793) dye **P10**. A similar trend of charge transfer is observed for Bilot–Kawski and Bakshiev plots which are shown in Figure S1 in supporting information. Slopes of polarity plots by different functions by Equation S1 and S2 for dye **P1–P10** are represented as Table S3 in supporting information. The difference in dipole moment is calculated by Equation S12 by using slopes of different functions and the value of Onsager radii for all dyes was taken from DFT computations and they are given in Table S4. The difference in dipole moment values in five solvents are collected in Table 11.2.

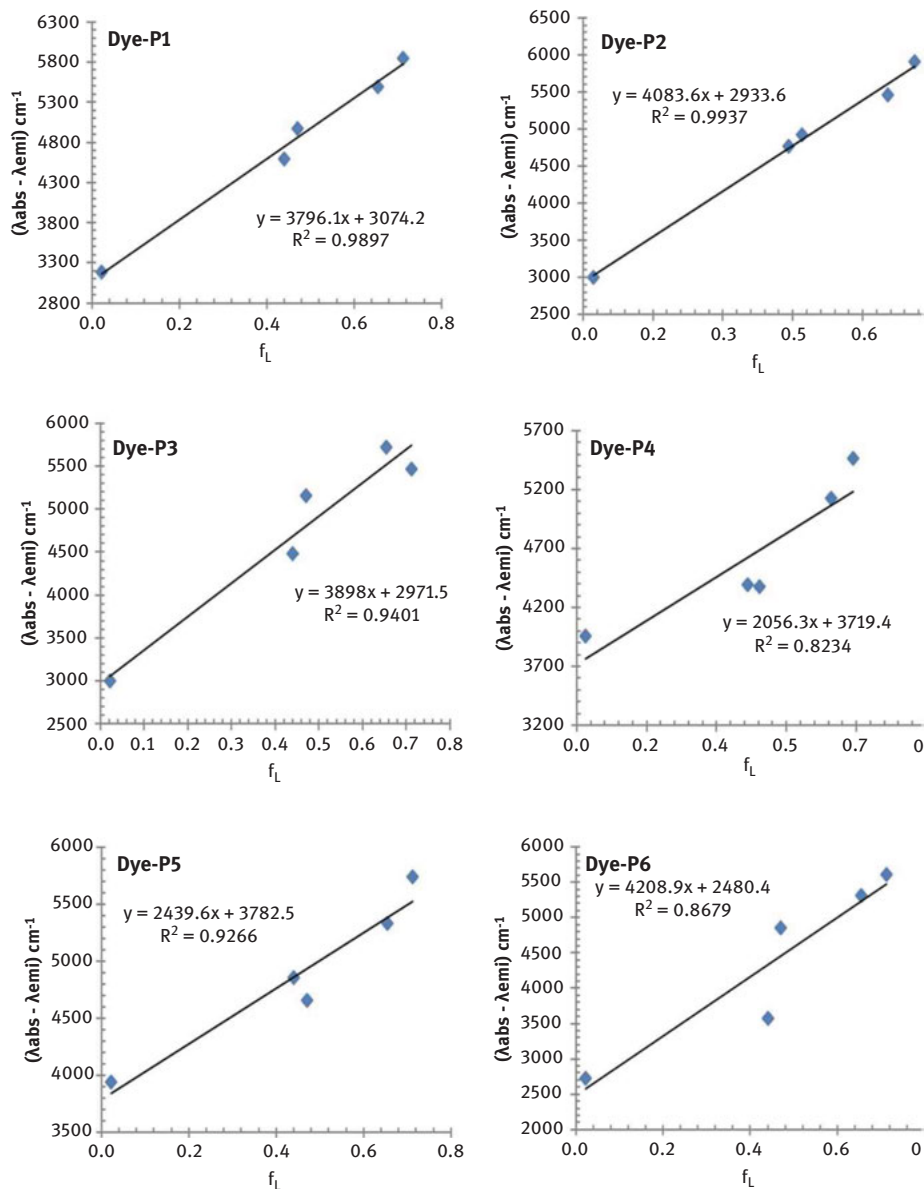


Figure 11.2: McRae's polarity function against Stoke shift plots of the dyes P1–P10.

The difference in dipole moment in DCM solvent were 3.17, 3.54, 5.33 and 4.04 by Bilot–Kawski, McRae, Lippert and Mataga and Reichardt method, respectively, and which is less than half than all other dyes. The ratio of the excited state dipole moment to the ground state dipole moment was calculated using Equation S10 and presented in

Table 11.2: Difference between the ground-state and singlet excited-state dipole moments (in Debye, D) of dyes **P1–P10**.

Solvents	Dye	Difference in dipole moments				Dye	Difference in dipole moments			
		BK	Mc	LM	Rt		BK	Mc	LM	Rt
Toluene	P1	7.55	8.43	13.04	7.64	P2	7.99	8.92	13.87	7.63
THF		7.51	8.38	12.97	7.68		7.85	8.76	13.62	7.77
DCM		7.39	8.25	12.77	7.80		8.20	9.16	14.23	7.44
ACN		7.22	8.06	12.46	7.99		7.74	8.65	13.44	7.88
DMSO		7.35	8.21	12.70	7.84		7.87	8.79	13.65	7.75
Toluene	P3	7.79	8.65	13.35	7.66	P4	5.70	6.38	9.68	5.68
THF		7.96	8.83	13.63	7.50		5.49	6.15	9.33	5.89
DCM		7.75	8.61	13.28	7.70		5.82	6.51	9.88	5.56
ACN		7.88	8.74	13.49	7.58		5.64	6.32	9.58	5.74
DMSO		7.77	8.63	13.32	7.68		5.63	6.30	9.55	5.75
Toluene	P5	6.58	7.37	11.34	5.60	P6	8.51	9.48	14.53	7.86
THF		6.46	7.24	11.14	5.70		8.70	9.70	14.85	7.69
DCM		6.29	7.04	10.84	5.86		8.32	9.27	14.20	8.04
ACN		6.30	7.06	10.86	5.85		8.27	9.22	14.13	8.08
DMSO		6.35	7.11	10.95	5.80		8.46	9.44	14.45	7.90
Toluene	P7	7.56	8.41	12.74	7.96	P8	6.34	7.08	10.88	6.22
THF		7.82	8.69	13.17	7.70		6.69	7.47	11.47	5.90
DCM		7.96	8.85	13.41	7.56		6.46	7.21	11.08	6.11
ACN		7.90	8.78	13.30	7.62		6.52	7.28	11.19	6.05
DMSO		7.86	8.74	13.24	7.66		6.42	7.17	11.02	6.14
Toluene	P9	8.19	9.14	14.23	6.76	P10	3.31	3.70	5.57	3.87
THF		7.91	8.82	13.74	7.00		3.21	3.59	5.41	3.98
DCM		7.89	8.80	13.71	7.02		3.17	3.54	5.33	4.04
ACN		7.61	8.49	13.23	7.27		3.20	3.58	5.39	3.99
DMSO		7.73	8.63	13.43	7.16		3.18	3.55	5.35	4.03

*BK = Bilot–Kawaski, Mc = McRae, Bk = Bakshiev and Rt = Reichardt method.

Figure 11.3. The ratio was more than unity for all dyes which indicates that the excited state is more polar and is being stabilized by the polar solvent environment.

It was observed that the ratio of dipole moment was more than twice than dye **P10** based on all methods. From the DFT method, the ground state dipole moments range from 3.04 to 10.50 D whereas excited state dipole moment was between 3.13 to 12.33 D and they are represented in Figure S2 and the values are given in Table S5. In dye **P6**, the largest dipole moment in the ground state is 10.39 D and in the excited state is 12.33 and these indicate the largest charge transfer from electron donating amino group. The experimental and computational results lead to higher dipole moment in the excited state and it increases as the polarity of the solvent increases.

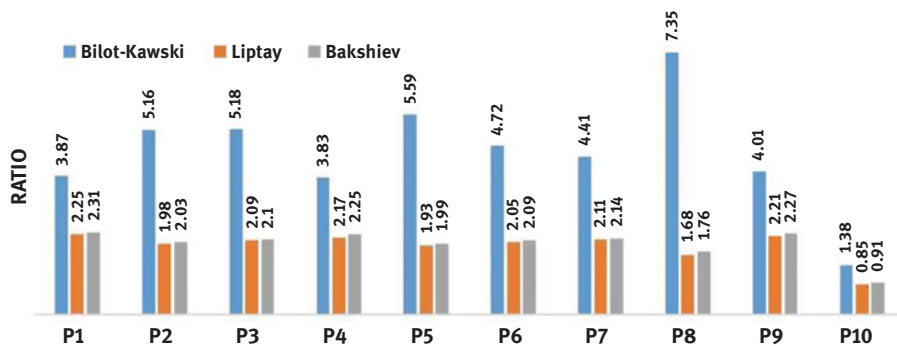


Figure 11.3: Ratio of dipole moments (μ_e/μ_g) of by Bilot–Kawski, Liptay and Bakshiev method of dyes **P1–P10**.

11.3.3 Frontier molecular orbitals (FMOs) of the push–pull chromophores

In order to have insights into the electronic behaviour of the dyes, it is vital to examine the FMOs in particular, the HOMO and LUMO energy levels. The FMO plots are given in Figure 11.4 for the selected dyes **P2**, **P4**, **P5**, **P6**, **P8** and **P10** in DCM. Diagrams for other dyes are represented in Figure S3 supporting information.

In dye **P4**, the electron density is completely localized on the central imidazo[1,2-a]pyridine ring and diethylamino group in the ground state while it is entirely shifted to the phenyl ring in the excited state. In dye **P5**, the electron density is localized on the central ring as well as attracted towards the phenyl ring due to the higher electronegativity of the chlorine atom in the ground state while it is shifted to the central ring in the excited state. In dye **P6**, the electron density is localized on the central ring in the ground state while it is shifted to 4-bromophenyl ring in the excited state. Overall in the ground state, the electron density is distributed in the dye but it is shifted towards the vinyl phenyl ring when alkylamino group is attached and shifted towards chlorophenyl due to higher electronegative chlorine. Hence the position of the ground state electron density depends upon the position, donor and acceptor capacity of the attached group. Overall in the excited state, the electron cloud is shifted towards the vinylic phenyl group and the central imidazo[1,2-a]pyridine ring, i.e. at the central part of the entire conjugation. The above observations can be explained by HOMO and LUMO diagrams represented in Figure 11.5 in DCM solvent. The polarity effect of various solvents on dye **P6** is represented in Figure S4.

The solvatochromic effect is realized by decreasing the HOMO-LUMO band gap by 0.56 eV (3.185–3.129 eV) by changing the solvents from toluene to DMSO for dye **P6**. Energy levels of the HOMO are higher for all the dyes except for dye **P10** because of the higher electron density alkylamino group being present at the vinyl side of imidazo[1,2-a]pyridine. The experimental absorption of **P10** is 373 nm whereas for the

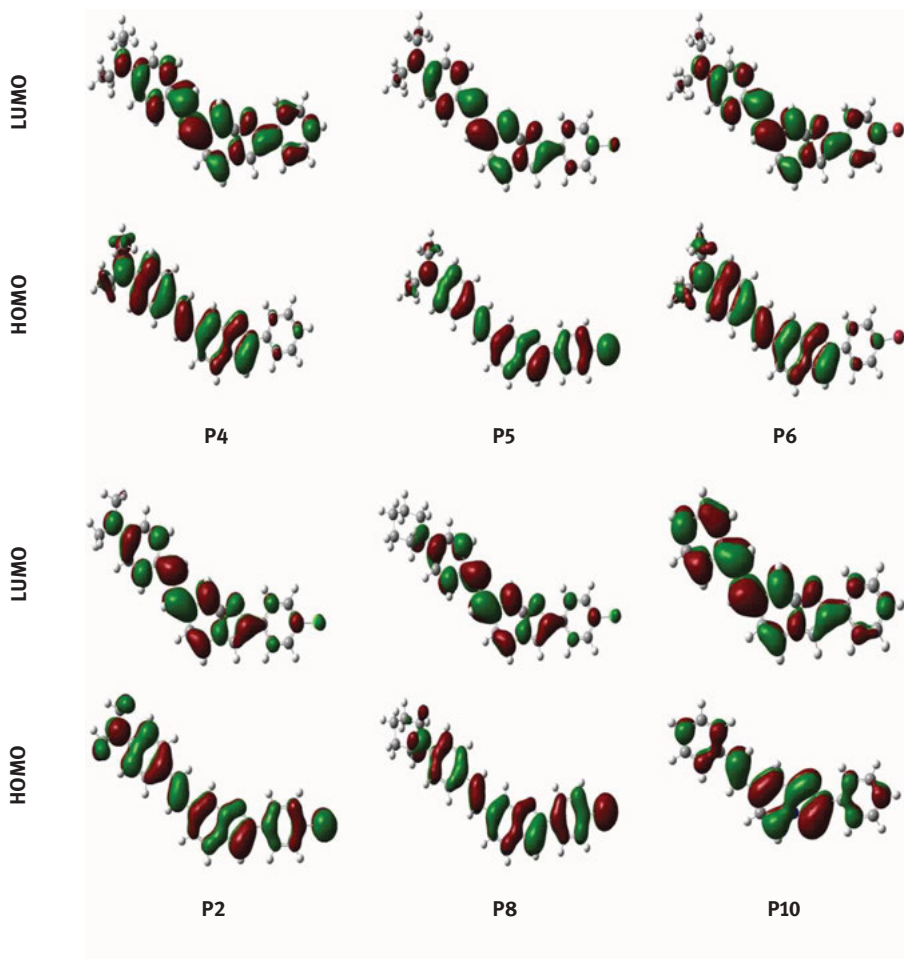


Figure 11.4: Electron density distribution of frontier molecular orbitals of representative dyes **P2**, **P4**, **P5**, **P6**, **P8** and **P10** obtained using B3LYP/6-31G(d) method.

other dyes it is in the range 372–387 nm and emission of **P10** is 416 nm whereas for the other dyes it is in the range 434–479 nm in DCM. The phenyl ring or bromophenyl is acting as an acceptor whereas chlorophenyl ring acts as a donor at the C-2 position of the imidazo[1,2-a]pyridine ring.

11.3.4 Mulliken charges analysis

The Mulliken charge distribution in the ground state and excited state in DCM solvent on atoms of the bromo derivative **P6** was explained in detail. The optimized structural diagram is shown in Figure 11.6 and charge distribution values for dye **P6** is shown in Figure 11.7.

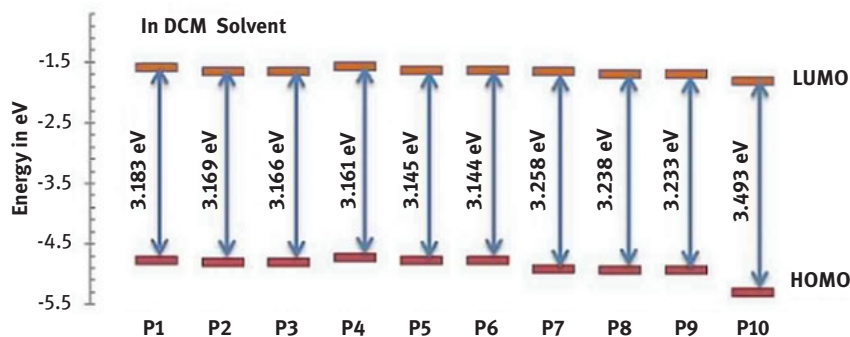


Figure 11.5: HOMO-LUMO energy level diagram of dyes **P1** to **P10** in DCM solvent.

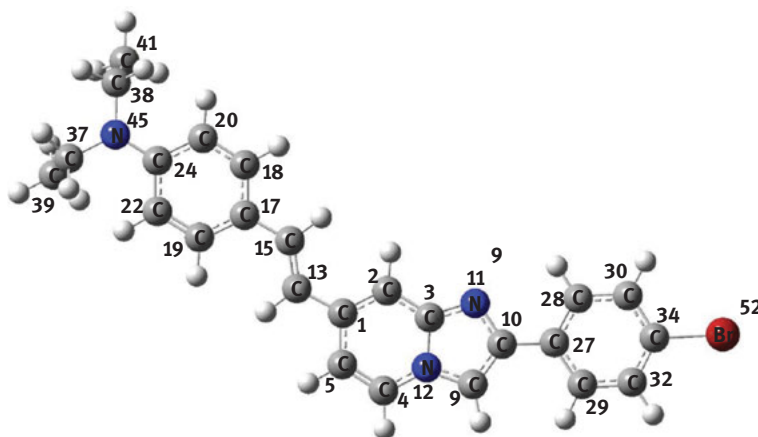


Figure 11.6: Optimized structural diagram of dye **P6**.

In the excited state, the dye **P6** shows an increase in the positive charge of 0.219 e for N_{45} and a decrease in charge of 0.738 e for C_{24} , 0.570 e for C_{19} . These suggest charge delocalization from diethylamine to neighbouring aromatic ring whereas increase in positive charge 0.738 e for C_{27} and a decrease in charge 0.73 e for C_{32} suggest movement of electron from bridge carbon to bromophenyl ring. Structures indicating charge distribution on the dyes were visualized using Gauss View 5.0 [50].

11.3.5 Natural bond orbital

Charge delocalization or charge transfer within the dye in selected microenvironment was estimated by NBO analysis using natural charges on the atoms in the ground state [51]. The numbering of atoms in chloro derivative **P5** is represented in Figure 11.8 and natural charges on atoms are represented in Figure 11.9.

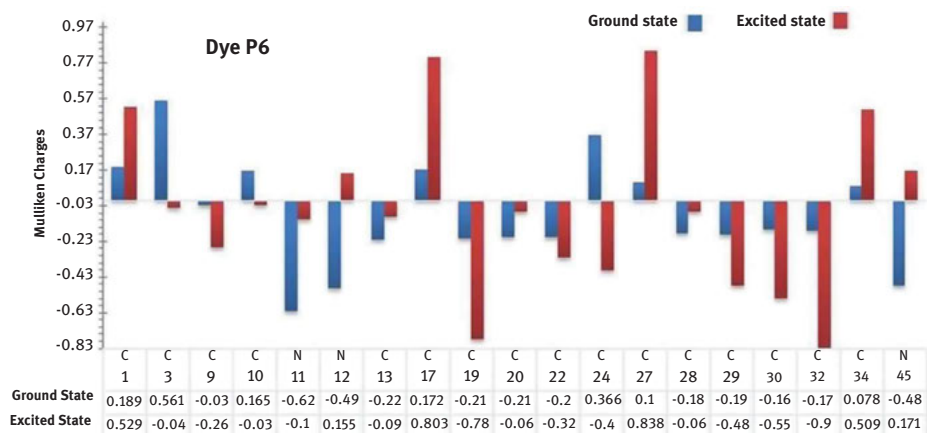


Figure 11.7: Mulliken charge representing the diagram of dye P6.

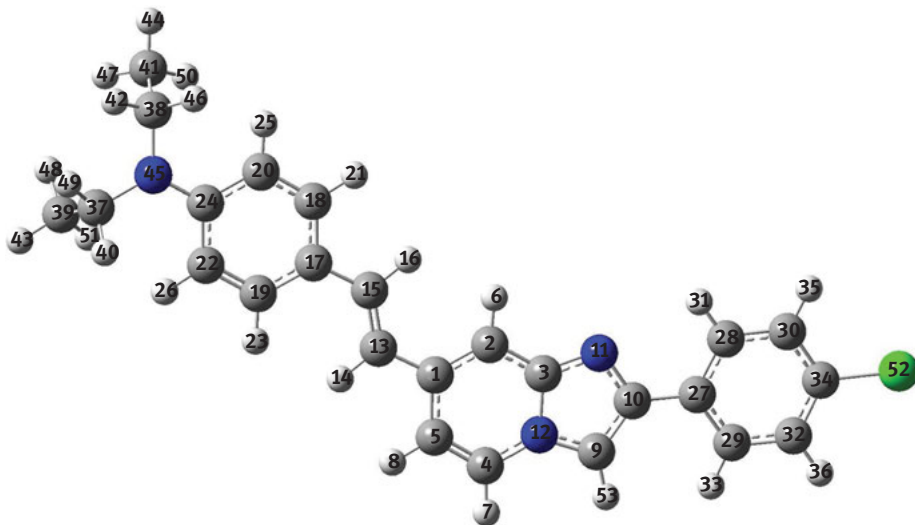


Figure 11.8: Optimized geometry of P5 in DMSO medium using B3LYP/6-311 + G(d,p) method.

The natural charges on atoms of dyes **P1–P4** and **P6–P10** are represented in Table S6 and Table S7 and structures with the numbering of atoms of the other dyes are given in Figure S5. Donor fragment carries a positive charge while acceptor fragment has a negative charge according to NBO analysis. Atom numbers C3, C4, C10 and C24 have positive charge indicating acceptor atoms whereas N11, N12, C39, C41 and N45 have higher negative charges indicating good electron donors.

Only in the case of **P10**, electron acceptor behaviour indicated by negative charge on C24 when amino group was not present in imidazo[1,2-a]pyridine. Interactions between electron donor and acceptor orbitals with corresponding stabilization

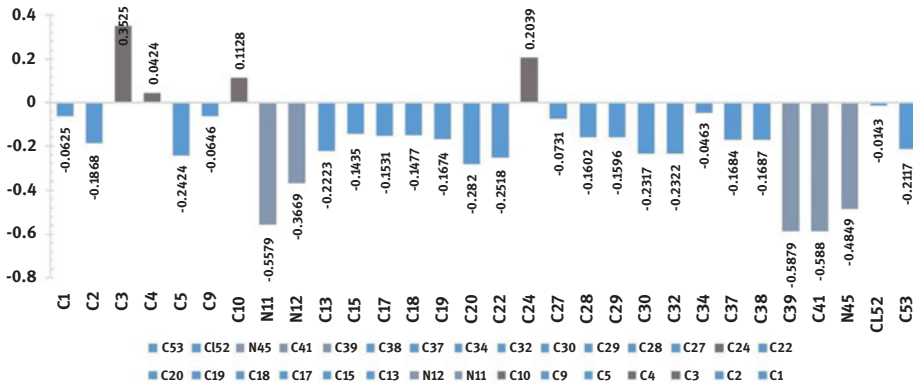


Figure 11.9: Natural charges on atoms of dyes P5 except for hydrogen in DMSO.

energy obtained from second-order perturbation theory have been previously reported [51]. In dye **P5**, perturbation energies of donor- π -acceptor interactions are above 20 kJ/mol and the highest antibonding electron density are mentioned in this work. The second-order Fock matrix analysis has been applied to investigate the interaction between the electron donors and acceptors and stabilization E2 energy within the dyes using B3LYP/6-311++ G(d,p) method and they are collected in Table 11.3 for dye **P5**.

Table 11.3: Second-order perturbation energies E(2) (Donor \rightarrow Acceptor interactions) of dye **P5** in DMSO medium.

Donor(i)	^a ED(e)	Acceptor (j)	^a ED(e)	E(2)	^c E(j)-E(i)	^d F(i,j)
				kJ/mol	a.u.	a.u.
LP(1)(N12)	1.4818	$\pi^*(C03-N11)$	0.5106	43.00	0.28	0.099
		$\pi^*(C04-C05)$	0.2288	32.58	0.31	0.096
		$\pi^*(C09-C10)$	0.3684	27.35	0.30	0.085
LP1(1)(N45)	1.7001	$\pi^*(C20-C24)$	0.4363	60.51	0.20	0.102
LP(2)(Cl52)	1.9730	$\pi^*(C20-C24)$	0.4363	53.08	0.16	0.092
$\pi (C01-C02)$	1.7085	$\pi^*(C03-N11)$	0.5101	26.49	0.26	0.079
$\pi (C17-C18)$	1.6268	$\pi^*(C20-C24)$	0.4363	22.49	0.21	0.062
		$\pi^*(C19-C22)$	0.3036	22.07	0.28	0.071
$\pi (C19-C22)$	1.7456	$\pi^*(C20-C24)$	0.4363	25.31	0.22	0.070
$\pi (C27-C29)$	1.6249	$\pi^*(C32-C34)$	0.4056	21.89	0.28	0.070

Where,

^a ED is the electron density;

^b E(2) means the energy of hyperconjugative interactions (stabilization energy);

^c Energy difference between donor and acceptor i and j NBO orbitals;

^d F(i, j) is the Fock matrix element between i and j NBO orbitals.

Strong interaction between electron donors and acceptor leads to a greater extent of conjugation and larger the $E(2)$ value for the whole system. N12 is composed of 100 % p-character with least occupancy (1.4818) in bonding orbital. A large number of interactions with electron density higher than 0.2288 are observed with stabilization energy between 21.89 and 60.51 kJ/mol. The lone pair on N12 is interacting with $\pi^*(C03-N11)$, $\pi^*(C04-C05)$ and $\pi^*(C09-C10)$ with stabilization energy 43, 32.58 and 27.35 kJ/mol. Cl52 is composed of 99.82 % p-character with bonding orbital occupancy 1.7009 hence 53.08 kJ/mol stabilization energy for chlorine to antibonding of C20-C24. Similarly, stabilization energy 27.41 kJ/mol is observed for $\pi(C1-C2)$ interaction with antibonding $\pi^*(C3-C11)$ and similar in other bonds as shown in the table. Hence in the dyes, large hyperconjugative interactions are observed indicating large charge transfer.

11.4 NLO properties

In this section, we have derived the nonlinear optical properties using experimental as well as DFT method. Solvatochromic styryl imidazo[1,2-a]pyridine dyes have good photophysical properties and good opportunity to explore NLO properties.

11.4.1 NLO properties by Solvatochromic method

Imidazo[1,2-a]pyridine styryls under study have remarkable altering solvent dependent photophysical properties and energy level HOMO-LUMO gap. Therefore, we were interested in understanding the NLO properties from solvatochromic shifts. The values for the first hyperpolarizability (β_{xxx}) obtained using the solvatochromic method are based on several assumptions and thus allow the only approximate estimate of a dominant tensor of total hyperpolarizability along the direction of charge transfer which is the major contributor to the total hyperpolarizability. The experimentally derived values for transition dipole moment, linear polarizability (α_{xx}) and first hyperpolarizability (β_{xxx}) obtained using reported method [52] and are summarized in Table 11.4.

For the unsubstituted styryl dye **P10**, the calculated range of transition dipole moment is between 9.38 and 9.61 D, linear polarizability (α_{xx}) is between 32.94 to 35.31×10^{-24} esu and first hyperpolarizability (β_{xxx}) is between 43.06 and 48.71×10^{-30} esu. For the dyes **P1-P9**, the range of transition dipole moment is between 10.39 and 10.93 D, linear polarizability (α_{xx}) is between 40.95 and 46.51×10^{-24} esu and first hyperpolarizability (β_{xxx}) is between 59.71 and 92.86×10^{-30} esu and which is higher than unsubstituted **P10** dye. NLO values are the highest for **dye P6** in DMSO solvent indicating highest charge transfer is possible when diethyl donor group is present. Polarizability and hyperpolarizability are higher for dyes **P4, P5** and **P6** and least for dye **P10** whereas the halo derivatives have higher charge transfer than the nonhalogenated dyes.

Table 11.4: Solvatochromic NLO properties of dyes **P1–P10**.

Dye	Solvent	ρ^a	σ^b	μ_{ge}^c	α_{xx}^d	β_{xxx}^e	$\mu\beta_{xxx}^f$	$\tilde{\gamma}^g$
		cm^{-1}	10^{-14} cm^2	(D)	10^{-24} esu	10^{-30} esu	10^{-48} esu	10^{-36} esu
P1	Toluene	26,385	7.27	10.65	43.22	73.62	783.78	22.46
	THF	26,385	11.28	10.53	42.32	71.72	755.57	22.67
	DCM	26,385	7.99	10.55	42.48	70.85	747.83	15.50
	ACN	26,596	8.37	10.42	41.07	66.35	691.41	17.73
	DMSO	25,907	10.29	10.64	43.98	74.32	790.92	19.05
P2	Toluene	26,042	11.82	10.69	44.17	80.73	863.11	36.96
	THF	26,316	11.82	10.51	42.23	75.01	788.29	33.20
	DCM	26,247	10.78	10.54	42.61	79.28	835.84	44.12
	ACN	26,525	10.06	10.39	40.95	71.21	739.91	30.60
	DMSO	25,707	12.66	10.64	44.31	80.79	859.62	34.84
P3	Toluene	26,042	8.17	10.74	44.60	79.04	849.21	28.43
	THF	26,178	15.94	10.59	43.07	77.52	820.63	34.86
	DCM	26,385	10.29	10.56	42.55	74.04	782.19	28.20
	ACN	26,042	14.54	10.54	42.89	76.79	809.00	33.39
	DMSO	26,042	6.80	10.62	44.60	77.06	818.63	29.27
P4	Toluene	25,840	13.26	10.86	45.93	82.10	891.71	27.78
	THF	26,042	12.66	10.72	44.38	75.91	813.60	20.27
	DCM	25,840	14.88	10.78	45.24	82.54	889.76	34.23
	ACN	26,042	12.66	10.65	43.83	76.94	819.46	27.29
	DMSO	25,575	11.28	10.83	46.12	82.24	890.44	25.71
P5	Toluene	25,773	10.29	10.87	46.09	90.90	987.76	55.67
	THF	25,907	11.28	10.72	44.63	86.06	922.56	50.78
	DCM	25,707	8.76	10.78	45.49	85.98	927.00	43.18
	ACN	26,110	8.17	10.61	43.36	80.89	858.13	43.56
	DMSO	25,575	10.06	10.80	45.90	88.08	951.38	46.65
P6	Toluene	25,773	11.03	10.91	46.47	92.29	1006.99	57.55
	THF	26,042	15.58	10.74	44.54	89.52	961.10	64.16
	DCM	25,907	11.28	10.78	45.15	87.20	940.18	50.76
	ACN	26,110	12.96	10.65	43.73	83.39	888.37	49.20
	DMSO	25,510	11.28	10.86	46.51	92.86	1008.44	58.14
P7	Toluene	26,455	11.82	10.87	44.93	74.90	814.11	15.02
	THF	26,738	10.53	10.74	43.41	74.05	795.36	23.60
	DCM	26,882	13.57	10.73	43.09	74.40	798.31	27.34
	ACN	26,596	8.37	10.71	43.41	75.20	805.59	26.66
	DMSO	26,316	9.83	10.84	44.95	78.29	848.80	24.66
P8	Toluene	26,316	12.96	10.91	45.52	65.52	714.88	0.561
	THF	26,596	12.09	10.76	43.83	65.80	708.19	12.30
	DCM	26,810	8.37	10.74	43.28	62.24	668.35	5.60
	ACN	26,954	7.46	10.63	42.20	60.98	648.33	8.90
	DMSO	26,110	11.28	10.88	45.62	67.03	729.34	2.51

(continued)

Table 11.4 (continued)

Dye	Solvent	λ^a	σ^b	μ_{ge}^c	α_{xx}^d	β_{xxx}^e	$\mu\beta_{xxx}^f$	$\bar{\gamma}^g$
		cm ⁻¹	10 ⁻¹⁴ cm ²	(D)	10 ⁻²⁴ esu	10 ⁻³⁰ esu	10 ⁻⁴⁸ esu	10 ⁻³⁶ esu
P9	Toluene	26,596	10.29	10.92	45.09	63.87	697.29	6.72
	THF	26,738	5.66	10.80	43.88	59.71	644.82	5.62
	DCM	26,738	11.28	10.82	44.03	59.76	646.43	5.54
	ACN	26,810	5.66	10.73	43.21	56.45	605.70	4.57
	DMSO	26,178	8.37	10.93	45.94	62.42	682.37	5.17
P10	Toluene	26,316	8.17	9.61	35.31	48.71	468.17	0.14
	THF	26,525	10.06	9.51	34.31	45.57	433.39	-1.99
	DCM	26,596	6.64	9.52	34.32	44.84	427.07	-3.60
	ACN	26,882	8.76	9.38	32.94	43.06	403.93	-0.73
	DMSO	26,385	8.96	9.56	34.87	46.06	440.44	-3.89

* λ^a = absorption wavelength in cm⁻¹, σ^b = absorption cross section, μ_{ge}^c = transition dipole moment, α_{xx}^d = linear polarizability, β_{xxx}^e = linear first hyperpolarizability, $\mu\beta_{xxx}^f$ = product of μ_{ge}^c & β_{xxx}^e , $\bar{\gamma}^g$ = solvatochromic descriptor values.

11.4.2 NLO properties by DFT method

NLO properties of the arylstyrylimidazo[1,2-a]pyridine derivatized with different groups were calculated by using CAM-B3LYP and BHandHLYP hybrid functionals and 6-311 + G(d,p) basis set on the basis of the finite-field approach [28, 53]. The static dipole moment (μ), the mean polarizability (α_0) and the anisotropy of the polarizability ($\Delta\alpha$) are summarized in Table 11.5 for dyes **P1–P10** by the CAM-B3LYP method.

The mean first hyperpolarizability (β_0), static second hyperpolarizability ($\bar{\gamma}$) and product of static dipole moment with mean first hyperpolarizability ($\mu\beta_0$) are summarized in Table S8 for dyes **P1–P10** using BHandHLYP method. The trends obtained using CAM-B3LYP and BHandHLYP methods are similar except for the negligible variation in static dipole moment. Unsubstituted dye is observed to have the lowest values for all the properties. All these properties are described separately on the basis of their remarkable different effects, i.e. solvent, amino and bromo substitution.

11.4.3 Solvent polarity effect

Static dipole moment, mean polarizability (α_0), polarizability anisotropy ($\Delta\alpha$), first hyperpolarizability (β_0) and second hyperpolarizability ($\bar{\gamma}$) increases steadily with the polarity of solvent for all dyes. We estimated the difference between the increased NLO properties by increasing the solvent polarity to understand micro effects in the molecule and these are represented in Table 11.6.

The increment of static dipole moment is higher for the halogenated dyes and highest for chlorine atom due to its electronegativity. The higher increment in mean

Table 11.5: Dipole moment and polarizability of dyes P1–P10.

Dye	Solvent	μ Debye		α_0 (10^{-24} esu)		$\Delta\alpha$ (10^{-24} esu)	
		CAM	BHand	CAM	BHand	CAM	BHand
		B3LYP	HLYP	B3LYP	HLYP	B3LYP	HLYP
P1	Gas	5.93	5.92	55.15	54.99	51,624	51,522
	Toluene	6.82	6.81	63.31	63.13	65,021	64,966
	THF	7.48	7.48	70.19	69.99	74,181	74,176
	DCM	7.55	7.54	70.89	70.69	74,995	74,995
	ACN	7.80	7.80	73.85	73.64	78,143	78,162
	DMSO	7.83	7.82	74.11	73.90	78,403	78,424
P2	Gas	8.17	8.22	57.79	57.54	61,064	60,738
	Toluene	9.27	9.32	66.08	65.80	77,224	76,874
	THF	10.05	10.10	73.01	72.70	89,060	88,698
	DCM	10.12	10.18	73.73	73.41	90,172	89,808
	ACN	10.41	10.47	76.70	76.37	94,578	94,208
	DMSO	10.43	10.49	76.96	76.63	94,949	94,581
P3	Gas	8.21	8.28	59.29	59.06	64,797	64,555
	Toluene	9.29	9.36	67.71	67.45	81,597	81,361
	THF	10.05	10.12	74.78	74.50	93,926	93,704
	DCM	10.12	10.20	75.51	75.23	95,083	94,863
	ACN	10.40	10.48	78.56	78.26	99,673	99,460
	DMSO	10.43	10.51	78.83	78.52	100,061	99,847
P4	Gas	6.04	6.05	59.40	59.18	58,829	58,709
	Toluene	6.96	6.97	67.90	67.65	73,704	73,668
	THF	7.65	7.67	75.11	74.84	84,038	84,090
	DCM	7.71	7.73	75.85	75.59	84,972	85,033
	ACN	7.98	8.00	78.97	78.70	88,607	88,704
	DMSO	8.01	8.03	79.25	78.97	88,910	89,009
P5	Gas	8.37	8.41	62.07	61.89	66,103	66,014
	Toluene	9.45	9.5	70.66	70.38	81,892	81,717
	THF	10.22	10.27	77.89	77.58	92,918	92,737
	DCM	10.30	10.36	78.64	78.32	93,926	93,744
	ACN	10.59	10.65	81.75	81.42	97,885	97,700
	DMSO	10.62	10.68	82.03	81.7	98,217	98,033
P6	Gas	8.40	8.49	63.58	63.30	70,238	70,019
	Toluene	9.45	9.54	72.30	71.99	86,698	86,528
	THF	10.21	10.31	79.67	79.33	98,267	98,166
	DCM	10.28	10.38	80.43	80.09	99,326	99,231
	ACN	10.57	10.67	83.62	83.26	103,468	103,405
	DMSO	10.60	10.70	83.90	83.54	103,813	103,752

(continued)

Table 11.5 (continued)

Dye	Solvent	μ Debye		α_0 (10^{-24} esu)		$\Delta\alpha$ (10^{-24} esu)	
		CAM B3LYP	BHand HLYP	CAM B3LYP	BHand HLYP	CAM B3LYP	BHand HLYP
P7	Gas	4.96	4.96	60.23	59.96	53,676	53,463
	Toluene	5.73	5.74	68.55	68.25	71,688	71,401
	THF	6.33	6.34	75.65	75.31	81,358	81,057
	DCM	6.39	6.40	76.39	76.04	82,259	81,956
	ACN	6.63	6.64	79.48	79.12	85,848	85,532
	DMSO	6.65	6.66	79.76	79.39	86,150	85,835
P8	Gas	7.32	7.38	63.02	62.66	67,977	67,506
	Toluene	8.26	8.33	71.45	71.05	83,433	22,425
	THF	8.93	8.99	78.58	78.13	94,377	93,780
	DCM	8.99	9.05	79.32	78.87	95,399	94,797
	ACN	9.24	9.31	82.43	81.94	99,483	98,856
	DMSO	9.26	9.33	82.71	82.23	99,846	99,220
P9	Gas	7.37	7.39	64.54	63.45	72,005	70,485
	Toluene	8.28	8.35	73.12	72.86	88,083	87,653
	THF	8.93	9.00	80.39	80.11	99,457	99,006
	DCM	8.99	9.07	81.15	80.87	100,513	100,059
	ACN	9.25	9.33	84.32	84.02	104,694	104,220
	DMSO	9.27	9.35	84.60	84.29	105,048	104,576
P10	Gas	3.36	3.37	46.40	46.47	23,662	23,838
	Toluene	4.04	4.05	53.22	53.34	30,557	30,823
	THF	4.64	4.65	58.89	59.03	36,161	36,459
	DCM	4.71	4.72	59.47	59.62	36,729	37,027
	ACN	4.98	4.99	61.84	62.00	39,061	39,355
	DMSO	5.00	5.01	62.05	62.21	39,265	39,559

μ = static dipole moment, α_0 = mean polarizability, $\Delta\alpha$ = polarizability anisotropy.

polarizability (α_0) and polarizability anisotropy ($\Delta\alpha$) are observed for dyes **P3**, **P6** and **P9** bromine derivatives with increasing polarity. Solvent polarity increases the first hyperpolarizability of the nonhalogenated alkylamino derivatives **P1**, **P4** and **P7** dyes. The second hyperpolarizability increases by approximately the same value about 444–465 (10^{-36} esu) in dyes **P1** to **P6** and by 372–381 (10^{-36} esu) for dyes **P7** to **P9**. For all properties, the least effect is observed for dye **P10**.

11.4.4 Effect of alkylamino substitution group

The introduction of alkylamino group increases the NLO properties, represented in Table 11.7. Static dipole moment increases for dyes **P1**, **P4** and **P7** but the increment is highest in **P4** indicating diethylamino group is a better electron good compared to the others.

Table 11.6: Incremental difference in NLO properties between toluene and DMSO for dyes P1–P10.

Dye	μ Debye		α_0 (10^{-24} esu)		$\Delta\alpha$ (10^{-24} esu)		β_0 (10^{-30} esu)		$\bar{\gamma}$ (10^{-36} esu)	
	CAB3LYP	BHandHLYP	CAMB3LYP	BHandHLYP	CAMB3LYP	BHandHLYP	CAMB3LYP	BHandHLYP	CAMB3LYP	BHandHLYP
*P1	1.01	1.01	10.8	10.8	13,382	13,458	64	62	445	448
*P2	1.16	1.17	10.9	10.8	17,725	17,707	62	60	444	449
*P3	1.14	1.15	11.1	11.1	18,464	18,486	62	61	451	456
*P4	1.05	1.06	11.4	11.3	15,206	15,341	68	67	459	465
*P5	1.17	1.18	11.4	11.3	16,325	16,316	63	62	453	457
*P6	1.15	1.16	11.6	11.6	17,115	17,224	64	63	459	465
*P7	0.92	0.92	11.2	11.1	14,462	14,434	41	39	372	375
*P9	1.00	1.00	11.3	11.2	16,413	16,795	39	37	373	376
*P9	0.99	1.00	11.5	11.4	16,965	16,923	39	38	379	381
*P10	0.96	0.96	8.8	8.9	8708	8736	6	8	204	218

*Difference values between toluene and DMSO solvent for respective dyes.

Table 11.7: Incremental difference in NLO properties after the introduction of amino group for **P1**, **P4** and **P7** dyes with respect to **P10** dyes in DCM solvent.

Dye	μ Debye		α_0 (10^{-24} esu)		$\Delta\alpha$ (10^{-24} esu)		β_0 (10^{-30} esu)		$\bar{\gamma}$ (10^{-36} esu)	
	CAB3LYP	BHandHLYP	CAMB3LYP	BHandHLYP	CAMB3LYP	BHandHLYP	CAMB3LYP	BHandHLYP	CAMB3LYP	BHandHLYP
Δ (P1–P10)	2.84	2.82	11.42	11.07	38,266	37,968	39	45	517	545
Δ (P4–P10)	3.00	3.01	16.38	15.97	48,243	48,006	115	102	501	480
Δ (P7–P10)	1.68	1.68	16.92	16.42	45,530	44,929	57	41	395	370

*Difference values between amino **P1**, **P4** and **P7** and unsubstituted P10 dyes.

Polarizability (α_0) and polarizability anisotropy ($\Delta\alpha$) are higher in cyclopentylamino dye **P7** whereas first hyperpolarizability (β_0) is highest in diethylamino derivative dye **P4** and second hyperpolarizability ($\bar{\gamma}$) is highest in dimethylamino derivative **P1** dye.

11.4.5 Effect of replacement of bromo with chloro group

Mean Polarizability (α_0), polarizability anisotropy ($\Delta\alpha$), first hyperpolarizability (β_0) and second hyperpolarizability ($\bar{\gamma}$) higher values are observed for the bromo derivatives amongst the related analogues and they are represented in Table 11.8.

Diethylamino substituted **P6** dyes have highest values of properties except for mean polarizability which is a little bit higher in dye **P9** using both DFT methods. Static dipole moment fluctuates by ± 0.02 D in CAM-B3LYP method and increases steadily by about 0.01–0.04 D using the BHandHLYP method. Mean polarizability (α_0) increased in the range of 1.61–2.06 ($\times 10^{-24}$ esu) using both methods by replacement of bromo (dyes **P3**, **P6** and **P9**) with chloro atom. First hyperpolarizability (β_0) in range of 2.8–3.3 using CAM-B3LYP and 2.84–4.73 using BH and second hyperpolarizability ($\bar{\gamma}$) in range of 22–34 increase using both methods after replacement of bromine with chlorine.

11.4.6 Fundamental limits and intrinsic NLO properties

The nonlinear-optical response of any organic molecule depends on the electric potential experienced by the electrons in an atom. The theory of the fundamental limits of nonlinear optics is a powerful means for experimentalists seeking to design molecules and materials with large responses. The fundamental limit is the function of a number of electrons and energy difference between the ground state and first excited state [54]. Accordingly, fundamental limit of the nonlinear response of the dyes plays very significant role in tuning chromophores for structural optimization for high tech applications. Already, researchers have greatly applied fundamental limits in molecular design using modulated conjugation through upper limits and high intrinsic hyperpolarizability by theoretical calculations [55–57]. Quantum sum rules are applied to calculate the absolute upper bound values of off-resonant electronic α , β and γ NLO properties allowed by nature [54, 55, 58–60] and estimated using the following equations.

$$\alpha_0^{\max} = \left(\frac{e\hbar}{\sqrt{m}} \right)^2 \frac{N}{E_{10}^2} \quad (11.1)$$

$$\beta_0^{\max} = 3^{1/4} \left(\frac{e\hbar}{\sqrt{m}} \right)^3 \frac{N^{3/2}}{E_{10}^{7/2}} \quad (11.2)$$

Table 11.8: Difference in NLO properties of different dyes.

Dye	Solvent	μ Debye		α_0 (10^{-24} esu)		$\Delta\alpha$ (10^{-24} esu)		β_0 (10^{-30} esu)		$\bar{\gamma}$ (10^{-36} esu)	
		CAB3LYP	BHand HLYP	CAMB3LYP	BHand HLYP	CAMB3LYP	BHand HLYP	CAMB3LYP	BHand HLYP	CAMB3LYP	BHand HLYP
$\Delta(P2-P3)$	Toluene	0.02	0.04	1.63	1.65	4373	4487	2.83	2.84	22	25
	THF	0	0.02	1.77	1.8	4866	5006	3.16	3.25	26	29
	DCM	0	0.02	1.78	1.82	4911	5055	3.20	3.30	26	29
	ACN	-0.01	0.01	1.86	1.89	5095	5252	3.38	3.51	29	31
	DMSO	0	0.02	1.87	1.89	5112	5266	3.4	3.72	29	32
$\Delta(P6-P5)$	Toluene	0	0.04	1.64	1.61	4806	4811	2.94	3.59	22	25
	THF	-0.01	0.04	1.78	1.75	5349	5429	3.19	4.36	26	30
	DCM	-0.02	0.02	1.79	1.77	5400	5487	3.21	4.43	27	30
	ACN	-0.02	0.02	1.87	1.84	5583	5705	3.26	4.72	28	32
	DMSO	-0.02	0.02	1.87	1.84	5596	5719	3.24	4.73	28	33
$\Delta(P9-P8)$	Toluene	0.02	0.02	1.67	1.81	4650	65,228	2.70	4.24	25	28
	THF	0	0.01	1.81	1.98	5080	5226	2.94	4.65	29	32
	DCM	0	0.02	1.83	2.00	5114	5262	2.94	4.67	29	32
	ACN	0.01	0.02	1.89	2.08	5211	5364	2.88	4.68	32	34
	DMSO	0.01	0.02	1.89	2.06	5202	5356	2.91	4.73	31	33

$$\gamma^{max} = 4 \frac{e^4 \hbar^4}{m^2} \left(\frac{N^2}{E_{10}^5} \right) \quad (11.3)$$

$$\gamma^{min} = - \frac{e^4 \hbar^4}{m^2} \left(\frac{N^2}{E_{10}^5} \right) \quad (11.4)$$

where the N is the total number of π -electrons responsible for optical excitation, e is a charge of an electron, \hbar is reduced planks constant, m is a mass of an electron and E_{10} is the energy difference between first excited state to a ground state of the molecule taken from linear absorption spectroscopy. Due to inaccurate two-level dispersion model and the resonance enhancement of the zero-frequency response, the frequency-independent hyperpolarizability is defective. Hence, intrinsic hyperpolarizability is a better way to measure the NLO response by removing resonance effect as estimated by following equations.

$$\alpha_0^{int} = \alpha_0 / \alpha_0^{max} \quad (11.5)$$

$$\beta_0^{int} = \beta_0 / \beta_0^{max} \quad (11.6)$$

$$\gamma^{int} = \gamma / \gamma^{max} \quad (11.7)$$

$$\gamma^{int} = \gamma / \gamma^{min} \quad (11.8)$$

Here, the ratio of static polarizability and hyperpolarizabilities values are used for intrinsic calculations. The intrinsic hyperpolarizability can be defined as the ratio of the off-resonant hyperpolarizability to the off-resonant fundamental limit of the hyperpolarizability and strongly required for molecular engineering. In this paper, we estimated the different imidazo[1,2-a]pyridine dyes with various substitution and show to the evaluation of higher limits of hyperpolarizabilities. Measured values of limits and intrinsic properties were represented in Table 11.9 for dyes **P1–P10** using representative CAM-B3LYP method.

All styryl dyes lie in the optimized intrinsic ranges, i.e. 0.268–0.370 polarizability; observed intrinsic range of the first hyperpolarizability is 0.021–0.074 while optimized range is less than or equal to (\leq) 0.71 and observed negative second hyperpolarizability is -0.056 to 0.109 and positive second hyperpolarizability is 0.014 – 0.027 while optimized range is $-0.15 \leq \gamma \leq 0.6$ [61, 62]. All the intrinsic property values are low in the unsubstituted dye **P10** compared to the other alkylamino substituted dyes. The fundamental limits provide a figure of merit for studied styryl dyes for future optical applications.

Table 11.9: Fundamental limits of NLO of the dyes **P1–P10** in DCM solvent medium by the CAM-B3LYP method.

Sr.	μ_{\max}	α_0	β_0	$\bar{\gamma}$	α_0^{max}	β_0^{max}	$\bar{\gamma}^{min}$	$\bar{\gamma}^{max}$	α_0^{int}	β_0^{int}	$\bar{\gamma}_{int}^{min}$	$\bar{\gamma}_{int}^{max}$
P1	24.32	71	137	952	225	1946	-9694	38,774	0.314	0.070	-0.098	0.025
P2	24.38	74	136	991	228	1982	-9952	39,808	0.324	0.069	-0.100	0.025
P3	24.32	76	139	1018	225	1946	-9694	38,774	0.335	0.071	-0.105	0.026
P4	24.57	76	154	1019	235	2093	-10,761	43,043	0.323	0.073	-0.095	0.024
P5	24.64	79	150	1062	238	2131	-11,042	44,167	0.331	0.070	-0.096	0.024
P6	24.54	80	153	1088	234	2074	-10,622	42,490	0.344	0.074	-0.102	0.026
P7	24.09	76	96	912	217	1823	-8831	35,323	0.352	0.052	-0.103	0.026
P8	24.12	79	100	961	218	1840	-8950	35,801	0.363	0.054	-0.107	0.027
P9	24.16	81	103	991	220	1857	-9071	36,283	0.370	0.055	-0.109	0.027
P10	24.22	59	39	517	222	1892	-9316	37,264	0.268	0.021	-0.056	0.014

μ_{\max} = maximum limit of transition dipole moment, α_0 = mean polarizability, β_0 = mean first hyperpolarizability, $\bar{\gamma}$ = static second hyperpolarizability, α_0^{max} = upper limit of polarizability, β_0^{max} = upper limit of first hyperpolarizability, $\bar{\gamma}^{min}$ = upper negative and $\bar{\gamma}^{max}$ = upper positive limit of second hyperpolarizability, α_0^{int} = intrinsic polarizability, β_0^{int} = intrinsic first hyperpolarizability, $\bar{\gamma}_{int}^{min}$ = static negative intrinsic second hyperpolarizability, $\bar{\gamma}_{int}^{max}$ = static positive intrinsic second hyperpolarizability.

11.4.7 Two-photon absorption cross section

TPA is a characteristic nonlinear optical property of a broadly conjugated system with potential charge transfer characteristics [63]. Based on linear spectroscopic properties, the dipole moment change, the extinction coefficient and the frequency of the maximum of the one-photon absorption band, the TPA cross section is generally described within the framework of a two-level system as follows [64, 65] by using following equation.

$$\sigma_2(\nu) = \frac{12}{5} \frac{\ln 10 \pi 10^3 L^4}{N_A h c^2 n^2} \left(\frac{\epsilon_{10(\nu)}}{\bar{\nu}_{10}} \right) \Delta\mu_{10}^2 \quad (11.9)$$

where L is the Lorentzian local field factor $L = \left(\frac{2n^2 + 2}{3} \right)$, $\epsilon_{10(\nu)}$ is molar extinction coefficient, Δ_{10} is emission frequency in wavenumber (cm^{-1}), $\Delta\mu_{10}$ is transition dipole moment obtained from solvatochromism, h is the Planck constant, c is the speed of light, n is the refractive index, and N_A is Avogadro's number. TPA cross-section values of dye **P1–P10** were presented in Table 11.10.

Dye **P10** has the lowest TPA cross-section below 100 GM and all other dyes above around 100 GM, which is comparable with dimethylaniline vinyl containing styryl type commercial LDS-698 (TPA = 0.49–395 GM at wavelength 770–1300 nm) TPA dye [66]. Substituted amino donor group shows that increasing the charge transfer is the strategy to increase the TPA cross-section.

Table 11.10: Two-photon absorption cross-section of dye **P1–P10** in DCM solvent.

2PA	P1	P2	P3	P4	P5	P6	P7	P8	P9	P10
Toluene	84	132	106	126	161	136	144	160	127	88
THF	114	120	163	122	133	158	111	128	102	86
DCM	84	114	110	98	163	126	138	117	128	99
ACNL	80	96	143	82	127	130	84	74	101	70
DMSO	125	156	83	127	142	145	125	146	109	96

The two-photon absorption cross section $\sigma_2(\nu)$ in GM units were $1 \text{ GM} = 10^{-50} \text{ photons cm}^{-4} \text{ s}^{-1}$.

11.5 Vibrational and electronic nonlinear optical properties

Study is extended to evaluate the contribution of vibrational and electronic counterparts of nonhalide imidazo[1,2-a]pyridines by optimally chosen polarization functions. Nonlinear optical processes are governed by molecular hyperpolarizabilities [67]. These properties of organic molecules can be divided into the electronic contribution originating from the effects of electric fields on electronic motions and the vibrational contribution arising from both the effects of electric fields on nuclear motions and the vibronic coupling. Therefore, the vibrational transitions play important role in determining the NLO properties accompanied by the electronic transitions [68]. The longitudinal components of electronic and vibrational polarizabilities and first hyperpolarizability as well as the ratio electronic over vibrational (α_e/α_v) and addition of electronic and vibrational ($\alpha_e + \alpha_v$) are summarized in Table 11.11.

The longitudinal components of electronic and vibrational first hyperpolarizability as well as the ratio electronic over vibrational (β_e/β_v) and addition of electronic and vibrational ($\beta_e + \beta_v$) are summarized in Table S9. Trend of polarizability is similar with the vibrational and electronic polarizabilities. In above table, lowest values are observed for unsubstituted imidazo[1,2-a]pyridine **P10** while highest for diethyl substituted **P6** derivatives. Electronic contribution is higher than vibrational contribution in the dyes. In above table, trends are not linear but electronic contribution is higher than vibrational contribution in all the dyes except dye **P7**. For some systems, vibrational properties are more important than the electronic ones. Static vibrational hyperpolarizabilities are higher than static electronic hyperpolarizability in non-conjugated or charged species [67] but the dyes show reversed observation which may be due to the conjugated and neutral species.

11.6 Linear and nonlinear properties trends and correlation with bond length alternation (BLA) and bond order alternation (BOA)

Nonetheless, the trends in the solvent systems coincide with experimental as well as computational values for studied dyes. The linear polarizability α_{CR} is sensitive to

Table 11.11: Longitudinal electronic and vibrational polarizability for dyes P1, P4, P7 and P10.

Dye	Solvent	Electronic			Vibrational			α_e / α_v	$\alpha_e + \alpha_v$	
		α_{xx}	α_{yy}	α_{zz}	α_{xx}	α_{yy}	α_{zz}			α_v
P1	Gas	748.74	2.19	302.57	351.17	43.81	233.88	96.52	3.64	447
	Toluene	865.98	6.49	359.42	410.63	61.80	521.77	200.12	2.05	610
	THF	951.92	10.93	412.02	458.29	78.51	581.34	227.10	2.02	685
	DCM	960.04	11.41	417.56	463.00	80.29	599.88	234.04	1.98	697
	ACN	992.40	13.42	440.62	482.15	87.73	653.67	255.14	1.89	737
P4	DMSO	995.14	13.60	442.65	483.80	88.39	656.96	256.51	1.89	740
	Gas	793.29	-2.64	323.47	371.38	54.66	240.88	104.61	3.55	476
	Toluene	914.21	1.01	383.69	432.97	75.09	273.16	123.42	3.51	556
	THF	1002.18	4.87	438.77	481.94	93.95	329.88	150.50	3.20	632
	DCM	1010.50	5.30	444.57	486.79	95.98	339.62	154.67	3.15	641
P7	ACN	1043.63	7.12	468.74	506.50	104.70	395.65	177.46	2.85	684
	DMSO	1046.43	7.28	470.87	508.19	105.51	402.67	180.23	2.82	688
	Gas	803.70	5.78	327.64	379.04	106.64	192.04	102.54	3.70	481
	Toluene	915.97	3.50	388.96	436.14	149.52	266.74	143.05	3.05	579
	THF	994.17	0.92	446.70	480.60	187.24	311.24	171.73	2.80	652
P10	DCM	1001.45	0.63	452.82	484.97	191.79	315.70	174.88	2.77	659
	ACN	1029.87	-0.53	478.44	502.59	214.06	337.70	190.34	2.64	692
	DMSO	1032.26	-0.63	480.70	504.11	216.37	339.16	191.66	2.63	695
	Gas	601.44	-4.68	270.45	289.07	13.59	226.79	81.15	3.56	370
	Toluene	689.52	-6.56	322.01	334.99	17.10	243.05	88.17	3.80	423
P10	THF	750.13	-8.11	369.24	370.42	19.67	327.61	117.67	3.15	488
	DCM	755.64	-8.25	374.18	373.85	19.91	343.76	123.19	3.03	497
	ACN	777.13	-8.85	394.71	387.66	20.89	415.27	147.57	2.63	535
	DMSO	778.91	-8.90	396.52	388.84	20.97	422.69	150.09	2.59	538

solvents and this is evident in both the experimental and computational studies. The solvatochromic behaviour of the dye is described in the literature [69]. Overall, by the computational method, there is an increase in the values of β_o from non-polar to polar solvents but it is fluctuating in experimental method. Experimentally and computationally, α_{CT} values are found to be higher in case of substituted dyes than unsubstituted dye **10** and in substituted dyes, halogen substituted dyes **P2**, **P3**, **P5**, **P6**, **P8**, **P9** are found to be higher values than non-halogen dyes **P1**, **P4** and **P7**. Experimentally and computationally, the first hyperpolarizability value is highest for dyes **P4**, **P5** and **P6** and lowest for unsubstituted dye **P10**. First hyperpolarizability is higher for **P4**, **P5** and **P6** than other dyes and ratio of the first hyperpolarizability with urea is higher and represented in Figure S6. In case of dyes **P6**, γ_{sd} values are found to be higher than other dyes and are in the order of 49.20×10^{-36} to 64.16×10^{-36} esu. Here, γ_{sd} values are positive for dyes **P1–P7** (for dye **10** in toluene) and negative for dyes **P8–P10**. Most of the solvatochromic descriptor γ_{sd} values are decreasing from non-polar to polar solvents by solvatochromic calculation but continuously increasing by both DFT methods.

BLA and BOA are the geometric and electronic parameters which depend on the length of π -conjugation, the strength of the donor–acceptor group and the surrounding media. Optical properties like linear polarizability (α), first hyperpolarizability (β) and second hyperpolarizability (γ) can be expressed in terms of the BLA or BOA structural parameters [28]. The BLA and BOA values were estimated from ground state optimized geometries of the molecule and correlated with optical properties of dyes in Figure 11.10.

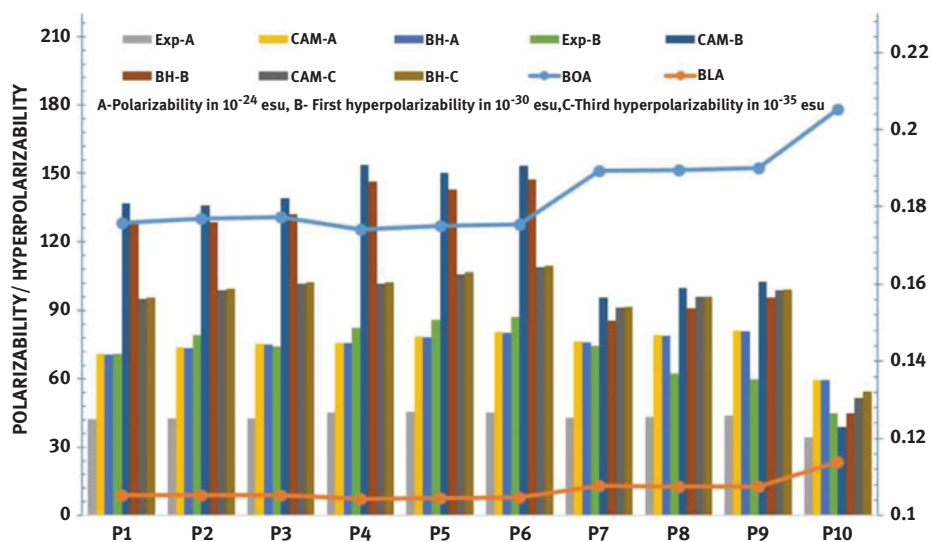


Figure 11.10: Relation of BLA and BOA with optical properties by solvatochromic, CAM-B3LYP and BHandHLYP method of dyes **P1–P10** in DCM solvent medium.

BLA and BOA values are lower for **P3**, **P6**, **P9** dyes of different groups while its optical property values are higher by all methods. Moreover, values of BLA and BOA tend to zero suggesting a high degree of polarization. The difference in dipole moment is higher in **P4**, **P5** and **P6** than other where diethyl amino is the donor and represented in Figure 11.11. Substituting different groups in dye **P10** linear polarizability (α) by 10 to 21×10^{-24} esu, first hyperpolarizability (β) by 17 to 114×10^{-30} esu and second hyperpolarizability (γ) 370 to 540×10^{-36} esu increase with decrease in BLA and BOA values.

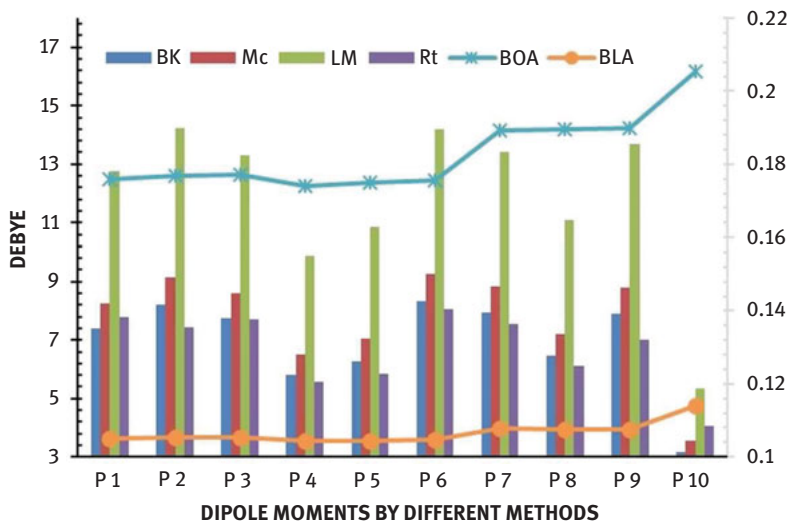


Figure 11.11: Difference in excited to ground state dipole moment by BK = Bilot–Kawaski, Mc = McRae, Bk = Bakshiev and Rt = Reichardt method for dyes **P1–P10** in DCM solvent.

The dyes having higher dipole moment difference have smaller BOA and BLA values. As expected, these imidazo[1,2-a]pyridine derivatives show a large polarizability and hyperpolarizability values, suggesting considerable charge transfer characteristics of the first excited state and this is supported by the large difference in the calculated and DFT dipole moments.

11.7 Conclusion

We have comprehensively discussed dipole moments and NLO properties of (E)-2-(4-halophenyl)-7-arylstyrylimidazo[1,2-a]pyridine obtained by solvatochromic and DFT method based on photophysical behaviour with structural modification. The difference in the dipole moment between ground and excited states was determined by Bilot–Kawaski, McRae, Lippert and Mataga and Reichardt theory and ratio the dipole moments were estimated by Bilot–Kawaski, Liptay and Reichardt correlation methods.

Dipole moment ratio is more than unity for dyes. More than twofold increase in ratio was observed after introduction of the alkylamino group. Similarly, at least three debye unit higher dipole moment differences were observed for amino and halo-substituted dyes indicating more polar or stable dye in the excited state. In NBO analysis, a large number of interactions with electron density higher than 0.2288 are observed with stabilization energy between 21.89 and 60.51 kJ/mol. CAM-B3LYP and BHandHLYP methods indicate polarizability enhancement factor of 1.22 for amino substituent and a factor 1.02 for replacing chloro with bromo substituent. Similarly, for first hyperpolarizability enhancement factor is 1.31 and factor is 1.01 for replacing chlorine to bromine. Solvatochromic method does not strictly follow the above-observed trends. In vibrational properties, electronic contribution is higher than vibrational contribution in dyes except for dye **P7**. TPA cross section is between 70 and 163 GM in different solvents and comparable with styryl type LDS-698 commercial TPA dye. The estimated range of the intrinsic first hyperpolarizability is 0.021 and 0.074 (limit range ≤ 0.71). Estimated second hyperpolarizability intrinsic negative range is -0.056 to -0.109 and the positive range is 0.014 – 0.027 (limit range $-0.15 \leq \gamma \leq 0.6$). Decrease of BOA by 0.03 and BLA by 0.0095 units were correlated with increasing optical properties of the dyes. All figures indicate the large opportunity to reach the maximum possible absolute value in analogous dyes. This investigation has the potential for designing strategy for the better nonlinear response for multisubstituted imidazo[1,2-a]pyridine dyes.

References

- [1] Kurteva VB, Lubenov LA, Antonova DV. On the mechanism of the direct acid catalyzed formation of 2,3-disubstituted imidazo[1,2-a]pyridines from 2-aminopyridines and acetophenones. Concurrence between ketimine and Ortoleva-King type reaction intermediated transformations. *RSC Adv.* 2014;4:175–84.
- [2] Ray PC. Size and shape dependent second order nonlinear optical properties of nanomaterials and their application in biological and chemical sensing. *Chem Rev.* 2010;110:5332–65.
- [3] Niziol J, Baran W, Gondek E, I V K, Mendys A, Żylewski M, et al. Synthesis and NLO properties XE “NLO properties” of new chromophores based on imidazo[1,2-a]pyridine. *Chem Eng Commun.* 2009;196:1466–74.
- [4] Couty F, Evano G. Bicyclic 5-6 systems with one bridgehead (ring junction) nitrogen atom: one extra heteroatom 1:0. *Compr Heterocycl Chem III.* 2008;11:409–99.
- [5] Jianliang Z, Jianchao L, Qiyuan C. Advances in synthesis of imidazopyridine derivatives. *Chinese J Org Chem.* 2009;29:1708–18.
- [6] Shibahara F, Yamaguchi E, Kitagawa A, Imai A, Murai T. Synthesis of 1,3-diarylated imidazo[1,5-a]pyridines with a combinatorial approach: metal-catalyzed cross-coupling reactions of 1-halo-3-arylimidazo[1,5-a]pyridines with arylmetal reagents. *Tetrahedron.* 2009;65:5062–73.
- [7] Nagarajan N, Velmurugan G, Prakash A, Shakti N, Katiyar M, Venuvanalingam P, et al. Highly emissive luminogens based on imidazo[1,2-a]pyridine XE “imidazo[1,2-a]pyridine” for electroluminescent applications. *Chem – Asian J.* 2014;9:294–304.
- [8] Leopoldo M, Lacivita E, Passafiume E, Contino M, Colabufo NA, Berardi F. High-affinity dopamine D3 receptor ligands as potential probes for receptor visualization. *J Med Chem.* 2007;50:5043–7.

- [9] Shao N, Pang G-X, Yan C-X, Shi G-F CY. Reaction of β -lactam carbenes with 2-pyridyl isonitriles: a one-pot synthesis of 2-carbonyl-3-(pyridylamino)imidazo[1,2-a]pyridines useful as fluorescent probes for mercury ion. *J Org Chem.* 2011;76:7458–65.
- [10] Laquintana V, Denora N, Lopodota A, Suzuki H, Sawada M, Serra M, et al. N-benzyl-2-(6,8-dichloro-2-(4-chlorophenyl)imidazo[1,2-a]pyridin-3-yl)-N-(6-(7-nitrobenzo[c][1,2,5]oxadiazol-4-ylamino)hexyl)acetamide as a new fluorescent probe for peripheral benzodiazepine receptor and microglial cell visualization. *Bioconjug Chem.* 2007;18:1397–407.
- [11] Padalkar VS, Seki S. Excited-state intramolecular proton-transfer (ESIPT)-inspired solid state emitters. *Chem Soc Rev.* 2016;45:169–202.
- [12] Mutai T, Sawatani H, Shida T, Shono H, Araki K. Tuning of excited-state intramolecular proton transfer (ESIPT) fluorescence of imidazo[1,2-a]pyridine XE “imidazo[1,2-a]pyridine” in rigid matrices by substitution effect. *J Org Chem.* 2013;78:2482–9.
- [13] Mutai T, Tomoda H, Ohkawa T, Yabe Y, Araki K. Switching of polymorph-dependent ESIPT luminescence of an imidazo[1,2-a]pyridine XE “imidazo[1,2-a]pyridine” derivative. *Angew Chemie Int Ed.* 2008;47:9522–4.
- [14] Xie X, Choi B, Largy E, Guillot R, Granzhan A, Teulade-Fichou M-P. Asymmetric distyrylpyridinium dyes as red-emitting fluorescent probes for quadruplex DNA. *Chem – A Eur J.* 2013;19:1214–26.
- [15] Aranda AI, Achelle S, Hammerer F, Mahuteau-Betzer F, Teulade-Fichou M-P. Vinyl-diazine triphenylamines and their N-methylated derivatives: synthesis, photophysical properties and application for staining DNA. *Dye Pigment.* 2012;95:400–7.
- [16] Kovalska VB, Losytskyy MY, D V K, Balanda AO, Tokar VP, Yarmoluk SM. Synthesis of novel fluorescent styryl dyes based on the imidazo[1,2-a]pyridinium chromophore and their spectral-fluorescent properties in the presence of nucleic acids and proteins. *Dye Pigment.* 2006;68:39–45.
- [17] Vabre R, Legraverend M, Piguel S. Synthesis and evaluation of spectroscopic properties of newly synthesized push-pull 6-amino-8-styryl purines. *Dye Pigment.* 2014;105:145–51.
- [18] Zhou G, Wang D, Ren Y, Yang S, Xu X, Shao Z, et al. Temporal and spectral properties of picosecond two-photon pumped cavity lasing of an organic dye HEASPS. *Appl Phys B Lasers Opt.* 2002;74:147–9.
- [19] Achelle S, Barsella A, Baudequin C, Caro B, Robin-Le Guen F. Synthesis and photophysical investigation of a series of push-pull arylvinylidiazine chromophores. *J Org Chem.* 2012;77:4087–96.
- [20] Qin C, Zhang W, Wang Z, Zhou M, Wang X, Chen G. Optical properties of stilbene-type dyes containing various terminal donor and acceptor groups. *Opt Mater (Amst).* 2008;30:1607–15.
- [21] Ruland G, Gvishi R, Prasad PN. Multiphasic nanostructured composite: multi-dye tunable solid state laser. *J Am Chem Soc.* 1996;118:2985–91.
- [22] He GS, Bhawalkar JD, Zhao CF, Prasad PN. Optical limiting effect in a two-photon absorption dye doped solid matrix. *Appl Phys Lett.* 1995;67:2433.
- [23] Deligeorgiev T, Vasilev A, Kaloyanova S, Vaquero JJ. Styryl dyes – synthesis and applications during the last 15 years. *Color Technol.* 2010;126:55–80.
- [24] Mashraqui SH, Ghorpade SS, Tripathi S, Britto S. A new indole incorporated chemosensor exhibiting selective colorimetric and fluorescence ratiometric signaling of fluoride. *Tetrahedron Lett.* 2012;53:765–8.
- [25] Suresh S, Ramanand A, Jayaraman D, Mani P. Review on theoretical aspect of nonlinear optics. *Rev Adv Mater Sci.* 2012;30:175–83.
- [26] Shi Y, Lou AJ-T, He GS, Baev A, Swihart MT, Prasad PN, et al. Cooperative coupling of cyanine and tictoid twisted π -systems to amplify organic chromophore cubic nonlinearities. *J Am Chem Soc.* 2015;137:4622–5.

- [27] Kang H, Facchetti A, Zhu P, Jiang H, Yang Y, Cariati E, et al. Exceptional molecular hyperpolarizabilities in twisted π -electron system chromophores. *Angew Chemie – Int Ed.* 2005;44:7922–5.
- [28] Meyers F, Marder SR, Pierce BM, Bredas JL. Electric field modulated nonlinear optical properties of donor-acceptor polyenes: sum-over-states investigation of the relationship between molecular polarizabilities (α , β , and γ) and bond length alternation. *J Am Chem Soc.* 1994;116:10703–14.
- [29] Kang H, Facchetti A, Jiang H, Cariati E, Righetto S, Ugo R, et al. Ultralarge hyperpolarizability twisted π -electron system electro-optic chromophores: synthesis, solid-state and solution-phase structural characteristics, electronic structures, linear and nonlinear optical properties, and computational studies. *J Am Chem Soc.* 2007;129:3267–86.
- [30] Zhang C-Z, Li T, Yuan Y, Gu C-Y, Niu M-X CH. Effect of bromine substituent on optical properties of aryl compounds. *J Phys Org Chem.* 2017;30:e3620–n/a.
- [31] Zhang C-Z, Wang C-Y, Im C, Lu G-Y, Wang C-S. Significant effect of bromo substituents on nonlinear optical properties of polymer and chromophores. *J Phys Chem B.* 2010;114:42–8.
- [32] Warde U, Sekar N. NLOphoric mono-azo dyes with negative solvatochromism and in-built ESIPT unit from ethyl 1,3-dihydroxy-2-naphthoate: estimation of excited state dipole moment and pH study. *Dye Pigment.* 2017;137:384–94.
- [33] Ciuciu AI, Firmansyah D, Hugues V, Blanchard-Desce M, Gryko DT, Flamigni L. Non-classical donor-acceptor-donor chromophores. A strategy for high two-photon brightness. *J Mater Chem C.* 2014;2:4552–65.
- [34] Laurent AD, Adamo C, Jacquemin D. Dye chemistry with time-dependent density functional theory. *Phys Chem Chem Phys.* 2014;16:14334–56.
- [35] Laurent AD, Jacquemin D. TD-DFT XE “DFT” benchmarks: a review. *Int J Quantum Chem.* 2013;113:2019–39.
- [36] Cramer CJ, Truhlar DG. Density functional theory for transition metals and transition metal chemistry. *Phys Chem Chem Phys.* 2009;11:10757–816.
- [37] Frisch MJ, Trucks GW, Schlegel HB, Scuseria GE, Robb MA, Cheeseman JR, et al. *Gaussian 09.* Wallingford CT: Gaussian, Inc.; 2010.
- [38] Kohn W, Sham LJ. Self-consistent equations including exchange and correlation effects. *Phys Rev.* 1965;140:A1133–8.
- [39] Menzel R, Ogermann D, Kupfer S, Weiß D, Görls H, Kleinermanns K, et al. 4-Methoxy-1,3-thiazole based donor-acceptor dyes: characterization, X-ray structure, DFT XE “DFT” calculations and test as sensitizers for DSSC. *Dye Pigment.* 2012;94:512–24.
- [40] Lee C, Yang W, Parr RG. Development of the Colle-Salvetti correlation-energy formula into a functional of the electron density. *Phys Rev B.* 1988;37:785–9.
- [41] Rajeev S, Husain MM. Solvent effect on coumarin dye: calculation of ground and excited state dipole moments. *J Indian Chem Soc.* 2011;88:1541–6.
- [42] Deshmukh MS, Sekar N. Dyes and pigments A combined experimental and TD-DFT XE “DFT” investigation of three disperse azo dyes having the nitroterephthalate skeleton. *Dye Pigment.* 2014;103:25–33.
- [43] Wong MW, Frisch MJ, Wiberg KB. Solvent effects. 1. The mediation of electrostatic effects by solvents. *J Am Chem Soc.* 1991;113:4776–82.
- [44] Dennington R, Keith TMJ. *Gaussview.* USA: Gaussian Inc., 2009.
- [45] Seferoğlu Z, Ihmels H, Şahin E. Synthesis and photophysical properties of fluorescent arylstyrylimidazo[1,2-a]pyridine-based donor-acceptor chromophores. *Dye Pigment.* 2015;113:465–73.
- [46] Mataga N, Kaifu Y, Koizumi M. No title. *Bull Chem Soc Jpn.* 1956;29:465–70.
- [47] Lippert E. No Title. *Z Naturforsch Tl A.* 2004;1955:541.
- [48] McRae EG. Theory of solvent effects on molecular electronic spectra. *Frequency Shifts J Phys Chem.* 1957;61:562–72.

- [49] Kothavale S, Sekar N. Novel pyrazino-phenanthroline based rigid donor- π -acceptor compounds: a detail study of optical properties, acidochromism, solvatochromism and structure-property relationship. *Dye Pigment*. 2017;136:31–45.
- [50] Frisch MJ, Trucks GW, Schlegel HB, Scuseria GE, Robb MA, Cheeseman JR, et al. Gaussian 09, Revision C.01. Gaussian 09, Revis B01. Wallingford CT: Gaussian, Inc; 2009.
- [51] Afroz Z, Mj A, Zulkarnain FM, Ahmad A, Ahmad S. DFT XE “DFT” and TD-DFT computation of charge transfer complex between o-phenylenediamine and 3,5-dinitrosalicylic acid. *AIP Conf Proc*. 2016;1731:90038.
- [52] Momicchioli F, Ponterini G, Vanossi D. First- and second-order polarizabilities of simple merocyanines. An experimental and theoretical reassessment of the two-level model. *J Phys Chem A*. 2008;112:11861–72.
- [53] Vidya S, Ravikumar C, Hubert Joe I, Kumaradhas P, Devipriya B, Raju K. Vibrational spectra and structural studies of nonlinear optical crystal ammonium D, L-tartrate: a density functional theoretical approach. *J Raman Spectrosc*. 2011;42:676–84.
- [54] Lytel R. Physics of the fundamental limits XE “fundamental limits” of nonlinear optics: a theoretical perspective [Invited]. *J Opt Soc Am B*. 2016;33:E66–82.
- [55] Kuzyk MG. Physical limits on electronic nonlinear molecular susceptibilities. *Phys Rev Lett*. 2000;85:1218–21.
- [56] Zhou J, Kuzyk* MG. Intrinsic hyperpolarizabilities as a figure of merit for electro-optic molecules. *J Phys Chem C*. 2008;112:7978–82.
- [57] Pérez-Moreno J, Zhao Y, Clays K, Kuzyk MG. Modulated conjugation as a means for attaining a record high intrinsic hyperpolarizability. *Opt Lett*. 2007;32:59–61.
- [58] Meyers F, Marder SR, Pierce BM, Bredas JL, F M, Marder, et al. Electric field modulated nonlinear optical properties of donor-acceptor polyenes: sum-over-states investigation of the relationship between molecular polarizabilities (α , β , and γ) and bond length alternation. *J Am Chem Soc*. 1994;116:10703–14. SR DOI: 10.1021/ja00102a040
- [59] Kuzyk MG. Fundamental limits of all nonlinear-optical phenomena that are representable by a second-order nonlinear susceptibility. *J Chem Phys*. 2006;125:154108.
- [60] Zhou J, Kuzyk MG, Watkins DS. Pushing the hyperpolarizability to the limit. *Opt Lett*. 2006;31:2891–3.
- [61] Kuzyk MG. Using fundamental principles to understand and optimize nonlinear-optical materials. *J Mater Chem*. 2009;19:7444–65.
- [62] Kuzyk MG, Dirk CW. Effects of centrosymmetry on the nonresonant electronic third-order nonlinear optical susceptibility. *Phys Rev A*. 1990;41:5098–109.
- [63] Kogej T, Beljonne D, Meyers F, Perry JW, Marder SR, Brédas JL. Mechanisms for enhancement of two-photon absorption in donor–acceptor conjugated chromophores. *Chem Phys Lett*. 1998;298:1–6.
- [64] Drobizhev M, Meng F, Rebane A, Stepanenko Y, Nickel E, Spangler CW. Strong two-photon absorption in new asymmetrically substituted porphyrins: interference between charge-transfer and intermediate-resonance pathways. *J Phys Chem B*. 2006;110:9802–14.
- [65] Rodrigues CAB, Mariz IFA, Ems M, Afonso CAM, Martinho JMG. Two-photon absorption properties of push–pull oxazolones derivatives. *Dye Pigment*. 2012;95:713–22.
- [66] Makarov NS, Campo J, Hales JM, Perry JW. Rapid, broadband two-photon-excited fluorescence spectroscopy and its application to red-emitting secondary reference compounds. *Opt Mater Express*. 2011;1:551–63.
- [67] Bishop DM, Champagne B, Kirtman B. Relationship between static vibrational and electronic hyperpolarizabilities of π -conjugated push–pull molecules within the two-state valence-bond charge-transfer model. *J Chem Phys*. 1998;109:9987–94.

- [68] Robert WG, Zale R, Lipkowski P, Bartkowiak W, Reis H, Papadopoulos MG. Electronic structure, bonding, spectra, and linear and nonlinear electric properties of Ti @ C 28 2011:10370–81.
- [69] Tathe AB, Gupta VD, Sekar N. Synthesis and combined experimental and computational investigations on spectroscopic and photophysical properties of red emitting 3-styryl coumarins. *Dye Pigment*. 2015;119:49–55.

Supplementary Material: The online version of this article offers supplementary material (DOI: <https://doi.org/10.1515/psr-2018-0032>).

Index

- Ab initio* 20–21, 30, 50, 51, 52, 59, 126, 153, 154, 156, 160, 161, 166, 169, 171, 177, 184
- Absorption coefficient 36, 69, 72, 75
- Absorption maxima 37
- Acceptor 37–40, 42, 43, 45, 128, 137, 203, 204, 206, 207, 208, 221
- Acetylene 88, 99, 108
- Activated Carbon 101
- Activator ions 54
- Adatom 67, 69, 72, 79
- Aerospace 67
- Agglomeration 55
- Aluminium nitrate 51
- AM1 184
- Analysis of the bonding 142
- Analytical 74, 84
- Anharmonic calculation 180
- Anharmonicity 148, 153, 154, 160, 161, 176, 180
- Aniline molecule 156, 166, 171, 176
- Anisotropic/Anisotropy 13, 72, 74, 75, 210, 212, 215
- Annealing 60, 118, 119
- Anthracene 37, 41, 42, 44
- Aqueous Alkanolamine Adsorbents 100
- Arrhenius equation 119
- Arsenic 66, 72
- Attenuation 69
- Band-gap 66, 136
- Band gap energy 52, 59
- Bare germanene 66, 67, 70, 72, 74, 75, 78
- Benchmark database 164
- Benzene molecule 154, 156, 167, 168, 171, 172, 173, 177
- Beryllium 2, 66, 74
- Binding energies/energy 29, 86, 88–93, 95, 96, 98, 99, 102, 115, 116, 137, 140, 142
- Biological 123, 124
- Birefringence 12–15
- BMC-CCSD 168
- Boron-vacancy 113–120
- Brillouin zone (BZ) 1, 68, 114
- BSSE correction 140, 142
- Buckled 65, 66, 67, 69, 78
- Calculated photoluminescence 60
- CAM-B3LYP 36, 39, 43, 138, 139, 141, 210, 215, 217, 218, 221, 223
- CAM-B3LYP/6-31G* 139, 141
- CAM-B3LYP/6-31G* level 138, 139
- C-center 113
- Cerium nitrate 51
- Charge density distribution 60
- Charge localization 52
- Charge-free carriers 60
- Charge-state controlled metastability 116
- Chemical hardness 126
- Chemical potential 59, 103, 115, 126, 127
- CO₂ 86, 94, 99–105, 109, 110, 111
- Collective excitation 4, 7, 10, 69
- Complex formation 137, 138, 139, 141–143
- Computational 2–4, 51–54, 57–60, 68–70, 74, 84, 85, 101, 105, 124, 136, 137, 140, 141, 143, 147, 148, 149, 150, 152, 154, 156, 160, 164, 166, 180, 184, 193–223
- Computational band structure 58
- Concentrations 51, 53, 66, 67, 69, 71, 73
- Conduction band 3, 4, 57, 58, 66, 118
- Conduction band minima (CBM) 4, 118, 119
- Conductivity 67, 69, 72, 77–78
- Configuration 36, 65, 66, 70, 71, 72, 74–79, 105, 113–120, 154
- Coordinatively unsaturated metal sites 94, 96, 110
- Coordinatively unsaturated sites 94
- Copper nitrate 51
- Core-modified metalloporphyrins 142
- Core-modified porphyrins 135–143
- Correlation coefficient 169, 174, 175
- Coupled Cluster 105, 154
- Crystallite size 53, 54, 56
- CuBTC 86
- Cytosine molecules 169, 171
- D4T 183
- Deep well pocket sites 96
- Defect 50, 52, 67, 113–120
- Defect complex 113, 116–118, 120
- Defective cubic spinel structure 61

<https://doi.org/10.1515/9783110568196-012>

- Density functional theory (DFT) 2, 20, 27, 35, 43, 45, 51, 66, 83, 84, 86–92, 95, 96, 98, 99, 102–105, 107, 110, 113, 124, 131, 147, 195
- Density functional theory with the Hubbard correction U (DFT+U) 52
- Device 34–37, 42, 66, 67, 79, 194
- DFT-D 95
- Dicyanopyrazine 33–45
- Dielectric constants 8, 9, 67, 72, 73, 74
- Diffraction rings 56
- Dihydroacridine 37
- Dipole moment 21, 126, 128, 160, 194, 195, 200, 201, 202, 208, 210, 212, 215, 218, 222, 223
- Dirac cone 67
- Direct bandgap transition
- Distortions 54, 137
- Donor 37–43, 45, 128, 137, 203, 204, 206–208, 218, 221, 222
- Donor-acceptor 37, 42, 43, 137, 221
- Doped alumina 50
- Doping 1, 52–56, 58, 59, 66, 67, 69, 71–76, 78, 79, 89–92, 102, 104
- Doping sites 66, 67, 73, 79
- Double hybrids 150, 165, 180
- EELF 4, 10–12, 15
- Electric field 1–15, 35, 67, 68, 219
- Electromagnetic 4, 33, 68
- Electromagnetic wave 68
- Electron energy loss spectra 76
- Electronegativity 61, 126, 203, 210
- Electronic cloud 60
- Electronic features 143
- Electronic properties 4, 35, 45, 53, 66, 67, 78, 137, 138, 143, 194
- Electrons 7, 10, 14, 34, 35, 38, 39, 52, 76, 84, 138, 194, 215, 217
- Emission 33, 34, 37, 49, 50, 58–60, 94, 100, 196–200, 204, 218
- Energy 1, 3–5, 7–10, 13, 14, 21, 29–31, 33–37, 39, 41–45, 51, 52, 56–60, 67–69, 72–78, 83–92, 94, 95, 98–100, 103, 114–119, 124, 126, 127, 129, 131, 137, 139, 150, 152–154, 162, 180, 203, 207, 208, 215, 217, 223
- ESFF procedure 162
- Excitation energy 28, 33, 34
- Experimental 1, 21–24, 36, 49–62, 78, 83, 86, 93–99, 101, 104, 105, 113, 114, 119, 120, 124, 125, 128, 131, 137, 147, 153, 154, 156, 161, 163, 168, 169, 172, 174, 175, 176, 181–184, 195, 196, 200, 202, 203, 208, 219, 221
- Experimental photoluminescence 60
- Fabricate 36, 66, 67, 79
- Fermi energy 1, 59
- Fermi level 67, 115, 117, 118
- Field effect transistor(s) 38, 66
- 5-fluorouracil 172
- 5-iodouracil 181, 182
- Fluorescence 33–45, 51, 194
- Fluorescence efficiency 37
- Fluorescence lifetime 34
- FMOF-1 86, 87
- Force constants 153, 156, 159–163, 180, 184
- Formation energies/energy 70, 72, 78, 114–119
- Franck-Condon principle 59
- Frequency 3, 7, 21, 26, 33, 36, 57, 68, 72, 77, 124, 162, 172, 180, 217, 218
- FT-IR 128
- Full width at half maximum 54
- Gallium 66, 72–73
- Gamma-alumina 54
- Gaussian 180
- Gaussian 09 program 152
- GaussView 124, 152, 195
- Germanane 67
- GGA 2, 4, 36, 86, 92, 99, 116, 149, 150
- Gradient Approximation 2, 68, 99, 116, 149, 150
- Grain size 56, 61
- Grain size diameter 56
- Graphene 1, 2, 65, 66, 67
- Halothane 181
- Harmonic wavenumber 21, 148, 152, 154, 155, 156, 159, 163, 164, 180, 184
- Heterocyclic 123, 126, 129
- Heterocyclic ring 126, 129
- Hexagonal 65, 66, 69, 72, 89
- HF 123–131, 150, 152, 156, 166, 168, 171, 176, 179, 184
- Higher stability of the Zn_6S_6 -ZnP(S)₄ complex 140
- Highest occupied molecular orbital (HOMO) 21, 35, 124, 130
- High-resolution transmission electron microscopy (HR-TEM) 51, 56, 61

- HKUST-1 86, 95, 99, 102, 105
 Hole-injection layer 35
 Hole-transport layer 35
 HSE06 114, 116, 120
 Huge 2, 67, 78, 162
 Hybridization 66
 Hydrogen 21, 23, 29, 88–94, 102, 104, 107, 108, 200, 207
 Hyperconjugative 131, 208
- Infrared absorbance 72
 Intensities 21, 25, 26, 53, 72, 74, 124, 152, 153, 156
 Interfrontier molecular orbital energy gap 41, 45
 Intersystem crossing (ISC) 34, 37
 Intramolecular charge transfer 44, 194
 IRMOF 89, 90, 94
- Jablonski Diagram 34
- Kramers-Kronig relation 4, 68
 Kubelka-Munk plot 58–59
- Larger NPs 143
 Lattice parameter 52
 Lattice sites 61, 66, 79
 Lattice strains 53, 54
 LDA 96, 99
 Light-emitting devices 34
 Linear scaling equation (LSE) 163, 168–179, 183, 184
 Linkers 89, 90, 95, 102–105, 111, 137, 141, 142
 Local Density Approximation (LDA) 52, 60, 92, 96, 98, 99, 149
 Loss function 4, 10–12, 76
 Lowest unoccupied molecular orbital (LUMO) 21, 27–29, 35, 37, 39, 40–45, 124, 126, 127, 129, 131, 200, 203–205, 208
 Lowest-energy transition 42
 Low-lying triplet 36
 LSE 168
 Luminescence/Luminescent 33, 34, 35, 37, 49, 50, 51, 194
- M052X 151, 170, 177
 M062X 151, 174, 177, 183
 M06L 151
 Magnetic properties 66, 67
 Magnification 55
- Maximum 4, 5, 36, 54, 58, 67, 72, 74–78, 115, 196, 218, 223
 Mean absolute deviation 23, 155
 Mechanical Force Field 160, 161
 Metalloporphyrins and their derivatives 136, 137, 141
 Metal-organic frameworks 83, 89, 101, 105, 106
 Metal-organic Frameworks:HKUST-1 86, 95, 99, 102, 105
 Metastability/Metastable 49, 113–120
 Metastable peaks 113
 Methane 88, 94–98, 108
 Miller indices 56
 MILs 102
 Minnesota functionals 168
 Minnesota Hybrid 150
 Mobility 2, 66
 Modes of binding 137
 Modification 14, 37, 67, 72, 73, 79, 105, 123, 161, 162, 194, 222
 Modulations 79
 Møller-Plesset 150
 MOLVIB program 161
 Monkhorst-Pack 2, 52, 68, 114, 116
 Mono-layers 65–79
 MP(P)4 compounds 137
 Mulliken bond lengths 54
 Multilevel method 168
 Multi-symmetry defects 118
- Nanoassemblies 136, 137, 141
 Nanopowders 50
 Nanosheet 66, 67, 72, 78, 79
 Nano-technology 66
 Natural bond orbital analysis(NBO) 130, 140, 142, 206, 223
 NBO charges 140, 142
 Nearly spherical 55, 61
 Negative 7, 13, 15, 35, 69, 78, 94, 105, 126, 128, 137, 139–142, 152, 156, 166, 171, 176, 195, 206, 217, 221, 223
 NIST 164
 Non-radiative triplets 37
 NP coordination to the core-modified Zn-porphyrin 138, 141
- Open Metal Sites 94, 96, 99
 Optical 1–15, 36, 49, 50–52, 57, 59–60, 65–79, 143, 193–223

- Optical absorbance 67
 Optical absorption spectrum 59
 Optical energy band gap 57
 Optical properties 1–15, 50–52, 65–79, 193–223
 Optimization 2, 21, 36, 69, 95, 124, 151, 152, 161, 180, 195, 215
 Opto-electronic 78, 79
 Orbitals 4, 5, 10, 37, 39, 40, 42, 43, 45, 61, 129–131, 140, 143, 150, 203, 204, 206, 207
 Organic films 35
 Organic Light Emitting Diode 35
 Organic semiconductors 36, 38
 Oscillator strengths 26, 28, 36, 196, 200
 Overall scale factor 149, 163, 167
 Oxygen vacancies 60
- Parallel 7–10, 12–15, 68, 72–79, 136, 194
 Parallel polarization 7–10, 12, 13, 15, 68, 72–78
 Partial density of states (PDOS) 2, 4, 5
 PBE functional 150
 PCN-11 95, 98
 Peaks 10, 53, 54, 56, 67, 72, 75, 76, 78, 118, 119
 Perpendicular 3, 5, 7–15, 61, 68, 72, 74–79, 136
 Perpendicular polarization 7–15, 68, 72, 74–79
 Phenanthrene 37, 40
 Phenanthrene pyrazine 40
 Phenoxazine 37
 Phenyl 96, 126, 129, 203
 Phosphorescence 34
 Photoexcitation 57
 Photoluminescence spectroscopy (PL) 51
 Physisorption 85, 88, 89
 Planarity 2, 41, 44, 137
 Plasma frequencies/frequency (PF) 7–9, 74
 Polarizability 128, 195, 208, 210, 212, 215, 217, 219, 222, 223
 Polarization 3, 7–15, 68, 72–79, 92, 102, 148, 152, 179, 219, 222
 Polarization functions 179, 219
 Polynomial scaling equation (PSE) 163, 175, 177, 183, 184
 Porphyrin-QD nanocomposites 137
 Positive 7, 13, 35, 69, 78, 116, 128, 137, 141, 156–158, 166, 171, 176, 195, 205, 206, 217, 221, 223
 Potential energy surface 36, 85, 152, 154, 180
 Predict the spectra 160
 Predictive modes 161
 Pre-exponential constant 119
- Pristine 1, 2, 4, 55, 59, 60, 66, 67, 69, 70, 72–75, 78, 79, 115, 116
 Pristine gamma-Al₂O₃ 55, 59
 Prominent 67, 75, 78, 137
 PSE 175
 PW91 86, 150
 Pyrene 37, 41, 42
- Quantum dots 136, 137, 141
- Radiation machineries 67
 Radiative exciton fraction 36, 37
 Red shift 58, 72, 183, 194, 196
 Reflectance spectrum 57
 Reflectivity 67, 69, 72, 76, 77
 Reflectivity modulation 69, 77
 Refractive index 4, 12, 13, 68, 72, 200, 218
 Resonant 75
 Response 36, 74–76, 78, 79, 215, 217, 223
 Reverse intersystem crossing 37
 Reversible transformation 120
 Rigid 40, 83, 85
 Root-mean-square (rms) error 155
 Rotational constants 126
- Scale factors 148, 156, 159–167, 172, 176, 177, 179, 184
 Scaling 26, 36, 147–184
 Scaling procedures 147–184
 Scanning electron microscopy (SEM) 51
 SCFEM 175
 Selected area electron diffraction (SAED) 51, 56, 61
 Selectivity 100, 103–105
 Selenium 123–131
 Self-Consistent-Field 3, 68, 153
 SEM analysis 55
 Semi-conductor 4, 36, 38, 39, 42, 52, 66, 67, 118, 135–143
 Semiconductor quantum dots 137, 141
 Semiempirical methods 171, 184
 SIESTA 2, 68
 Silicene 2, 65–67
 Singlet state 34
 Singlet–triplet exchange energy 42
 Sol-gel 50, 51, 55, 61
 Solid state 181–184, 194
 Specific scale factor 163, 175, 176, 177
 Specific scale factors for each mode (SCFEM) 163, 175–177, 180, 184

- Spectrum 20, 26, 27, 33, 56–59, 69, 72, 75–78, 113, 119, 148, 156, 162, 163, 165, 181
 SQM technique 161
 Stability 2, 67, 84–86, 92, 100, 101, 105, 127, 129, 131, 140, 142
 Standard deviation 155, 156
 Static dielectric constant (SDC) 7–9
 Stiffness 2
 Structural analysis 53
 Structures 1–5, 8–10, 15, 21, 23, 36, 38, 40–44, 50, 53, 54, 60, 61, 65–70, 72–74, 76–78, 83–87, 89–91, 94, 95, 96, 98, 101, 105, 114, 123–131, 136–139, 141, 143, 148, 152, 169, 171, 172, 176, 181, 194, 195, 205, 206
 Sub-lattice 1, 2, 66, 67, 69, 79
 Sulphur 123–125, 127, 131
 Superlattices 66–67

 TADF 37, 38, 40, 42–45
 TD-DFT 27, 36, 43
 Tetracoordinated 2, 14
 Tetramer form 181, 182
 The second order perturbative method 180
 Theoretical 20, 21, 23, 25, 52, 61, 67, 78, 83, 86, 93, 94, 103–105, 113, 114, 128, 131, 137, 147, 148, 149, 152, 156, 162, 163, 169, 172, 175, 181, 195, 215
 Theoretical prediction 147
 Thermally activated delayed fluorescence 33–45
 Thermodynamic transition levels 59, 117–119
 Thiazolidinone 123, 124
 Thiophene 37, 40, 41, 43
 Thiophene oligomers 37, 43
 TLSE 172, 175, 177, 183, 184
 Toluene molecule 176

 Transferability 159, 160, 162, 169
 Transition levels 59, 117–119
 Transition state energy 119
 Triphenylamine 37, 42
 Two-dimensional (2D) 1, 65
 Two-dimensional materials 1, 65

 Ultra-violet region 72
 Uniform scaling 163, 172
 Unity 78, 200, 202, 223
 Uracil molecule 156, 171, 172, 175, 177, 184

 Vacancy 69, 74–76, 78, 113, 114
 Vacuum 3, 68, 69, 94
 Valence band 3, 57, 66, 118
 Valence band maxima (VBM) 4
 Vibrational assignments 25, 148, 152
 Vibrational wavenumbers 148, 150–153, 155, 156, 159, 166, 169, 179, 180
 Visible region 33, 75
 Visible spectrum 58

 Wilson notation 176

 X3LYP 89, 151, 169, 175, 177, 183, 184
 XCrySDen 50, 53
 X-ray 23, 50, 51, 54, 67
 X-ray diffraction (XRD) 50, 53–54

 Zeolites 84, 88, 92, 101, 105
 Zero frequency 72, 217
 Zero-point energies 148
 ZIFs 92, 102, 103
 ZnP(P)4 species 137, 139, 141
 Zn-S bond distances 139, 142

